Aggregation, Chirality and Reduction of Nonplanar Polycyclic Aromatic Hydrocarbons

Dissertation zur Erlangung des

naturwissenschaftlichen Doktorgrades der

Julius-Maximilians-Universität Würzburg

vorgelegt von

Rebecca Renner

aus Lauda-Königshofen

Würzburg, 2021

Eingereicht bei der Fakultät für Chemie und Pharmazie:

17.08.2021

Gutachter der schriftlichen Arbeit:

1. Prof. Dr. Frank Würthner
2. Jun.-Prof. Dr. Ann-Christin Pöppler

Prüfer des öffentlichen Promotionskolloquiums:

1. Prof. Dr. Frank Würthner
2. Jun.-Prof. Dr. Ann-Christin Pöppler
3. Prof. Dr. Holger Helten

Datum des öffentlichen Promotionskolloquiums:

04.10.2021

Doktorurkunde ausgehändigt am:

_____

List of Abbreviations

2D	two dimensional
3D	three dimensional
AFM	atomic force microscopy
BHJ	bulk-heterojunction
CD	circular dichroism
CNT	carbon nanotube
CPL	circularly polarized luminescence
CPP	cycloparaphenylene
CT	charge transfer
CV	cyclic voltammetry
DCM	dichloromethane
DCTB	*trans*-2-[3-(4-*tert*-butylphenyl)-2-methyl-2-propenylidene]malononitrile
DFT	density functional theory
DIP	direct insertion probe
Dipp	2,6-diisopropylphenyl
DMF	*N*,*N*-dimethylformamide
DOSY	diffusion ordered spectroscopy
ee	enantiomeric excess
ESI	electrospray ionization
Fc	ferrocene
GNR	graphene nanoribbon
HBC	hexabenzocoronene
HOMO	highest occupied molecular orbital
HPLC	high-performance liquid chromatography
ICT	intermolecular charge transfer
in silico	experiment performed on a computer
lat.	Latin
LUMO	lowest unoccupied molecular orbital
MALDI	matrix assisted laser desorption ionization
MCH	methyl cyclohexane
NBI	naphthalene bis(dicarboximide)
NFA	non-fullerene acceptor

NIR	near infra-red
NMR	nuclear magnetic resonance
OLED	organic light emitting diode
OSC	organic solar cell
OTFT	organic thin-film transistor
P3HT	poly-3-hexylthiophene
PAH	polycyclic aromatic hydrocarbon
PBI	perylene bis(dicarboximide)
$PC_{61}BM$	[6,6]-phenyl-C_{61}-butyric acid methyl ester
PCE-10	Poly[4,8-bis(5-(2-ethylhexyl)thiophen-2-yl)benzo[1,2-b;4,5-b']dithiophene-2,6-diyl-alt-(4-(2-ethylhexyl)-3-fluorothieno[3,4-b]thiophene-)-2-carboxylate-2-6-diyl)]
PMI	perylene monodicarboximide
ppm	parts per million
SWV	squarewave voltammetry
TA	transient absorption
TAPA	2-(2,4,5,7-tetranitro-9-fluorenylidene aminooxy) propionic acid
TAPP	tetraaza peropyrene
TBAHFP	tetrabutylammonium hexafluorophosphate
TCE	1,1,2,2-tetrachloroethan
TCSCP	time-correlated single-photon counting
TD-DFT	time-dependent density functional theory
THF	tetrahydrofuran
TOF	time of flight
TPA	*n*-tetradecylphosphonic acid
UV	ultraviolet
Vis	visible

Physical Constants, Variables and Units

α_{agg}	molar fraction of aggregated molecules
a.u.	arbitrary unit
c	speed of light
c_0	concentration
ε	molar extinction coefficient
ε_0	vacuum permittivity
Φ_f	fluorescence quantum yield
FF	fill factor
$\Delta G^{\ddagger}$	free enthalpy of activation
g_{lum}	luminescence dissymmetry factor
h	Planck constant
ΔH	molar enthalpy
J_{SC}	short-circuit current
k	rate constant
K_a	association constant
K_D	dimerization constant
λ	wavelength
μ_{eg}	transition dipole moment
N_A	Avogadros number
$\Delta\tilde{\nu}_{Stokes}$	Stokes shift
$r_{C\text{-}C}$	center-to-center distance
σ	cooperativity factor
ΔS	molar entropy
τ_F	fluorescence lifetime
$t_{1/2}$	half lifetime
T_c	coalescence temperature
V_{OC}	open-circuit voltage

Table of Contents

Chapter 1

Introduction and Aim of the Thesis

The increased awareness about our environment over the course of the last decades came along with the continuous investigation of polycyclic aromatic hydrocarbons (PAHs) and daily news about their ubiquitous presence as well as their harmfulness.[1,2] PAHs originate from natural as well as antropogenic sources due to the incomplete combustion of predominantly organic materials like oil, coal and wood. They can be detected in the atmosphere,[3] surface water,[4] soil[5] as well as in food especially in grilled meat.[6] Since the industrialization, the share of man-made PAH emissions increased globally due to the higher energy demand resulting from increased industrial activities and urbanization until the 1990s, when protests from the general public and new regulations led to a decrease of the overall emissions.[7] Many of these molecules are highly toxic, mutagenic and carcinogenic while also being highly persistent in the environment and bioaccumulative in organisms.[8,9] This poses a challenge to preserve the health and ecosystems of all organisms as well as to improve the air quality all over the world. Generally, PAHs originating from combustion are found as complex mixtures, but due to the increased interest in their properties, numerous PAHs are nowadays manufactured and sold as individual compounds.[10]

Despite their negative reputation, PAHs have drawn significant attention from different fields of sciences by serving as model compounds in the development of elementary molecular orbital theory,[11,12] as chromophores in combination with auxochromic groups in organic dye-stuff chemistry,[13,14] as carbon-containing material in interstellar space,[15,16] in cancer theranostics[17,18] as well as by opening an entry into chirality with their helical derivatives.[19-21] Especially since the ground-breaking work by Geim and Novoselov on graphene the field of nanographenes and graphene nanoribbons (GNRs) received a significant upturn. Graphene is a two-dimensional single layer of sp^2-hybridized carbon atoms, which was obtained by exfoliation of graphite and the work on this extraordinary carbon allotrope was later awarded with a Nobel Prize in physics.[22-24] Small PAHs can be considered graphene cut-outs with diameters of 1 to 100 nm and are of interest for the bottom-up synthesis of graphene nanoribbons (Figure 1). They also help in the deduction of important structure-properties

relationships to optimize the graphene edges and thus the physical properties thereof.[25-27] GNRs and PAHs themselves exhibit beneficial properties for material sciences, which is impressively illustrated by their versatile application as semiconducting materials in organic electronics like organic light emitting diodes (OLEDs),[28,29] organic thin-film transistors (OTFTs)[30,31] and organic solar cells (OSCs).[32,33]

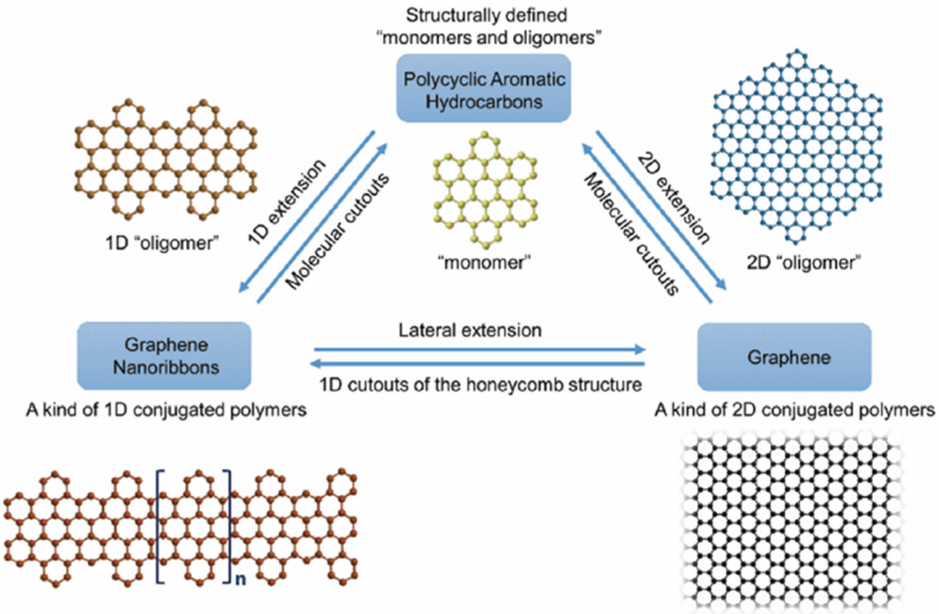

27]. Copyright 2019, Springer Nature.

While PAHs are usually planar, scientists have long been intrigued by the nonplanar arrangement of π-conjugated carbon atoms, especially since the 1996 Nobel Prize in chemistry for the discovery of fullerenes[34,35] as well as the 2008 Kavli Prize in Nanoscience for carbon nanotubes (CNTs).[36] These hydrocarbons exhibit outstanding electronic, thermal and mechanical properties and accordingly new ways to introduce distortion into the π-system of GNRs and PAHs are thoroughly investigated. These large nonplanar systems are usually extracted from soot containing the desired carbon networks as well as smaller PAHs which can be obtained by laser ablation of graphite or chemical vapor deposition. These methods are quite laborious and thus new methods for the bottom-up synthesis of tailored large, contorted carbon-containing materials are highly desired. The search of new synthetic pathways has picked up especially since fullerene C_{60} and its more soluble derivative [6,6]-phenyl-C_{61}-butyric acid methyl ester ($PC_{61}BM$) have been established as state-of-the-art acceptor materials for OSCs, leading to an increased demand for highly pure fullerenes as well as other distorted PAHs. In *Chapter 2* various methods for the introduction of distortion into the π-system of PAHs are

elucidated and the intriguing opto-electronic properties of nonplanar organic imides are illustrated.

In this regard the exact understanding of intermolecular interactions in solution as well as in the solid state between nonplanar PAHs is extremely important to further enhance the performance of customized devices built from PAHs. One extensively studied cut-out of fullerene C_{60} with promising properties for application in organic materials is corannulene, which consists of a five membered central ring surrounded by five annulated benzene rings. Studies suggesting the use of corannulene derivatives as potential electron acceptors in organic electronic devices were substantiated by the successful incorporation of electron-withdrawing naphthalimide substituted corannulene in OSCs, although these devices only showed moderate performance.[37] Therefore, one aim of this thesis was to investigate the interactions between novel corannulene derivatives in solution as well as in the solid state by changing the imide residue of a literature known extended corannulene dicarboximide from the sterically demanding 2,6-diisopropylphenyl (Dipp) to a more flexible and less bulky alkyl chain in order to evaluate the π-π-interactions of the PAHs in solution as well as in the solid state, in order to obtain a better understanding of the packing and possible charge transport in potential applications. Accordingly, the goal of the work presented in *Chapter 3* is to synthesize and investigate an electron-poor corannulene bis(dicarboximide) based on previously published work but with higher solubility and less steric encumbrance in imide position to enable self-assembly in solution (Figure 2).

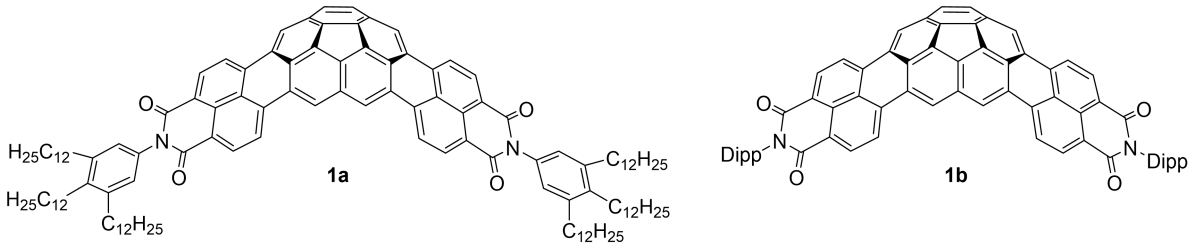

Figure 2 Chemical structures of corannulene bis(dicarboximides) **1a** and **1b** described in *Chapter 3* (Dipp = 2,6-diisopropylphenyl).

Perylene bis(dicarboximides) (PBIs) are among the most studied organic chromophores of the rylene dyes based on a PAH system due to their high thermal, chemical and photochemical stability, electron-deficient character, and intriguing optical properties such as visible light absorption and high fluorescence quantum yields.[14, 38, 39] Furthermore, they are readily functionalized in *bay* position to distort the originally planar chromophore π-surface, introduce axial chirality and modify the energy levels of the frontier orbitals. Depending on the number and type of substituents, the *P*- and *M*-atropoenantiomers of the chiral twisted PBIs are either

stable under ambient conditions or able to racemize. To obtain further insights into the conformational stability, structure and chiroptical properties of heavily twisted PBIs the aim of *Chapter 4* was the design, synthesis, and optoelectronic investigation of various fourfold directly arylated PBIs (Figure 3) by substitution in *bay* position with smaller hydrocarbons with different steric demand, i.e., benzene, naphthalene and pyrene, which should be separable by chiral high performance liquid chromatography (HPLC).[40]

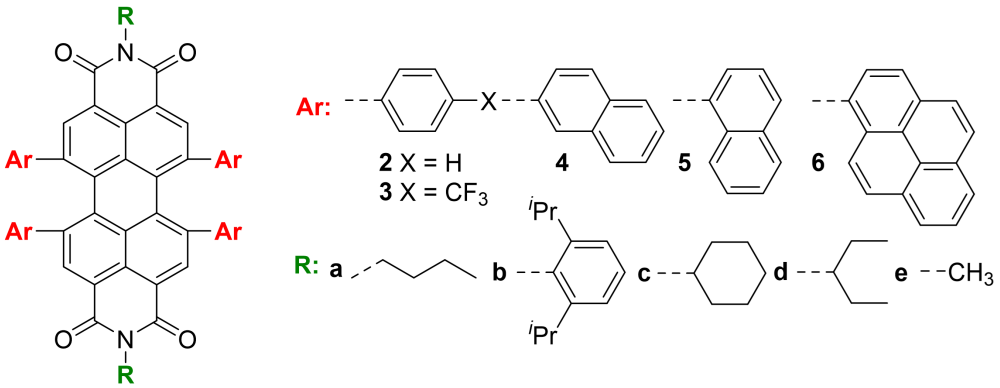

Figure 3 Chemical structures of tetraarylated PBIs **2a-6a** investigated in *Chapter 4*.

PBIs are furthermore used as model systems in many fundamental studies for electron- and energy-transfer dynamics, e.g., for the generation of molecular hydrogen[41] and in light-harvesting systems for artificial photosynthesis,[42] which rely on the reducibility of the chromophore. Additionally, PBIs have gained more recognition as non-fullerene acceptors (NFAs) for energy storage and conversion in organic electronics, also depending on readily available reduced states of the PBIs. As of yet, no concise study concerning the optical and electronic properties of differently core-substituted PBIs in the neutral as well as the mono- and dianionic state in solution is available, which also elucidates the origin of the different optical transitions observed in the absorption and emission spectra. Thus, in *Chapter 5*, the investigation of five PBI derivatives with different frontier energetic levels to produce a reference work of reduced PBIs was tackled (Figure 4).

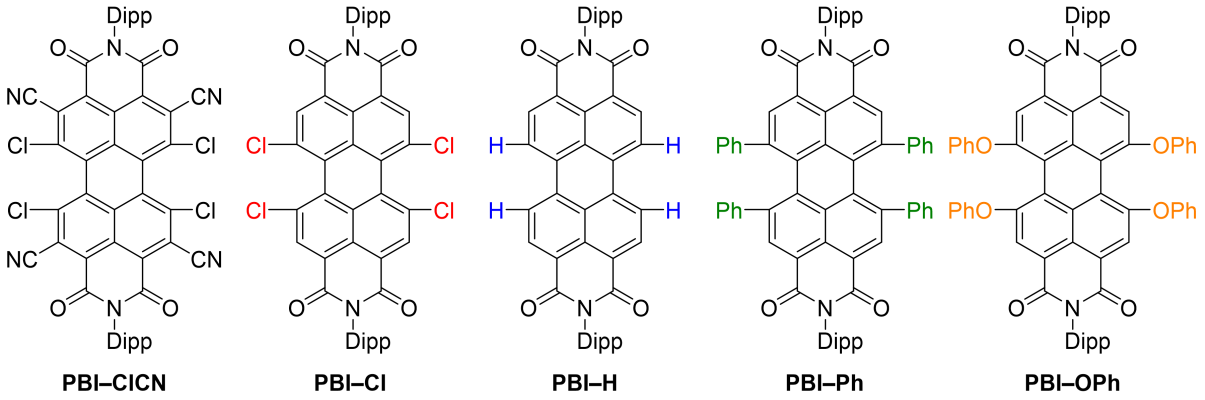

Figure 4 Chemical structures of **PBI-ClCN**, **PBI-Cl**, **PBI-H**, **PBI-Ph** and **PBI-OPh**, which are discussed in their neutral and reduced states in *Chapter 5*.

Chapters 6 and *7* summarize and conclude this work in both English and German.

Chapter 2

State of Knowledge

2.1. Polycyclic Aromatic Hydrocarbons

Polycyclic aromatic hydrocarbons (PAHs), a group of substances consisting of fused aromatic rings with a high carbon content and few or no heteroatoms embedded in the framework,[32] have attracted the research interest of scientists all over the world. Due to their high stability, rigid structure, and their unique electronic and optoelectronic properties, they are suitable candidates for the application in organic electronics, biological systems as well as supramolecular building blocks for intriguing structures.[43,44] PAHs can be considered small cut-outs from graphene.[45] The aromatic rings in these systems can be connected via *cata*- (linear) or *peri*- (branched) condensation, which can be defined by connecting the centers of each aromatic ring. If the resulting graph contains no cycle, the PAH is *cata*-condensed, while a cycle is present in the schematic diagrams of *peri*-condensed PAHs (Figure 5a).[46] They have been effectively employed as molecular precursors for the synthesis of larger graphene nanoribbons (GNRs) via bottom-up synthesis, which exhibits a higher precision concerning the exact structure of the GNR compared to the top-down approach of cutting graphene or unzipping carbon nanotubes (CNTs).[27] The edges of PAHs offer a variety of different topologies, which heavily influence their physical and chemical properties. The typical edges in planar PAHs include the bay- or armchair-edge, the *K*-area, which is a carbon-carbon double bond that is not assigned to a Clar sextett, and the *Z*-region, which is also called zig-zag edge. Further edge topologies found prevalently in nonplanar PAHs are the cove and fjord regions, as they introduce distortion into the π-system due to steric encumbrance (Figure 5b).

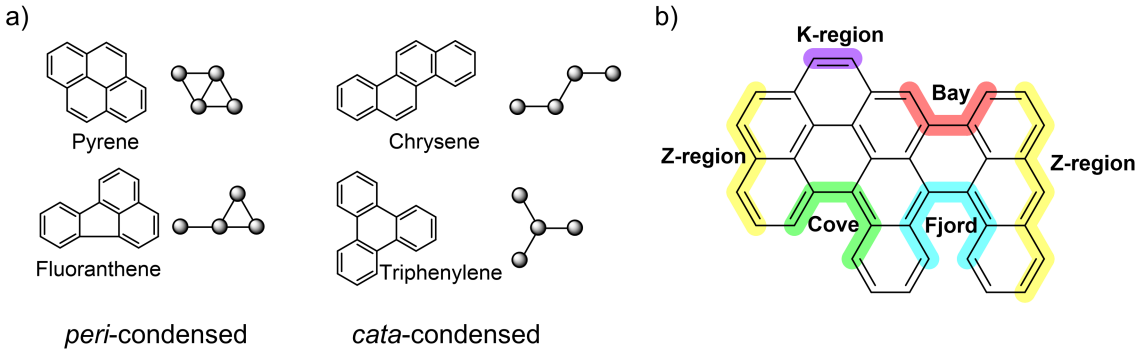

47]. Copyright 2003 CABI.

The characteristics of these small hydrocarbons as well as the GNRs derived thereof, can be tailored by rational design and synthesis, allowing for a large variety of different sizes and shapes in benzenoid PAHs, as well as their straightforward adjustment of the electronic and optical properties.[48] Depending on the steric interactions between the different edges and attached groups and the presence of aromatic rings, which are smaller or larger than six-membered rings in the π-system, planar and non-planar PAHs can be realized. While the planar systems exhibit high rigidity and poor solubility due to strong π-π-interactions which often result in the formation of extended aggregates, the non-planar PAHs are usually highly soluble in common organic solvents[49] and less likely to form extended structures in solution or the solid state.[50] Thus, non-planar PAHs are easier to process from solution and are less prone to phase separation than their planar congeners. Furthermore, the π-overlap across the PAH core is altered in the contorted derivatives, effectively lowering the bandgap by variation of the highest occupied molecular orbital (HOMO) and lowest unoccupied molecular orbital (LUMO). The propensity for intermolecular charge-transfer (ICT), the Stokes shift as well as the semiconducting properties are enhanced in non-planar derivatives compared to their planar congeners,[51] which are desired traits for the application in functional organic materials.

2.2. Introduction of Nonplanarity into PAHs

2.2.1. Positive and Negative Curvature in PAHs

Upon the introduction of rings smaller or larger than six-membered into the π-system of PAHs, the molecules usually adopt a contorted structure to relieve the strain with only rare exceptions like the planar fluoranthene or acenaphthene. The curvature of the π-surface is commonly described by mathematical terms as Gaussian-positive, if four- or five-membered rings are introduced into the system and Gaussian-negative, if larger rings, especially seven-membered rings are introduced into the system to induce a hyperbolic saddle shape.[52] A general trend observed for systems containing rings smaller than the six-membered carbon rings is the higher strain and thus instability of the systems due to the pyramidalization of the carbon atoms. While this is less of a problem if five-membered rings are introduced, the energetic penalty for the pyramidalization is significantly higher upon insertion of even smaller rings into a graphitic system. Due to the highly strained cup-like structure of four-membered ring containing PAHs, the only successful example of the bottom-up synthesis of a small *cata*-tetrabenzoquadrannulene, which is also called tetrabenzo[4]circulene **7**,[53] utilizes the favorable aromatization during the cobalt-promoted cyclotrimerization of four benzenoid rings to overcome the high energy barrier (Figure 6a). Nevertheless, this reaction suffers from low yields, which hamper elaborate investigations on the utilization of this interesting molecule.[54,55] Thus, usually five-membered rings are embedded in the carbon framework to introduce positive curvature due to the smaller strain energies and resulting higher stability as well as better availability of the precursors. The two most prominend examples of such Gaussian-positive PAHs are corannulene and sumanene (Figure 6b). They can be regarded as cut-outs of the fullerene C_{60}, which is also commonly called buckyball, and are accordingly often denoted as buckybowls. Corannulene, also known as [5]circulene, is a C_{5v} symmetric PAH consisting of the central five-membered ring, the heart (*lat.* cor), within five six-membered rings (*lat*. annula) and has seen a constant increase of interest after the first synthesis by Barth and Lawton in 1966[56] and through successive improvement of the synthesis up to kilogram scale.[57,58] The C_{3v} symmetric sumanene consists of a central benzene ring fused in alternating manner to three additional benzene and three cyclopentadiene rings, making the molecule look like flower petals, hence the name (*suman* meaning flower in Hindi and Sanskrit).[59] Sumanene possesses the advantage of three benzylic positions, which facilitate the functionalization compared to corannulene, but only in 2003 the successful synthesis has been reported by Sakurai and Hirao[60] and thus has been made commercially available since then.

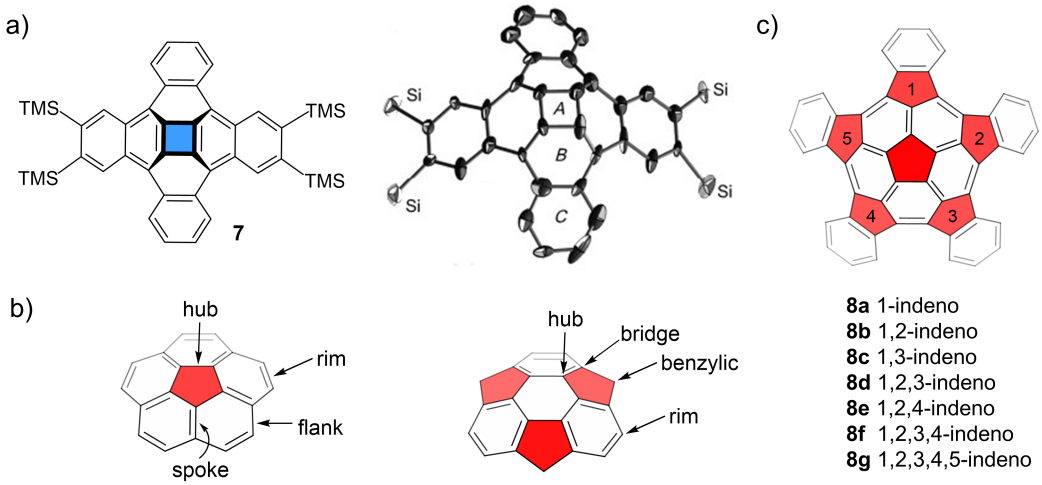

54]. Copyright 2009, John Wiley and Sons.

The introduction of the five-membered rings creates a disruption of the conjugation and geometry of sumanene and corannulene due to inefficient overlap of the p-orbitals and increased s-orbital character in the sp^2 hybridized carbon atoms resulting in an energetic decrease of the LUMOs and an enhancement of the electron accepting properties. Due to the concave and convex faces in the buckybowls, stereoelectronic effects concerning the endo- and exo-substitution can be observed. A dipole moment of 2.07 D in corannulene and 2.70 D in sumanene were measured, making them promising candidates for chiral recognition and ferroelectric materials.[61-64] While sumanene exhibits a bowl-to-bowl inversion barrier of 82 kJ mol^{-1} at 144 °C and thus rigidity in its structure due to the three cyclopentadienyl rings, corannulene exhibits a fast bowl-to-bowl inversion with an energy barrier of merely 43 kJ mol^{-1} at –64 °C,[65] which might allow for the development of molecular switches and chemical machines. The bowl-to-bowl inversion of corannulene is heavily influenced by the substitution of the molecule and the presence of heteroatoms in the core structure to the point, where the geometry of the system is locked, and no bowl-to-bowl inversion is observable anymore.[66,67] Further examples of Gaussian-positive curvature in buckyballs can be found primarily in larger derivatives of corannulene, including the family of seven variably substituted indenocorannulenes **8a-g** in which the bowl depth as well as the inversion barrier are increasing with a higher number of annulated groups from 0.87 Å for pristine corannulene up to 1.43 Å for **8g**, which is only slightly smaller than the 1.48 Å in fullerene C_{60} (Figure 6c).[68] For the synthesis of these molecules, usually corannulene is used as precursor. On the contrary, larger derivatives of sumanene like circumtrindene[69] and hemifullerene[70,71] utilize other small precursor molecules which are more readily available for their synthesis.

Due to its unique curved structure and large convex and concave π-surface corannulene and congeners thereof are commonly used in supramolecular chemistry. Pristine corannulene exhibits a lower degree of curvature than fullerene C_{60} allowing for the formation of curved-π-curved-π interactions. However, no evidence of such 1:1 complex formation in solution has been found indicating that the interactions are not strong enough to overcome the entropy penalty needed for the complex formation. By modification of the electronic properties by substitution with 2-naphthylthio- as well as 4-methoxyphenylthiogroups, fullerene hosts **9** and **10** were obtained (Figure 7), which were able to bind C_{60} with an association constant K_a of up to 474 M^{-1} for a 1:1 complex with **9** in toluene-d^8, due to enhanced face-to-face π-π-interactions of the methoxyphenyl groups compared to the sterically demanding naphthyl substituents in **10**.[72] This method was further investigated by the group of Xie, who synthesized a flexible decapyrrylcorannulene **11**, in which the corannulene mimics the palm of a hand while the ten pyrryl groups resemble ten fingers catching different fullerenes. Due to its electron-rich nature, the fitting shape, flexibility as well as additional π-surface contacts, **11** is able to engulf the 15 most common unsubstituted, substituted, hetero- and dimeric fullerenes in the solid state, as proven by single crystal X-ray analysis in a 2:1 complex. In solution, fullerene C_{60} as well as C_{70} form 1:1 complexes with **11** with association constants K_a of 8252 and 5686 M^{-1} in toluene-d^8 respectively, showing the higher binding tendency compared to **9** and **10**.[73]

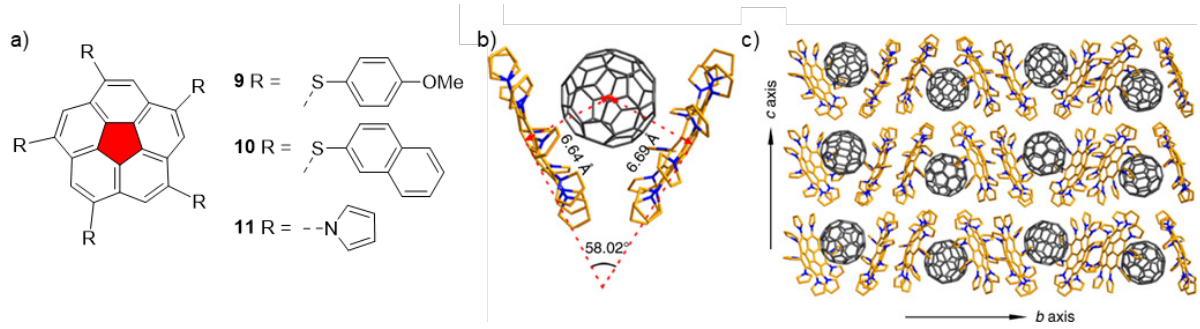

73].

PAHs with negative Gaussian curvature can be obtained by e.g., the introduction of seven-membered rings into a benzenoid structure, the simplest example being [7]circulene **12**, which is also called pleiadannulene[74] and exhibits a saddle shape (Figure 8a).[75] This molecule has been synthesized by the Nagazaki group in 1983 for the first time and was subsequently investigated by X-ray crystallography to confirm the distorted shape of the molecule.[76,77] Several smaller PAHs containing seven-membered rings have been obtained by bottom-up synthesis employing palladium catalyzed cross-couplings with subsequent arylation

reaction,[78] oxidative coupling[79,80] and vinylnaphthyl π-extension.[81,82] In some cases, the formation of large seven-membered ring-containing PAHs is achieved by the coupling of smaller precursors already containing seven-membered rings[83] or the insertion of heteroatoms to obtain heteroaromatic PAHs.[84] Similar to [7]circulene, [8]circulene is predicted to exhibit a negative curvature and is even more strained than the former, making the synthesis challenging and thus has not been achieved yet.[85] Heteroatom containing [8]circulenes have been known since 1970,[86,87] but just in 2013 the synthesis of a fully benzenoid and substituted derivative was successfully reported by Feng *et al.*[88] Due to their challenging synthesis and comparably low yields, the properties of the saddle-shaped derivatives besides their isomerization barriers e.g. in organic materials is rarely investigated.

Often, a combination of different ring sizes is utilized to obtain distorted non-planar PAHs with the desired geometry and properties.

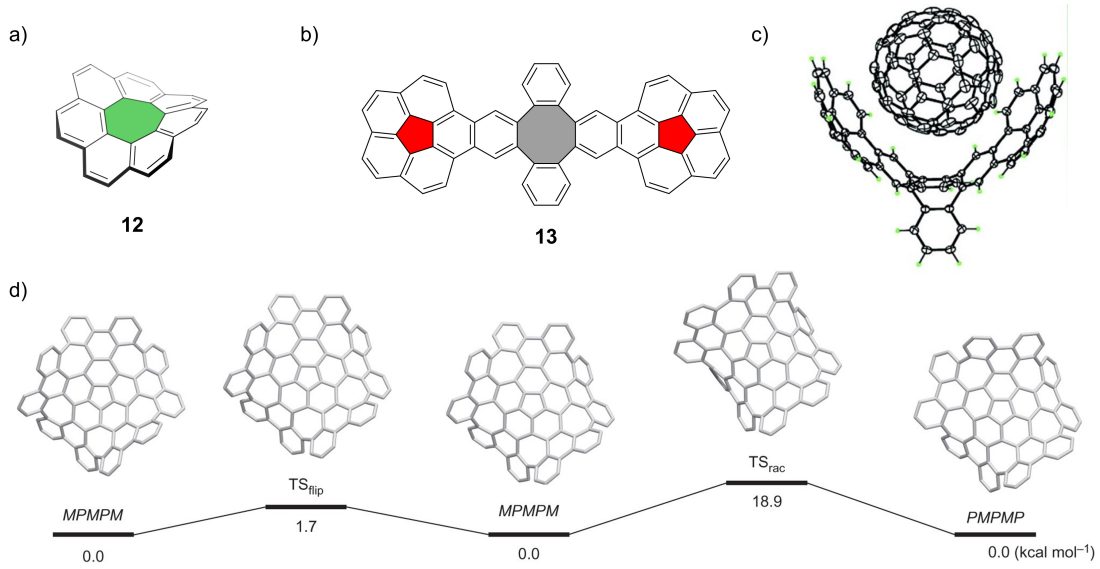

Figure 8 Chemical structures of a) [7]circulene **12** and b) buckycatcher **13** as well as c) the single crystal X-ray structure of a 1:1 complex of **13** and C_{60}. Adapted with permission from Ref. [89]. Copyright 2007 American Chemical Society. d) Bowl-to-bowl inversion and racemization pathways of grossly warped nanographene **14** determined by DFT calculations. Adapted with permission from Ref. [90]. Copyright 2013 Springer Nature.

The most prominent example for non-planar PAHs containing different ring sizes is the so called buckycatcher **13**, which is a molecular clip consisting of two concave corannulene moieties which are connected by a bridge containing an eight-membered ring (Figure 8b,c).[89] This leads to a crescent-like shape with a distance of 9.84 - 11.86 Å between the two corannulene units, which is able to effectively bind C_{60} fullerene by complementary π-π-interactions. While the unsubstituted corannulene does not show any evidence for complexation, the buckycatcher binds to C_{60} with a binding constant K_a of approximately 8600 M^{-1} in deuterated toluene. Theoretical calculations confirm the slight preference for the

concave-concave conformer found in the crystal structure by 0.25 kJ mol^{-1} over the concave-convex alignment as well as by 0.79 kJ mol^{-1} over the convex-convex arrangement of the two corannulene subunits, respectively. Another example for a grossly warped nanographene **14** containing five-and seven-membered rings was reported by Itami and coworkers which has been obtained by expansion of a borylated corannulene precursor via Suzuki-coupling and subsequent oxidative coupling to form five seven-membered rings, demonstrating impressively the improvement of C-H-activation reactions over the last years.[90] Investigation of this nanographene showed the dramatically enhanced solubility and the alteration of the electronic and optical properties compared to planar nanographenes. Interestingly, the bowl-to-bowl inversion barrier is significantly lower than for pristine corannulene, presumably due to the shallower bowl depth (0.37 Å for **14** and 0.87 Å for corannulene) which lowers the energy cost for the inversion. The presence of five hexa[7]circulene moieties in this molecule results in *P*- or *M*-helical chirality around each circulene subunit resulting in the formation of the two enantiomers with *MPMPM* and *PMPMP* configuration respectively, which can be interconverted at elevated temperatures (Figure 8d).

2.2.2. Contortion in Helicenes and Related PAHs

Helical structures in PAHs introduce strain into the system due to sterical crowding in the bay, cove or fjord regions resulting in an out-of-plane distortion. The simplest group of molecules to exhibit contortion due to this are helicenes, which consist of *ortho*-annulated benzene or heteroaromatic ring systems. They adopt an axial chiral helicity by minimization of the steric interactions, which is energetically favored over the torsional strain in the system resulting from the out-of-plane structure (Figure 9a).[19,91,92] Interestingly, according to theoretical calculations the deviation from planarity does not affect the aromaticity of the system severely,[93] indicating that the σ-π-interactions do not interfere with the delocalization of the π-electrons.[94] Furthermore, the solubility of helicenes is significantly higher than that for comparable planar PAH systems, as observed for most non-planar congeners of planar hydrocarbons, although some derivatives are still hardly soluble. By substitution with alkyl or alkoxy chains, this issue can be resolved.[95] The first helicene to be reported was [4]helicene, consisting of four ortho-annulated benzene rings as early as 1913,[96] followed by [5]helicene in 1918 which was obtained by Pschorr cyclization.[97,98] After the first report of the photochemical synthesis of [4]helicene in 1967,[99] the interest in these systems steadily increased due to their intriguing chiroptical properties. Helicenes exhibit a helical chirality and while [4]helicene is

configurationally instable under ambient conditions due to fast interconversion between the *P*- and *M*-enantiomers,[100] enantiomers of [5]helicene can be separated by complexation with either (+)-2-(2,4,5,7-tetranitro-9-fluorenylideneaminooxy)propionic acid (TAPA) or (–)-TAPA and subsequent column chromatography to obtain the pure helicene. However, it is still susceptible to racemization over time at room temperature.[101] The smallest unsubstituted carbohelicene to exhibit configurational stability at room temperature is [6]helicene in which the benzene rings already overlap partially. Although the racemization energy $\Delta G^{\ddagger}$ increases with increasing number of benzene rings from 17.2 kJ mol^{-1} to 151.5 kJ mol^{-1} for [4]- and [6]helicene, respectively, the torsion angles of the bay-region are comparably similar in all carbohelicenes with around 20°.[91] Due to the distortion from planarity, the transition state is unfavorable (Figure 9b).[102] By elongation of the *ortho*-fused benzene chain, the large [16]helicene, which is the longest helicene up to date could be obtained in a one-step procedure through sextuple photocyclization, establishing a synthetic pathway towards large helicenes by proper design of the precursors.[103] Further advances to stabilize one configuration especially in [4]- and [5]helicene for the separation of the enantiomers include the substitution of helicenes at the edge of the fjord region in 1 or 2 position, respectively,[104] as well as the introduction of heteroatoms inside the helical backbone to vary the bond angles.[105]

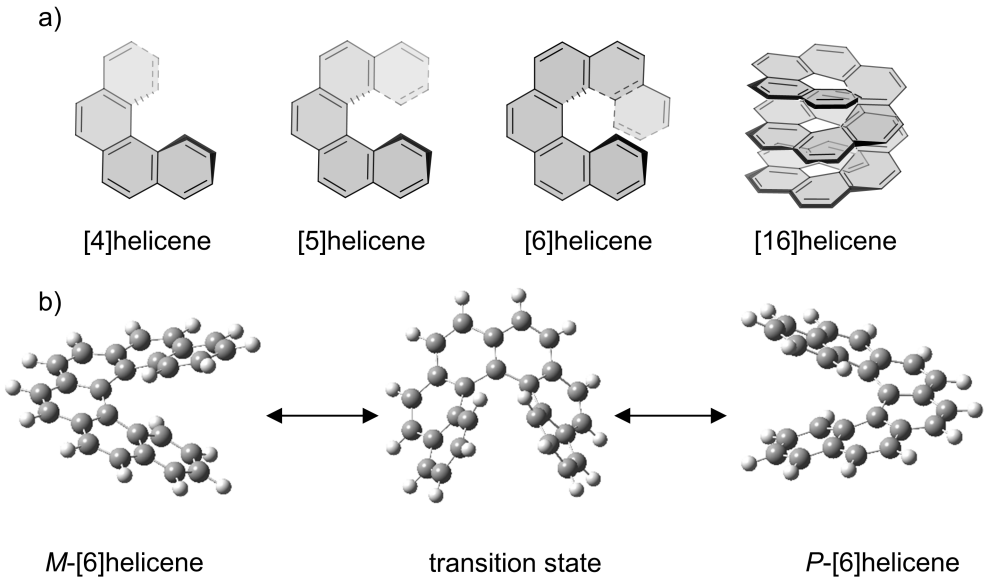

Figure 9 a) Molecular structure of differently sized carbohelicenes; b) Molecular structures of the *P*- and *M*-[6]helicene enantiomers as well as the transition state corresponding to a local minimum as suggested by Lindner[106] and Merino[107].

Helicene subunits are often found in larger contorted π-systems, which are commonly synthesized by Scholl-type oxidative cyclodehydrogenation reactions as the key step and many different structurally intriguing motifs have been reported until today. In an attempt to elucidate

the regioselectivity of the Scholl reaction, Pradhan *et al*. found that the highly twisted molecule **16'** was formed preferentially, while the planar and not strained derivative **16** could only be obtained in low yields from polyphenylene precursor **15** indicating a high selectivity of this reaction to contorted molecules (Figure 10).[108] To explore this reactivity further, they created *tert*-butyl substituted, propeller-shaped hexabenzotriphenylene **18**, which incorporates three [5]helicene units and is D_3 symmetric, like the earlier reported unsubstituted congeners thereof. By Scholl reaction, they were able to isolate a racemic mixture of (+)-**18** and (−)-**18** in a good yield of 63%. Surprisingly, the tilt angle of the blades found in the crystal structure of **18** of 47° is similar to the tilt angle found in the unsubstituted propeller (49°), despite the additional sterically demanding *tert*-butyl groups.[109,110]

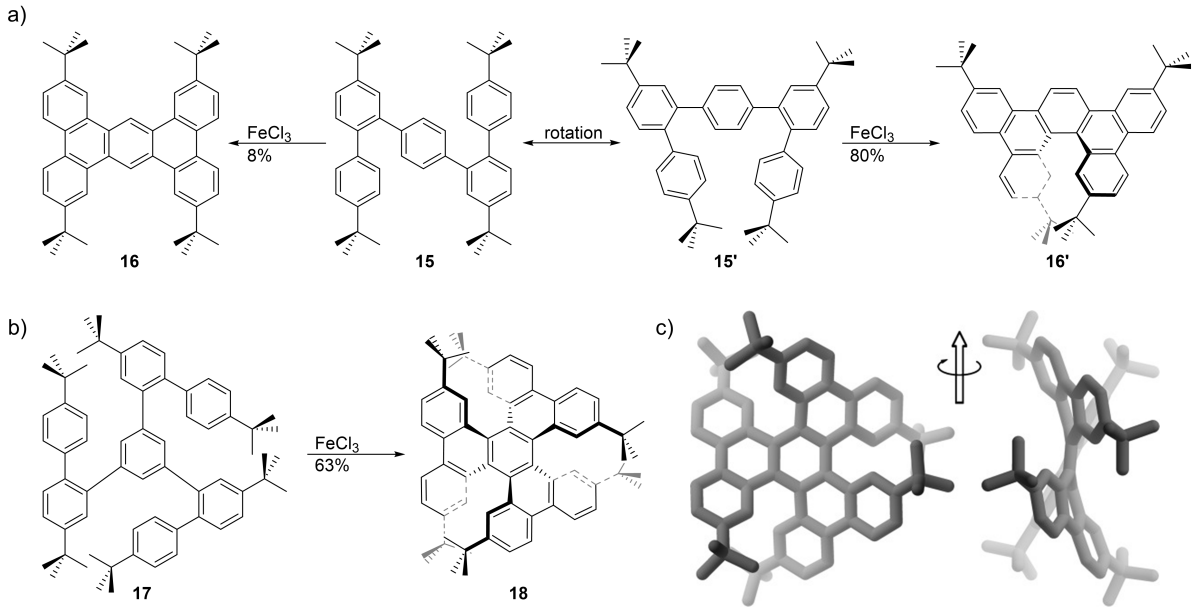

Figure 10 a) Synthetic route to **16** and **16'** via oxidative coupling in dependence of the rotational preorganization of **15**/**15'**; b) Synthetic route to **18** by Scholl reaction as well as c) top and side view onto the crystal structure of **18**. Reproduced with permission from Ref. [108]. Copyright 2011 John Wiley & Sons.

Conceptually, an even larger agglomeration of helicenes can be found in the contorted hexabenzocoronene (HBC) **19a**, which can be seen as a superposition of six [4]helicene subunits (Figure 11a). Clar *et al.* described the synthesis of this molecule as early as 1965 and stated the unlikelyhood of this molecule to be a planar graphite cut-out,[111] which could be verified forty years later by the group of Nuckolls by single crystal X-ray analysis.[112] Upon substitution with long alkyl chains, **19b** was found to behave like a discotic liquid crystal, aligning in columns parallel to the substrate, which has been shown to be beneficial for electronic applications. By fusing three substituted [5]helicenes, another propeller shaped chiral PAH **20** embedding six helicene units was synthesized independently by Gingras and coworkers[113] and Hosokawa *et al*.[114] Both groups confirmed the highly distorted structure of

the molecule by single crystal X-ray analysis and proved the extraordinary stability of the structure by separation of the two most stable conformers as well as by investigating the thermal racemization by chiral HPLC giving a racemization energy of $\Delta G^{\ddagger}$ = 147 kJ mol^{-1} at 182 °C in 1,2-dichlorobenzene and by theoretical calculations (Figure 11b).

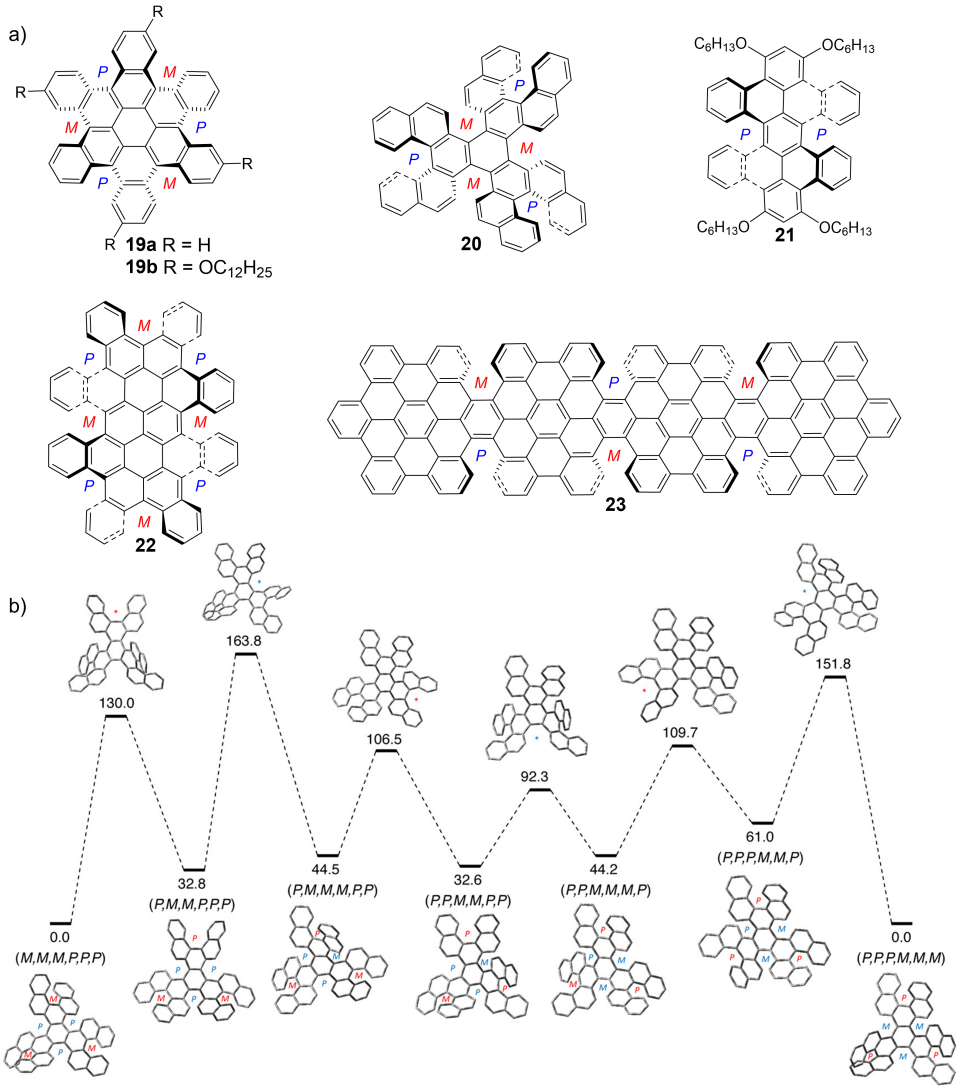

Figure 11 a) Molecular structures of one possible enantiomer of helicene containing PAHs **19-23** as well as the helicity of the respective helicene subunit denoted in *P* (blue) and *M* (red). b) Calculated enantiomerization pathway of **20** with energies in kJ mol^{-1}. Reproduced with permission from Ref. [113]. Copyright 2017 American Chemical Society.

When trying to synthesize a HBC derivative from alkoxylated polyphenylene precursors, only the incompletely cyclodehydrogenated hexabenzoperylene **21** could be isolated by the group of Miao.[83] They attributed the incomplete ring closure to the alkoxy groups, which direct the C-C-bond formation in *ortho* and *para* position with respect to the substituent itself. This leads to a highly crowded fjord region consisting of two [5]helicene units and preventing the closing of the last two C-C bonds of the desired HBC. X-ray analysis of **21** confirmed a highly twisted arrangement of the core with torsion angles as large as 42.1° and 39.2°. The structurally related

octabenzocircumbiphenyl **22** can be seen as an extension of **21** and is one of the largest PAHs obtained by photocyclization to date.[115] This large molecule formally consists of the superposition of six [4]helicene and two [5]helicenes and could be applied in organic field effect transistors (OFETs) and organic solar cells (OSCs).

Supertwistacene **23**, which consists of four HBC units fused linearly in a helical manner and thus contains six [5]helicene subunits was synthesized in a sophisticated seven step procedure with a dehydrocyclization as the key-step towards the product.[116] It is also one of the largest contorted PAHs reported up to date with a length of 4.3 nm and an end-to-end twist of 117°. The helical configuration proves to be extremely stable, even when heated to 200 °C overnight. By heating to 260 °C, the helical **23** slowly transforms to a waggling or mixed structure, prohibiting the detailed analysis of the kinetic parameters, due to complicated interconversion between those structural isomers.

Another group of PAHs, which are commonly found to exhibit a contorted structure are extended pyrenes, i.e., peropyrene, tetraazaperopyrene (TAPP) and teropyrene. Peropyrenes consist of a comparably rigid backbone and can be functionalized in *bay* position by double or quadruple alkyne benzannulation reactions, using a Brønsted acid. The non-planar structure of not only peropyrenes but also teropyrenes synthesized by this procedure could be verified via single crystal X-ray crystallography, showing a twist of the central π-system of 13° for the double arylated peropyrene **24** and approximately 23° and 25° for the different *bay* areas in terropyrene **25** (Figure 12).[117,118] The tetra-*bay*-arylated peropyrene **26** exhibits stable atropo-enantiomers, which could be separated by chiral HPLC, with a twist of the two naphthalene subunits of 29° and a racemization barrier of 28.9 kJ mol^{-1}.[119]

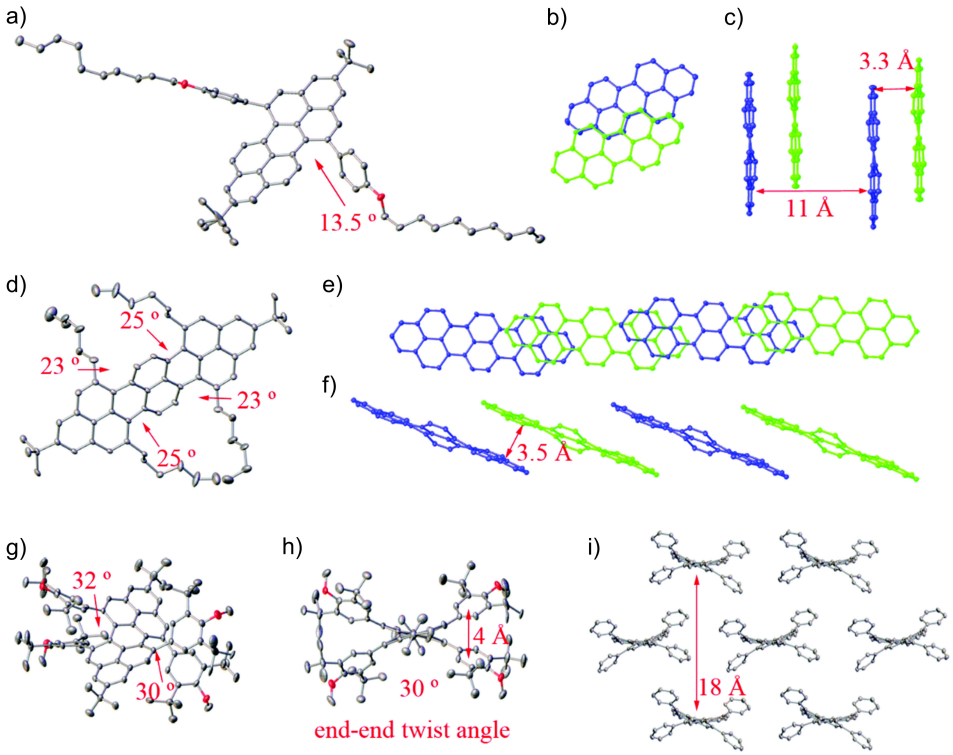

Figure 12 Single crystal X-ray structures and molecular packing of a-c) **24**, d-f) **25** and g-i) **26**. Adapted with permission from Ref. [118]. Copyright 2018 Chinese Chemical Society (CCS), Shanghai Institute of Organic Chemistry (SIOC), and the Royal Society of Chemistry.

TAPPs are usually harder to functionalize in *bay* position than peropyrenes, as the electrophilic substitution takes place in *ortho* position rather than in *bay* position, making the synthesis fo twisted TAPPs more challenging. By a sophisticated synthetic route with functionalized precursors, Gade and coworkers were able to overcome this challenge and obtained different tetrachloro-TAPPs with torsion angles of 29.4°, 30.1° and 32.4°, respectively, which is quite large for *bay* twisted extended pyrenes.[120] The isomerization barrier has been calculated to be 99.2 kJ mol^{-1} considering a racemization sequence via the planarization of one side of the TAPP *bay* area resulting in a decreased twist angle of 10° in the non-planarized *bay* area and *syn* oriented chloro substituents. A potential one step mechanism involving the complete planarization of the core would prevent the molecule from racemization due to the high energy of 301.2 kJ mol^{-1}.

2.2.3. Propellers and Nanobelts

To obtain sophisticated three-dimensional PAH structures with intriguing properties, two approaches are most common. The first approach is the attachment of more than one planar PAH to a 3D linker unit while the inherent planarity of the original carbon network is

maintained. The second approach is the formation of macrocyclic structures to induce strain in the π-system, which results in a contortion of the surface of the carbon network.

Triptycene, which is a classic building block for the synthesis of 3D networks, has been used numerous times in polymer backbones to disrupt the solid-state packing and to obtain highly porous materials with sufficient solubility and good emission properties. The Mastalerz group synthesized π-extended D_{3h} symmetric nonplanar triptycene derivative **27** with a high internal free molecular volume in the solid state (Figure 13).[121] By investigation of different single crystal X-ray structures, four different polymorphs could be identified, indicating the lack of supramolecular interactions in the packing of **27**. Attempts to activate the molecule by exchanging the intercalated mesitylene by *n*-pentane in order to maximize the surface area did not result in the desired higher porosity and instead amorphous material was formed but by thermal treatment a surface area of up to 350 $m^2 g^{-1}$ could be generated.[122]

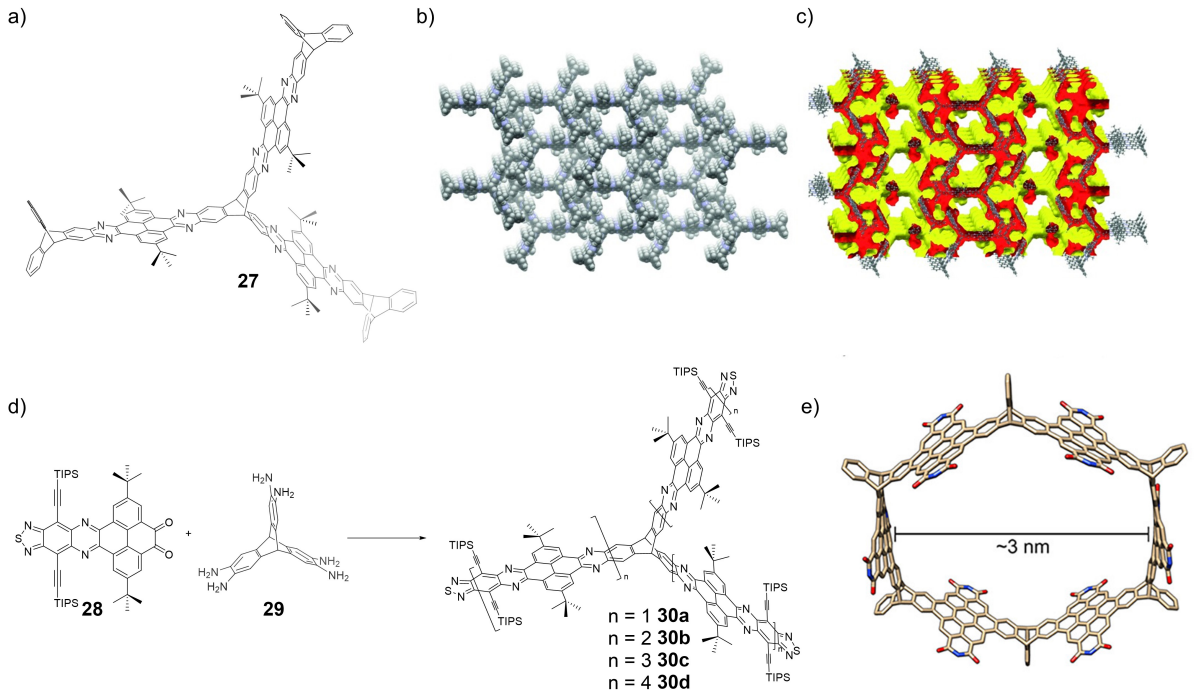

Figure 13 a) Chemical structure of extended triptycene **27** as well as b) the packing of **27** in the structure obtained by single crystal X-ray analysis and c) surface area and voids for an *in silico* evacuated crystal (yellow: outer surface, red: inner surface); Reproduced with permission from Ref. [122]. Copyright 2015 John Wiley & Sons. d) Synthesis of Baumgartens 3D pyrene-fused *N*-heteroacenes **30a-d**. e) Calculated energy optimized structure of one macrocyclic subunit of Nuckolls fused polymer capacitor. Reproduced with permission from Ref. [124]. Copyright 2018 American Chemical Society.

Even larger *N*-doped pyrene fused heteroacenes **30a-d** with average diameters between 3.66 and 10.9 nm could be obtained by the group of Baumgarten by stepwise condensation of precursors **28** and **29** and subsequent reduction of the thiadiazole units (Figure 13d).[123] Like other non-planar PAHs, even the largest derivative **30d** with 22 annulated rings in one arm of

the molecule exhibits good solubility in all common solvents, even though the solubility decreases slightly with increasing ring number, whereas their linear counterparts are only hardly soluble even in hot *o*-dichlorobenzene. Molecule **30d** is the largest pyrene-fused *N*-heteroacene which has been reported to date, giving a new perspective for large molecules applicable in energy storage and energy conversion devices. By copolymerization of PBI and triptycene subunits via Suzuki-coupling and subsequent photocyclization, Nuckolls and coworkers were able to synthesize stable cyclized polymers.[124] To form porous materials from these polymers, thermal activation in order to remove the long alkyl chains in imide position was necessary, yielding nanopores with inner diameter of 3 nm (Figure 13e), resulting in an outstanding performance as *n*-type capacitor of 352 F g^{-1} as well as high stability for over 10000 cycles.

The formation of nanobelts containing curved π-surfaces is highly desirable due to their structural similarity to CNTs and their possible use as precursors in the formation thereof. However, the bottom-up synthesis proved to be rather challenging due to the high strain inherent to these π-conjugated macrocyclic structures. Therefore, attempts to convert nanobelts into CNTs are most of the time prevented by strain-relieving rearrangements,[125] which can be circumvented by blocking of the relevant positions in the molecule with functional groups, e.g., methyl groups.[126] Methods to overcome the high energetic barrier needed for the cyclization include the ring-opening olefin methatesis,[127] a sequence of McMurry coupling reactions followed by bromination, elimination,[128] Sonogashira,[129] Yamamoto[130] as well as Glaser coupling[131] reactions and alkyne metathesis,[132] which were applied in the synthesis of different cycloparaphenylenes (CPPs). To obtain larger CNT fragments by bottom-up synthesis, bigger annulated aromatic fragments are often incorporated into the ring system as precursors. These fragments include smaller PAHs like chrysene,[133] anthanthrene[134] or pyrene[135] as well as larger structures like peropyrene[136] and HBC. In HBC macrocycles, the subunits can either be connected by a *para*-phenylene chain or directly attached to each other. The number of HBC molecules in such a linker-connected macrocyclic structure is variable from one, connected by seven phenyl-rings exhibiting a crown-ring like structure in **31**[137] to up to four, in which each HBC subunit is connected by a biphenylene moiety like in molecule **32** (Figure 14).[138] Calculations as well as spectroscopic investigation by ^{1}H-NMR spectroscopy revealed the flexibility of the core HBC units in larger systems, as the rotation thereof is possible, while the energetic barrier is too high in the cyclic trimer, preventing a structural rearrangement. Directly interconnected HBC units are commonly found to complex fullerenes in a 1:1 complex, due to their concave surface, which might in principle be of interest for the application in OSCs. Due to the low yields of the cyclization towards CNT segments,

only small amounts of the respective nanohoops can be prepared, hampering the investigation in organic electronic devices.[139]

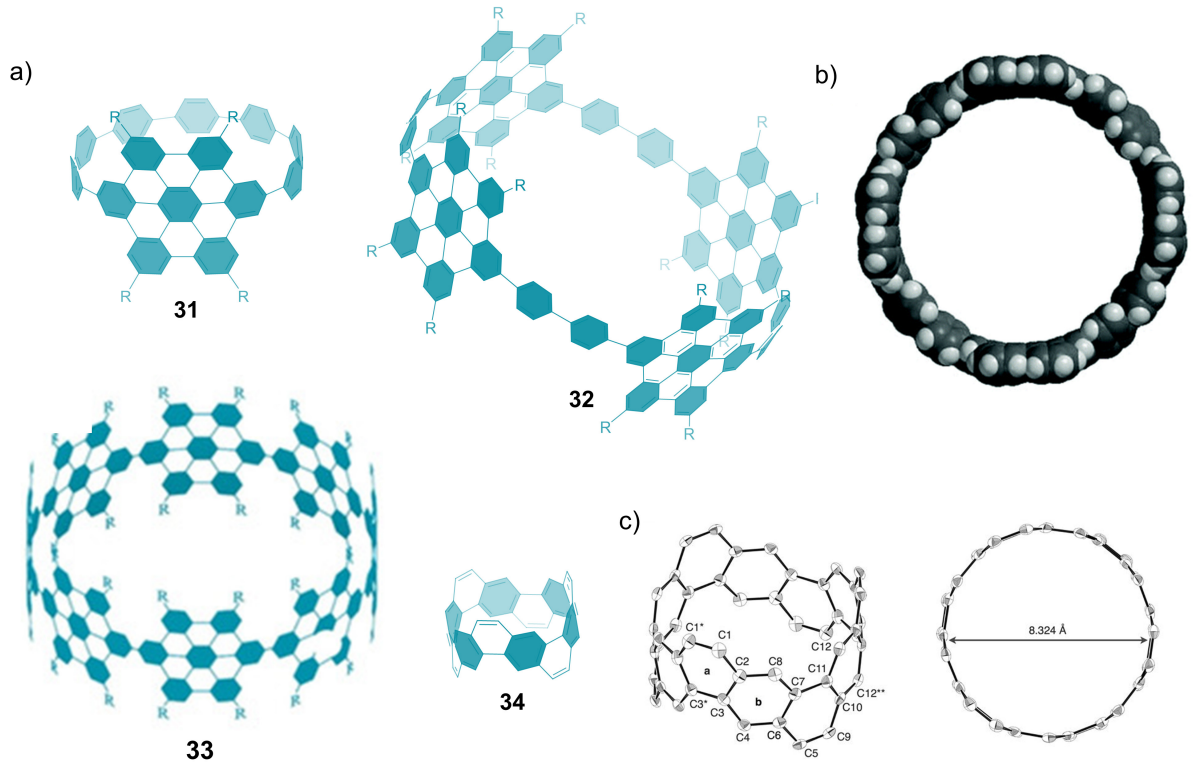

Figure 14 a) Chemical structures of nanohoops **31-34**, R = 2,4,6-trimethylphenyl. Reproduced with permission from Ref. [140]. Copyright 2020 John Wiley & Sons; b) Top view onto the DFT-optimized structure of **32** without the substituents. Reproduced with permission from Ref. [138]. Copyright Royal Society of Chemistry; c) Structure of **34** obtained by single crystal X-ray analysis (hydrogen molecules omitted for clarity). From Ref. [141]. Reprinted with permission from AAAS.

The largest cyclic conjugated molecular CNT segment reported to date contains eight directly connected HBC molecules **33**, which exhibited a significantly reduced strain energy of -81.3 kJ mol^{-1} compared to smaller derivatives like the cyclic hexamer with −17.6 kJ mol^{-1} due to the larger diameter of the macrocycle.[140] Although several research groups previously produced possible precursors for the bottom-up synthesis of CNTs, the synthesis of a fully fused carbon nanobelt **34** containing edge-sharing benzene rings was realized only in 2017 by Itami and coworkers by aryl-aryl coupling reaction with Ni(cod)$_2$ in a yield of 1%.[141] Despite the low yield, they were able to fully characterize the molecule unambiguously by NMR spectroscopy, optical measurements and single crystal X-ray crystallography, revealing the small diameter of only 8.32 Å. The optoelectronic properties were found to be unusual, like the absorption which is assigned to forbidden transitions but becomes allowed due to the structural rigidity preventing deformation, and the red emission. They proposed the utilization of this nanobelt in nanoelectronics and photonics in the future and ultimately the programmable synthesis of single-chirality CNTs.

2.2.4. Miscellaneous Compounds

In the design and synthesis of novel nonplanar PAHs, numerous of the above elaborated structural features can be combined to obtain even more intriguing and highly functional molecules. By covalently linking six [5]helicene units using oxidative photocyclization and subsequent Yamamoto coupling reactions, the first fused-ring π-conjugated cage-shaped molecule **35** was obtained by the Watanabe group in 2018 (Figure 15).[142] This molecule possesses an inherent chirality due to the steric repulsion of the helicene subunits resulting in the formation of two separable enantiomers and unique structural features like the outer helical groves and the inner cavity. As proven by single crystal X-ray analysis, the cavity which has the shape of a three-leaf clover cannot be accessed even by small molecules due to the narrow windows preventing further utilization in the recognition of chiral molecules.

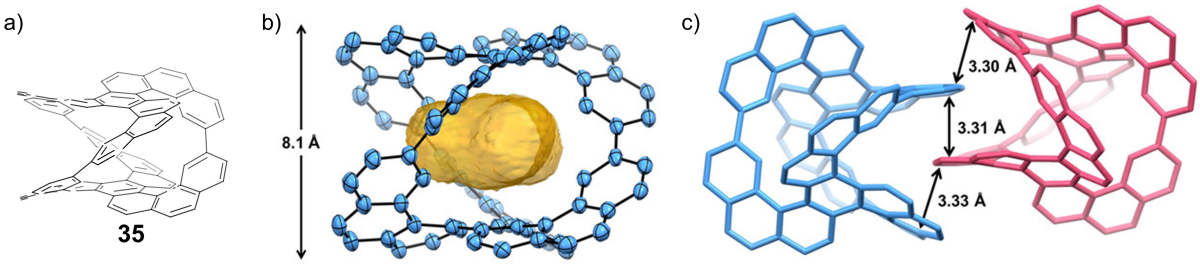

Figure 15 a) Chemical structure of triple helicene cage (*P*)-**35**; b) Single crystal X-ray structure of (*P*)-**35**; c) Crystal packing of (*P*)-**35** (blue) and (*M*)-**35** (pink) as well as the shortest distances between neighboring enantiomers. Reproduced with permission from Ref. [142]. Copyright 2018 John Wiley & Sons.

By fusion of corannulene and smaller planar molecules like naphthalene or phenanthrene, helicene decorated geodesic bowls can be synthesized which exhibit intriguing shapes and properties. By Wittig reaction of formyl corannulene with the respective ylide phosphonium salts, Scott and coworkers were able to prepare [5]- and [6]helicene decorated corannulene derivatives **36-38** (Figure 16).[143] The two inherent structural features, the bowl and the helix, result in the formation of four stereoisomers in which the helix faces either the concave or convex side of the bowl. The structure found in the solid state contained a convex corannulene moiety which is by 31.4 kJ mol^{-1} (**36**) and by 26.4 kJ mol^{-1} (**37**) more stable than the respective concave structure according to calculations. The bowl-to-bowl inversion barriers of 44.4 and 42.3 kJ mol^{-1} for **36** and **37** respectively are slightly lower than for pristine corannulene (48.1 kJ mol^{-1}), illustrating the steric influence of the helicene moiety, which facilitates the inversion. Similarly, the calculated helix inversion barriers are also slightly lowered compared to pristine [5]helicene and [6]helicene due to the curved structure of the corannulene, which resembles the deformations found in the transition states. Thus, both structural motifs mutually influence their respective inversions, lowering the energetic barriers.

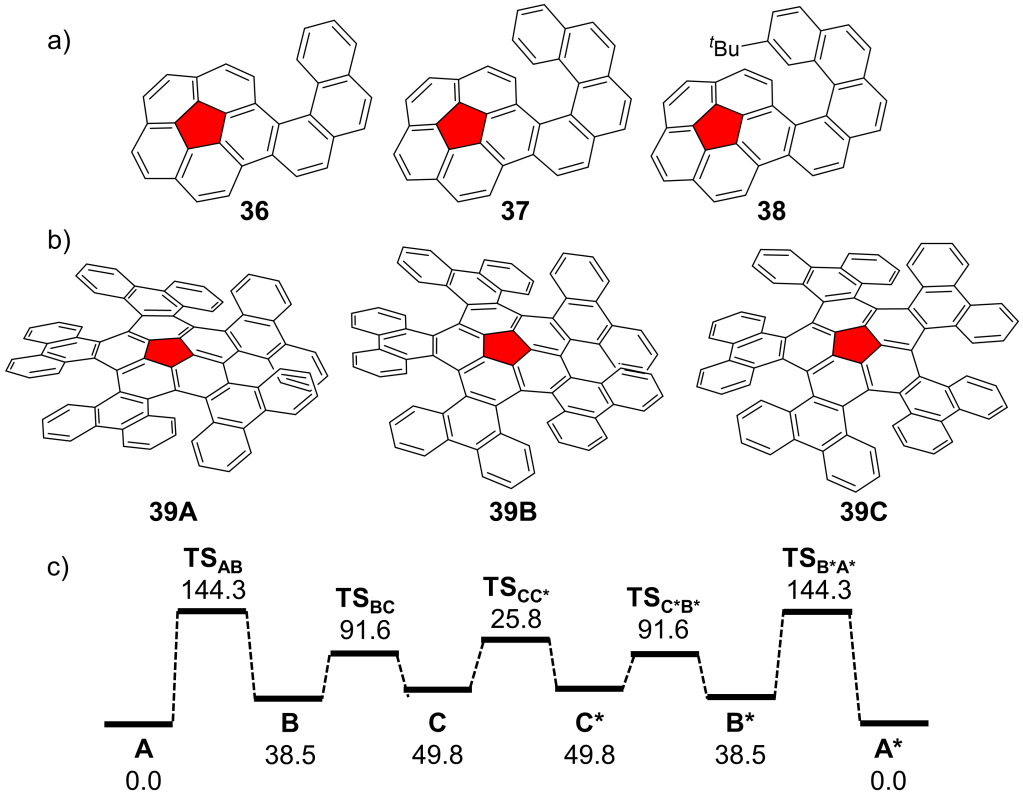

Figure 16 a) Chemical structures of one enantiomer of helicene decorated corannulenes **36-38**; b) Chemical structure of three stereoisomers (A-C) of propeller shaped **39** as well as c) the lowest enantiomerization pathway from **39A** (all-*P*) to **39A*** (all-*M*). Reproduced with permission from Ref. [144]. Copyright 2018 John Wiley and Sons.

In the propeller shaped corannulene derivative **39**, five [6]helicenes are formed by Suzuki coupling and successive intramolecular arylation, resulting in a ten-fold symmetric structure in solution as well as in the solid state.[144] Due to the chiral inversion of the [6]helicene moieties, four pairs of enantiomers as well as ten transition states could be identified, of which the isomers with the highest symmetry are energetically favoured. The experimental racemization barrier of 143 kJ mol^{-1} obtained by monitoring the decrease of the enantiomeric excess *ee* by chiral HPLC is consistent with the highest barrier obtained by DFT calculations and emphasizes the stability of the contorted system at room temperature. Due to the high symmetry and stability, the system should give useful information for the design of organic quasicrystals as well as potential applications in chiroptical materials.

2.3. Nonplanar Dicarboximides

2.3.1. Nonplanar Rylene Dicarboximides

Rylene diimide dyes such as perylene (PBI), terrylene (TBI) and quaterrylene (QBI) bis(dicarboximide) usually consist of *peri*-condensed naphthalene molecules, which form a planar π-core. Upon substitution in *bay* position, the steric demand of the introduced substituents leads to contortion of the system. Depending on the Van der Waals radius and flexibility, the twist angle of the naphthalene planes can vary from only 4° in the difluoro-substituted PBI **40** up to 37° in the tetrabromo-substituted PBI **43** (Figure 17).[145,146] This molecular twist of the chromophore core introduces axial chirality into the systems. For the separation of the atropo-enantiomers by HPLC a racemization barrier of >93 kJ mol^{-1} is required, otherwise interconversion of the enantiomers is observed and prevents the separation.[147] Among the rylene dyes, PBIs are the most investigated compounds due to the good availability of precursors as well as their straightforward and established synthetic adaptability. Even some of the PBIs predominantly used as precursors already exhibit highly twisted structures, e.g., 1,6,7,12-tetrachloro PBI **42** (35°/36°)[146] or tetrabromo PBI **43** (37°).[146] The free enthalpy of activation $\Delta G^{\ddagger}$ of both derivatives of 97.3 (**42**, 293 K) and 118.2 kJ mol^{-1} (**43**, 363 K) is high enough to separate the two atropo-enaniomers. While fourfold substitution in *bay* position with highly flexible aryloxy groups leads to fast interconverting *P*- and *M*-enantiomers due to the comparably low barrier of 54 kJ mol^{-1} (244 K),[148] Suzuki-coupling of **42** or **43** with phenylboronic acid gives tetraarylated PBI **44**,[40,149] of which the racemization barrier is estimated to be around 250 kJ mol^{-1} (180 K). Also, for this derivative **44**, the separation of enantiomers by HPLC was successful and the chiral nature of these tetrasubstituted compounds could be proven by circular dichroism (CD) measurements.

A possibility to obtain stable aryloxy substituted PBI atropo-enantiomers is by connecting the diagonally adverse *bay* substituents with alkyl or alkoxy chains, thus forming a handle and effectively preventing the racemization of the PBI core. Enantiopure macrocycles containing this structural motif have furthermore been shown to be able to transfer their chiral information on carbohelicenes like [4]helicene and catalyze the deracemization of [5]helicene.[150]

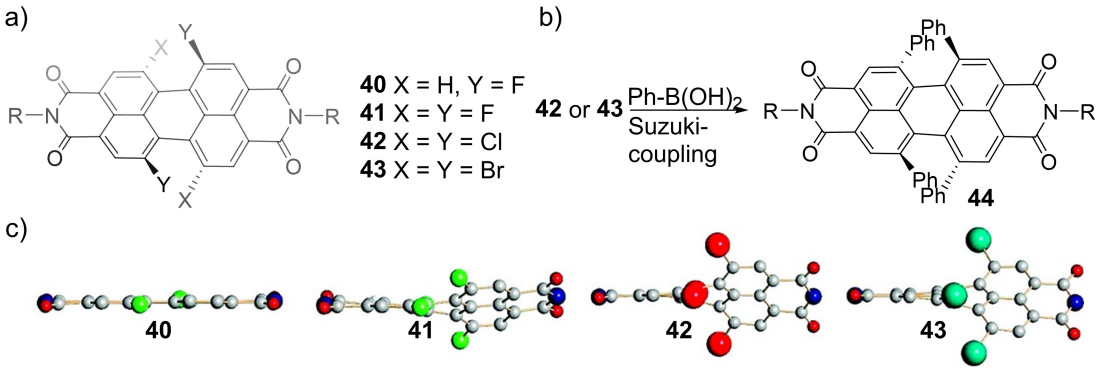

Figure 17 Chemical structure of a) halogenated as well as *bay*-twisted PBIs **40-43** and the b) reaction scheme to obtain tetraarylated PBI **44**. c) Side view onto the structures of the aromatic systems of **40-43** obtained by single crystal X-ray analysis. Reprinted with permission from Ref. [146]. Copyright 2009 American Chemical Society.

By copper iodide mediated Ullmann-type coupling of tetrahalogenated PBIs, different oligomeric structures which form ladder-type GNRs could be obtained by the group of Wang (Scheme 1). The exact structure is dependent on the halogen attached in the precursor and the reaction temperatures. Using **42** as precursor and lower reaction temperatures, the halogenated dimer **45** was obtained, while at more elevated temperatures, the dehalogenated nanoribbon **46** was isolated. PAH **45** could be transformed to **46** by using the same reaction conditions as for the reaction from **42** to **46**, thus helping in the elucidation and further investigation of the reaction mechanism (Scheme 1).[151]

To circumvent dehalogenation under the Ullmann-type conditions, catalytic amounts of copper nanoparticles as well as an additional palladium catalyst were used in the subsequent reaction of **45** to the two structural isomers **47a** and **47b**. The third possible isomer **47c** was not formed as the analysis of the two obtained products by ^{1}H-NMR spectroscopy, UV/Vis/NIR spectroscopy as well as theoretical calculations indicated.[152] Using **43** instead of **42** as precursor even lower reaction temperatures are sufficient for the lateral fusion of the two PBI moieties to obtain tetrabromo nanoribbon **48**. At higher temperatures, bromine-iodine halogen exchange is generally observed under the modified Ullmann conditions due to an excess of copper iodide. Highly distorted tetraiodo-nanoribbon **49** could accordingly be synthesized by increasing the temperature to 60 °C.[153] At even more elevated temperatures, the cleavage of the C-Br bonds was expected, but instead the two fully conjugated structural isomers of tri-PBIs **50a** and **50b** were obtained at 110 °C.[154] These related non-planar PBI derivatives impressively demonstrate the tremendous influence of already minor changes to the reaction system upon coupling of tetrahalogenated PBIs under Ullmann-type conditions to obtain contorted PAHs.

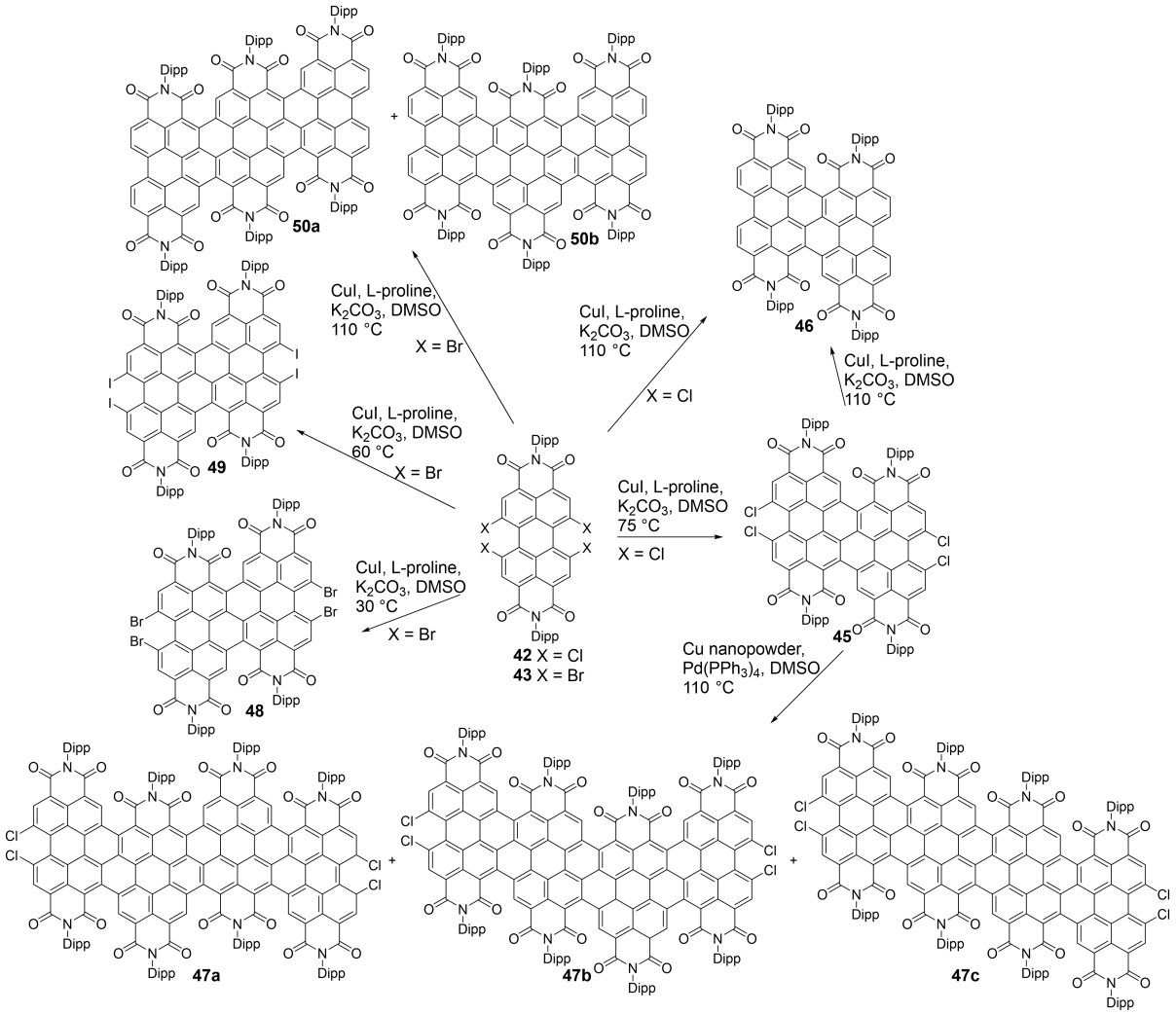

Scheme 1 Synthesis of the different ladder-type GNRs from PBIs **42** or **43** by copper mediated Ullmann-type coupling. Dipp = 2,6-diisopropylphenyl.

Using **45** as precursor, S- and N-heterocycle annulated PBI dimers can be obtained by coupling of the halogenated *bay* position with either $S(Bu_3Sn)_2$ or aniline.[155] Due to the steric congestion between the carbonyl oxygen and neighboring hydrogen atoms, the precursor already forms *cis* and *trans* type conformers. While the PBI cores are almost planar in the *trans* conformer, the *cis* conformer of the S-heterocyclic annulated PBI dimer exhibits a shallow bowl-shaped structure. This effect is even more pronounced in the N-annulated dimer, due to the larger strain introduced by the annulated pyrrole rings. In both derivatives, the energies of the *trans* and *cis* configuration are closer than in the unsubstituted **46**, indicating the better stabilization of the *cis* conformer while destabilizing the *trans* conformation due to the annulation, making the *cis* configuration energetically favored. Additional confirmation of the lower energy of the *cis* configuration was found by X-ray analysis of single crystals, where only one isomer was found as well as by temperature-dependent ^{1}H-NMR studies, in which no traces of two isomers could be observed. The different heteroatoms introduce a simple way to tune the electrochemical and

optical properties, which also makes them interesting candidates for applications in materials science.

By fusing PBIs only in their *bay* positions, chiral nanoribbons were obtained by copper-mediated homocoupling of tetrachloro PBI **42** by the group of Wang.[156] The dimer **51** as well as the trimer **52** could be obtained in moderate yields of 25% and 10%, respectively (Figure 18).

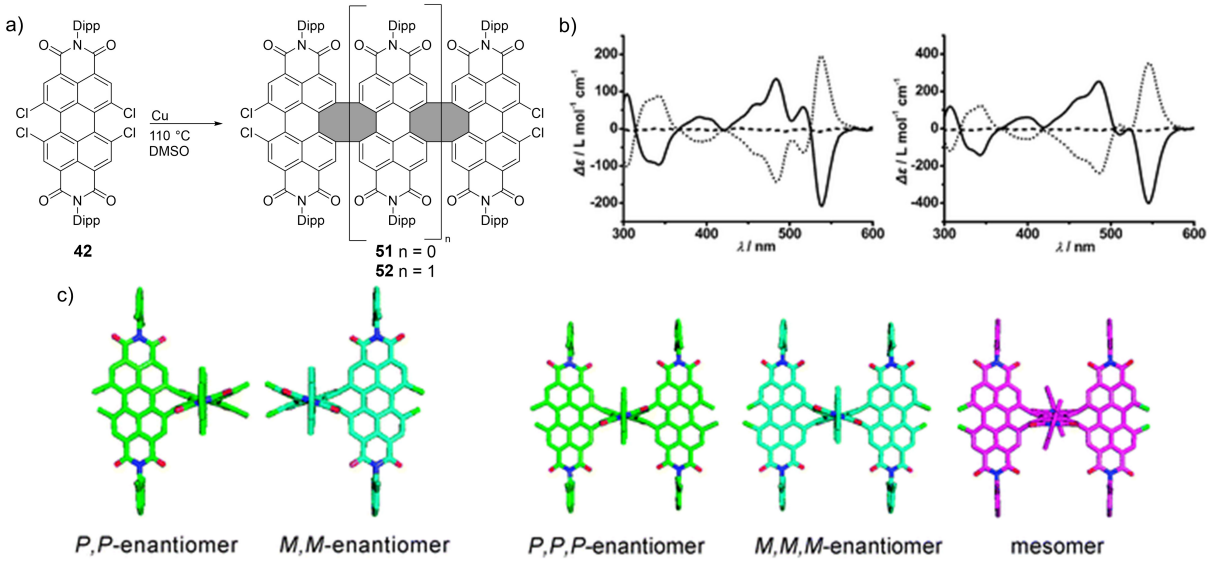

Figure 18 a) Synthesis of chiral nanoribbons **51** and **52** as well as b) their CD spectra after successful separation of the enantiomers on the chiral HPLC. c) Calculated structures for all enantiomers of dimer **51** and trimer **52**. Hydrogen atoms are omitted for clarity. Reproduced with permission from Ref. [156]. Copyright 2010 The Royal Society of Chemistry.

Higher homologues up to the tetradecamer were detectable by matrix-assisted laser desorption/ionization time of flight (MALDI-TOF) measurements, but it was not possible to isolate them. The chromophore subunits in these contorted PAHs are aligned almost perpendicular with respect to each other due to the eight-membered ring formed by the coupling in *bay* position, which also prevents the effective conjugation along the short axis of the PBI subunit. This results in a decrease of the fluorescence quantum yield from 85% in the monomer via 66% in the dimer **51** down to 51% in the trimer **52**. Furthermore, each PBI subunit exhibits a core twisted structure due to the steric crowding in *bay* position, which gives rise to two enantiomeric configurations for the dimer (*P*,*P* and *M*,*M*) and three configurations for the trimer (*P*,*P*,*P*; *M*,*M*,*M* as well as mesomeric), which could be separated by chiral HPLC and characterized by CD spectroscopy and are configurationally stable even at 150 °C for 3 h. Interestingly, the central PBI unit in the energy optimized *meso*-structure of the trimer **52** has a *syn*-configuration, while the two outer PBIs are in the lower energy *anti*-configuration. This results in an overall higher energy by 36.0 kJ mol^{-1} compared to the two enantiomeric helical forms. The chloro-substituents in the peripheral *bay* positions enable further functionalization

to improve the processability and enable a tuning of the optical and electronic properties for further applications e.g., in special opto-electronic devices and for the enantioselective recognition and design of chiral supramolecules.

Another C-C coupling method for the efficient synthesis of highly twisted large PAHs is the Stille coupling between exclusively PBIs or heterocoupling between PBIs and naphthalene bis(dicarboximides) (NBIs) along their equatorial axis.[157,158] Utilizing a stannylated ethene building block and brominated precursors **53a** and **53b**, larger, fully conjugated graphene nanoribbons **55**, **57** and **59** containing up to four PBI subunits were synthesized by Stille coupling and subsequent photocyclization, with the prospect of substiantially larger systems due to the good yields and high solubility of the largest product (Scheme 2).

By bridging two PBI moieties with an ethene unit, two [4]helicene subunits are created and thus the two hydrogen atoms in the fjord region are in spatial proximity, leading to a twist of the two PBI subunits with respect to each other. Upon further addition of PBIs to the structure, more configurations become possible. While only one conformational option is possible in the dimer, already two conformers with similar relative energies become possible in the trimer. One is the helical structure, where both fusing points exhibit the same handedness and the molecule has an inherent axial chirality and the other the waggling structure, where the fusing points exhibit opposite handedness. In addition to both energetically similar conformers, a mixed structure is possible for the tetramer. Wang and coworkers were able to extend the formation of nanoribbons by Stille coupling to heterosystems consisting of alternating PBI and NDI subunits by coupling of stannylated NDIs to chlorosubstituted PBIs.[159] The steric proximity of the carbonyl oxygens of the NDI to the *ortho* hydrogens in the PBI lead to an overall twisted structure. No inversion of the stable configuration could be observed, even at elevated temperatures of 250 °C for six hours and a calculated racemization barrier of a PBI-NDI dimer of 255 kJ mol^{-1} further supports the configurational stability.[160] In the homo- as well as hetero-coupled oligomeric systems, the lateral extension of the π-system shifts the absorption region towards the NIR and increases the electron affinity, making these systems interesting candidates for applications as organic photovoltaic material.

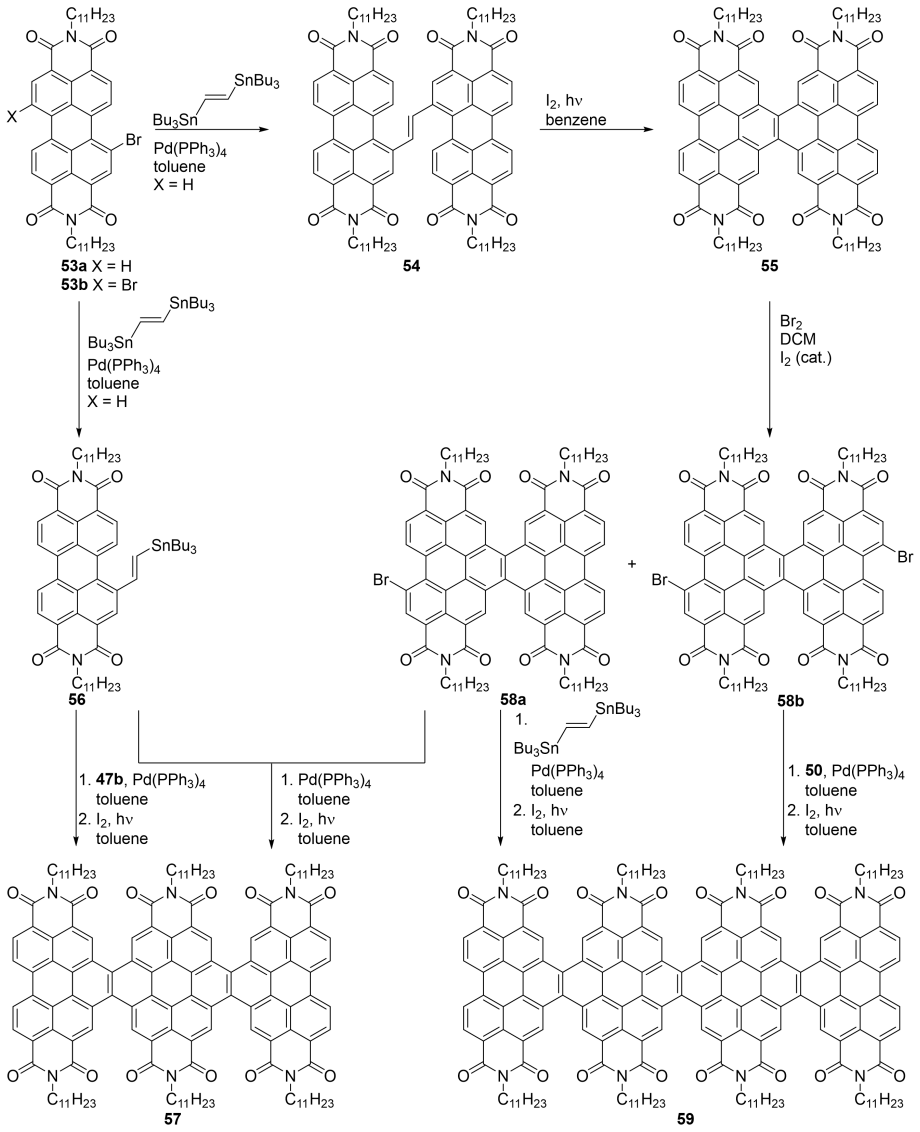

Scheme 2 Synthesis of the fully conjugated ethylene-bridged nanoribbons **55**, **57** and **59** via Stille coupling.

A propeller shaped molecule combining the introduction of a five-membered ring as well as high steric influence to obtain a contorted PAH has been synthesized by the Wang group with an extraordinary structure consisting of a corannulene center with PBI moieties annulated to every rim position via the *bay* area of the PBI. The molecule was synthesized by Suzuki coupling followed by photocyclic aromatization in high yields.[161] In theory, eight stereoisomers which contain four pairs of enantiomers can be formed, but only the highest D_5 symmetric **60a** (Figure 19) in which all helicene units exhibit the same configuration and the imide groups of the PBIs are arranged up and down in an alternating manner as well as the C_2 symmetric **60b** with six imide groups of three successive PBIs arranged up and down and the entire next PBI up and the following or vice versa are found. The other two possible configurations were calculated to be higher in energy and thus disfavored under the applied reaction conditions. No conversion from **60b** to **60a** was observed even up on heating to 205 °C

for 6 h in solution, emphasizing the high steric crowding around the corannulene core and the resulting high stability of the isomers formed during the reaction. Due to the steric repulsion of the PBI units, the bowl depth of the corannulene is shallower with 0.32 Å in **60a** and 0.63 Å in **60b** compared to pristine corannulene (0.87 Å). In the single crystal X-ray structure, three molecules of the D_2 symmetric **60a** were found to assemble into a tubular structure, which then stacks alternately to form large, achiral 3D honeycomb lattices, while the C_2 symmetric **60b** forms dimers by intramolecular π-π-stacking.

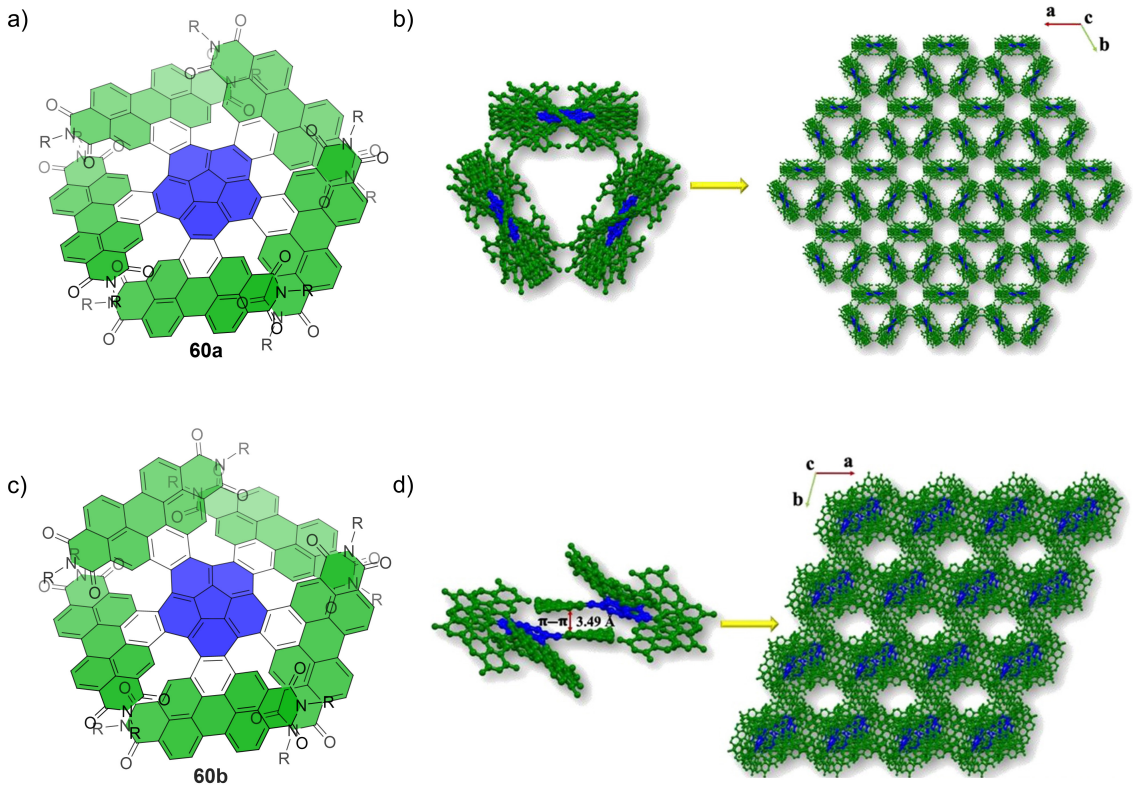

Figure 19 Chemical structures of the a) D_5 as well as the c) C_2 symmetric isomers of corannurylene penatpetalae **60**. Single crystal X-ray structures of b) **60a** and d) **60b** as well as their respective molecular packing. The alkyl chains and hydrogen atoms are omitted for clarity. Adapted with permission from Ref. [162]. Copyright 2021 CCS Chemistry.

These packing motifs have been shown to be advantageous for the facilitation of electron transport, making these extraordinary molecules interesting candidates for the investigation of supramolecular architectures in the application in organic electronics. Recently, they were able to obtain the highest value for PBI based OSCs with corannurylene pentapetalae **60a**, with a PCE_{max} of 11.2% and appreciable high open circuit voltages (V_{OC} = 1.06 V), short-circuit current (J_{SC} = 15.3 mA cm^{-2}) as well as fill factor (FF = 68%) using poly-3-hexylthiophene (P3HT) as donor polymer.[162] The C_2 symmetric conformational isomer thereof exhibits a PCE_{max} of 10.3%, underlining the importance of proper assembly to achieve high-performance OSCs and providing guidance for the design of even more efficient PBI derivatives for OSCs.

To this date, significantly less studies of nonplanar terrylene bis(dicarboximide) (TBI) derivatives are available compared to their shorter perylene congeners. Müllen and coworkers published the synthesis of the fourfold *bay* substituted TBI **61** by bromination and obtained the twisted **62** by subsequent Rosemund von Braun cyanation using copper(I) cyanide (Scheme 3).[163]

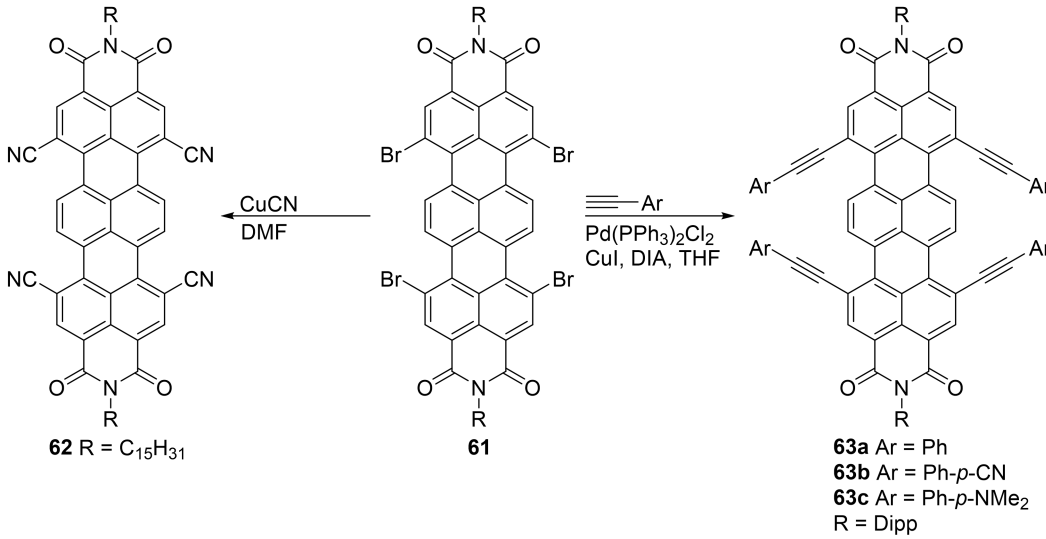

Scheme 3 Synthetic pathways towards *bay* twisted TBIs **62** and **63a-c** from brominated precursor **61**.

The calculated twist of two neighboring subunits in **62** is about 15° making the molecule significantly more soluble in chloroform and *o*-dichlorobenzene (7 mg mL^{-1}) compared to a similar *ortho* substituted TBI, which is virtually insoluble (<1 mg mL^{-1}). Using the same brominated precursor, Regar *et al.* synthesized three ethinylphenyl flanked TBI derivatives **63a-c** to investigate the influence of electron withdrawing and donating groups attached in the *para* position of the aryl residues. All derivatives exhibit good solubility in common organic solvents like chloroform and dichloromethane (DCM), whereas only **63c** with dimethylamino groups is poorer soluble in toluene and THF. They were able to unambiguously prove the twisted structure of *bay* substituted TBIs by single crystal X-ray analysis for the first time, even for the brominated precursor. While the ethinylphenyl substituted derivative **63a** exhibits dihedral angles of 18.0° and 9.34°, the twist is significantly higher in the tetrabromo precursor with 21.4° and 25.7° due to the larger Van der Waals radius of the bromine atoms attached directly to the *bay* position compared to the ethinyl carbon atoms.

The chemistry of twisted QBIs is even less studied due to the mostly electron rich molecules, which are often unstable under ambient conditions. The group of Müllen reported in 1998 the synthesis of fourfold and eightfold alkoxylated QBIs, which exhibited good chemical,

photochemical and thermal stability as well as a high solubility, but no further investigations concerning the twist thereof were conducted.[164]

2.3.2. Further Nonplanar Dicarboximides

Most nonplanar imides, which are not based on PBIs, or their higher congeners use the inherent contortion of corannulene to achieve the desired structural properties. Electron-poor bowl shaped naphthalimides based on corannulene have been synthesized and investigated by Shoyama *et al.* and contain one (**64**) or two (**1b**) naphthalimide moieties (Figure 20).[165] They exhibit a high luminescence as well as low-lying frontier orbital levels, as desired for n-type semiconductors. By adaption of the synthetic procedure, a nanocone **65** which is not only structurally intriguing but also opens up the route for a new class of 3D functional materials has been obtained.[166] Due to the challenging synthesis and purification, no studies concerning the application of **66** in organic materials like OSCs were conducted.

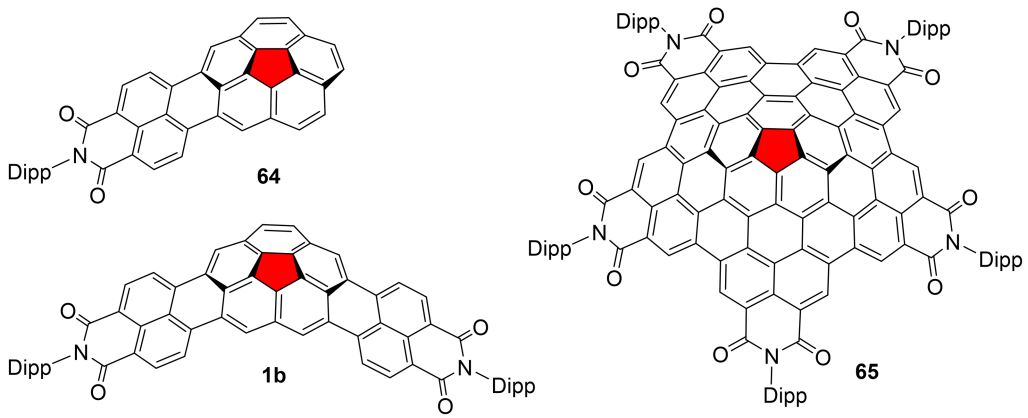

Figure 20 Chemical structures of electron-poor bowl shaped naphthalimides **64** and **1b** as well as nanocone **65**.

Overall, only few examples of corannulene based electron acceptors in OSCs have been reported, despite their easier synthetic modification and thus adjustment of the energy levels as well as absorption and charge carrier transport properties compared to the widely applied fullerenes. Lu *et al.* introduced electron-withdrawing phthalimide (**66a**) and naphthalimide (**66b**) groups to the corannulene core, effectively lowering the LUMO level (Figure 21).[37] With these materials, the first solution-processed bulk heterojunction (BHJ) solar cells using P3HT as donor material afforded PCEs up to 0.32% for **66a** and 1.03% for **66b** compared to 0.19% for pristine corannulene.

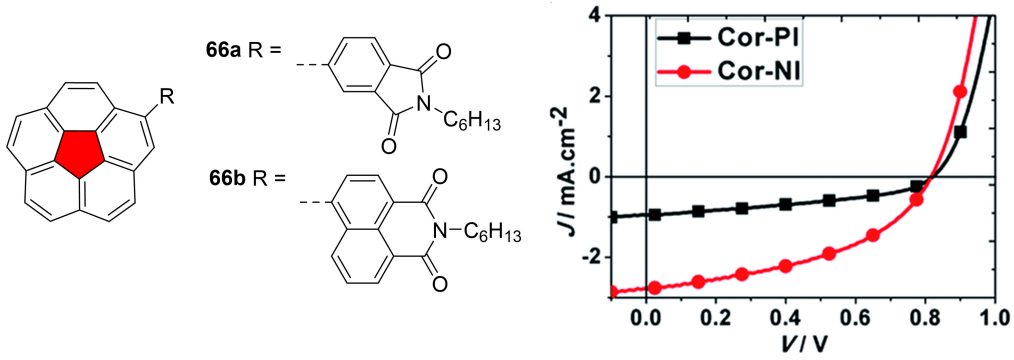

Figure 21 Chemical structure and *J-V* curves of organic BHJ solar cells of **66a** and **66b**. Reproduced with permission from Ref. [37]. Copyright 2014 Royal Society of Chemistry.

The fusion of an imide ring directly to the nonplanar corannulene in **67** extends the π-system and promotes the bowl-in-bowl stacking (Figure 22).[167] The long alkyl chain in imide position improves the solubility and enables additional interactions between the bowls, while the annulation of benzene rings at the core leads to a slight lowering of the LUMO level. Interestingly, this molecule acts as n-type OTFT with an electron mobility of 0.02 $cm^2\ V^{-1}\ s^{-1}$ under vacuum, while under ambient conditions a hole mobility up to 0.05 $cm^2\ V^{-1}\ s^{-1}$ was observed. Subsequently, the attachment of cyano groups (**68**) to the corannulene instead of the annulation of benzene rings lowers the LUMO level even more significantly and enables intercolumnar electronic coupling, which was successfully utilized in an air-stable n-type OTFT showing an electron mobility of 0.07 $cm^2\ V^{-1}\ s^{-1}$.[168]

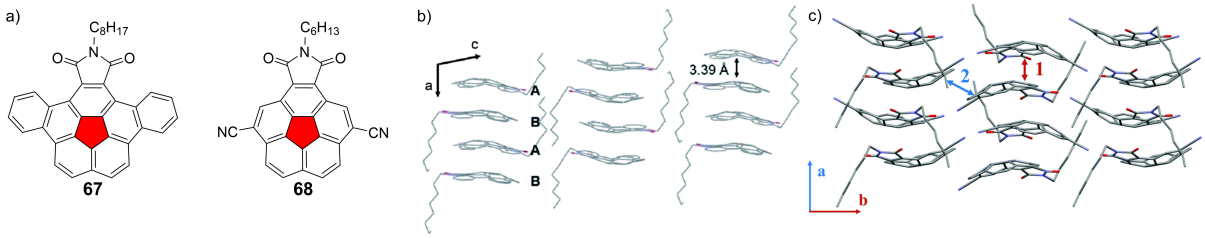

Figure 22 a) Chemical structures of nonplanar corannulene imides **67** and **68** as well as the molecular packing found by single crystal X-ray analysis of b) **67** and c) **68**. Reproduced with permission from Ref. [167] and Ref. [168]. Copyright 2013 and 2015 Royal Society of Chemistry.

Other nonplanar imides rely on the steric demand of helicene-like structures. By formally attaching imide groups on the two outermost benzene rings of differently sized and shaped helicenes, the groups of Hu and Ravat just recently developed a novel class of nonplanar helicene bis(dicarboximides) **69-72** with either one or two helical subunits and [4]- to [7]helicene as their backbone (Figure 23).[169,170]

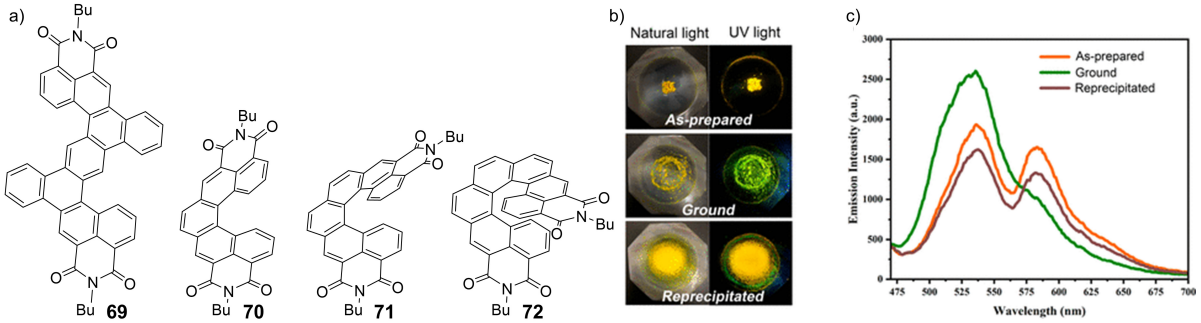

Figure 23 a) Chemical structure of helical bis(dicarboximides) **69-72** (Bu = *n*butyl) as well as b) photographs of the powder as prepared, grounded and reprecipitated under natural and UV light (365 nm). c) Solid state fluorescence spectra of **69** of the as-prepared grounded and reprecipitated powder. Reprinted with permission from Ref. [169]. Copyright 2021 American Chemical Society.

They are synthesized by photocyclization or cyclodehydrogenation from suitable precursor molecules in good yields. All four derivatives exhibit good fluorescence properties in solution with high fluorescence quantum yields Φ_f up to 47% in toluene for **69** as well as in the solid state compared to their counterparts without the imide groups. Helicene bis(dicarboximide) **69** shows additionally mechanofluorochromism from yellow for the as-prepared powder to green upon grinding which corresponds to a decrease of intensity of the emission peak at 580 nm, while the maximum at 538 nm is increased (Figure 23c). This behavior suggests the application in mechanosensors or optical storage.

Chapter 3

Self-Assembly of Bowl-Shaped Naphthalimide-annulated Corannulene

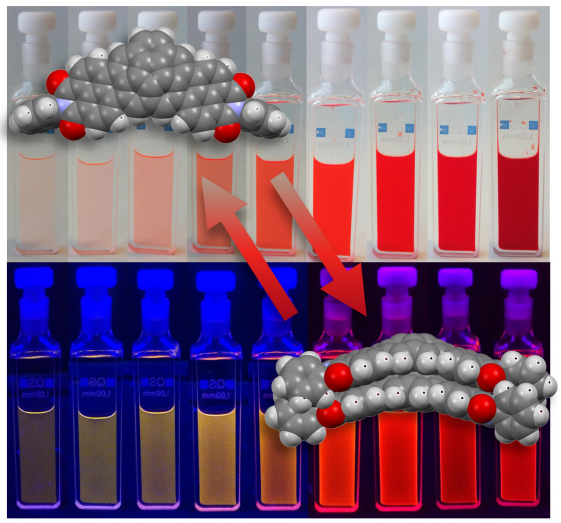

This chapter and the corresponding supporting information has been published:

R. Renner, M. Stolte, F. Würthner, *ChemistryOpen* **2020**, *9*, 32-39.

Abstract: The self-assembly of a bowl-shaped naphthalimide-annulated corannulene of high solubility has been studied in a variety of solvents by NMR and UV/Vis spectroscopy. Evaluation by the anti-cooperative K_2-K model revealed the formation of supramolecular dimers of outstanding thermodynamic stability. Further structural proof for the almost exclusive formation of dimers over extended aggregates is demonstrated by atomic force microscopy (AFM) and diffusion ordered spectroscopy (DOSY) measurements as well as by theoretical calculations. Thus, herein we present the first report of a supramolecular dimer of an annulated

corannulene derivative in solution and discuss its extraordinarily high thermodynamic stability with association constants up to $>10^6$ M^{-1} in methylcyclohexane, which is comparable to the association constants given for planar phthalocyanine and perylene bisimide dyes.

3.1. Introduction

Corannulene, a non-planar polycyclic aromatic hydrocarbon (PAH), has recently attracted significant attention. Due to its bowl-shaped structure, it exhibits a moderate ground state dipole moment (μ_g = 2.1 D)[172] and enhanced solubility in common organic solvents[173] compared to planar PAHs. Other bowl-shaped molecules like subphthalocyanines[174,175] and sumanenes[63] also exhibit these properties, due to the two different faces of the molecules. By functionalization of the rim, the bowl depth and thus the packing in the solid state as well as in solution can be controlled, making these non-planar systems interesting candidates for application in supramolecular host-guest chemistry to obtain complex functional structures.[176-178] Furthermore, corannulene was shown to be a useful precursor for the synthesis of large non-planar nanographenes by annulative π-extension to give new, structurally alluring molecular shapes and motifs.[90,166,179]

Bowl-shaped molecules are widely applied in the field of supramolecular chemistry as hosts for fullerene molecules after Scott and coworkers first showed the assembly of C_{60} with corannulene in the solid state[180] and in solution[72] due to the complementary intimate concave-convex π-π-interactions. By connecting two bowl-shaped precursors with a rigid bridge, it was further possible to synthesize the "buckycatcher", a molecular tweezer which is able to form a supramolecular 1:1 complex with C_{60} through concave-convex π-π-interactions.[89] Different types of buckycatchers have been synthesized and investigated accordingly to exploit this unique feature in search of selectivity in the binding of different fullerene derivatives.[73,181]

An important property to be considered in the supramolecular self-assembly of bowl-shaped molecules is the bowl-to-bowl inversion. This effect is commonly observed for corannulene systems, due to the relative low-lying barrier for the bowl inversion, depending on the substituents. Usually, the activation barrier in sumanene systems is higher and subphthalocyanines usually do not undergo bowl inversion at all due to very high barriers.[182] Conformationally stable systems, in which the bowl-to-bowl inversion is hindered, can be aligned in the presence of an electric field to form one-dimensional columnar liquid crystalline materials due to their axial dipole moment, which is of interest for device applications.[183] Upon chemical reduction of corannulene and sumanene, highly negatively charged bowl-shaped ligands are obtained, forming a variety of intriguing sandwich-like complexes with different alkali metal cations on both the convex and the concave surface of the ligand, which have been characterized in their crystalline state and by NMR spectroscopy.[184,185]

By introducing electron-withdrawing substituents e.g. halogens or nitrile groups on the rim of the corannulene system the electronic properties of the molecules can be altered which is of interest for their use in organic electronics as n-type semiconductors.[161, 186, 187] The same attributes can be achieved via extension of the aromatic π-system with naphthalimide moieties using a Suzuki-Miyaura cross coupling/Heck type arylation cascade annulation reaction to establish an interesting new class of bowl-shaped PAHs.[165] These new molecules exhibit intriguing optical and electronic properties, being among the highest fluorescent π-conjugated bowl-shaped dyes. Their low-lying frontier orbitals offer the possibility to use them in supramolecular photosystems and as n-type semiconductors, making them promising candidates for bulk-heterojunction solar cells.

In this work, we explore the self-assembly of a new, highly soluble derivative of our recently reported first bowl-shaped bis-naphthalimide-annulated corannulene.[165] Our previously described molecule containing diisopropylphenyl units at the imide position was not able to self-assemble in solution within the available concentration range due to the bulky isopropyl substituents. Thus, the new derivative **1a** was synthesized with solubilizing tridodecylphenyl side chains. Here we will show that **1a** forms supramolecular dimers of outstanding thermodynamic stability in various solvents. To the best of our knowledge, we herein explore the thermodynamics of self-assembly for a corannulene derivative for the first time. The applied techniques for structural elucidation, AFM and DOSY, reveal the formation of dimers. Theoretical calculations were conducted to propose two possible structures for the dimer, one based on the maximization of the π-π-interactions between two molecules and the other based on dipolar interactions.

3.2. Results and Discussion

3.2.1. Synthesis

The synthesis of **1a** could be achieved by altering a literature known route for Suzuki-Miyaura coupling and direct arylation, as it was not possible to synthesize the product using the literature known procedure in sufficient yield and purity (Scheme 4).[188] Using tri(*m*-tolyl)phosphine instead of tricyclohexylphosphine tetrafluoroborate as ligand in the reaction, the product **1a** was isolated as a dark red solid in a yield of 28%. The new molecule as well as the precursor **74a** were characterized using ^{1}H- and ^{13}C-NMR spectroscopy (Figure 29-32) and mass

spectrometry (MALDI, DIP, ESI). The literature known molecule **1b** could also be synthesized under these new conditions in a yield of 24%.

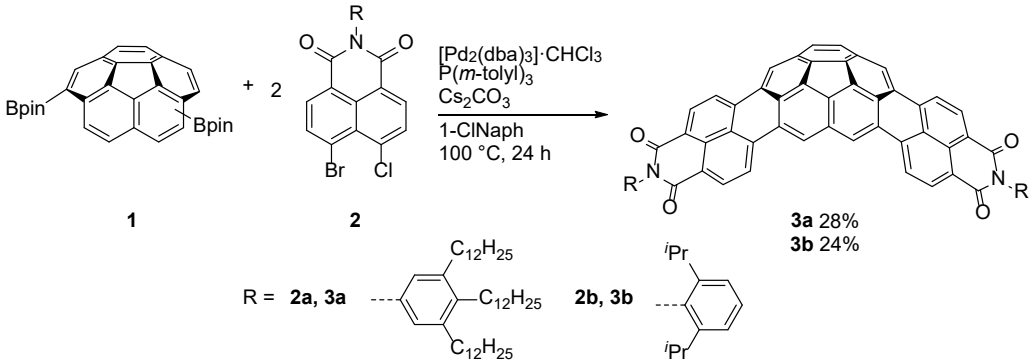

Scheme 4 Synthesis of bowl-shaped polycyclic aromatic bis(dicarboximides) **1a** and **1b**. a) $[Pd_2(dba)_3]\cdot CHCl_3$ (5 mol%), P(*m*-tolyl)$_3$ (20 mol%), Cs_2CO_3 (6 equiv.), 1-chloronaphthalene; Bpin: boron(pinacol)ester.

3.2.2. Optical Properties

The optical properties of the new corannulene derivative **1a** were firstly investigated in dichloromethane (DCM, Figure 24) and compared with the previously reported molecule **1b**. In this highly polarizable solvent, the band shape as well as the absorption maximum of the S_0-S_1 transition, that appears at λ_{max} = 536 nm, are in good accordance with the reported vibronic progression, which is typical for this type of corannulene derivative, and wavelength for the diisopropylphenyl derivative **1b** (λ_{max} = 538 nm), along with a slightly higher overall extinction coefficient of 56200 M^{-1} cm^{-1}.

Accordingly, also the almost identical fluorescence spectra revealed emission maxima for both investigated dicarboximides at λ_{max} = 572 nm with only small Stokes shift of 1140 cm^{-1}. The fluorescence quantum yield of **1a** (Φ_f = 43%) is only slightly lower for **1b** (Φ_f = 48%). Despite the varying imide substituents, the shapes and positions of the absorption as well as the fluorescence spectra are similar in their monomeric, non-aggregated state.

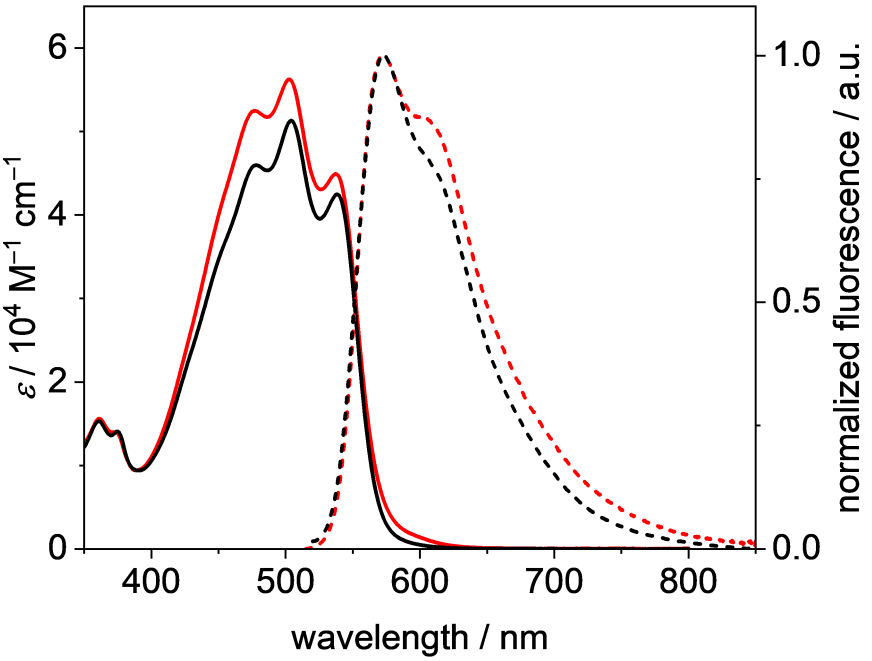

Figure 24 UV/Vis absorption (solid line) and fluorescence (dashed line, λ_{ex} = 501 nm) spectra of **1a** (red) and **1b** (black) in dichloromethane ($c_0 = 1 \cdot 10^{-5}$ M, 25 °C).

3.2.3. Self-assembly behavior

Because the bowl-to-bowl inversion was considered to hamper self-assembly of naphthalimide-annulated corannulene derivatives, we investigated this process by temperature-dependent ^{1}H-NMR spectroscopy in deuterated 1,1,2,2-tetrachloroethane (TCE-d_2).[182] Molecule **1a** is however, not suitable for this kind of investigation due to the fast rotation of the phenyl rings attached to the imide units on the NMR time scale, making its protons indistinguishable. In contrast, due to the two different faces (convex, concave) of the corannulene derivative and the steric hindrance of the diisopropylphenyl groups in molecule **1b**, the isopropyl groups attached at the phenyl ring in *ortho* position and the protons in *meta* position have different chemical environments and can therefore be distinguished at room temperature (Figure 33). Temperature-dependent ^{1}H-NMR studies revealed a coalescence temperature T_c = 370 K. At temperatures above this temperature the bowl-to-bowl interconversion is very fast and thus the signals are not distinguishable anymore. It is possible to calculate the rate constant of the inversion at the coalescence temperature as k = 65.2 s^{-1} and the free energy of activation to be $\Delta G^{\ddagger}$ = 78.4 kJ mol^{-1}, which is in good accordance with value obtained by theoretical calculations (B3LYP/def2svp) of ΔG = 76.6 kJ mol^{-1} (Figure 34). These values indicate the slow bowl-to-bowl interconversion of naphthalimide-annulated corannulene at room temperature, which should accordingly not disturb the self-assembly.

At room temperature, the signals of **1b** appear quite sharp in TCE-d_2, indicating the lack of aggregation due to the sterically demanding diisopropyl groups (Figure 33). In contrast, in the absence of sterically demanding *ortho* substituents, the aggregation of molecule **1a** can be observed utilizing temperature-dependent ^{1}H-NMR spectroscopic investigations in the high-boiling solvent TCE-d_2. At low temperatures, broad signals are observed in the aromatic region of the spectra, whereas upon the increase of the temperature a significant narrowing of the signals occurs and a downfield shift of the signals of the aromatic protons can be observed, which is attributed to the formation of the monomer (Figure 35). The aliphatic region of the spectra is also affected by the aggregation-dependent broadening of signals. Similar behavior is observed in temperature-dependent ^{1}H-NMR spectra of **1a** in toluene-d_8. In this low-polar aromatic solvent, the change towards sharp signals is monitored at higher temperatures than in TCE-d_2, indicating the higher thermodynamic driving force for the formation of aggregates (Figure 36), which is in accordance with common observations of other dye aggregates like perylene bisimides (PBIs)[189] and phthalocyanines.[190]

Table 1 Optical properties of corannulene derivatives **1a** and **1b** as well as PBI **75**[a] in dichloromethane and toluene at 25 °C.

	Solvent	λ_{abs} [nm]	ε [M^{-1} cm^{-1}]	λ_{em} [nm]	Φ_{Fl} [%]	τ [ns]	Stokes shift [cm^{-1}]
1a	DCM	536, 503, 477	52500, 56200, 44900	572	43[b]	4.92	1140
1a (M)	Toluene	540, 504, 477	55250, 65400, 59000	562	54[c]	4.32	730
1a (D)	Toluene	555, 466	24100, 46600	612	24[c]	8.56 (89%) 2.81 (11%)	1680
1b	DCM	538, 504, 478	45900, 51300, 42500	573	48[b]	5.00	1140
75[191]	DCM	527, 491, 460	96300, 58100, 21000	532	63	3.2	180

[a] For molecular structure of PBI **75**, see Figure 25c. [b] Fluorescence quantum yields were determined relative to a standard dye (*N*,*N*'-bis(2,6-diisopropylphenyl)-3,4,9,10-perylenetetracarboxylic diimide.[192] [c] Fluorescence quantum yields were determined with an integrating sphere and corrected for reabsorption.

Deeper insights into the formation of aggregates were obtained by concentration-dependent UV/Vis spectroscopy in toluene due to the low polarity of the solvent and the good solubility up to 150 mg mL^{-1} of **1a** in this solvent, which is one order of magnitude higher than the solubility of **1b** (Figure 25a).

Upon increasing the concentration of **1a** a pronounced broadening of the absorption band and a loss of its vibronic structure is detectable, suggesting distinct intermolecular interactions between the chromophores. Clear isosbestic points at 410 nm and 555 nm can be observed which indicate the existence of an equilibrium between the monomer and an aggregated species. The data could be fitted with the anti-cooperative K_2-K aggregation model[193] with a nucleus

size of 2, giving $K_2 = 2.4 \cdot 10^4$ M^{-1} and a cooperativity factor $\sigma = 58$ (see Figure 38). Accordingly, the initial dimerization is highly favored over the elongation ($K = 4.1 \cdot 10^2$ M^{-1}) and the elongation constants are prone to significant errors because only small amounts of the dimers further aggregate under the given experimental conditions. For this reason, the more simple monomer-dimer[190] model also afforded a good fit of the experimental data and was therefore applied for the following solvent-dependent aggregation studies. The dimerization constant K_D, that is obtained by application of this model in toluene, is $2.4 \cdot 10^4$ M^{-1}, which is in perfect accordance with the nucleation constant obtained by the anti-cooperative model. The resulting Gibbs energy change ΔG^0 was calculated to be –24.5 kJ mol^{-1} and the ideal monomer and dimer spectra were obtained as well (Figure 25a).

Similar spectral changes from the monomeric to the dimeric species could be observed by a decrease of the temperature of a solution of **1a** in toluene (Figure 37). The thermodynamic parameters could be determined by performing concentration-dependent UV/Vis measurements at five different temperatures in toluene with the help of a van't Hoff plot to be ΔH^0 = –33.1 kJ mol^{-1}, ΔS^0 = –10.8 J K^{-1} and ΔG^0 = –23.6 kJ mol^{-1}. The value for the Gibbs energy change obtained from this analysis is comparable to the one obtained from the dimerization constant at room temperature. The negative enthalpy and entropy reveal an enthalpy-driven self-assembly process for **1a** in toluene.

Table 2 Comparison of the dimerization constant K_D of **1a** and the isodesmic aggregation constant K of PBI **75** in different solvents at 25 °C.

	K_D(**1a**) [M^{-1}]	K(**75**) [M^{-1}][c]
Hexane	-[a]	$1.2 \cdot 10^6$
MCH	~$3 \cdot 10^6$[b]	$9.7 \cdot 10^4$
MCH/Toluene 2:1	$1.8 \cdot 10^5$	-
Toluene	$2.4 \cdot 10^4$	$5.9 \cdot 10^2$
CCl_4	$2.1 \cdot 10^4$	$6.5 \cdot 10^2$
TCE	$2.4 \cdot 10^2$	-

[a] Insufficient solubility at room temperature; [b] the value could only be estimated due to the small change in the absorption band even at the most diluted conditions; [c] Taken from Ref. [189]; MCH = methylcyclohexane, TCE = 1,1,2,2-tetrachloroethane.

Additional concentration-dependent investigations have been conducted in solvents of different polarity to assess the aggregation behavior and strength in dependence of the different environments. For this purpose, unpolar methylcyclohexane (MCH), a mixture of MCH and toluene in a ratio of 2:1, tetrachloromethane and 1,1,2,2-tetrachloroethane (TCE) have been chosen.

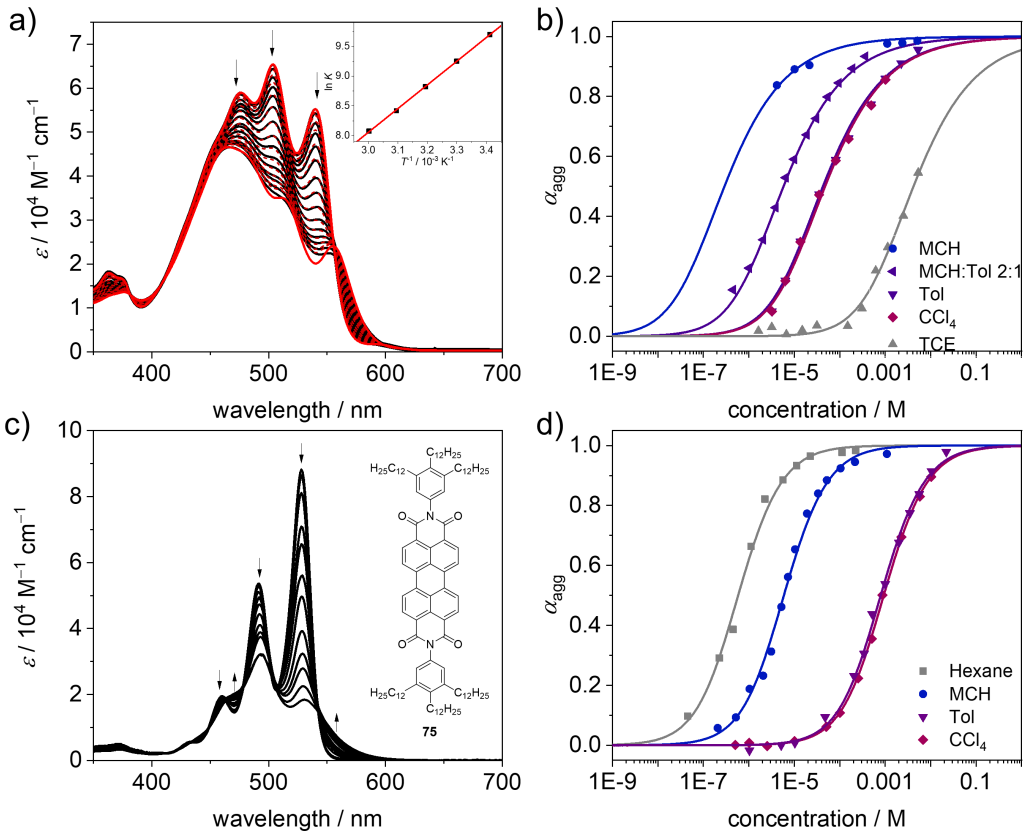

Figure 25 a) Concentration-dependent UV/Vis spectra at 25 °C of a) **1a** (black, $c_0 = 4.5 \cdot 10^{-7}$ - $4.0 \cdot 10^{-3}$ M) in toluene, the global fit analysis according to the monomer-dimer model for **1a** (red, dashed lines) and the ideal monomer and dimer spectra (red solid lines). Inset: Van't Hoff plot for the calculation of the thermodynamic parameters; b) Molar fraction of aggregated molecules α_{agg} as a function of concentration of **1a** fitted with the dimer model; c) Concentration-dependent UV/Vis spectra of PBI **75** in toluene ($c_0 = 1.0 \cdot 10^{-6}$ - $2.2 \cdot 10^{-2}$ M) and d) molar fraction of aggregated molecules (α_{agg}) as a function of concentration of **75** fitted with the isodesmic model. Reproduced with permission from Ref. [189]. Copyright 2003 Royal Society of Chemistry.

All spectral data could be fitted with the monomer-dimer model as well as with the anti-cooperative model (Figure 38). Due to the above-mentioned reasons, the values obtained by the monomer-dimer model are discussed in the following paragraph. For the lowest (MCH) and highest (TCE) polar solvents, the values obtained by the fitting routine represent an approximation due to too strong (MCH) or rather weak (TCE) dimerization, respectively. As all the other data can be fitted according to the monomer-dimer model, it is reasonable to presume comparable aggregation behavior in MCH and TCE as well. The obtained values for the dimerization constant K_D are summarized in Table 2 and depicted as a function of the molar fraction of aggregated molecules in dependence of the concentration in Figure 25b. K_D is, as expected highly solvent-dependent, varying from the lowest value of $2.4 \cdot 10^2$ M^{-1} in polar TCE to a four orders in magnitude higher value $3 \cdot 10^6$ M^{-1} in low polarity solvent MCH.

To the best of our knowledge, this is the first report of aggregation constants for corannulene derivatives in solution. The herein obtained values are comparable to the values reported for phthalocyanine dimers ($K_D = 3.0 \cdot 10^6$ M^{-1}) in CCl_4,[194] extended PBI aggregates ($K =$

$1.5 \cdot 10^7$ M^{-1}) in MCH[195] and merocyanine dimers ($K_D = 8.0 \cdot 10^6$ M^{-1}) in dioxane.[196] As these systems exhibit the highest aggregation constants reported so far, the new corannulene derivative is among the strongest self-assembling motifs, when decorated with proper substituents.

As *bay* unsubstituted PBI dyes are congeners of the investigated corannulene derivative **1a**, a comparison to the well-studied PBI **75**, with the same solubilizing chains, might help to predict the properties of other new derivatives. Similar trends for the self-assembly should be observed for both molecules in different solvents, thus future optimization of the side chain for even higher aggregation constants might be performed analogous to PBI molecules.[189] A loss of the vibronic structure and broadening of the UV/Vis spectra upon aggregation is found for **1a** in a solution of toluene as well as for PBI **75** (Figure 25c). The comparison of the aggregation constants *K* of molecule **1a** and the congener PBI **75**, shows a significant increase by approximately two orders of magnitude for the three solvents, which were investigated for both molecules, MCH, toluene and CCl_4 of **1a** (Table 2).[189] This shows the extraordinary high tendency of the new class of corannulene derivatives bearing brush-like imide residues to self-assemble, which seem not to hinder the aggregation by their steric demand.

3.2.4. Structural elucidation

The changes in the emission spectra of dye **1a** (Figure 26) are also of high interest for the characterization of the aggregate and a comparison to PBI **75**. Depending on the concentration, the color of the emitted light changes from yellow ($c_0 = 1 \cdot 10^{-7}$ M) via orange to red ($c_0 = 2 \cdot 10^{-3}$ M). A similar change of the color depending on the fraction of aggregated molecules in solution and the emission band is observed for the congener **75** in MCH.[195] Upon aggregation, a broad, structureless emission band, that is attributed to the dimer, emerges at 550 nm to 850 nm, which is also very similar to the excimer emission of PBI **75**[197,198]. The fluorescence quantum yield (Φ_f) of **1a** in toluene is even higher (54%) than the already substantial quantum yield of the monomer in DCM (43%, Table 1). Remarkably, the aggregate also exhibits a quite high quantum yield of 24% despite of the contortion of the π-scaffold that is known to favor intersystem crossing.[199] Time-resolved measurements indicated a significant increase of the lifetime from $\tau = 4.32$ ns for the monomer to 8.56 ns for the dimer. Similar as for PBI **75**,[197,198] the longer lifetime is characteristic for a partially forbidden radiative process, presumably from an excimer-like excited state. This view is also corroborated by the absorption spectra of dimer **1a** which show a decrease of the intensity of the 0,0 transition and a hypsochromic shift of the

absorption maximum compared to the monomer which are indicative for a H-type exciton coupling.[200,201]

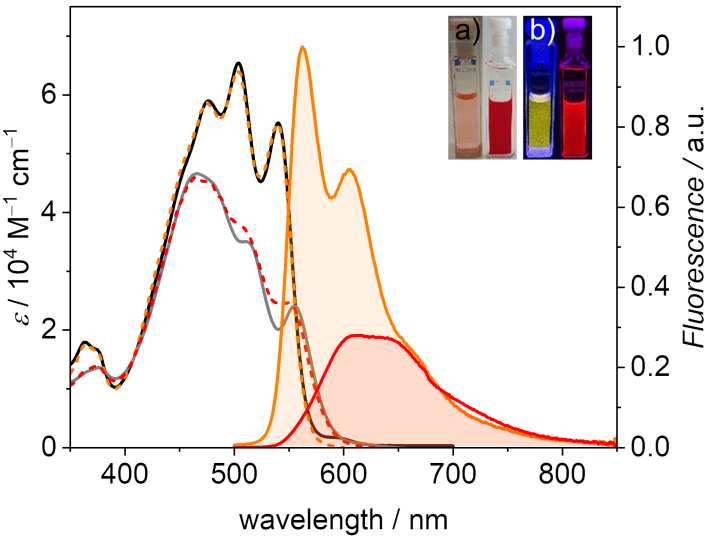

Figure 26 UV/Vis absorption spectra (monomer: black; dimer: grey) of **1a** in toluene at 25 °C and the respective fluorescence (solid lines; λ_{ex} = 469 nm) as well as excitation (dashed lines) spectra of monomer (orange, c_0 = $1 \cdot 10^{-7}$ M; λ_{em} = 605 nm) and dimer (red, $c_0 = 2 \cdot 10^{-3}$ M; λ_{em} = 650 nm). The inset shows the optical photographs of the sample solutions under a) ambient and b) black light illumination.

Supporting evidence for the formation of dimers has been obtained by AFM measurements that were performed by spin coating solutions of different concentrations of **1a** in toluene (monomeric: $c_0 = 2 \cdot 10^{-5}$ M and aggregated: $c_0 = 3 \cdot 10^{-3}$ M) onto TPA-modified SiO_2/AlO_x substrates (Figure 27). Spin-coating leads to the formation of a multi-layered film consisting of small spherical particles with the height of 0.5 - 0.9 nm for the diluted sample, which is in accordance with the height found for **1b** in the crystal structure[165] and 0.5 - 1.0 nm of the concentrated sample respectively. The height values indicate the presence of species of similar size in the order of the individual molecules in both solutions (Figure 27). Obviously, the AFM images do not indicate the formation of any larger-sized columnar aggregates which were observed for PBI **75** and other related PBI aggregates whose self-assembly is characterized by an isodesmic growth.[197] Accordingly, the preferentially dimerized **1a** species in solution obviously do not form defined extended aggregates upon solvent evaporation during the spin-coating process.

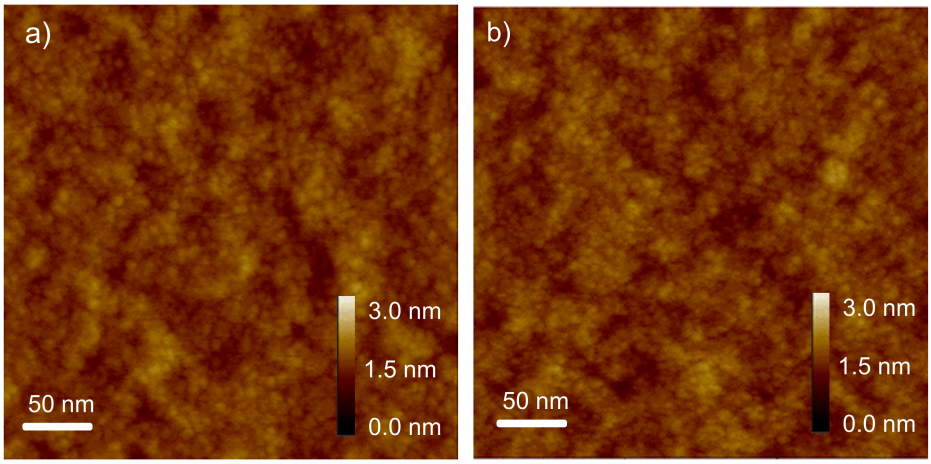

Figure 27 AFM height images of **1a** prepared by spin-coating onto TPA-modified SiO_2/AlO_x substrates from toluene at a concentration of a) $c_0 = 2 \cdot 10^{-5}$ M ($\alpha_{agg} = 0.11$) and b) $c_0 = 3 \cdot 10^{-3}$ M ($\alpha_{agg} = 0.91$).

To further confirm the presence of dimers of **1a** in solution, DOSY NMR studies were performed in TCE-d_2 ($c_0 = 5 \cdot 10^{-3}$ M) at 260 K as well as 390 K, where either mostly dimers ($\alpha_{agg} = 0.9$) or monomers ($\alpha_{agg} = 0.1$) are present. The diffusion coefficients of $D_M = 4.19 \cdot 10^{-10}\,m^2\,s^{-1}$ for the monomeric species at elevated temperatures and $D_D = 4.31 \cdot 10^{-11}\,m^2\,s^{-1}$ for the dimeric species at low temperatures have been determined. The hydrodynamic radii of both species were obtained by solving the Stokes-Einstein equation using the inherent solvent as standard, giving $r_M = 13.7$ Å for the monomer and $r_D = 15.6$ Å for the dimer, respectively (Figure 39). The obtained values match the dimension of a dimer at high concentrations and room temperature in solution. Furthermore, the two obtained radii are very similar, and thus in agreement with the AFM measurements which revealed similar sized particles for the monomer and the aggregate on TPA-modified surfaces.

To gain further insight into the precise arrangement of the molecules within the dimers, semi-empirical calculations (PM6-D3H4) were performed. Geometry optimizations for the dimer of **1a** afforded two structures of lowest energy, driven either primarily by the maximization of π-overlap (dispersion interactions) or the antiparallel alignment of the ground state dipole moments (electrostatic interactions). The maximization of π-π-interactions between the concave and convex face of the corannulene derivative is realized in the structure shown in Figure 28a, making the system overall 11 kJ mol^{-1} lower in energy compared to the structure in Figure 28b. The structural motif in Figure 28a also resembles the one calculated for corannulenes without appended naphthalimide units which suggested the formation of eclipsed dimers to be energetically favored.[202]

In this favored structure, depicted in Figure 28a, two corannulene moieties stack on top of each other in a parallel fashion. As a consequence, the overall ground state dipole moments sum up

to μ_g = 7.5 D compared to the monomeric species (μ_g = 3.8 D). Previous theoretical investigations of corannulene dimers showed that the interactions between these curved π-systems are of comparable magnitude to those of similarly sized planar systems. In these studies an equilibrium distance between two bowl-shaped corannulene molecules of 3.6 Å has been determined. In contrast, the equilibrium distance between two planarized corannulene moieties has been calculated to be 3.4 Å, which is similar to the π-π-distance in PBI molecules.[202]

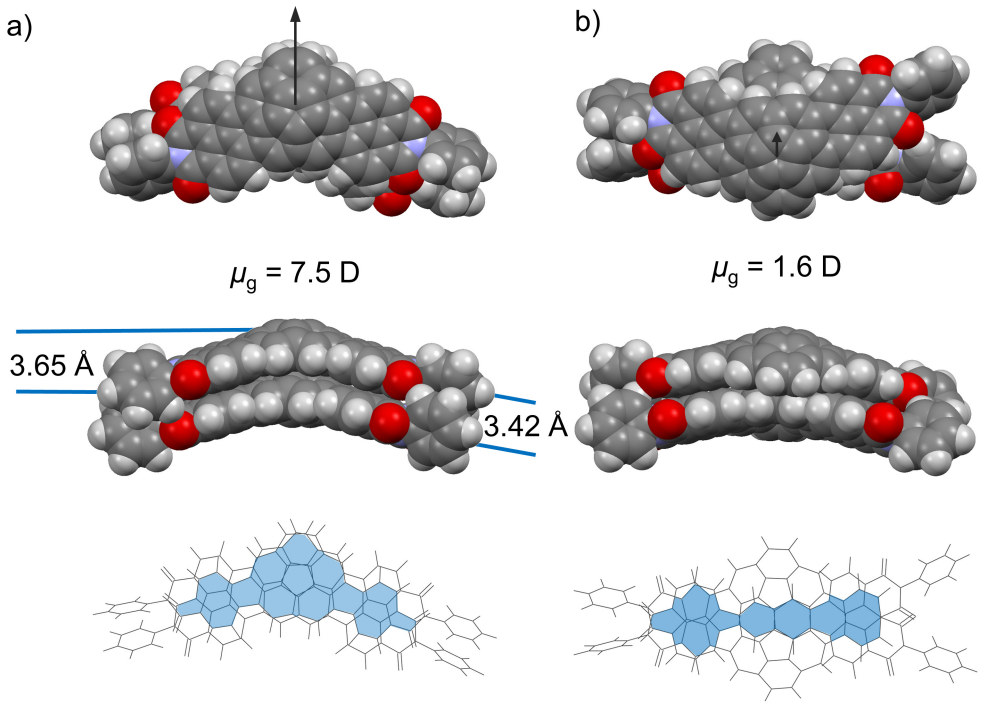

Figure 28 Top and side views onto two geometry-optimized (PM6-D3H4) structures that are lowest in energy for the dimer of **1a** governed either by a) intimate π-π-stacking or b) electrostatic dipole-dipole interactions. Bottom: Comparison of the minimal overlap of the π-systems (light blue area) of both dimeric structures of **1a**. The dodecyl chains were omitted for the geometry optimization.

Both values can be found in our new system, as the distance between the two bowls is calculated to be 3.65 Å in average, whereas the distance between the planar naphthalene moieties is about 3.45 Å. In our opinion, this minor distortion of the π-scaffold to enable a closer contact between neighboring naphthalimide units is the reason for the increase of the dimerization constant and the concomitant decrease of the elongation constant for this molecule. Similar observations have been made for PBIs which self-assemble with equal *K*-values for the two π-faces (i.e. isodesmic) as long as they are planar[197] but prefer to only dimerize after distortion by substituents in the bay area.[203] Another minor influence could be given by sterical congestions between the sidechains that are located rather close in space due to the small rotational displacements for the lower energy dimer structure displayed in Figure 28a. Notably, this rotational displacement is by far smaller than for perylene bisimides.[197]

In contrast, in the second structure shown in Figure 28b, the dimerization is strongly governed by the antiparallel alignment of the two corannulene moieties, almost completely cancelling the ground state dipole moment to μ_g = 1.6 D. In this structure, less overlap of the two π-systems is observed. Both structures are quite similar in size and energy, thus it is not possible to differentiate them in solution by the applied experimental techniques.

3.3. Conclusions

In conclusion, we have studied the self-assembly of a new naphthalimide-annulated corannulene derivative, with tris(dodecyl)phenyl substituents to obtain high solubility even in low polar solvents such as MCH. The ability to form supramolecular dimers of outstanding thermodynamic stability in solution in the investigated concentration range was confirmed by UV/Vis, ^{1}H- and DOSY-NMR spectroscopy as well as AFM. To the best of our knowledge, this is the first report on the self-assembly of a corannulene derivative in solution. The dimerization constants of up to > 10^6 M^{-1} in MCH are among the highest ones reported for π-conjugated systems, being in the same order of magnitude as those reported for phthalocyanine dimers ($K_D = 3.0 \cdot 10^6$ M^{-1}) in CCl_4, extended PBI aggregates ($K = 1.5 \cdot 10^7$ M^{-1}) in MCH and merocyanine dimers ($K_D = 2.1 \cdot 10^7$ M^{-1}) in CCl_4. Direct comparison to a structurally related PBI congener demonstrated the high propensity of our naphthalimide-annulated corannulene to self-assembly in a variety of solvents. The small size of the aggregates has been confirmed by AFM and DOSY measurements. By taking into account the different forces (dispersion, electrostatics) participating in the dimerization, we were able to propose two optimized structures for the aggregate by semi-empirical calculations, one showing parallel alignment driven by π-π-interactions and the other antiparallel alignment, supported by dipolar interactions. Having a significantly higher degree of π-overlap and a 11 kJ mol^{-1} higher stability, the likelihood for the prevalence of the parallel structure is higher. Further variations of the naphthalimide-annulated corannulene motif might provide a variety of new self-assembled supramolecular structures in solution. Such aggregates may also enable applications of these bowl-shaped molecules as electron accepting materials in organic solar cells and photodetector devices in combination with p-type semiconducting polymers.[38,204]

3.4. Supporting Information to Chapter 3

Materials and Methods

Reagents were purchased from commercial suppliers and used as received without further purification. Dichloromethane and ethyl acetate were distilled prior to use. All reactions were carried out under nitrogen atmosphere. Column chromatography was performed with commercial glass columns using silica gel 60M (particle size 0.04-0.063 mm; Merck KGaA) as stationary phase. Size-exclusion chromatography was performed on BioBeads S-X1 using HPLC grade solvents. NMR spectra were recorded on a Bruker *Avance III HD 400* or *Avance III HD 600* spectrometer and are calibrated to the residual proton signal of the used deuterated solvent. The chemical shifts (δ) are reported in parts per million (ppm) and coupling constants J in Hertz (Hz). Multiplicities for proton signals are abbreviated as s, d and m for singlet, doublet and multiplet, respectively. MALDI-TOF mass spectra were recorded with an *autoflex II* mass spectrometer (Bruker Daltonics GmbH) using DCTB (2-[(2E)-3-(4-*tert*-butylphenyl)-2-methylprop-2-enylidene]malononitrile) as matrix. High resolution mass spectra (ESI) were recorded with an *ESI micrOTOF Focus* mass spectrometer (Bruker Daltronics GmbH). UV/Vis absorption spectra were recorded on a *JASCO V-770* or *Perkin-Elmer Lambda 950* spectrometer and fluorescence spectra on a *FLS980* fluorescence spectrometer (Edinburgh Instruments). Absolute quantum yields were determined on a Hamamatsu Absolute PL Quantum Yield Measurement System *CC9920-02*. AFM Measurements were performed using a Bruker *Multimode 8 SPM* system operating in tapping mode. The samples were prepared by spin-coating toluene solutions of the molecule **1a** onto TPA-functionalized SiO_2/AlO_x-substrates. Theoretical calculations were performed by Gaussian 09 program using DFT B3LYP/def2svp or the semi-empirical PM6-D3H4 method[205, 206] as implemented in MOPAC2016[207]. Optimized ground-state geometries were examined by frequency analysis to possess no negative frequency.

4-Bromo-5-chloronaphthalene-1,8-dicarboxylic anhydride[165] and 3,4,5-tridodecylaniline[191] were synthesized according to procedures reported in the literature. Molecule **1b** was resynthesized according to the literature.[165]

Synthesis of 74a

4-Bromo-5-chloronaphthalene-1,8-dicarboxylic anhydride (8.68 mg, 27.9 µmol), 3,4,5-tridodecylaniline (50 mg, 83.6 µmol) and acetic acid (1 mL) were charged in a flask. The reaction mixture was stirred at 110 °C for 16 h. After cooling, the product was obtained by silica gel column chromatography (cyclohexane: dichloromethane 9:1) to give **74a** (4.3 mg, 4.82 µmol, 17%) as a slightly orange solid. Mp. 34 °C. ^{1}H-NMR (400 MHz, $CDCl_3$): δ [ppm] = 8.56 (d, J = 8.0 Hz, 1H), 8.44 (d, J = 8.0 Hz, 1H), 8.21 (d, J = 8.0 Hz, 1H), 7.94 (d, J = 8.0 Hz, 1H), 6.91 (s, 2H), 2.63 (m, 6H), 1.39-1.25 (m, 60 H), 0.87 (t, J = 7 Hz, 9H); ^{13}C-NMR (100 MHz, $CDCl_3$): δ *[ppm]* = 163.5, 163.3, 142.2, 139.4, 139.2, 136.1, 131.87, 131.80, 131.74, 131.67, 127.3, 127.1, 126.9, 126.0, 123.3, 122.8, 33.1, 31.93, 31.90, 31.2, 30.7, 30.39 ,30.37, 29.9, 29.73, 29.71, 29.68, 29.67, 29.66, 29.64, 29.59, 29.5, 29.4, 29.38, 29.35, 28.8, 22.70, 22.68, 14.12, 14.11; MS (MALDI-TOF, pos. mode, DCTB in $CHCl_3$): m/z calculated for $C_{54}H_{81}BrClNO_2^+$ $[M+H]^+$: 890.52, found: 890.54; HRMS (DIP-MS, pos. mode): *m/z* calculated for $C_{54}H_{82}BrClNO_2^+$ $[M]^+$: 890.5212, found: 890.5208.

Synthesis of 1a

Corannulene diboronic acid bis(pinacol)ester **73** (100 mg, 199 µmol), precursor **74a** (223 mg, 440 µmol), tris(dibenzylideneacetone) dipalladium(0)-chloroform adduct (10.4 mg, 10.0 µmol), tri(*m*-tolyl)phosphine (12.2 mg, 40.0 µmol), caesium carbonate (391 mg, 1.20 mmol) and 1-chloronaphthalene (6 mL) were placed in a Schlenk tube. The reaction mixture was stirred at 100 °C for 1 d. After cooling to room temperature, cyclohexane was added, and the mixture was purified by column chromatography using ethyl acetate as eluent followed by DCM. Size-exclusion chromatography on BioBeads S-X1 (DCM:MeOH 9:1) gave **1a** as a dark red solid (100 mg, 55.6 µmol, 28%). Mp. 330 °C. ^{1}H-NMR (400 MHz, TCE-d_2, 390 K): d [ppm] = 8.68 (d, J = 7.9 Hz, 2H), 8.65 (d, J = 7.9 Hz, 2H), 8.49 (d, J = 7.9 Hz, 2H), 8.43 (d, J = 7.9 Hz, 2H), 8.32 (s, 2H), 8.24 (s, 2H), 7.81 (s, 2H), 6.94 (s, 4H), 2.67 (m, 12H), 1.66 – 1.62 (m, 12H), 1.45 – 1.25 (m, 108H), 0.90 – 0.86 (m, 18H); ^{13}C-NMR (100 MHz, TCE-d_2, 390 K): d [ppm]= 162.8, 162.7, 141.3, 138.4, 136.8, 136.0, 135.8, 133.0 132.4, 132.2, 132.1, 132.0, 130.5, 130.0, 129.5, 128.2, 127.9, 126.7, 126.3, 122.7, 122.52, 122.47, 121.2, 32.6, 31.3, 31.2, 30.6, 29.9, 29.4, 29.07, 29.04, 28.98, 28.88, 28.65, 28.62; 21.9 MS (MALDI-TOF, neg. mode, DCTB in $CHCl_3$): *m/z* calculated for $C_{128}H_{168}N_2O_4^-$ $[M]^-$: 1797.301, found: 1797.298; HRMS (ESI-TOF, pos. mode, acetonitrile/chloroform 1/1) *m/z*: calculated for $C_{128}H_{168}N_2NaO_4^+$: 1820.2896 $[M+Na]^+$, found: 1820.2807; UV/Vis (c_0 = 1·10^{-5} M, DCM,

293 K): $\varepsilon_{max}(\lambda_{max})$ = 56200 M^{-1} cm^{-1} (503 nm); Fluorescence (DCM): λ_{max} (λ_{ex}) = 573 nm (501 nm); Φ_f = 0.43±0.04.

NMR spectra

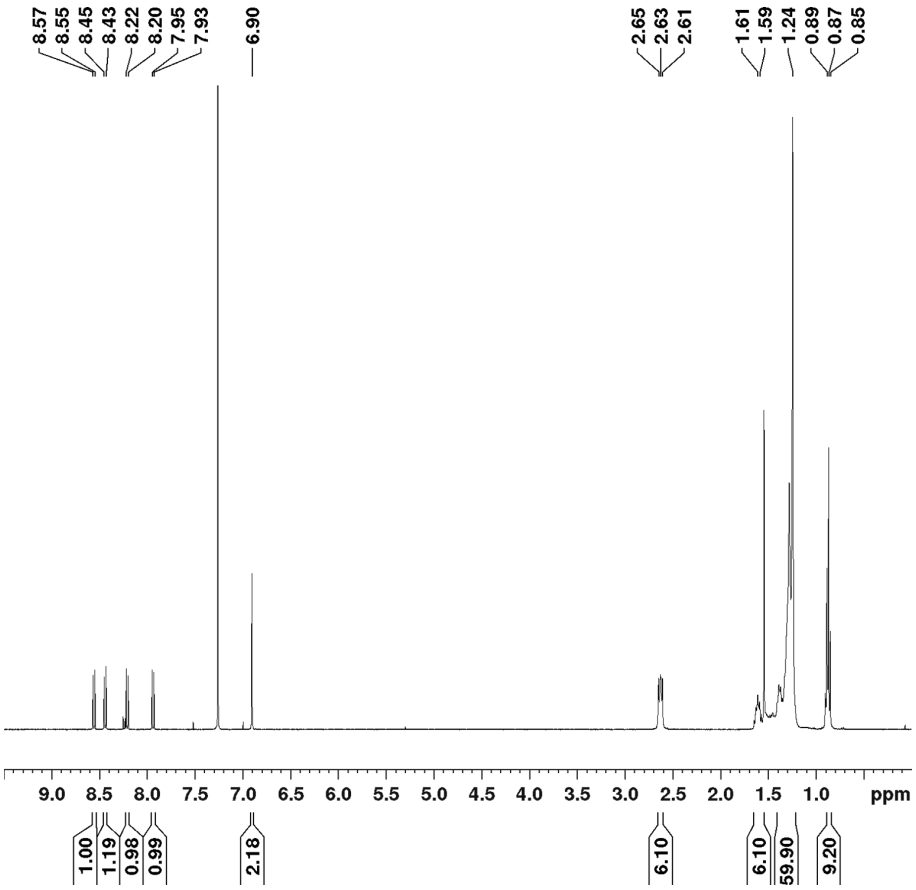

Figure 29 ^{1}H NMR spectrum (400 MHz) of **74a** in $CDCl_3$ recorded at 295 K.

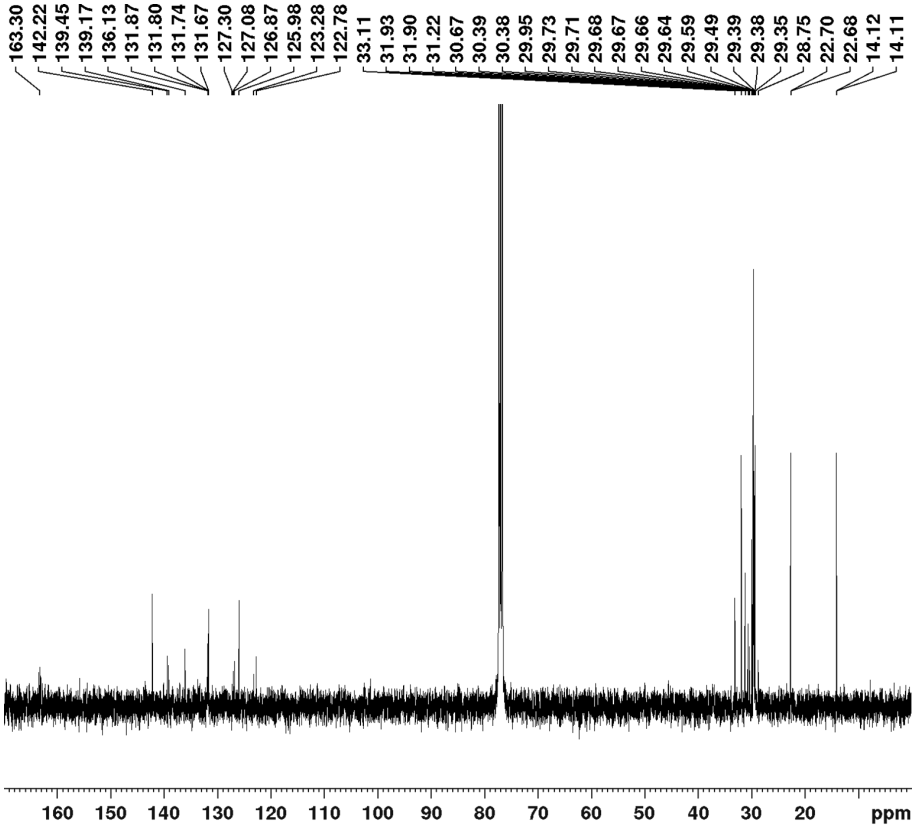

Figure 30 ^{13}C NMR spectrum (101 MHz) of **74a** in $CDCl_3$ recorded at 295 K.

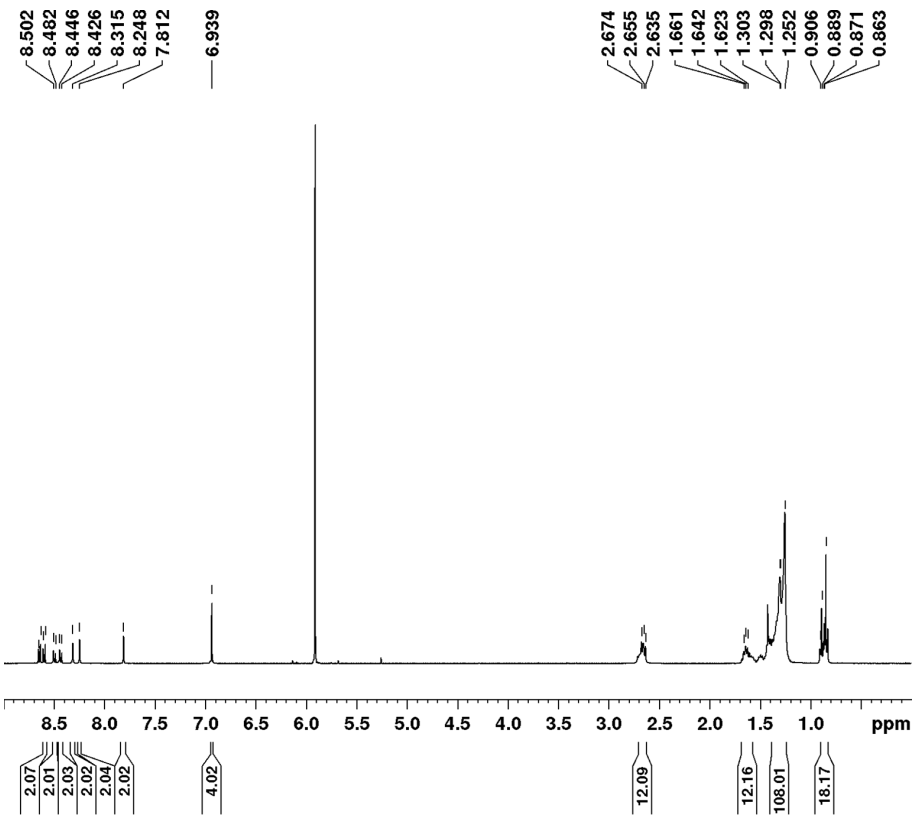

Figure 31 ^{1}H NMR spectrum (400 MHz) of **1a** in TCE-d_2 recorded at 390 K.

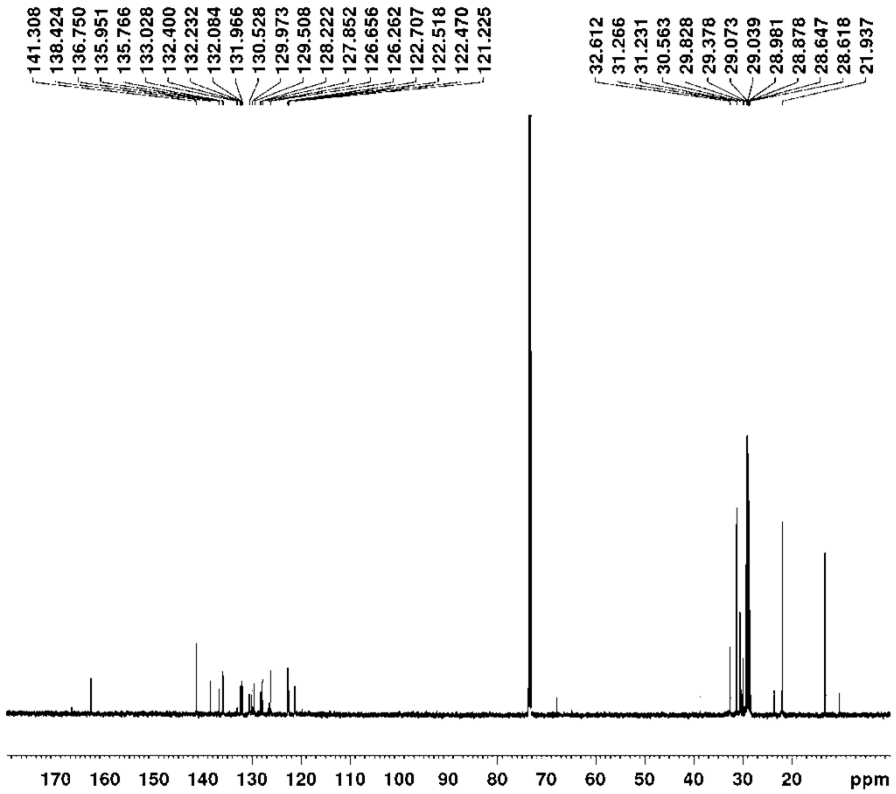

Figure 32 ^{13}C NMR spectrum (101 MHz) of **1a** in TCE-d_2 recorded at 390 K.

Temperature-dependent NMR spectroscopy

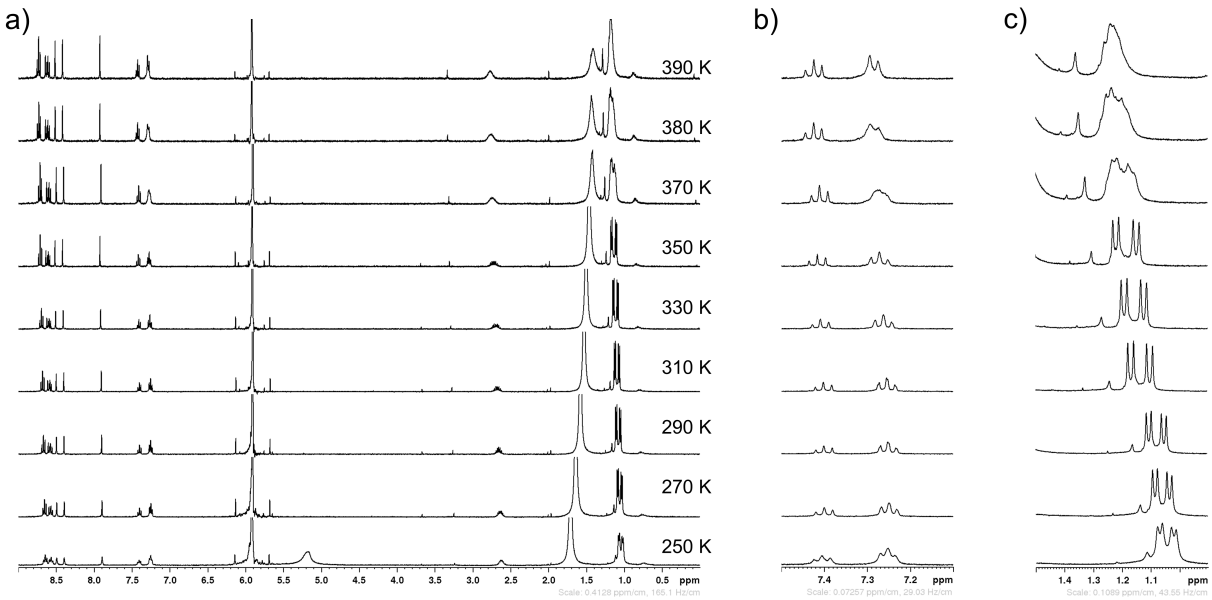

Figure 33 a) Temperature-dependent ^{1}H-NMR spectra of **1b** in TCE-d_2 and zoom on the signals for the diisopropyl group in the b) aromatic and c) aliphatic region at different temperatures in steps of 20 K (250 K to 390 K).

Calculations of the rate constant were performed by equation (Eq 1) and calculations of the estimated free enthalpy of activation $\Delta G^{\ddagger}$ for **1b** at the coalescence temperature (T_c = 370 K) were performed using the Eyring equation (Eq 2).[208]

$$k_c = 2.22 \cdot \sqrt{(\Delta\nu)^2 + 6J(AB)} \qquad \text{(Eq 1)}$$

$$\Delta G_c^{\ddagger} = 4.58\, T_c(10.32 + \log(T_c/k_c)) \qquad \text{(Eq 2)}$$

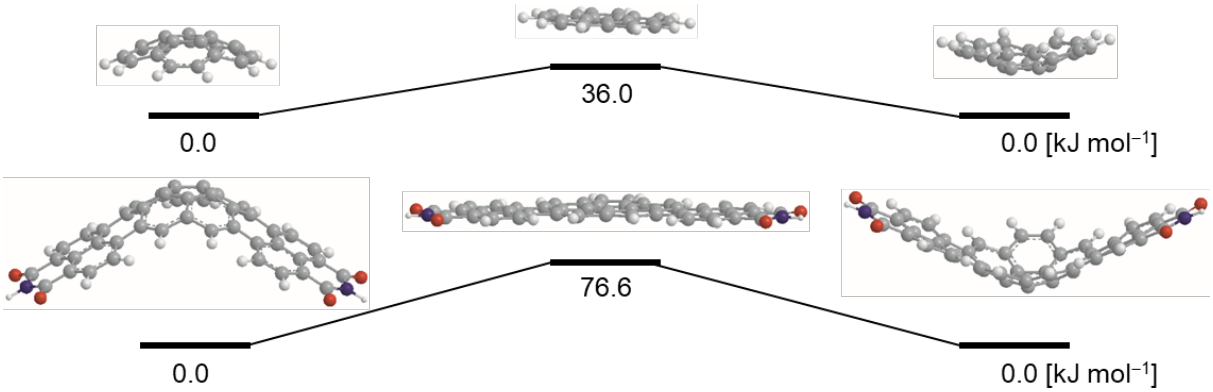

Figure 34 Inversion energies of corannulene (top) and a naphthalimide-annulated derivative (bottom) calculated by DFT at the B3LYP/def2svp level. The residues in imide position were replaced by hydrogen atoms for the geometry optimization.

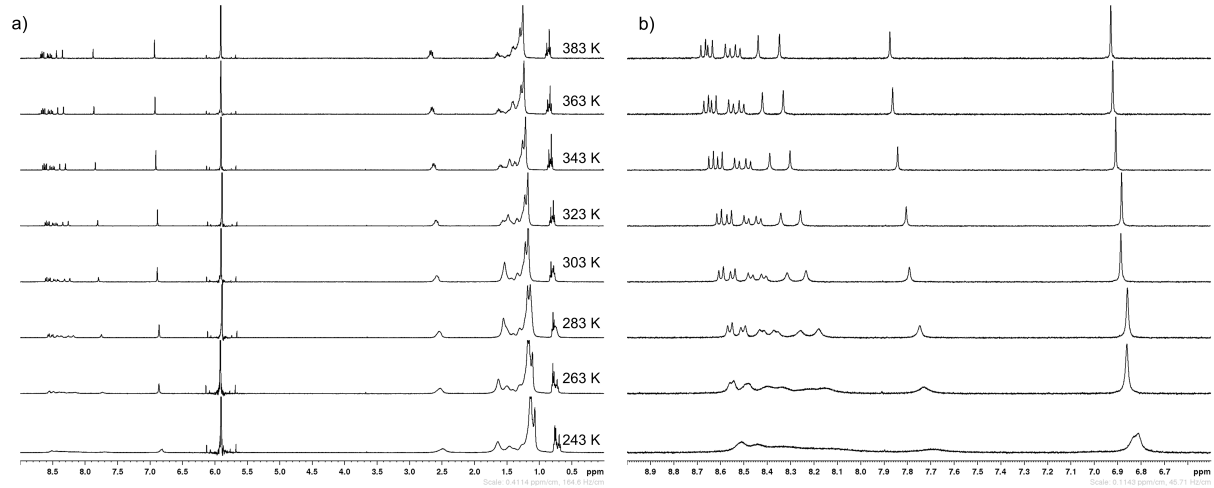

Figure 35 a) Temperature-dependent ^{1}H-NMR spectra of **1a** in TCE-d_2 and b) zoom on the aromatic region at different temperatures measured in steps of 20 K.

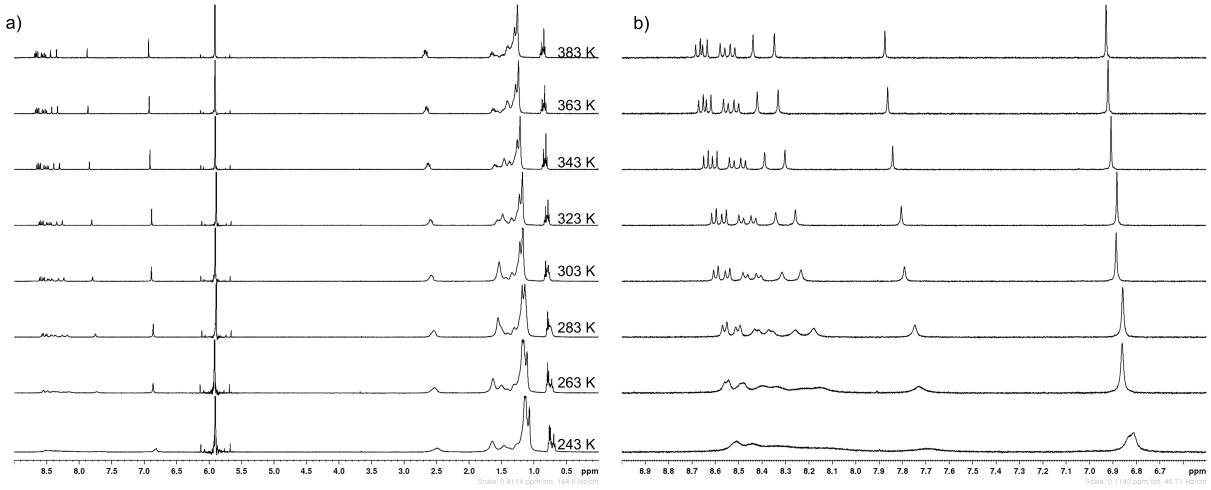

Figure 36 a) Temperature-dependent ^{1}H-NMR spectra of **1a** in toluene-d_8 and b) zoom on the aromatic region at different temperatures measured in steps of 20 K.

Temperature-dependent UV/Vis absorption studies

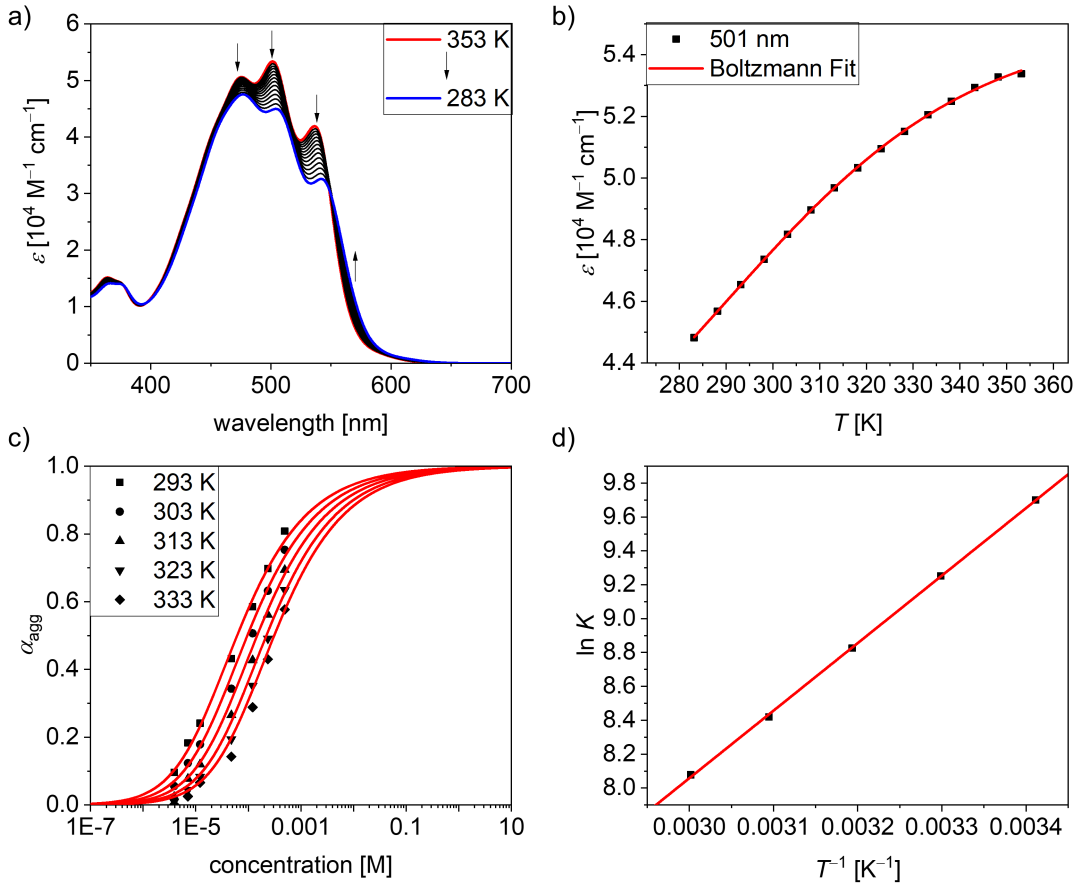

Figure 37 a) Density-corrected temperature-dependent (353 K to 283 K) UV/Vis absorption spectra of **1a** ($c_0 = 5 \cdot 10^{-5}$ M) in toluene. Arrows indicate changes with decreasing temperature. b) Plot of the extinction coefficient ε at 501 nm in dependence of the temperature T. c) Plot of the degree of aggregation α_{agg} against the concentration c_0 from concentration-dependent UV/Vis absorption data of 3a ($c_0 = 4.92 \cdot 10^{-4} - 3.90 \cdot 10^{-6}$ M) in toluene at different temperatures from 293 K to 333 K according to the dimer model. d) Van't Hoff plot for the determination of the thermodynamic parameters.

Comparison of different aggregation models

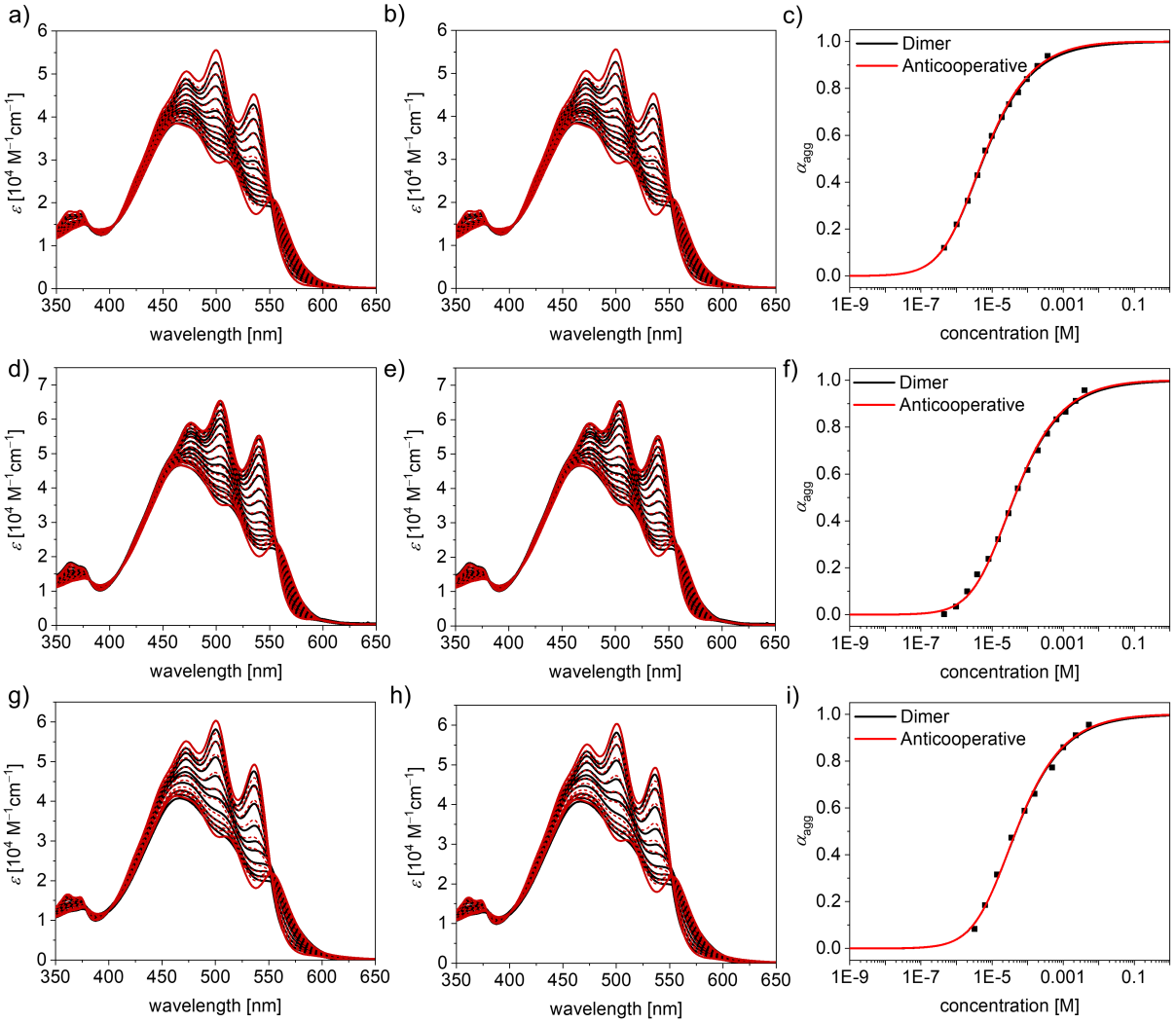

Figure 38 Concentration-dependent UV/Vis spectra of **1a** at 25 °C (c_0 = 4.5·10^{-7} M - 4.0·10^{-3} M, black) in a) – c) a mixture of MCH and toluene (2:1), d) – f) toluene, and g) – i) CCl_4, fitted with the global fit according to the monomer-dimer model (a), d), g); red) and the anti-cooperative model (b), e), h), red). Direct comparison of the molar fraction of aggregated molecules (α_{agg}) as a function of concentration for the dimer (black) and the anticooperative (red) aggregation model in the respective solvent or solvent mixtures.

DOSY NMR spectroscopy

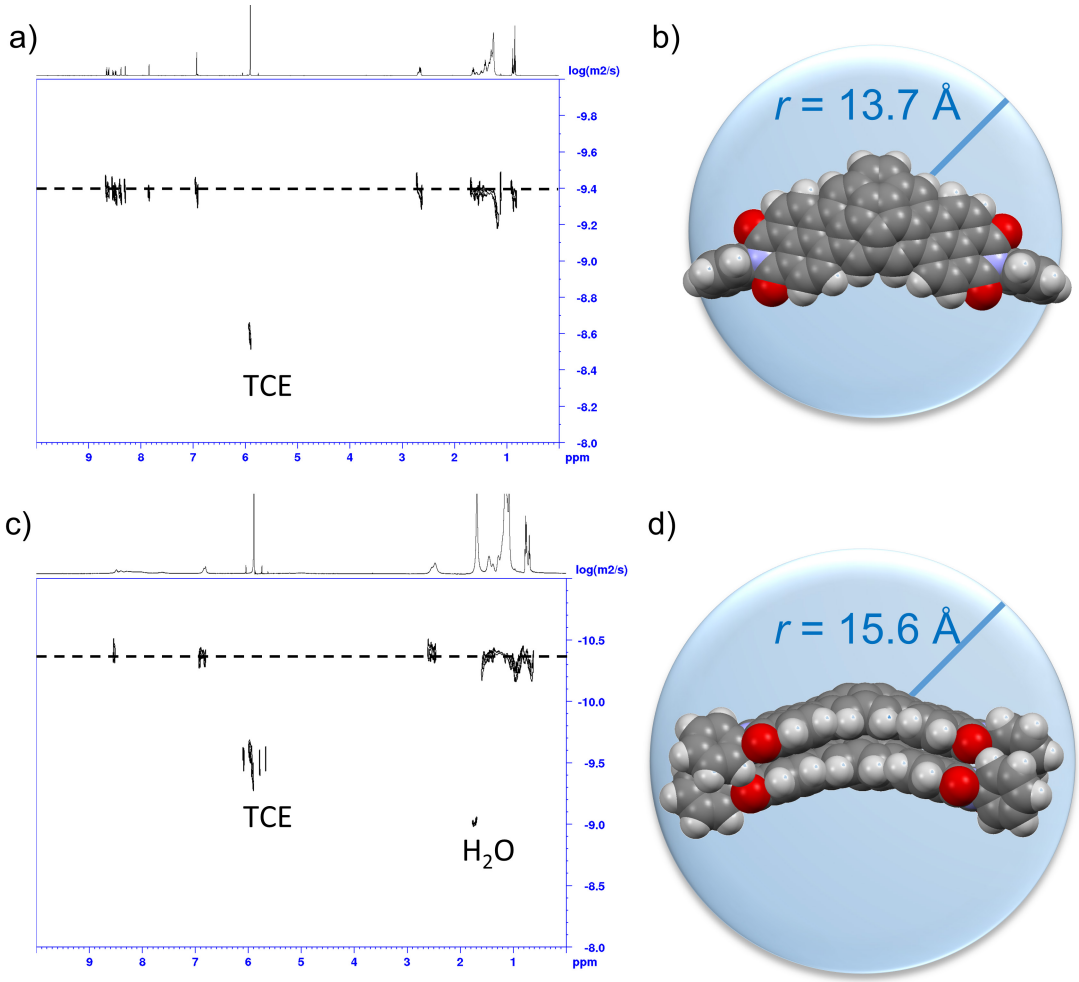

Figure 39 2D plot of DOSY NMR (600 MHz) spectra of **1a** in toluene-d_8 ($c_0 = 5 \cdot 10^{-3}$ M) at a) 390 K and c) 260 K. Illustration of the energy minimized b) monomer and d) dimer structures of **1a** obtained from semi-empirical calculations (PM6-D3H4) and hydrodynamic radii as deduced from the Stokes-Einstein equation using the inherent solvent TCE-d_2 of known size as reference.[209]

Fluorescence spectroscopy

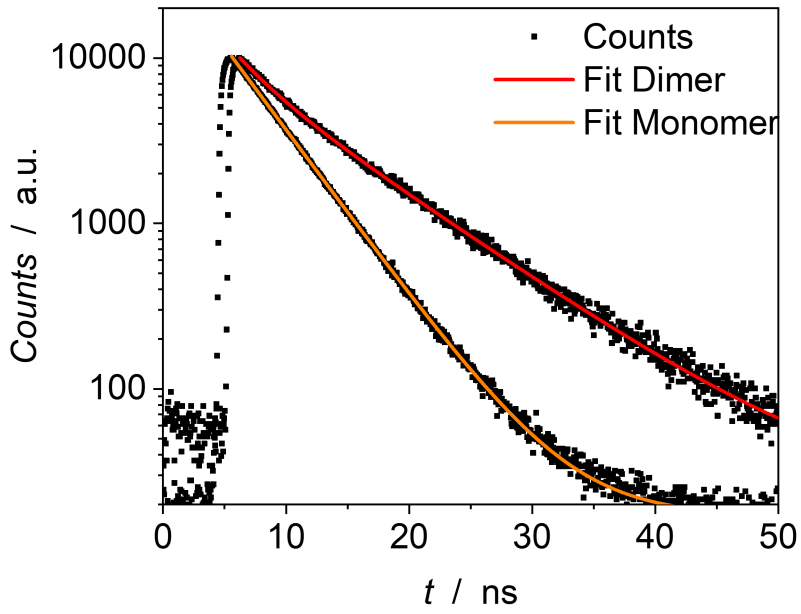

Figure 40 Fluorescence lifetime measurements (dots) of monomer (M: orange; $c_0 = 1 \cdot 10^{-7}$ M) and dimer (D: red; $c_0 = 1 \cdot 10^{-3}$ M) of **1a** in toluene at 25 °C measured under magic angle conditions (54.7°) after excitation with a EPL laser diode ($\lambda_{ex} = 479.9$ nm). The regression curves (solid lines) for evaluation of the fluorescence lifetimes are depicted as well.

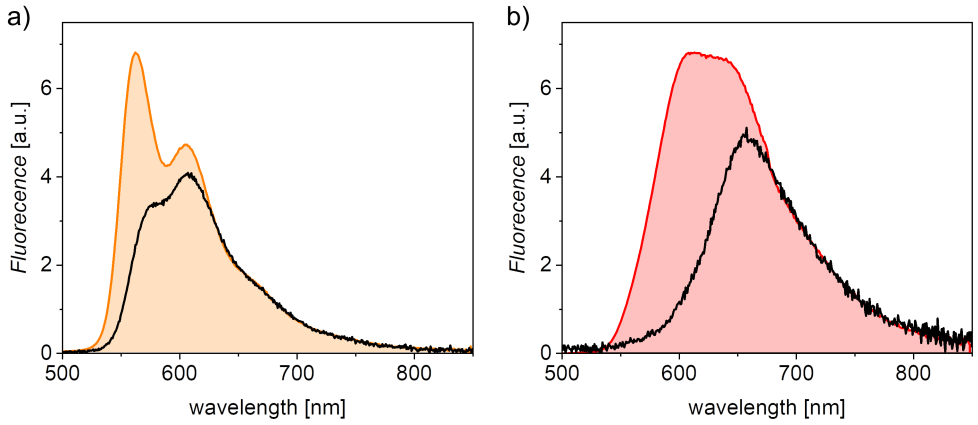

Figure 41 Fluorescence spectra recorded with an integrating sphere setup (black solid line) of a) monomers ($c_0 = 1 \cdot 10^{-6}$ M, $\lambda_{ex} = 470$ nm) and b) dimers ($c_0 = 1 \cdot 10^{-4}$ M; $\lambda_{ex} = 470$ nm) of **1a** in toluene at 25 °C for absolute quantum yield determination as well as the reabsorption-free emission profile.

Theoretical investigations

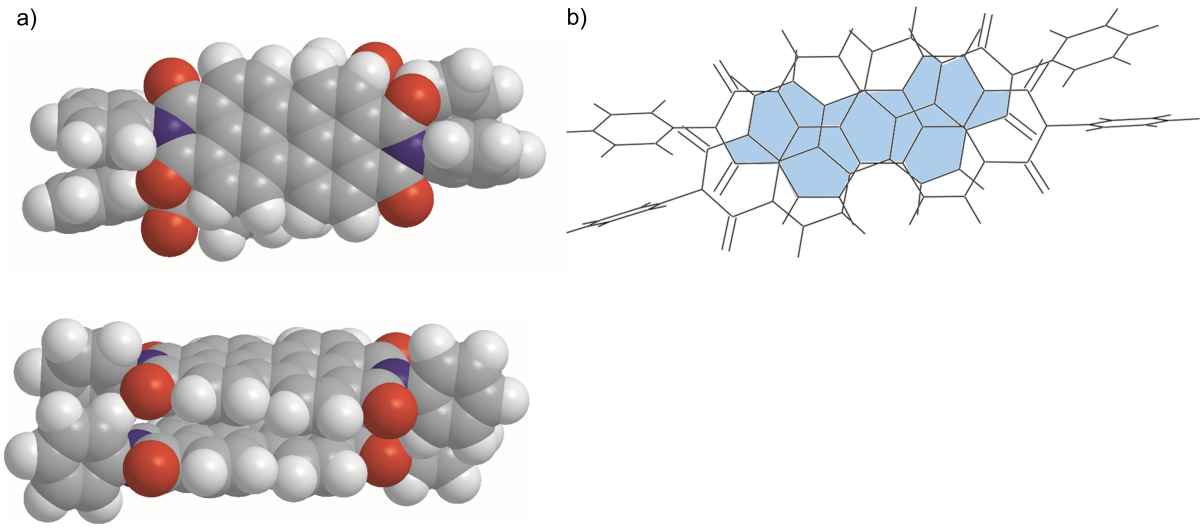

Figure 42 a) Top and side views onto the geometry-optimized (PM6-D3H4) structure that are lowest in energy for the reference PBI **75**. The dodecyl chains were omitted for the geometry optimization. b) Minimal overlap of the π-systems (light blue area) of the structure in (a).

Chapter 4

Chiral Perylene Bisimide Dyes by Interlocked Arene Substituents in the Bay Area

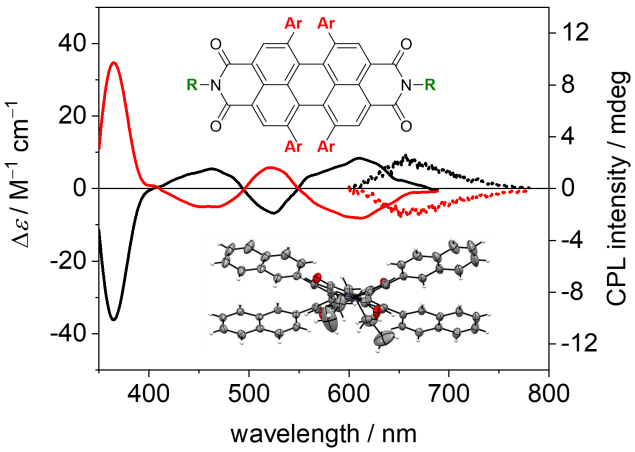

This chapter and the corresponding supporting information has been published:

R. Renner, B. Mahlmeister, O. Anhalt, M. Stolte, F. Würthner, *Chem. Eur. J.* **2021**, *27*, https://doi.org/10.1002/chem.202101877.

Adapted or reprinted with permission from Ref. [210].

Abstract: A series of perylene bisimide (PBI) dyes bearing various aryl substituents in 1,6,7,12 *bay* positions has been synthesized by Suzuki cross-coupling reaction. These molecules exhibit an exceptionally large and conformationally fixed twist angle of the PBI π-core due to the high steric congestion imparted by the aryl substituents in *bay* positions. Single crystal X-ray analyses of phenyl-, naphthyl- and pyrenyl-functionalized PBIs reveal interlocked π-π-stacking

motifs, leading to conformational chirality and the possibility for the isolation of enantiopure atropoisomers by semipreparative HPLC. The interlocked arrangement endows these molecules with substantial racemization barriers of about 120 kJ mol^{-1} for the tetraphenyl- and tetra-2-naphthyl-substituted derivatives, which is among the highest racemization barriers for axially chiral PBIs. Variable temperature NMR studies reveal the presence of a multitude of up to fourteen conformational isomers in solution that are interconverted via smaller activation barriers of about 65 kJ mol^{-1}. The redox and optical properties of these core-twisted PBIs have been characterized by cyclic voltammetry, UV/Vis/NIR and fluorescence spectroscopy and their respective atropo-enantiomers were further characterized by circular dichroism (CD) and circular polarized luminescence (CPL) spectroscopy.

4.1. Introduction

Perylene bisimides (PBIs) have been known for more than a century.[211] Initially used as vat dyes and pigments with superb tinctorial strength and photostability,[212-214] more applications have emerged over the last decades due to the unique properties of these molecules. These include outstanding fluorescence quantum yields,[215] excellent stability against environmental influences and high electron affinity, allowing for fairly stable radical anionic states[216,217] as required for ambient stable n-type semiconductors.[146,218,219] Their easy accessibility and the tailored properties arising by core functionalization promoted the application of PBI dyes in organic light emitting diodes (OLEDs),[220,221] organic thin-film transistors (OTFTs),[219,222] and organic lithium batteries.[223,224] In particular, a wide range of applications of PBIs were recently explored in organic solar cells (OSCs) where they found use in interlayers,[41] as sensitizers,[225] or as non-fullerene acceptors (NFAs).[38,226] Furthermore, PBIs are applied as fluorescence labels for bioimaging[227,228] and as fluorescence dyes for single-molecule spectroscopy and microscopy.[229]

The molecular properties of PBIs can be tailored by substitution in the *bay*[212] or headland (*ortho*)[230,231] positions whilst the imide residues have only a minor influence on the molecular properties and are commonly used to control the solubility and guide the molecular arrangement in supramolecular aggregates or in the solid state.[13] Most significantly, the substitution in the central *bay* positions not only changes the molecular structure along with the optical and electronic properties but influences solubility and molecular packing as well. Usually, the corresponding bis- and tetra-bay-halogenated PBIs[149,232] are used as precursors for the *bay* functionalization. By nucleophilic substitution of the halogen atoms with alcohol-, amino-, and thiol-groups, a broader variety of PBI chromophores with adjustable optical and redox properties are accessible.[212,214,233] Another option for the variation of functional groups in *bay* position of a halogenated PBI are palladium-catalyzed C-C coupling reactions like the Suzuki coupling[40,149,234] and the Sonogashira reaction.[235,236] However, due to the steric vicinity of the substituents in 1 and 12 as well as in 6 and 7 position, respectively, the synthesis of tetra *bay* substituted PBIs via coupling reactions remains challenging.[149] Depending on the steric demand of each substituent, a twist of the two naphthalene subunits of the PBI π-scaffold is observed, resulting in axial chirality. Variation of the twist angle affects both solubility and electronic properties of the molecule. The angle between the two naphthalimide sub-planes can be as large as 37.2° for the tetrabromo substituted PBI, as proven by single crystal X-ray crystallography.[146] Despite the close proximity and steric demand of the four *bay* substituents,

fast interconversion between the *P*- and *M*-atropo-enantiomers is typically observed for tetrasubstituted PBIs, hampering the separation of the two isomers.[237] Strategies hitherto applied to increase the racemization barrier comprise the fixation of one atropo-enantiomer with aryloxy-substituents into a macrocyclic structure[148,150,238] or the introduction of groups with large Van der Waals radii like bromine or phenyl.[237] The isolation of the respective *P*- and *M*-atropo-enantiomers at ambient conditions requires a racemization barrier higher than 93 kJ mol^{-1}.[237] A systematic experimental investigation of the racemization process has previously been conducted for halogenated PBIs but to the best of our knowledge, no similar reports are found for tetraarylated PBIs, which have first been synthesized by Zhu and coworkers in 2006 via Suzuki-cross coupling reaction[149] and were further explored by Hoffmann and co-workers.[40,234]

Inspired by the intriguing crowding of four aryl groups in *bay* area and in this regard surprisingly high yields for the synthesis of 1,6,7,12-tetraphenyl-PBIs by fourfold Suzuki coupling,[40,149,234] we herein systematically investigate the influence of a broader variety of substituents attached at the four *bay* positions on the properties of these chromophores, i.e. their racemization barriers, UV/Vis/NIR absorption and fluorescence as well as circular dichroism (CD) and circular polarized luminescence (CPL). Furthermore, we present the first single crystal X-ray analyses of different tetraarylated PBIs that reveal a π-π-stacking enforced interlocked motif and twist angles of up to 36.6°. Our systematic investigations by temperature-dependent NMR spectroscopy provide insights into the activation energies for racemization and reveal an amazing variety of conformational isomers that are stabilized by π-π-stacking interactions.

4.2. Results and Discussion

4.2.1. Synthesis

The whole series of tetraarylated PBIs investigated in this study was synthesized by Suzuki-coupling of the respective 1,6,7,12-tetrachloro PBI with the corresponding arylboronic acid. The reactions were conducted in the presence of the catalyst $Pd(PPh_3)_4$ and potassium carbonate in a solvent mixture of toluene, ethanol and water by application of three freeze-pump-thaw cycles, to ensure deoxygenated conditions (Scheme 5). Utilizing this straightforward synthetic approach, a variety of *bay* tetraarylated PBIs are synthesized. These include literature-reported derivatives **2a**-**c** and new derivatives with different substituents (**2d**-**e**, **3a**, **4a**, **5a**, **6a**). PBIs **2a**,

2b and **2c**, which were previously reported in literature,[40,234] could be resynthesized with increased yields for all three derivatives of 73%, 75% and 66% respectively. The other two derivatives with phenyl substituents in *bay* position, **2d** and **2e**, could be obtained in slightly lower yields of 46% and 51% respectively, which might arise from lower conversion from the starting material to the product and losses during column chromatography and HPLC purification due to the lower solubility. Molecule **3a** with the electron-withdrawing trifluoromethyl group attached in the phenyl-*para*-position could be obtained in a similarly high yield of 60%. Upon extension of the aryl residues, the yield decreases notably. Derivative **4a** with 2-naphthyl substituents was obtained in a yield of 28%, whereas for **5a** with 1-naphthyl substituents 38% of the product could be isolated. The largest 1-pyrene substituent in **6a** gives the lowest yield of all synthesized derivatives of 22%. These observations can be rationalized by the investigation of the side products formed in this reaction, that reveal increasing amounts of triarylated PBI, due to the dehalogenation of the fourth *bay* position. Additionally, a mixture of the different double arylated and double dehalogenated PBIs can be isolated after the workup of the reaction mixture. This dehalogenation competes with the arylation reaction and becomes favored upon increasing steric demand of the aryl substituents as seen within the series **2a** (73%), **4a** (28%) to **6a** (22%).[40,149]

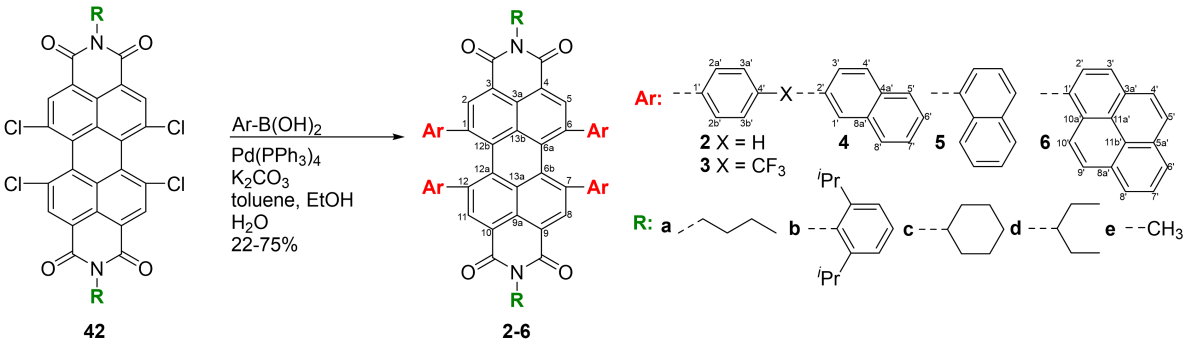

Scheme 5 Synthesis of a series of tetraarylated (Ar, red) PBIs **2a**-**2e**, **3a**, **4a**, **5a** and **6a** by Suzuki cross-coupling bearing different imide substituents (R, green) with labelling of the carbon atoms of the chromophore core.

4.2.2. Structural Analysis in the Solid State

For the characterization in the solid state, single crystals of the tetraarylated PBIs **2c**, **4a** and **6a** suitable for X-ray structure analysis could be obtained. This was realized by slow evaporation of either a chloroform (**2c**) or chlorobenzene (**4a**, **6a**) solution of the racemic mixture of the respective PBI that was carefully covered by a layer of *n*-hexane. The molecular structures in the crystal provide unambiguous evidence for the heavily twisted PBI π-scaffolds as well as the π-π-stacking enforced interlocked arrangement of the aryl substituents in *bay* position. While

2c crystallizes in the monoclinic C2/c space group, **4a** and **6a** crystallize in the triclinic P-1 space group. All crystals include both atropo-enantiomers (*M* and *P*) and the structures of **2c** and **4a** contain additional solvent molecules in the unit cell. For comparison, only the *M*-atropo-enantiomers for each derivative are depicted in Figure 43 while omitting the small disorder of the imide substituents as well as all solvent molecules.

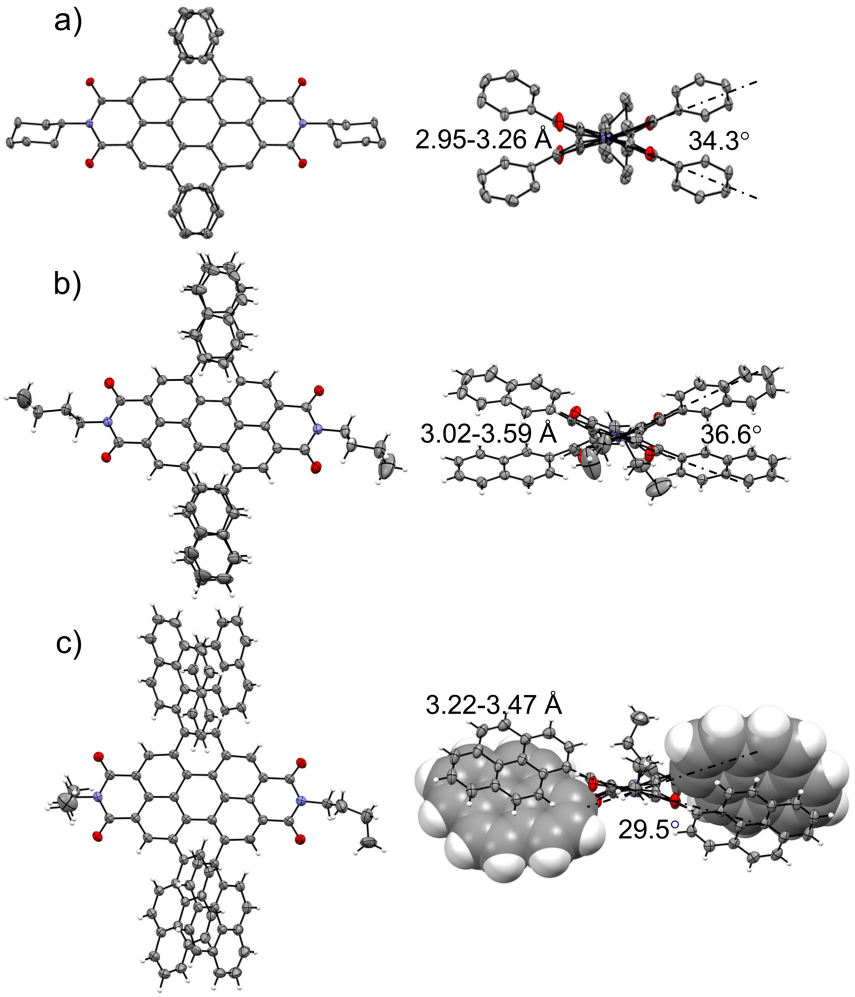

Figure 43 Molecular structures of each *M*-atropo-enantiomer of the single crystal structures of a) **2c**, b) **4a** and c) **6a** in top view onto the PBI-π-system (left) and along the *N*,*N*'-axis (right). The ellipsoids are set to 50% probability (C: gray, O: red, N: blue, H: white). Disorder of the imide residues as well as solvent molecules are omitted for clarity.

In **4a** and **6a**, only the conformational isomers with the highest symmetry with respect to the orientation of the four *bay* substituents are found in the respective single crystal structure. This might originate from their predominance in solution compared to the other possible isomers as observed by ^{1}H-NMR spectroscopy (*vide infra*) and their higher propensity to crystallize, i.e., structures I for **4a** (Figure 53) and **6a** (Figure 54), respectively. This conformational selection might be guided additionally by the maximization of π-π-interactions between the two π-stacked aryl residues in each of the bay areas.

The distortion of the PBI cores can be assessed by the consideration of the naphthalimide units as two planes and was measured to be 34.3°, 36.6° and 29.5° for **2c**, **4a** and **6a**, respectively (Table 4). These values are among the highest reported twist angles for PBI chromophores to be observed in single crystal structures. The twist angle of 36.6° of **4a** is only slightly smaller than the record value of 37.2° for the tetrabromo-substituted PBI,[146] but significantly larger than the structurally related tetraarylated peropyrenes reported by Chalifoux, which exhibit a twist angle of 29°.[119] This emphasizes the high strain in the PBI core imposed by the attachment of four directly conjugated aryl substituents. While the bromine atoms in the tetrabromo-substituted congener exhibit a very large steric crowding directly in *bay* position due to the large Van der Waals radius of bromine, the aryl substituents are able to establish intramolecular π-π-stacking interactions between 2.95 to 3.59 Å as shown in Figure 43. A second method to assess the distortion of the perylene core is to measure the dihedral angle of the four carbon atoms in the *bay* area ∠(C1, C12b, C12a and C12) (numbering according to Scheme 5). The dihedral angles for **2c** and **6a** differ slightly for both sides of the PBI, indicating a broken symmetry in the solid state, presumably due to packing effects. In contrast in **4a** both *bay* areas exhibit the same dihedral angle of 33.5° due to the presence of three perpendicular C_2 axes resulting in overall D_2 symmetry of the core. In **2c** the dihedral angles were found to be 32.7° and 33.4° respectively, while the difference is less pronounced in **6a** with 29.2° and 29.9° with the larger pyrene substituents. Such broken symmetry has been reported before for tetraphenoxy-PBIs[239,240] where it is an intrinsic feature of the perylene core rather than a packing effect in the solid state.[241] The carbon-carbon bond distances within the perylene core in all three molecules are comparable to previously reported PBIs. The larger carbon-carbon distances between the two naphthalene subunits compared to the shorter bonds within the naphthalene subunits explain the higher susceptibility of the PBI scaffold to distortions in the *bay* area.[239] While the single crystal X-ray structure of PBI **2c** contains a large amount of solvent molecules and shows almost no interactions between the individual chromophores, the molecular packing in the crystal of **4a** shows a slip-stacked packing arrangement of *P*- and *M*-PBI atropo-enantiomers at a center-to-center distance ($r_{C\text{-}C}$) of 8.04 Å with chlorobenzene occupying the solvent accessible voids within the unit cell (Figure 44a). The most interesting crystal structure is, however, the one of tetra-pyrenyl-substituted PBI **6a** that contains only a small void with only one disordered chlorobenzene molecule and is accordingly guided to a large degree by intermolecular interactions among the chromophores and their *bay* aryl-substituents. Similar as for **4a**, also for **6a** the characteristic slip-stacked packing arrangement

of *P*- and *M*-PBI chromophores at $r_{C\text{-}C}$ of 7.67 Å can be observed, that is here, however, directed by additional CH-π-interactions between the pyrene *bay* substituents (Figure 44b).

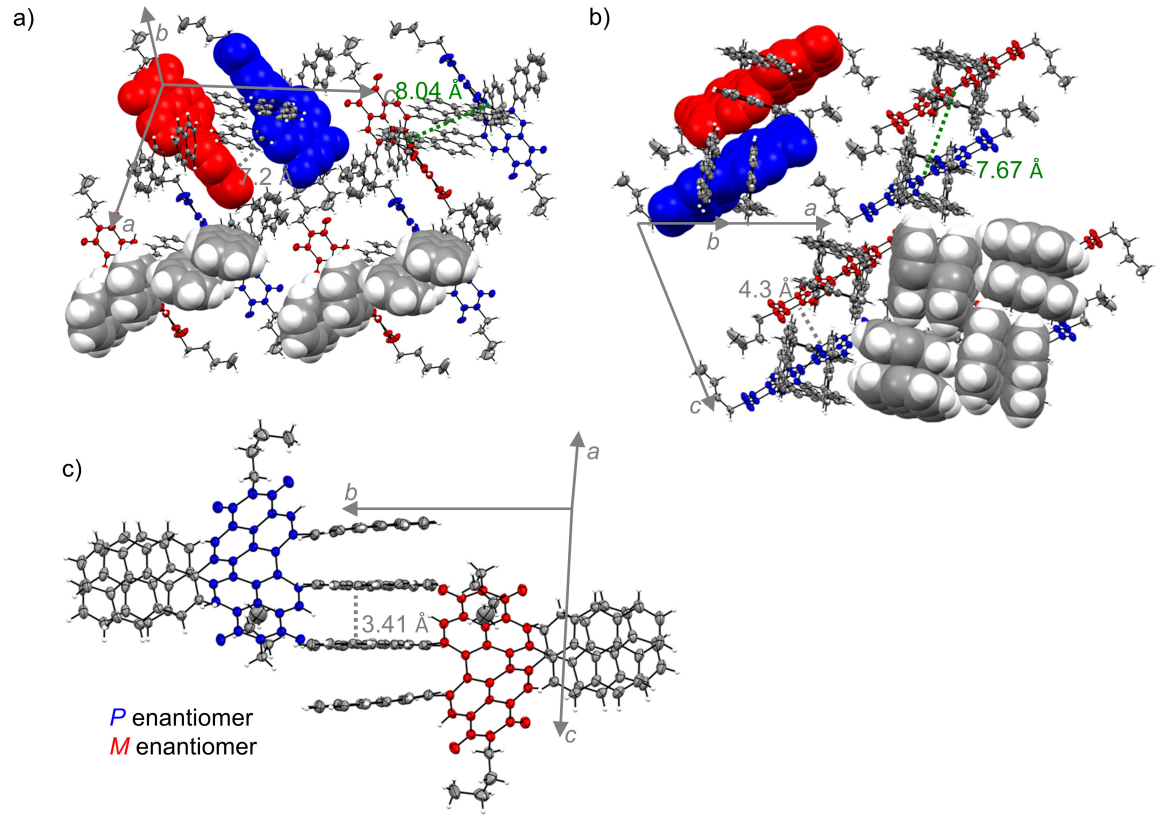

Figure 44 a) Molecular packing of **4a**, as well as b) side view onto the PBI π-surface and c) side view onto the π-stacked pyrene substituents of **6a** in their respective single crystal structures. PBI atropo-enantiomers are colored in blue (*P*) and red (*M*). The ellipsoids are set to 50% probability (C: gray, O: red, N: blue, H: white). Disorder of the imide residues as well as solvent molecules are omitted for clarity.

It is interesting to note that the co-facially stacked pyrene dimers are organized in tetrameric squares in these crystals, obviously directed by CH-π-interactions and that this kind of packing motif of π-stacked dimers interconnected by CH-π-interactions mimic the molecular arrangement found in single crystals of pristine pyrene.[242] Furthermore, along another crystallographic axis a quadruple π-stacking motif consisting of two pyrene dimers can be identified (Figure 44c). Thus, it can be concluded, that the crystal packing in **6a** is strongly influenced by the pyrene substituents rather than by the PBI core, while in **2c** and **4a** the core governs the crystal packing more than the respective aryl substituents.

4.2.3. Conformational Analysis in Solution

The characterization of the different *bay* substituted PBIs by ^{1}H-NMR spectroscopy in 1,1,2,2-tetrachloroethane-d^2 (TCE-d^2) and CD_2Cl_2 revealed structural differences in solution in

dependence of the type and connection of the respective *bay* substituents. It is important to state, that the subsequently discussed ^{1}H-NMR spectra were always obtained, regardless of the fraction of isolated material after purification or its temperature treatment. At room temperature, the signals assigned to the *ortho*- and *meta*-position of the phenyl substituents in **2a** are broadened (7.08 ppm and 6.70 ppm), while the signal of the *para*-proton (7.22 ppm) and the protons in *ortho* position of the PBI core (8.24 ppm) exhibit sharp signals. Upon heating, the broad *ortho*- and *meta*-proton signals become a sharp doublet and triplet respectively, indicating a fast exchange between the protons, while upon cooling two sets of signals can be observed, which are assigned to slow exchange of the protons due to decelerated rotation of the phenyl units (Figure 49).[243] The coalescence temperature T_c for the observed process is 303 K and the rotational barrier $\Delta G^{\ddagger}$ of 64.7 kJ mol^{-1} is comparable to values obtained for the rotation of different imide substituents in PBIs around the terminal C-N single bond, indicating the feasibility of this rotation at room temperature.[244] DFT calculations (Figure 52) provide a reasonable approximation for the rotational barrier and insights into the distortions required for the rotation of the aryl groups and the energetically more demanding enantiomerization that resembles the related processes in carbohelicenes[245] and in tetramethoxy perylene bisimides.[246]

For the 2-naphthyl-functionalized PBI **4a**, the T_c (323 K) and the $\Delta G^{\ddagger}$ (66.9 kJ mol^{-1}) are slightly higher than in **2a**, which can also be accounted for by an increased π-π-stacking interaction between the larger substituents (Figure 43a,b). Still, rotations of the interlocked 2-naphthyl substituents are possible at elevated temperatures, enabling a multitude of different conformations in solution. At lower temperatures (263 K), a second set of signals becomes visible, which is assigned to a less symmetric conformational isomer compared to the conformation responsible for the major signal (see Figure 45a, top, Figure 53).

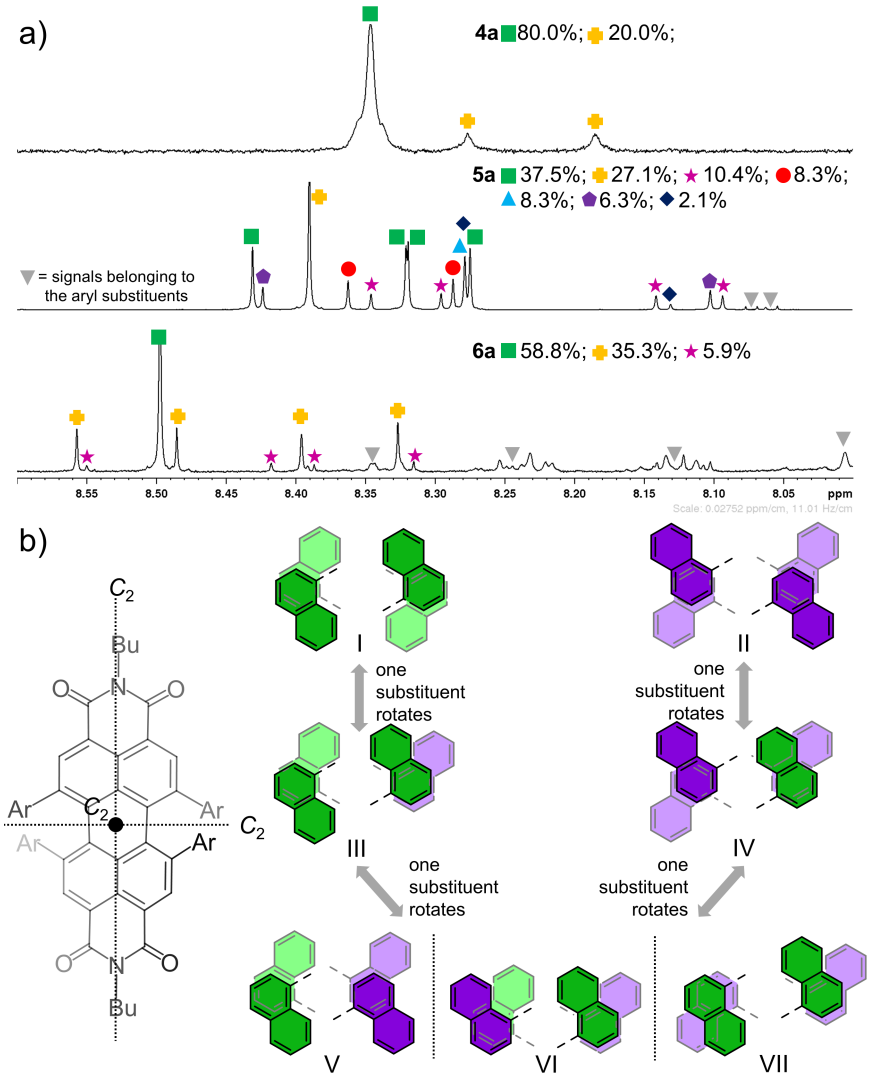

Figure 45 a) Aromatic region of the ^{1}H-NMR spectra of **4a** (top, 263 K, TCE-d^2), **5a** (middle, 293 K, CD_2Cl_2) and **6a** (bottom, 293 K, CD_2Cl_2) assigned to the *ortho* protons of the PBI core as well as ratio of the different conformational isomers found in the respective region; b) possible structures and transformations of the seven conformational isomers for the *P*-atropo-enantiomer of **5a**.

Taking advantage of the molecular structure derived from single crystal X-ray analysis (Figure 43b) we ascribe the major set of signals for the PBI *ortho*-protons, a singlet at 8.38 ppm at low temperatures of 263 K, to the highest symmetry conformation I, which exhibits the largest π-π-overlap of both pairs of neighboring naphthalene units and the least shielded protons in *ortho* position of the chromophore core (Figure 53). The smaller set of signals, which is slightly upfield shifted and composed of two singlets of equal size, is ascribed to one of the C_2 symmetric structures V, VI or VII (Figure 53). Based on the presumably favored larger π-overlap provided between two naphthalene subunits in one of the two *bay* areas we tentatively assigned these peaks to conformational isomer V, which could originate from a concerted rotation of two adjacent 2-naphthyl substituents starting from the symmetric structure I. According to the sizes of their respective integrals, structures I and V presumably exist at 263 K

in CD_2Cl_2 in a ratio of 4:1 (Figure 45a), while only the dominant one is found in the respective single crystal structure of **4a** (Figure 43b).

In contrast to **4a**, upon attachment of four naphthalene units via the 1-position (**5a**), a multitude of signal sets is found at room temperature in CD_2Cl_2 in the ^{1}H-NMR for the PBI *ortho* protons, which cannot be assigned to the respective conformational isomers in a straightforward manner (Figure 45a, middle). Additionally, no significant differences are observable by variable temperature ^{1}H-NMR at the lowest and highest temperatures, indicating the formation of either conformationally stably interlocked or easily interchangeable isomers due to the higher steric demand of the substituents in solution (Figure 51). Closer inspection of the aromatic region results again in the assignment of the peaks between 8.50 and 8.08 ppm to the four *ortho* protons of the PBI core, as the integral of this area corresponds exceptionally well to four protons, when calibrating the integrals to the alkyl chain in the aliphatic region of the NMR spectrum. By precise integration, seven sets of singlets could be distinguished for these proton signals and assigned to the overall fourteen conformers with varying symmetry that are obviously all present in solution (Figure 45b), considering that the *P*- and *M*-atropo-enantiomers cannot be distinguished by ^{1}H-NMR spectroscopy. A tentative assignment of the peaks was possible by taking into account the symmetry of the respective conformation, the π-overlap of the four aryl-substituents as well as the shielding and de-shielding of the *ortho* protons by the 1-naphthyl substituents. Thus, the most intense and isolated singlet at 8.39 ppm (orange cross, Figure 45a) should again correspond to structure I with D_2 symmetry (Figure 45b), while the other highly symmetric conformer II also with three C_2 axes should correspond to the singlet at 8.28 ppm (blue triangle). These structures account to about 27.1% (I) and 8.3% (II) of all the present conformations in solution (Figure 45a). The rotation of only one naphthalene substituent from either structure I or II leads to a tremendous loss of symmetry and thus four independent singlets are expected for structures III and IV, as observed in the ^{1}H-NMR spectrum (green rectangle equal 37.5%, pink star equal 10.4%). The subsequent rotation of another naphthalene unit can result in three different conformational isomers V, VI and VII, which all contain again one C_2 axis resulting in two singlets in the ^{1}H-NMR spectrum. Two sets of signals are identified unambiguously (purple pentagon equal 6.3%, red circle equal 8.3%), while the second singlet for the third conformer (dark blue diamond equal 2.1%) is presumably located beneath other signals at about 8.27 ppm, taking the integral and shapes of the signals as well as expected position into account. The coexistence of all seven conformational isomers for one enantiomer of PBI **5a** in solution at 293 K in contrast to only two isomers for PBI **4a** at 263 K might be explained by the larger preference of structure I of the latter due to better stabilization by

π-π-interactions of the adjacent π-stacked substituents (Figure 45b, Figure 53). The large conformational heterogeneity observed for **5a** in solution might also explain our failure to obtain single crystals suitable for X-ray crystallography while for **4a** this was achieved in a straightforward manner.

Interestingly, again in contrast to **5a** only three different conformationally stable species are observed at room temperature in the ^{1}H-NMR spectrum of **6a** in CD_2Cl_2, of which the derivative with the highest symmetry is the main conformer (Figure 45a, bottom). This can be rationalized by the even higher sterical demand of the pyrene groups, providing significantly larger interacting π-surfaces and disfavoring the rotation of the aryl substituents. Guided again by the structure found in the solid state (Figure 43c), the derivative with the highest symmetry and highest share of 58.8% of all conformational isomers should be structure I (Figure 45a, Figure 54). Subsequently, taking into consideration that symmetry breaking upon rotation of one pyrene unit should result in four singlets in the ^{1}H NMR spectrum, the other signals for the *ortho* protons of the PBI core might be tentatively assigned to conformers III and IV. We like to note that it was not possible for us to further assess the structures by 2D-NMR spectroscopy due the proximity of the signals and their very different intensity in the ^{1}H-NMR spectrum which prevents the attribution of signals to exclusively one proton. Indeed, the small amount of some of these conformational isomers results in signals that are poorly distinguishable from the baseline of the spectra.

To summarize our conformational analysis by NMR studies, the four *bay* substituents not only result in twisted PBIs bearing conformationally stable *M*- and *P*-atropo-enantiomers but may in addition afford the coexistence of up to seven conformational isomers for PBIs **4a**, **5a** and **6a** in solution due to the activated rotation around the respective PBI-aryl bonds at room temperature. The prevalence of one single conformer and the number and amount of the others could be explained by comparison of the rotational barriers of the aryl substituents, the resulting π-π-overlap of the neighboring *bay* substituents as well as sterical and symmetry considerations.

4.2.4. Absorption and Emission Properties

The series of PBI chromophores **2a**-**6a** in dichloromethane (DCM) exhibits colors from pink (**3a**), a reddish blue (**2a**) over violet (**4a**, **5a**) up to turquoise (**6a**) (Figure 46a, Inset). Their molar absorption coefficients (ε_{max}) in DCM are significantly decreased to 17100-28900 M^{-1} cm^{-1} compared to the unsubstituted *N*,*N*'-bis(2,6-diisopropylphenyl)perylene-3,4:9,10-bis(dicarboximide) **76** (92900 M^{-1} cm^{-1}) and *N*,*N*'-bis(2,6-diisopropylphenyl)-

1,6,7,12-tetraphenoxyperylene-3,4:9,10-bis(dicarboximide) **77** (48800 M^{-1} cm^{-1}).[40,241] However, in contrast to these most utilized strongly emissive PBIs, the absorption bands of the tetraaryl-PBIs are also significantly broadened and bathochromically shifted thereby reaching into an interesting spectral range. For tetraphenyl-substituted PBI **2a**, two major absorption bands are distinguishable in the visible range. The absorption maximum (λ_{max}) at 602 nm can be assigned to the S_0-S_1 transition of the PBI, while the band at 452 nm is assigned to the S_0-S_2 transition which gains in oscillator strength due to the core twist resulting from the sterical crowding in *bay* area by the four phenyl groups. The impact of the imide substituent on both spectral shape and position as well as the absorption coefficient is only marginal for **2b**-**2e** (see Figure 56). In contrast, the different aryl substituents induce variations in spectral shapes and position of the respective absorption maxima, thereby suggesting some degree of conjugation with the PBI core (Figure 46a). Compared to **2a**, the absorption maximum of **3a** is hypsochromically shifted by 19 nm (540 cm^{-1}) to 583 nm (24800 M^{-1} cm^{-1}) which might be explained by a weaker conjugation due to the more electron withdrawing character of the trifluoromethyl phenyl groups (*vide infra*). In case of PBIs **4a**-**6a** bearing larger aromatic substituents that no longer exhibit axial symmetry with respect to the connection to the PBI core, no proper separation of the two absorption bands is observable anymore and their spectra are even more broadened than the spectra of **2a** and **3a**. The broadening might be attributed to the conformational heterogeneity of the PBI *bay* substituents (*vide supra*), which are a result of the rotation and arrangement of the aryl substituents with respect to each other as well as the twist in *bay* position. Each conformer exhibits a different absorption spectrum and thus the ensemble spectrum observed by the measurements of solutions results from overlapping spectra of the different conformational isomers identified by our NMR studies. The absorption band of **4a** and **5a** between 450 and 650 nm exhibits two poorly distinguishable absorption maxima. DFT calculations suggest the presence of the S_0-S_1 transition as well as higher transitions underneath the main S_0-S_1 absorption band, resulting in a higher overall molar absorptivity (Table 11 and Table 12). Interestingly, in the absorption spectrum of derivative **6a** bearing four 1-pyrenyl substituents only one broad and even more bathochromically shifted absorption band is observed. The increased conjugation of these electron-rich substituents and the electron-poor perylene core results in a red-shift of the absorption maximum up to 628 nm which can be attributed to a charge transfer (CT). DFT calculations of the HOMO and the LUMO show a localization of the HOMO mainly on the pyrene units and *bay* area of the PBI, while the LUMO is localized on the central PBI moiety, supporting the assumption of the charge transfer as source of the broadened absorption band. For all other derivatives, the HOMO is delocalized

over the whole molecule including the aryl substituents (Figure 57). Additionally, similar to **5a**, stable conformational isomers are formed, thereby broadening the absorption spectrum. Below 400 nm, intense absorption bands are present in all spectra. These are commonly assigned to higher energy transitions localized on the respective aryl substituents.

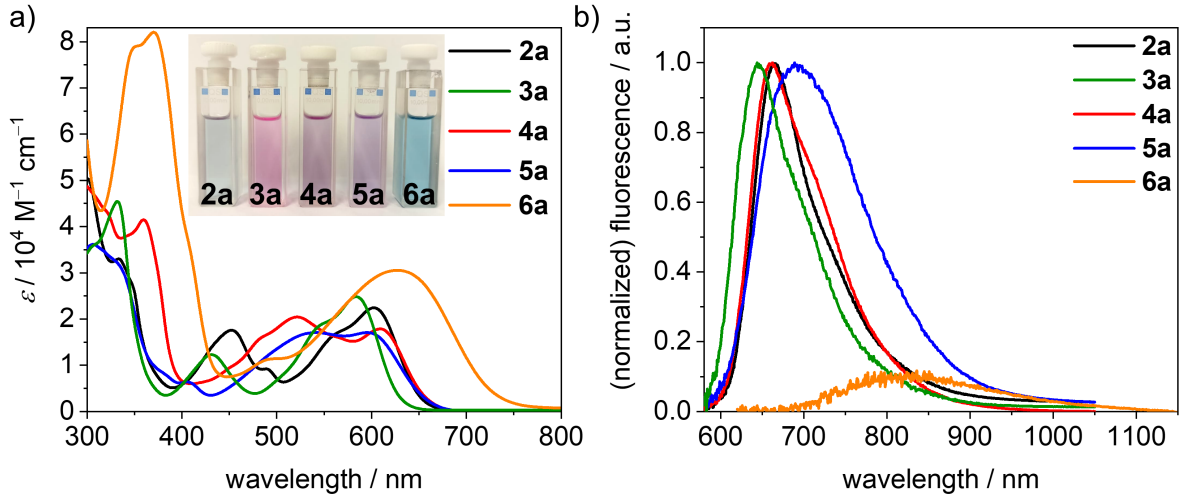

Figure 46 a) UV/Vis/NIR absorption spectra and b) partially normalized emission spectra of PBIs **2a** (black), **3a** (green), **4a** (red), **5a** (blue) and **6a** (orange) measured in DCM (c_0 = 4·10^{-4} M) at room temperature. Inset: Photograph of the solutions **2a** - **6a** (left to right, c_0 = 4·10^{-4} M).

The fluorescence spectra of **2a**-**6a** upon excitation at 560 nm (600 nm for **6a**) are shown in Figure 46b. No vibronic structure is observed for the tetraarylated PBIs in contrast to the emission spectrum of the unsubstituted parent PBI **76**. Further, the Stokes shifts ($\Delta\tilde{\nu}_{\mathrm{Stokes}}$) of **2a**-**6a** are quite large with values between 1200 and 1700 cm^{-1} (Table 3). For **6a** the $\Delta\tilde{\nu}_{\mathrm{Stokes}}$ of 3700 cm^{-1} is even larger. The overall larger $\Delta\tilde{\nu}_{\mathrm{Stokes}}$ compared to the parent PBI and other PBI derivatives[241] can be ascribed to the participation of the aryl substituents in the lowest excited state upon electronic and structural relaxation after photoexcitation. The fluorescence quantum yields (Φ_f) are decreasing from 72% for **3a**, bearing a rather electron-withdrawing aryl substituent, to 43% for **2a**, 33% for **4a**, 15% for **5a** and 1% for **6a** with the more electron-rich phenyl, naphthalene and pyrene substituents, respectively. The fluorescence lifetimes (τ_F) range between 9.7 and 12.8 ns for PBIs **2a**-**5a** with the exception of **6a** whose reduced value of 2.22 ns is again attributable to the CT character of the transition. This is also reflected by investigation of the radiative rate constants k_r that decrease from about 56.3·10^7 s^{-1} for **3a** to 15.4·10^7 s^{-1} for **5a** and the non-radiative rate constants k_{nr} that increase even more significantly from 21.9·10^7 s^{-1} to 87.4·10^7 s^{-1} for **3a** and **5a**, respectively. The substitution of the imide position exhibits only a minor influence on the emission spectra, fluorescence lifetimes and fluorescence quantum yields. The values and spectra of **2a**-**2e** are almost identical with emission maxima between 663 and 680 nm and comparable shapes of the spectra.

Table 3 Summary of the optical and electrochemical properties of compounds **2a**-**6a** in DCM at 298 K.

PBI	λ_{abs}[a] [nm]	ε_{max} [M^{-1} cm^{-1}]	λ_{em} [nm]	$\Delta\tilde{\nu}_{Stokes}$ [cm^{-1}]	Φ_F[b] [%]	τ_F[c] [ns]	E_{red1}[d] [V]	E_{red2}[d] [V]	E_{ox1}[d] [V]	E_{ox2}[d] [V]	E_{HOMO}[e] [eV]	E_{LUMO}[e] [eV]	E_{gap} [eV]
2a	602	22500	663	1500	43	11.9	–1.05	–1.21	0.97	-[f]	–6.12	–4.10	2.02
	452	17600											
3a	583	24800	644	1600	72	12.8	–0.93	–1.20	1.22	1.53	–6.37	–4.22	2.15
	429	12200											
4a	609	17900	662	1300	33	11.6	–1.08	–1.26	0.95	-[f]	–6.10	–4.07	2.03
	521	20400											
5a	596	17100	689	1200	15	9.7	–1.07	–1.24	0.98	1.17	–6.13	–4.08	2.05
	541	17100											
6a	628	28900	816	3700	1	0.6 (47%)	–1.04	–1.23	0.69	0.94	–5.84	–4.11	1.73
	370	80900				2.2 (53%)							

[a] Spectra were measured in DCM ($c_0 \approx 4 \cdot 10^{-6}$ M) at room temperature. [b] Fluorescence quantum yields were determined using the dilution method (OD < 0.05) and Oxazine 1 (for **2a**, **4a** - **6a**, $\Phi_F = 0.11$ in EtOH)[247] or *N*,*N*'-bis(2,6-diisopropylphenyl)- 1,6,7,12-tetraphenoxy-perylene-3,4:9,10-bis(dicarboximide) (for **3a**, $\Phi_F = 0.96$ in $CHCl_3$)[215] as reference. [c] Fluorescence lifetimes were determined with EPL picosecond pulsed diode lasers for time-correlated single photon counting (λ_{ex} = 505.8 nm). [d] Half-wave potentials were determined by cyclic or square wave voltammetry measured in DCM (0.1 M TBAHFP) vs. Fc/Fc^+. [e] Calculated according to literature known procedure using the experimentally determined redox potentials ($E_{HOMO} = -[E_{ox1} + 5.15\ eV]$ and $E_{LUMO} = -[E_{red1} + 5.15\ eV]$) and the energy level of Fc/Fc^+ with respect to the vacuum level (– 5.15 eV).[19] [f] Not observed

4.2.5. Chiroptical Properties

Due to the large effective Van der Waals radii of the aryl substituents these tetraaryl-substituted PBIs afford stable *P*- and *M*-atropo-enantiomers with axial chirality.[40,237] The separation of the enantiomers has been achieved for PBIs **2a**, **3a** and **4a** by semipreparative HPLC using a column packed with amylose tris-(3,5-dimethylphenyl) carbamate immobilized on silica gel. In contrast, the separation of the atropo-enantiomers was not possible for derivatives **5a** and **6a**, probably due to the numerous conformational isomers present in solution (*vide supra*, Figure 58). Circular dichroism (CD) spectra of the separated atropo-enantiomers of PBIs **2a**-**e**, **3a** and **4a** were recorded and are shown in Figure 47 and Figure 58. They exhibit a mirror image relation and broad monosignated bands for the S_0-S_1 spectral region (500 – 600 nm for **2a**-**e**, **3a**) and a bisignate Cotton effect for the higher energy S_0-S_2 spectral region (400 - 500 nm for **2a-e**, **3a**). The longest wavelength absorption in the visible region between 500 and 600 nm can be assigned to a transition dipole moment polarized along the long molecular *N*,*N*'-axis, while the second band between 450 and 500 nm can be assigned to a transition polarized along the short molecular axis (the two twisted naphthalene planes).[40,148] The enantiomers of **4a** show bisignate bands for the S_0-S_2 transition band, that are shifted to longer wavelength, thereby

relating to the absorption maximum at 521 nm. The enantiomer with the positive Cotton effect for the lowest energy transition is assigned in accordance with our earlier work on tetraphenoxy-PBIs[148] and theoretical calculations to the *P*-enantiomer, while the negative signature in the visible region correspond to the *M*-enantiomer.

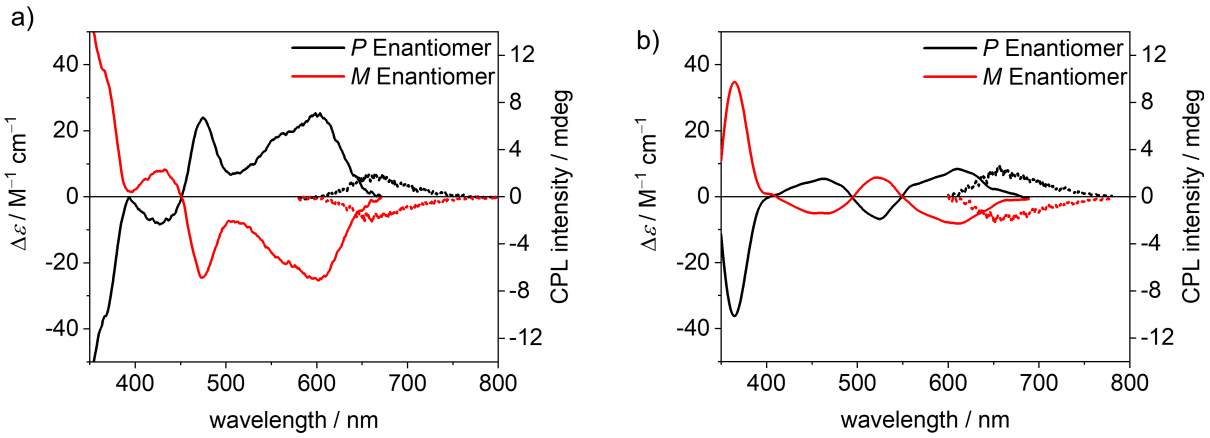

Figure 47 Circular dichroism (CD, $c_0 = 1 \cdot 10^{-5}$ M) absorption and circularly polarized luminescence (CPL, $c_0 = 2 \cdot 10^{-6}$ M) spectra of *P*-(black) and *M*-(red) atropo-enantiomers of PBIs a) **2a** and b) **4a** in DCM at room temperature.

The racemization of the *P*-enantiomers of **2a** and **4a** have been investigated by time-dependent CD measurements, which were performed at four elevated temperatures between 383 and 398 K in 1,1,2,2-tetrachloroethane (Figure 60, Figure 61, Table 7). Accordingly, the rate constants could be determined from the change of the amplitude of the CD signal at 480 nm for **2a** and 460 nm for **4a**, respectively. For both derivatives half-lifetimes of 59 and 43 min at 383 K were recorded, respectively, which are even longer than the reported half-lifetime of 36 min at 383 K for the tetrabromo-substituted PBI.[237] This emphasizes the extraordinary conformational stability of the enantiomers resulting from π-π-stacked interlocking motif of the aryl substituents revealed from the crystal structures (Figure 43 a-c). The free enthalpies of activation $\Delta G^{\ddagger}$ at 383 K were determined to be 119.6 kJ mol^{-1} for **2a** and 118.6 kJ mol^{-1} for **4a** respectively, indicating only a minor influence of the size of the aryl substituent when attached via the naphthalene β-position. The values for the free enthalpy of activation of **2a** and **4a** are comparable to the ones of hexahelicene (154.3 kJ mol^{-1})[248] or a trisubstituted biphenyl (125.4 kJ mol^{-1})[249] which also exhibit conformationally stable isomers. DFT calculations of the transition state confirmed the high free activation enthalpy (Figure 52a). Furthermore, the free activation enthalpy of the rotation of the phenyl substituents was found to be significantly lower (Figure 52b). This explains that this process could be monitored by ^{1}H-NMR spectroscopy (Figure 49), while the enthalpy of the racemization is too high to be determined by this technique.

In addition, we were able to study the circular polarized luminescence (CPL) for the enantiomers **2a** (λ_{ex} = 452 nm), **3a** (λ_{ex} = 430 nm) and **4a** (λ_{ex} = 510 nm) (Figure 47, Figure 58e). The g_{lum} values of around $1 \cdot 10^{-3}$ for the heavily twisted molecules are of typical magnitude and are comparable to those of chiral peropyrene reported by Chalifoux *et al*. and other chiral organic molecules.[119,250-253] The monosignated spectra of the two respective *P*-/*M*-enantiomers are again mirror images, and the observed Stokes shifts are in accordance with the Stokes shifts obtained by UV/Vis/NIR and fluorescence measurements. The sign of the CPL spectrum matches the sign of the longest wavelength transition in the CD spectrum. The CPL spectra up to 655 nm for **4a** correspond well with the PBI emission spectra and are among the most red-shifted CPL spectra reported to date.[254]

4.2.6. Redox Properties

The electronic effect imparted by the different aryl substituents in *bay* position has been investigated by cyclic voltammetry (CV) and square wave voltammetry (SWV) in DCM with tetrabutylammonium hexafluorophosphate (TBAHFP) as electrolyte. The data obtained from these measurements are summarized in Table 3 and the voltammograms are depicted in Figure 48 and Figure 62 to Figure 65. All investigated PBIs exhibit two reversible reduction waves. With the exception of **3a**, the first reduction of all derivatives is observed at approximately −1.05 V, while the second reduction occurs at approximately −1.23 V (Figure 48a). These reduction potentials can be attributed to the formation of the respective radical anions and dianions of the PBIs. The comparison to the unsubstituted parent PBI **76** (−1.06 V/−1.26 V) reveals only a minor impact of the aryl substituents on the reduction potentials although the chromophore core is heavily distorted. However, the introduction of *para*-(trifluoromethyl) phenyl substituents in **3a** (-0.93 V/-1.20 V) led to a more easy reduction which suggests a stabilization of the negative charge by the electron-withdrawing substituent. A similar trend is observed upon oxidation of the PBIs. All derivatives with the exception of **6a**, exhibit at least one oxidation process at approximately +0.97 V, which is comparable to the oxidation potential of tetraphenoxy-substituted PBIs.[239] In contrast, the first oxidation of PBI **6a** already occurs at +0.69 V, which is approximately 0.3 V lower than the oxidation of the other PBIs and also with its increased current indicative for a two-electron process (Figure 48b). As the HOMO of **6a** is localized mainly on the pyrene subunits (Figure 57) this oxidation can be assigned to two simultaneous one-electron oxidations ($E_{ox,pyrene}$ = +0.63 V, Table 8). If we consider the structural features deduced from the single crystal X-ray analysis (*vide supra*) these

observations suggest that each of the two pyrene dimers located on each side of the PBI share one positive charge, i.e., forming so-called π-dimer cations.[255,256] The second two-electron oxidation at +0.94 V might accordingly be attributed to the second oxidation of the π-dimer upon which each pyrene unit is oxidized. It is noteworthy, however, that at this potential also the perylene core might be oxidized according to studies with the other PBI derivatives.[239]

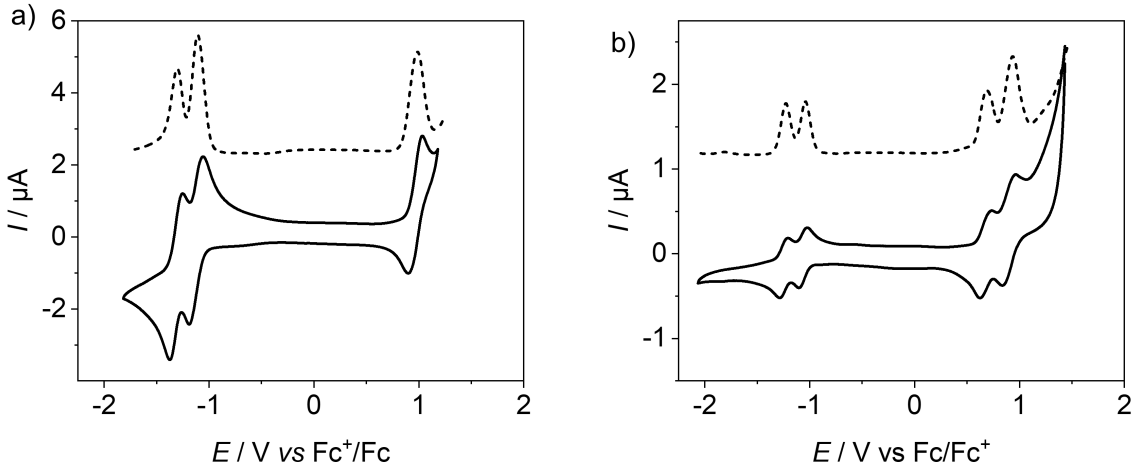

Figure 48 Cyclic voltammograms (solid lines) and square wave voltammograms (dashed lines) of PBIs a) **2a** and b) **6a**. Measurements were performed using DCM solutions ($c_0 = 2 \cdot 10^{-4}$ M) at 293 K, using TBAHFP ($c_0 = 0.1$ M) as electrolyte.

The HOMO and LUMO energy levels included in Table 3 are calculated from the first oxidation and first reduction potential respectively with the energy level of Fc/Fc^+ set to −5.15 eV vs. vacuum.[38] The HOMOs of all PBIs are located at about −6.10 eV, with the exception of **6a**, whose HOMO level is approximately 0.4 eV higher in energy. The LUMO energies of the PBIs are approximately −4.10 eV, which render them all suitable candidates as NFAs in OSCs. All HOMO-LUMO gaps are about 2.00 eV. The only exceptions are **3a** (enlarged gap of 2.15 eV due to the lower LUMO) and **6a** (reduced gap of 1.73 eV due to the higher HOMO attributed to the pyrene substituents).

4.3. Conclusion

In conclusion, we synthesized a series of tetraarylated PBIs by Suzuki coupling with variation in the *bay* as well as the imide positions. These dyes exhibit extraordinarily high solubility in common organic solvents and are readily available due to their straightforward synthesis from easily available precursors. The up to 36.6° twisted structure of these chromophores could for the first time be unambiguously characterized by X-ray crystallography for three derivatives bearing different aryl substituents which revealed the presence of interlocked π-π-stacking

motifs between these substituents. A complex ensemble of up to fourteen isomers for the PBIs due to rotation of their large *bay* substituents in solution was observed and assigned by ^{1}H-NMR spectroscopic analysis. The optical properties were characterized by UV/Vis/NIR and fluorescence spectroscopy, showing compared to the unsubstituted parent PBI reduced molar absorption coefficients but a significant bathochromic shift along with spectral broadening. Depending on the aryl substituent, the fluorescence quantum yield decreases from 72% for the most electron-poor arene to about 1% for the most electron-rich pyrene substituent. The atropo-enantiomers could be separated by HPLC for several derivatives using a chiral stationary phase. Even at elevated temperature their racemization was slow (several hours) according to time-dependent CD measurements. Circularly polarized luminescence of tetraarylated PBIs was investigated as well, revealing one of the most bathochromic shifted CPL spectra reported to date for small organic molecules.

4.4. Supporting Information for Chapter 4

4.4.1. Experimental Part

General Methods

Unless otherwise stated, all chemicals, reagents and solvents were purchased from commercial suppliers and used after appropriate purification. The 1,6,7,12-tetrachloroperylene bis(dicarboximides) **42a-e** were synthesized according to literature.[40,257-259] Toluene was of HPLC grade and dried prior to use by an Innovative Technology PureSolv solvent purification system. Dichloromethane was distilled prior to use. Column chromatography was performed with commercial glass columns using silica gel 60 M (particle size 0.04 – 0.063 mm; Merck KGaA) as stationary phase. Normal phase HPLC was performed on a Japan Analytical Industry (JAI) recycling preparative HPLC system *LC-9105* equipped with a VP 250/21 NUCLEOSIL 100-7 column of Macherey-Nagel. For the chiral separation of the enantiomers, the same HPLC system was equipped with a Reprosil 100 Chiral-NR 8 µm column from *Trentec*. NMR spectra were recorded on a Bruker *Avance III HD* 400 MHz NMR spectrometer and are calibrated to the residual proton signal of the used deuterated solvent. The chemical shifts (δ) are reported in parts per million (ppm). Multiplicities for proton signals are abbreviated as s, bs, d, bd, t, sep, m and bm for singlet, broad singlet, doublet, broad doublet, triplet, septet, multiplet and broad multiplet respectively. MALDI-TOF mass spectra were recorded with a Bruker Daltonics GmbH *ultrafleXtreme* mass spectrometer using DCTB (2-[(2*E*)-3-(4-*tert*-butylphenyl)-2-methylprop-2-enylidene]malononitrile) as matrix. High resolution mass spectra were measured by electrospray ionization (ESI) with an *ESI microTOF Focus* mass spectrometer from Bruker Daltonics GmbH. The melting points were determined using a SMP50 from *Stuart*. UV/Vis/NIR absorption spectra were recorded on a Jasco V-770 or Jasco V-670 spectrometer. Fluorescence spectra were recorded on a *FLS980* fluorescence spectrometer (Edinburgh Instruments) and were corrected against the photomultiplier sensitivity and the lamp intensity. CD spectra were recorded on a Jasco *J-810* spectropolarimeter. CPL spectra were recorded with a Jasco *CPL-300/J-1500* Hybrid spectrometer. Cyclic voltammetry measurements were conducted on an *EC epsilon* (BASi instruments, UK) potentiostat connected to a three-electrode single-compartment cell. A Pt disc electrode was used as working electrode, a platinum wire as counter electrode and an Ag/AgCl reference electrode. The spectra were referenced using the ferrocenium/ferrocene redox couple as an internal standard. Single crystal X-ray diffraction data were collected at 100 K on a Bruker D8 Quest Kappa diffractometer with a Photon II CPAD detector and multi-layered mirror monochromated CuK_α radiation. The structures were

solved using direct methods, expanded with Fourier techniques and refined with the Shelx software package.[260] All non-hydrogen atoms were refined anisotropically. Hydrogen atoms were included in the structure factor calculation on geometrically idealized positions. Crystallographic data have been deposited with the Cambridge Crystallographic Data Centre as supplementary publication no. 2086018 (**2c**), 2086019 (**4a**) and 2086020 (**6a**). These data can be obtained free of charge from The Cambridge Crystallographic Data Centre via www.ccdc.ac.uk/data.request/cif. Theoretical calculations were performed by the Gaussian software[261] using B3LYP/6-31G(d) level of theory for structure optimization and B3LYP/def2-SVP level of theory for TD-DFT simulation of electron transitions.

General Procedure for the synthesis of tetraarylated PBI derivatives

The respective 1,6,7,12-tetrachloroperylene bis(dicarboximide) (100 µmol), the arylboronic acid (2.00 mmol, 20 eq.), anhydrous potassium carbonate (145 mg, 1.05 mmol, 10.5 eq.) and tetrakis(triphenylphosphine)palladium (34.7 mg, 30.0 µmol, 0.3 eq.) were added to a Schlenk tube. Toluene (3.2 mL), ethanol (0.6 mL) and water (1.6 mL), which were degassed prior to use, were added and the solution was subjected to three freeze-pump-thaw cycles. After stirring overnight at 80 °C, the mixture was extracted with dichloromethane and washed three times with water. The organic phases were combined, and the solvent removed under reduced pressure. The crude product was purified by column chromatography and HPLC.

Synthesis of 2a

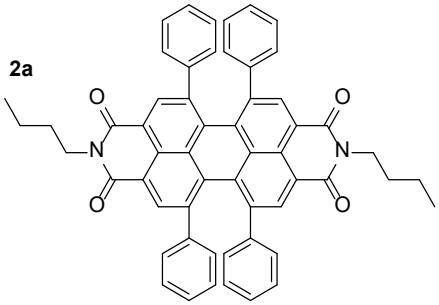

Solvent column chromatography and HPLC: hexane/dichloromethane = 1/3; Yield: 58.9 mg (73.0 mmol, 73%) of a blue-purple solid. ^{1}H NMR (400 MHz, CD_2Cl_2, 293 K): δ = 8.24 (s, 4H), 7.22 (t, 4H), 7.08 (bs, 8H), 6.70 (bs, 8H), 4.18 (t, 4H), 1.74 (m, 4H), 1.47 (m, 4H), 1.00 (t, 6H); ^{13}C-NMR (100 MHz, CD_2Cl_2, 293 K): δ = 163.9, 142.7, 140.9, 133.6, 132.3, 131.7, 129.2, 127.9, 126.4, 122.8, 40.6, 30.7, 20.8, 14.1; MS (MALDI-TOF, pos. mode, DCTB in $CHCl_3$): *m/z* calculated for $C_{56}H_{42}N_2O_4^+$ $[M]^+$: 806.31, found: 806.30; HRMS (ESI-TOF, pos. mode, MeCN/$CHCl_3$): *m/z* calculated for $C_{56}H_{42}N_2NaO_4^+$ $[M+Na]^+$: 829.3037, found 829.3040; m.p. >390 °C.

Synthesis of 2b

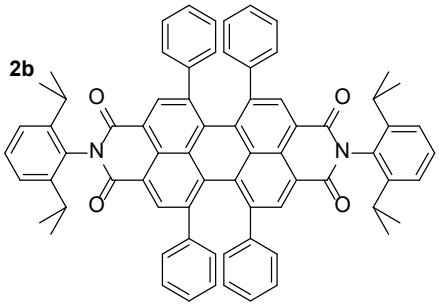

Solvent column chromatography and HPLC: hexane/dichloromethane = 1/3; Yield: 75.8 mg (74.6 mmol, 75%) of a dark blue-purple solid. ^{1}H NMR (400 MHz, CD_2Cl_2, 293 K): δ = 8.35 (s, 4H), 7.53 (t, 2H), 7.38 (d, 4H), 7.26 (m, 4H), 7.15 (bs, 8H), 6.83 (bs, 8H), 2.87 (sep, 4H), 1.22 (d, 12H), 1.15 (d, 12H); ^{13}C-NMR (100 MHz, CD_2Cl_2, 293 K): δ = 166.1, 148.4, 145.3, 142.9, 136.3, 134.6, 134.1, 133.5, 133.0, 131.8, 131.1, 130.0, 129.0, 126.4, 124.5, 31.4, 26.1, 26.05; MS (MALDI-TOF, pos. mode, DCTB in $CHCl_3$): *m/z* calculated for $C_{78}H_{58}N_2O_4^+$ $[M]^+$: 1014.43, found: 1014.40; HRMS (ESI-TOF, pos. mode, MeCN/$CHCl_3$): *m/z* calculated for $C7_8H_{58}N_2NaO_4^+$ $[M+Na]^+$: 1037.4289, found 1037.4310; m.p. >390 °C.

Synthesis of 2c

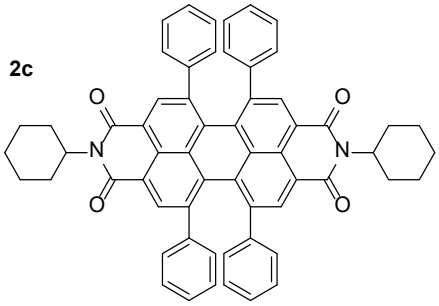

Solvent column chromatography and HPLC: hexane/dichloromethane = 1/3; Yield: 56.6 mg (65.9 mmol, 66%) of a dark black-purple solid. ^{1}H NMR (400 MHz, CD_2Cl_2, 293 K): δ = 8.22 (s, 4H), 7.20 (m, 4H), 7.08 (bs, 8H), 6.70 (bs, 8H), 5.04 (m, 2H), 2.56 (m, 4H), 1.90 (m, 4H), 1.75 (m, 4H), 1.46 (m, 4H), 1.34 (m, 4H); ^{13}C-NMR (100 MHz, CD_2Cl_2, 293 K): δ = 164.3, 142.6, 141.0, 133.5, 132.0, 131.6, 129.0, 127.8, 126.4, 123.3, 32.0, 29.6, 29.5, 27.0, 25.9, 23.0, 14.3; MS (MALDI-TOF, pos. mode, DCTB in $CHCl_3$): *m/z* calculated for $C_{60}H_{46}N_2O_4^+$ $[M]^+$: 858.35, found: 858.34; HRMS (ESI-TOF, pos. mode, MeCN/$CHCl_3$): *m/z* calculated for $C_{60}H_{46}N_2NaO_4^+$ $[M+Na]^+$: 881.3350, found 881.3339; m.p. >390 °C.

Synthesis of 2d

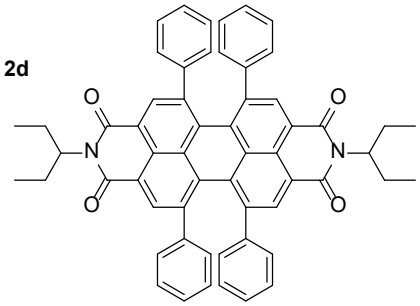

Solvent column chromatography and HPLC: hexane/dichloromethane = 1/3; Yield: 38.1 mg (45.6 mmol, 46%) of a dark purple solid. ^{1}H NMR (400 MHz, CD_2Cl_2, 293 K): δ = 8.23 (s, 4H), 7.20 (m, 4H), 7.10 (bs, 8H), 6.72 (bs, 8H), 5.05 (m, 2H), 2.25 (m, 4H), 1.94 (m, 4H), 0.95 (m, 12H); ^{13}C-NMR (100 MHz, CD_2Cl_2, 293 K): δ = 142.8, 141.0, 133.7, 132.1, 131.7, 130.7, 129.0, 127.7, 126.6, 122.8, 57.8, 25.44, 25.40, 11.56, 11.55; MS (MALDI-TOF, pos. mode, DCTB in $CHCl_3$): *m/z* calculated for $C_{58}H_{46}N_2O_4^+$ $[M]^+$: 834.35, found: 834.37; HRMS (ESI-TOF, pos. mode, MeCN/$CHCl_3$): *m/z* calculated for $C_{58}H_{46}N_2NaO_4^+$ $[M+Na]^+$: 857.3350, found 857.3317; m.p. >390 °C.

Synthesis of 2e

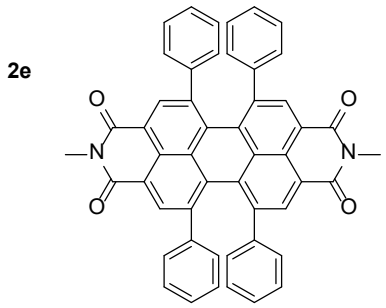

Solvent column chromatography and HPLC: dichloromethane/ethylacetate = 99/1; Yield: 36.6 mg (50.6 mmol, 51%) of a dark black-purple solid. ^{1}H NMR (400 MHz, CD_2Cl_2, 293 K): δ = 8.24 (s, 4H), 7.19 (bs, 4H), 7.06 (bs, 8H), 6.65 (bs, 8H), 3.63 (s, 6H); ^{13}C-NMR (100 MHz, CD_2Cl_2, 293 K): δ = 142.5, 140.6, 133.4, 132.2, 131.6, 131.0, 129.0, 127.8, 126.4, 123.3, 27.1; MS (MALDI-TOF, pos. mode, DCTB in $CHCl_3$): *m/z* calculated for $C_{56}H_{42}N_2O_4^+$ $[M]^+$: 722.22, found: 722.19; HRMS (ESI-TOF, pos. mode, MeCN/$CHCl_3$): *m/z* calculated for $C_{56}H_{43}N_2NaO_4^+$ $[M+Na]^+$: 745.2098, found 745.2093; m.p. >390 °C.

Synthesis of 3a

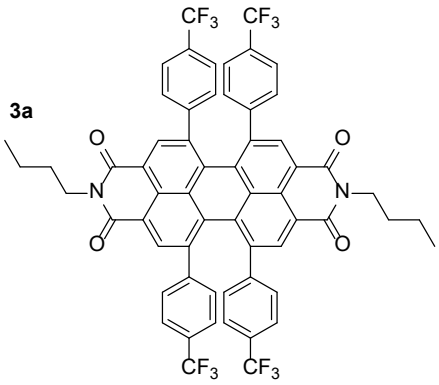

Solvent column chromatography and HPLC: hexane/dichloromethane = 1/3; Yield: 65.1 mg (60.3 mmol, 60%) of a-purple solid. ^{1}H NMR (400 MHz, CD_2Cl_2, 293 K): δ = 8.33 (s, 4H), 7.39 (bs, 8H), 6.88 (bd, 8H), 4.21 (t, 4H), 1.75 (m, 4H), 1.48 (m, 4H), 1.01 (t, 6H); ^{13}C-NMR (100 MHz, CD_2Cl_2, 293 K): δ = 163.4, 144.2, 141.2, 133.8, 131.8, 131.6, 130.1, 129.7, 127.2, 125.8, 123.7, 40.8, 30.7, 20.8, 14.1; MS (MALDI-TOF, pos. mode, DCTB in $CHCl_3$): *m/z* calculated for $C_{60}H_{38}N_2O_4^+$ $[M]^+$: 1078.26, found: 1078.30; HRMS (ESI-TOF, pos. mode, MeCN/$CHCl_3$): *m/z* calculated for $C_{60}H_{38}N_2NaO_4^+$ $[M+Na]^+$: 1101.2532, found 1101.2589; m.p. >390 °C.

Synthesis of 4a

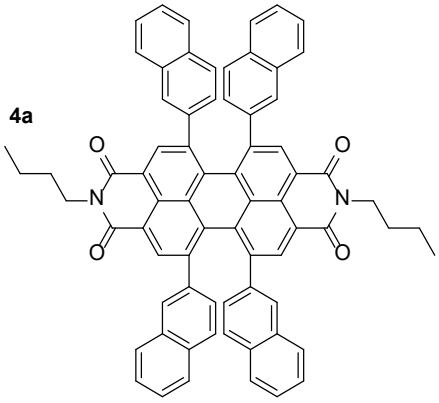

Solvent column chromatography and HPLC: hexane/dichloromethane = 1/3; Yield: 28.3 mg (28.1 mmol, 28%) of a purple solid. ^{1}H NMR (400 MHz, CD_2Cl_2, 293 K): δ = 8.37 – 6.61 (bm, 32H), 4.03 (bs, 4H), 1.71 (bs, 4H), 1.45 (m, 4H), 1.00 (t, 6H); ^{1}H-NMR (400 MHz, TCE-d_2, 390 K): δ = 8.38 (s, 4H), 7.70 (d, 4H), 7.43 (t, 4H). 7.31 (bm, 8H), 6.90 (bm, 8H), 6.63 (d, 4H), 4.23 (t, 4H), 1.80 (m, 4H), 1.50 (m, 4H), 1.02 (t, 6H); ^{13}C-NMR (100 MHz, CD_2Cl_2, 293 K): δ = 163.9, 142.5, 138.2, 135.0, 134.0, 132.5, 132.2, 131.8, 128.4, 127.9, 127.4, 126.9, 126.5, 123.1, 40.5, 30.6, 20.8, 14.1; MS (MALDI-TOF, pos. mode, DCTB in $CHCl_3$): *m/z* calculated for $C_{72}H_{50}N_2O_4^+$ $[M]^+$: 1006.38, found: 1006.36; HRMS (ESI-TOF, pos. mode, MeCN/$CHCl_3$): *m/z* calculated for $C_{72}H_{50}N_2NaO_4^+$ $[M+Na]^+$: 1029.3663, found 1029.3660; m.p. >390 °C.

Synthesis of 5a

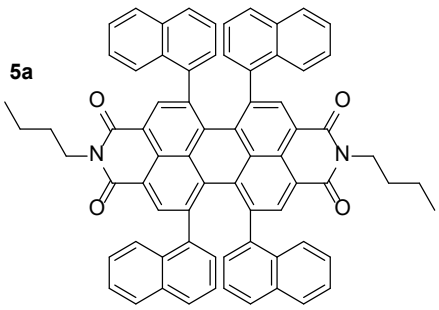

Solvent column chromatography and HPLC: hexane/dichloromethane 1/3; Yield: 37.8 mg (37.5 mmol, 38%) of a purple solid; ^{1}H-NMR (400 MHz, CD_2Cl_2, 293 K): δ = 8.42 – 6.14 (m, 32H), 4.12 (m, 4H), 1.71 (m, 4H). 1.44 (m, 4H), 0.97 (m, 6H); ^{13}C-NMR (100 MHz, CD_2Cl_2, 293 K): δ = 164.0, 163.8, 142.3, 141.9, 141.0, 140.6, 139.9, 139.8, 139.2, 139.0, 138.9, 138.8, 137.2, 136.9, 135.4, 135.1, 135.0, 134.9, 134.8, 134.6, 134.5, 134.0, 133.96, 133.91, 133.8, 133.6, 132.4, 131.9, 131.2, 131.2, 131.1, 131.0, 130.9, 129.9, 129.6, 129.4, 129.2, 128.9, 128.8, 128.5, 128.4, 128.3, 126.8, 126.7, 126.5, 126.4, 126.1, 125.92, 125.88, 125.79, 125.7, 125.5, 125.3, 125.2, 124.4, 124.3, 123.4, 123.3, 123.2, 121.7, 121.6, 121.4, 40.6, 30.6, 20.8, 14.0; MS

(MALDI-TOF, pos. mode, DCTB in $CHCl_3$): *m/z* calculated for $C_{72}H_{50}N_2O_4^+$ $[M]^+$: 1006.38, found: 1006.38; HRMS (ESI-TOF, pos. mode, MeCN/$CHCl_3$): *m/z* calculated for $C_{72}H_{50}N_2NaO_4^+$ $[M+Na]^+$: 1029.3663, found 1029.3648; m.p. >390 °C.

Synthesis of 6a

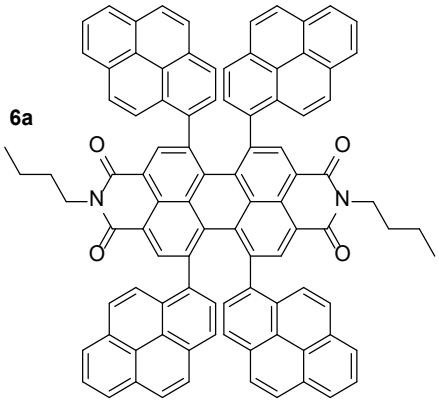

Solvent column chromatography and HPLC: hexane/dichloromethane 1/3; Yield: 28.1 mg (21.6 mmol, 22%) of a blue solid; ^{1}H-NMR (400 MHz, CD_2Cl_2, 293 K): δ = 8.55 – 5.93 (m, 40H), 4.15 (m, 4H), 1.75 (m, 4H), 1.45 (m, 4H), 0.99 (m, 6H); ^{13}C-NMR (100 MHz, CD_2Cl_2, 293 K): δ = 164.1, 142.5, 137.0, 136.0, 134.3, 134.23, 134.18, 132.3, 130.7, 130.6, 130.2, 129.0, 128.7, 127.4, 127.0, 126.2, 125.8, 125.6, 125.2, 125.0, 123.6, 122.1, 121.6, 40.7, 30.7, 20.8, 14.1; MS (MALDI-TOF, pos. mode, DCTB in $CHCl_3$): *m/z* calculated for $C_{96}H_{59}N_2O_4^+$ $[M+H]^+$: 1302.44, found: 1302.53; HRMS (ESI-TOF, pos. mode, MeCN/$CHCl_3$): *m/z* calculated for $C_{96}H_{58}N_2NaO_4^+$ $[M+Na]^+$: 1325.4289, found 1325.4214; m.p. >390 °C.

4.4.2. Structural Analysis

Table 4 Structural parameters found in the single crystal structures of **2c**, **4a** and **6a.**

PBI	Space Group	Core twist[a] [°]	*Θ* (C1-C12b-C12a-C12)[b] [°]	*Θ* (C13a-C12a-C12b-C13b)[b] [°]	*Θ* (C12b-C1-C1'-C2')[b,c] [°]
2c	P2/c	34.3	32.7/33.4	33.2/33.6	42.1/42.1/43.1/43.1
4a	P–1	36.6	33.5/33.5	34.1/35.4	39.4/41.2/41.2/43.3
6a	P–1	29.5	29.2/29.9	27.7/29.1	46.6/50.2/54.6/56.9

[a] Angle between the two naphthalene subunits of the PBI; [b] Numbering of carbon atoms according to Scheme 5; [c] For **4a** the angle was measured between C12b-C1-C2'-C3'.

Table 5 Crystallographic data for compounds **2c**, **4a** and **6a**.

	Compound **2c**	Compound **4a**	Compound **6a**
CCDC Number	2086018	2086019	2086020
Empirical Formula	$C_{60}H_{46}N_2O_4$	$C_{72}H_{50}N_2O_4$	$C_{96}H_{58}N_2O_4$
Formula weight / g mol^{-1}	859.04	1007.20	1303.53
Crystal size / mm	0.295 x 0.2687 x 0.192	0.132 x 0.108 x 0.044	0.180 x 0.072 x 0.020
Measurement Temperature	100(2) K	100(2) K	100(2) K
Crystal system	monoclinic	triclinic	triclinic
Space group	C2/c	P-1	P-1
Lattice parameters			
a /Å	11.0037(3)	13.6566(11)	15.5878(5)
b / Å	22.5842(7)	14.4337(12)	15.6577(5)
c / Å	21.5026(6)	17.9111(15)	16.4702(5)
α / °	90	93.237(4)	70.229(2)
β / °	101.5000(10)	105.997(4)	68.009(2)
γ / °	90	94.521(4)	61.8400(10)
Volume/ Å^3	5236.3(3)	3371.7(5)	3221.40(19)
Z value	4	2	2
Calculated Density / g m^{-3}	1.337	1.103	1.344
F(000)	2196	1172	1360
Number of reflections measured	39057	50760	63653

Number of unique reflections	5171	13160	12693
Theta range for data collection	3.915 ° to 72.295 °	2.575 ° to 72.593 °	2.952 ° to 72.267 °
Completeness	100%	99.6%	99.9%
R_{int}	0.0243	0.0321	0.0448
Minimum and maximum transmission	0.5924/0.7536	0.6806/0.7536	0.5985/0.7536
Goodness of fit indicator	1.059	1.056	1.035
Final R_1 indices [$I > 2\sigma(I)$] (R_{obs}, wR_{all})	0.0418, 0.1114	0.0639, 0.1615	0.0508, 0.1343
R indices [all data] (R_{obs}, wR_{all})	0.0425, 0.1120	0.0718, 0.1670	0.0652, 0.1438
Largest diff peak and hole ($e \cdot Å^{-3}$)	0.410/–0.289	0.522/–0.414	0.482/–0.432

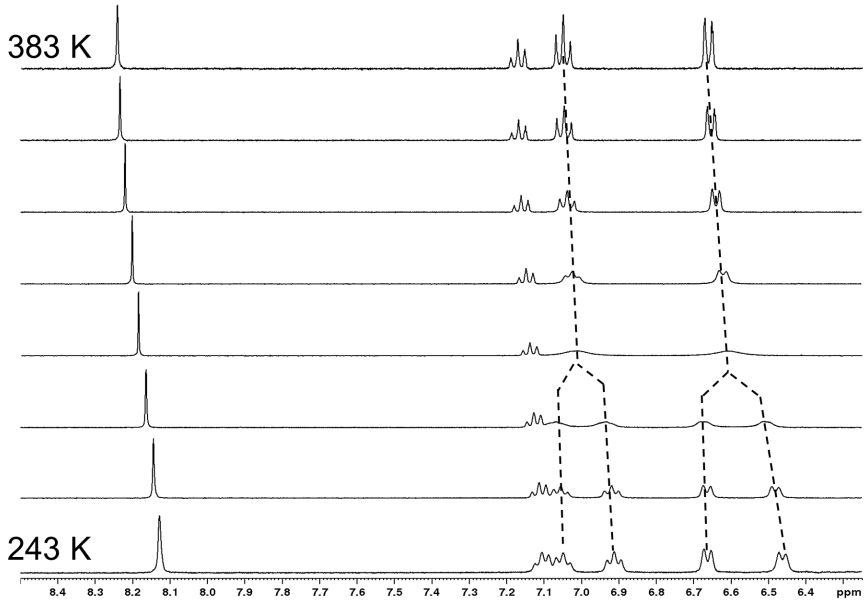

Figure 49 Aromatic region of ^{1}H-NMR spectra of **2a**, measured in 1,1,2,2-tetrachloroethane-d^2 at different temperatures in steps of 20 K from 243 K (bottom) to 383 K (top).

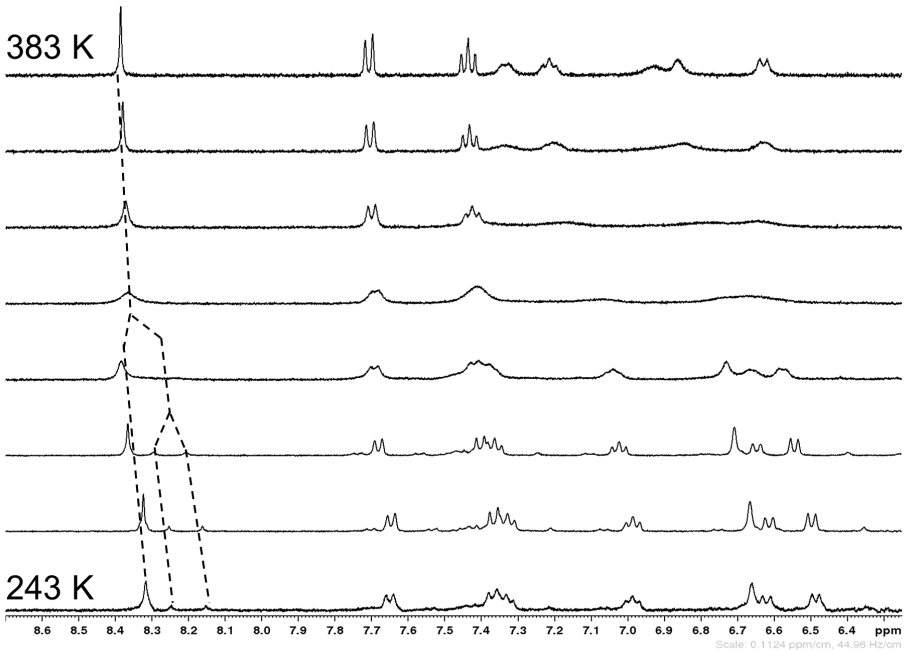

Figure 50 Aromatic region of ^{1}H-NMR spectra of **4a**, measured in 1,1,2,2-tetrachloroethane-d^2 at different temperatures in steps of 20 K from 243 K (bottom) to 383 K (top).

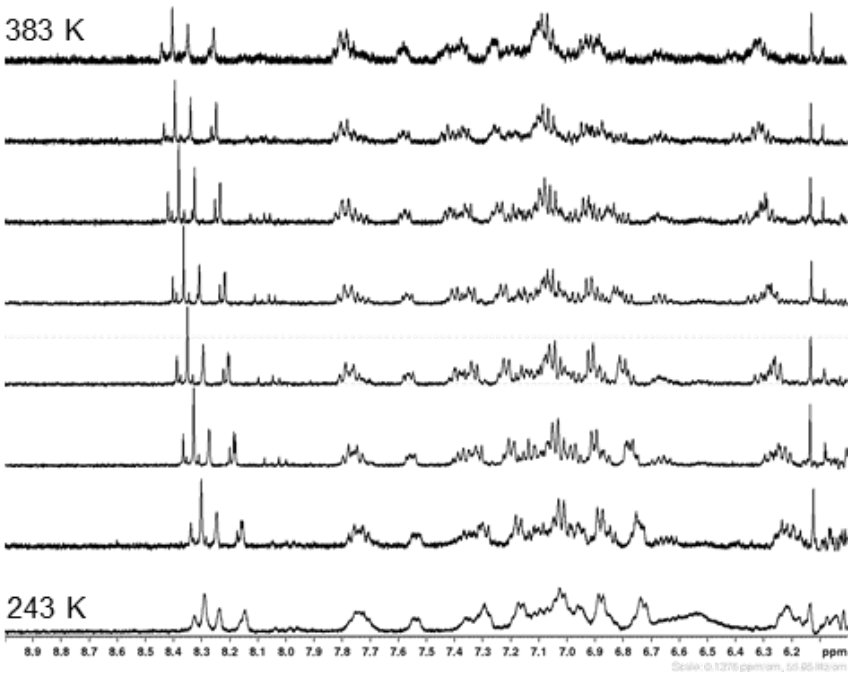

Figure 51 Aromatic region of ^{1}H-NMR spectra of **5a**, measured in 1,1,2,2-tetrachloroethane-d^2 at different temperatures in steps of 20 K from 243 K (bottom) to 383 K (top).

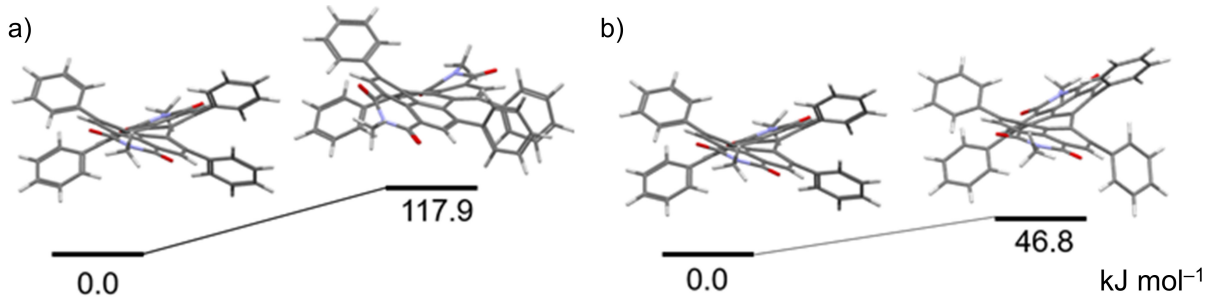

Figure 52 Relative energies in kJ mol^{-1} of the transition states of the a) M/P-racemization and b) rotation of one phenyl ring relative to the ground state energies of the *M*-Enantiomer of PBI derivative **2e** calculated by the Gaussian 09 program using DFT B3LYP/6-31G(d).

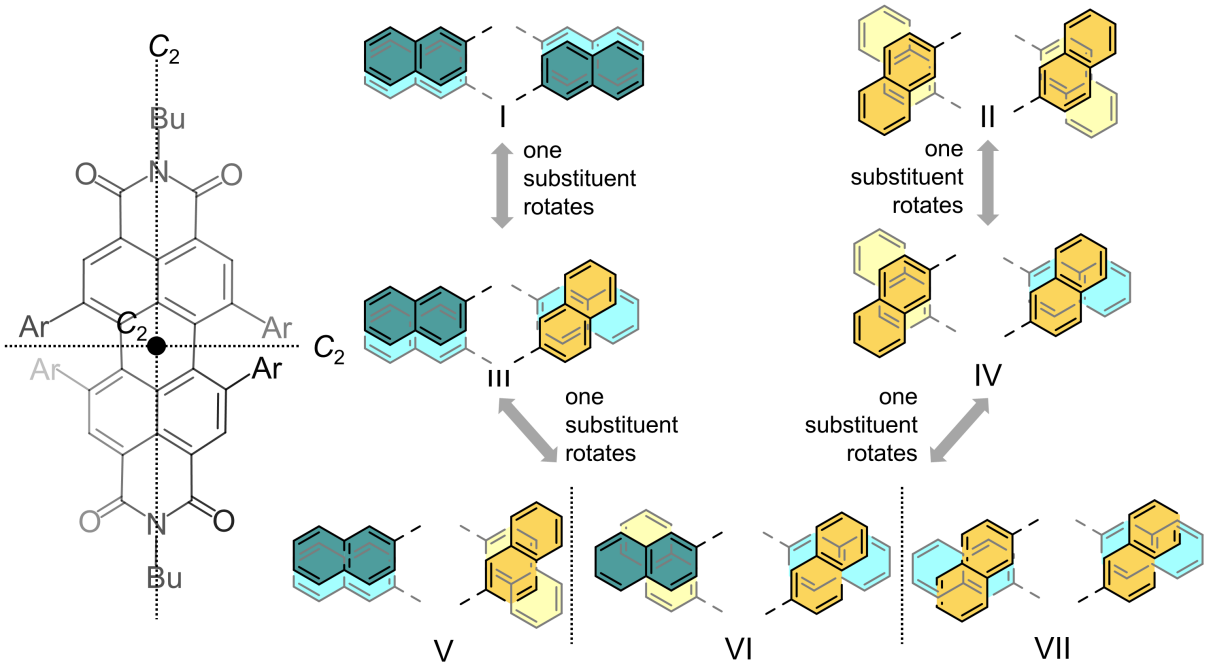

Figure 53 Possible arrangements of the four 2-naphthalene substituents in the *bay* region of the *P*-atropo-enantiomer of **4a**.

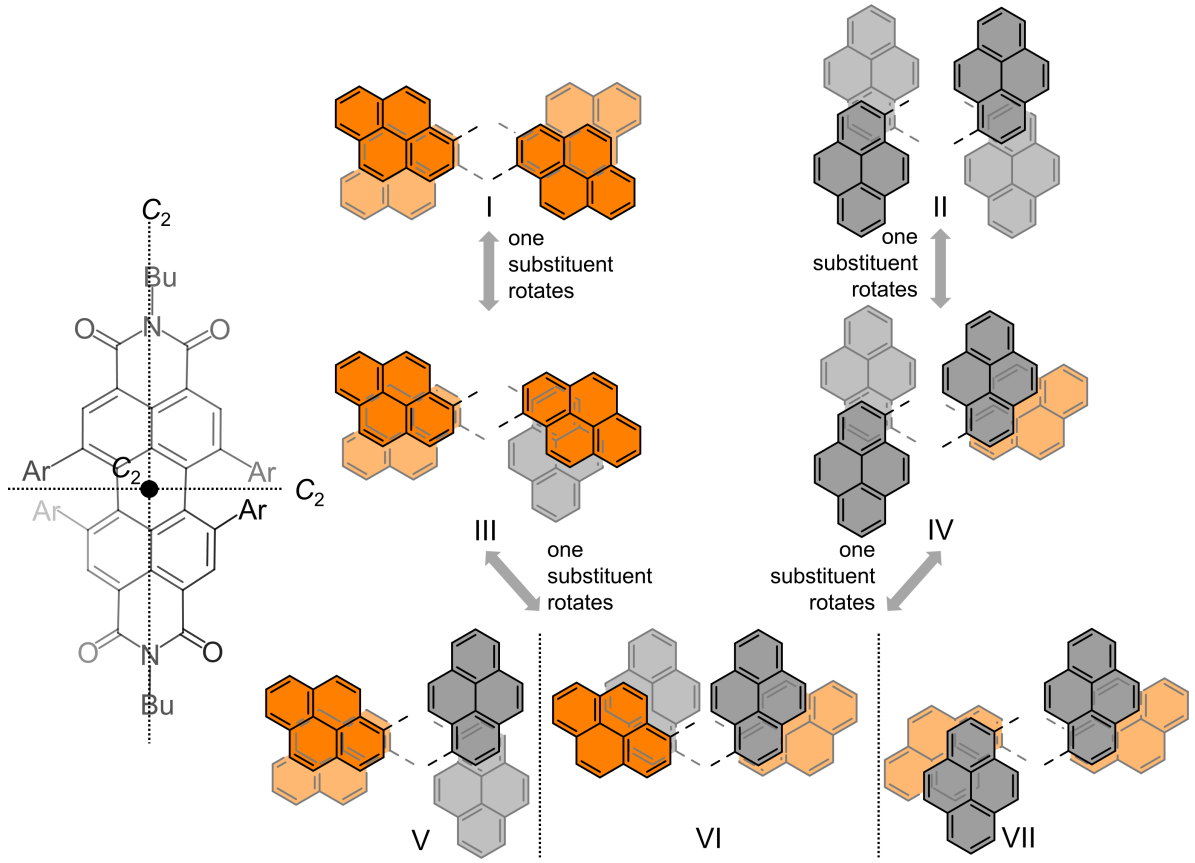

Figure 54 Possible arrangements of the four 1-pyrene substituents in the *bay* region of the *P*-atropo-enantiomer of **6a**.

4.4.3. Optical and Electrochemical Characterization

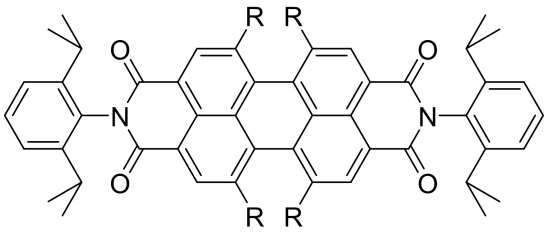

76 R = H
77 R = OPh

Figure 55 Chemical structures of reference compounds **76** and **77**.

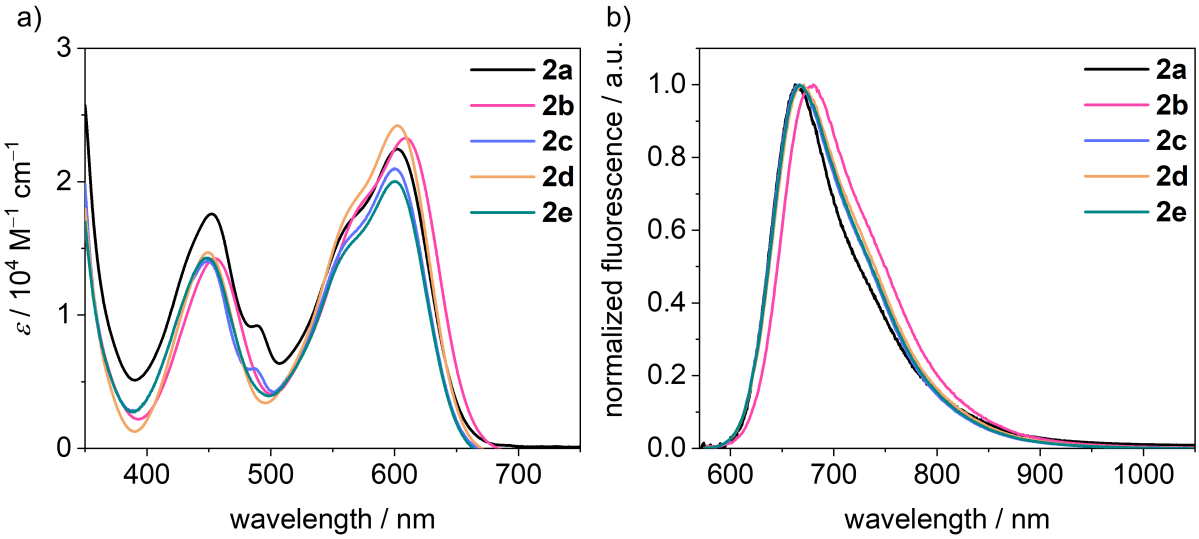

Figure 56 a) UV/Vis/NIR absorption spectra of **2a-2e** as well as b) normalized emission spectra measured in DCM ($c_0 \approx 4 \cdot 10^{-6}$ M) at 293 K.

Table 6 Summary of the optical properties of **2a**-**2e** measured in DCM at 293 K.

PBI	λ_{abs}[a] **[nm]**	ε_{max} **[M^{-1} cm^{-1}]**	λ_{em} **[nm]**	$\tilde{\nu}_{Stokes}$ **[cm^{-1}]**	Φ_f[b] **[%]**	τ_F[c] **[ns]**
2a	602 452	22500 17600	663	1530	43	11.9
2b	609 455	23300 14300	680	1690	46	10.9
2c	601 449	21000 14100	666	1620	49	12.0
2d	602 449	24200 14700	671	1740	55	11.7
2e	601 448	20000 14300	667	1650	41	12.3
76	527 491	93000 60800	534	210	99	3.7
77	576 444	48800 16500	608	920	96	6.0
Pyrene	337 322	34400 23400	372[d,S4]	700[d,S4]	64[d,262]	354[d,262]

[a] Spectra were measured in dichloromethane ($c_0 \approx 4 \cdot 10^{-6}$ M) at 293 K. [b] Fluorescence quantum yields were determined using the dilution method (OD < 0.05) with Oxazine 1 in ethanol (Φ_f = 11%) as standard.[247] [c] Fluorescence lifetimes were determined with EPL picosecond pulsed diode lasers (λ_{ex} = 560 nm) for time correlated single photon counting; [d] in hexane.

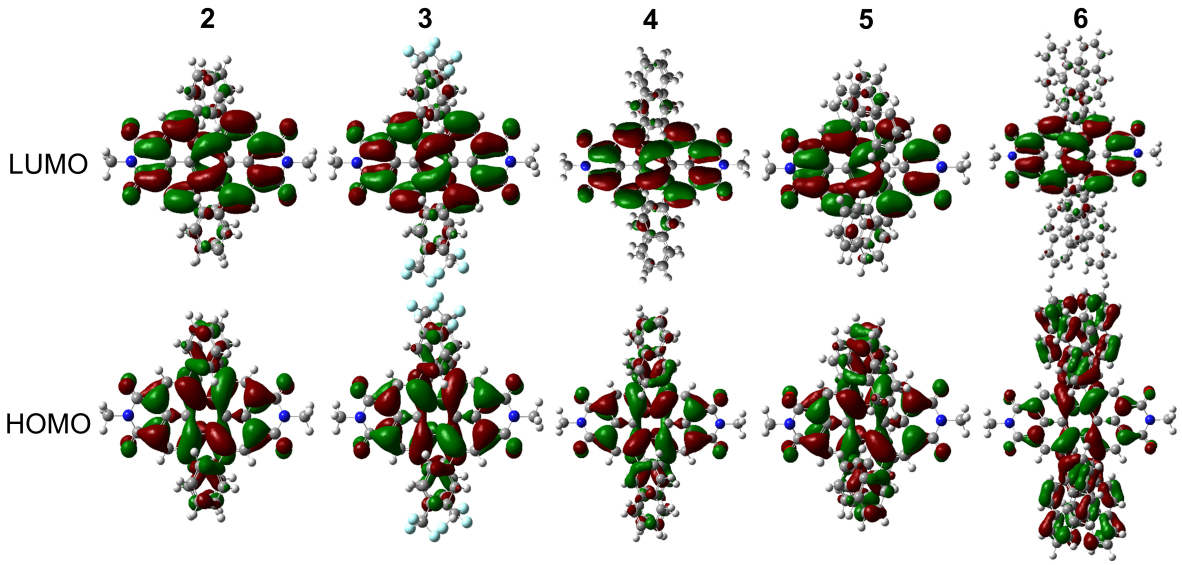

Figure 57 Calculated HOMO (bottom) and LUMO (top, isovalue = 0.2 a.u.) of PBIs **2**-**6** at B3LYP/6-31g(d) level theory. The imide-substituents have been replaced by methyl groups for simplicity.

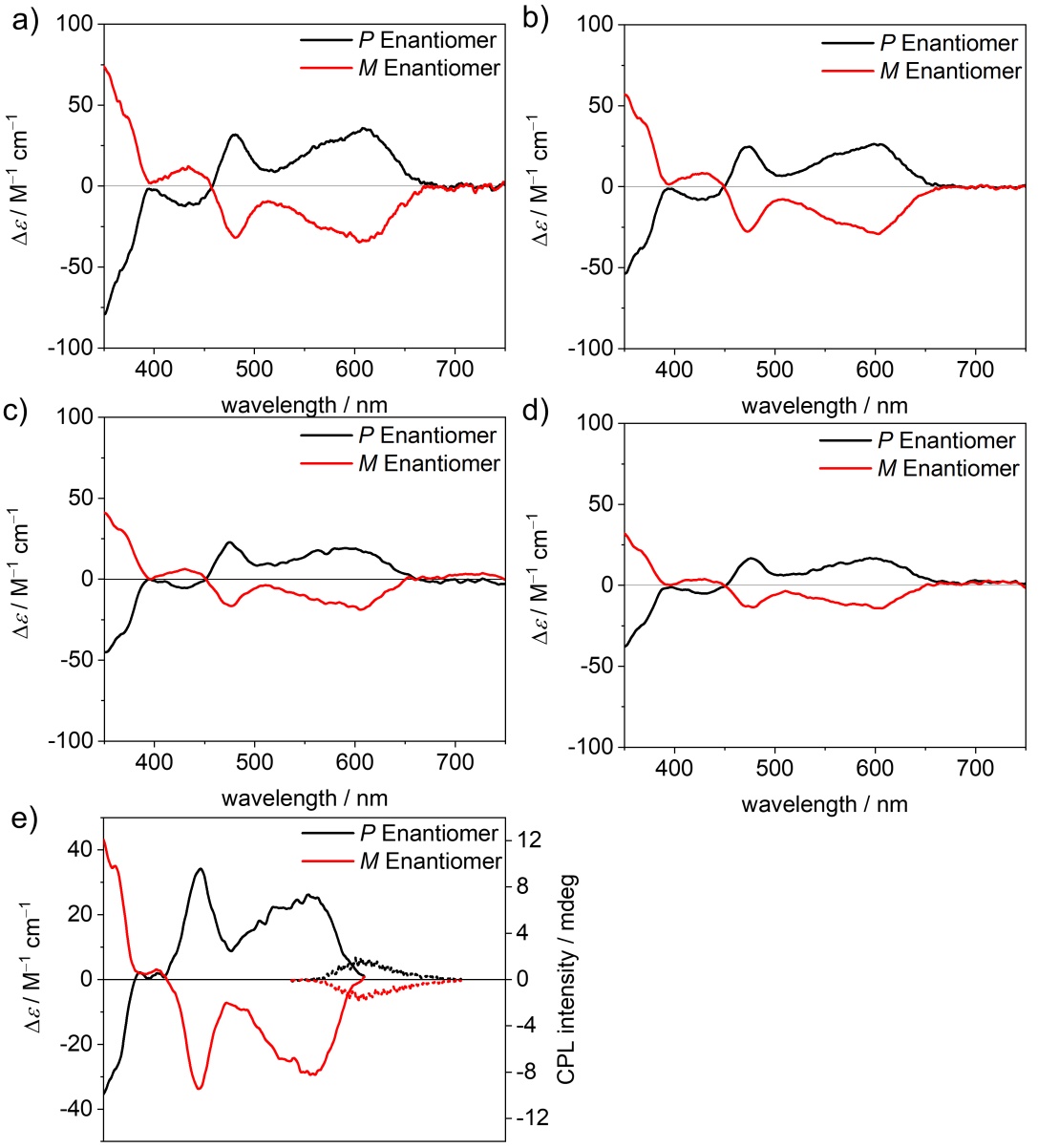

Figure 58 Circular dichroism (CD, $c_0 = 1 \cdot 10^{-5}$ M) spectra of *P*- (black) and *M*- (red) atropo-enantiomers of PBIs a) **2b**, b) **2c**, c) **2d**, d) **2e** and e) **3a** as well as circularly polarized luminescence (CPL, $c_0 = 2 \cdot 10^{-6}$ M) spectra of **3a** in DCM at 293 K.

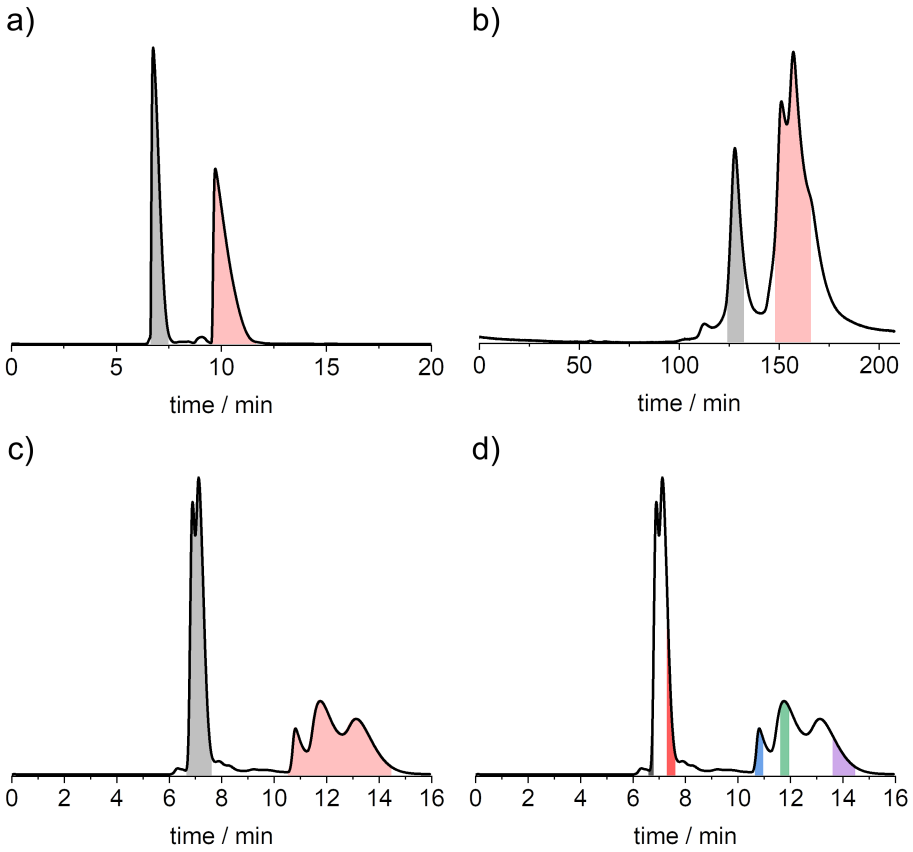

Figure 59 Elugrams of the HPLC separation on a chiral stationary phase of a) the successful separation of the atropo-enantiomers of **4a**, and the non-successful separations of b) **6a**, as well as c) and d) for **5a** using mixtures of hexane and DCM as eluent. The collection times of the respective fractions are highlighted. Detection by UV/Vis analysis at 550 nm. According to CD spectral analysis, no separation of atropo-enantiomers was achieved for **5a**. Thus, **5a** was for one run separated in c) two fractions and for another separated in d) five fractions. For each fraction a CD spectrum and a ^{1}H-NMR spectrum was measured, but no CD signals were obtained, and the ^{1}H-NMR spectra all look identical to the spectrum shown in Figure 82. Similar results were obtained for **6a**.

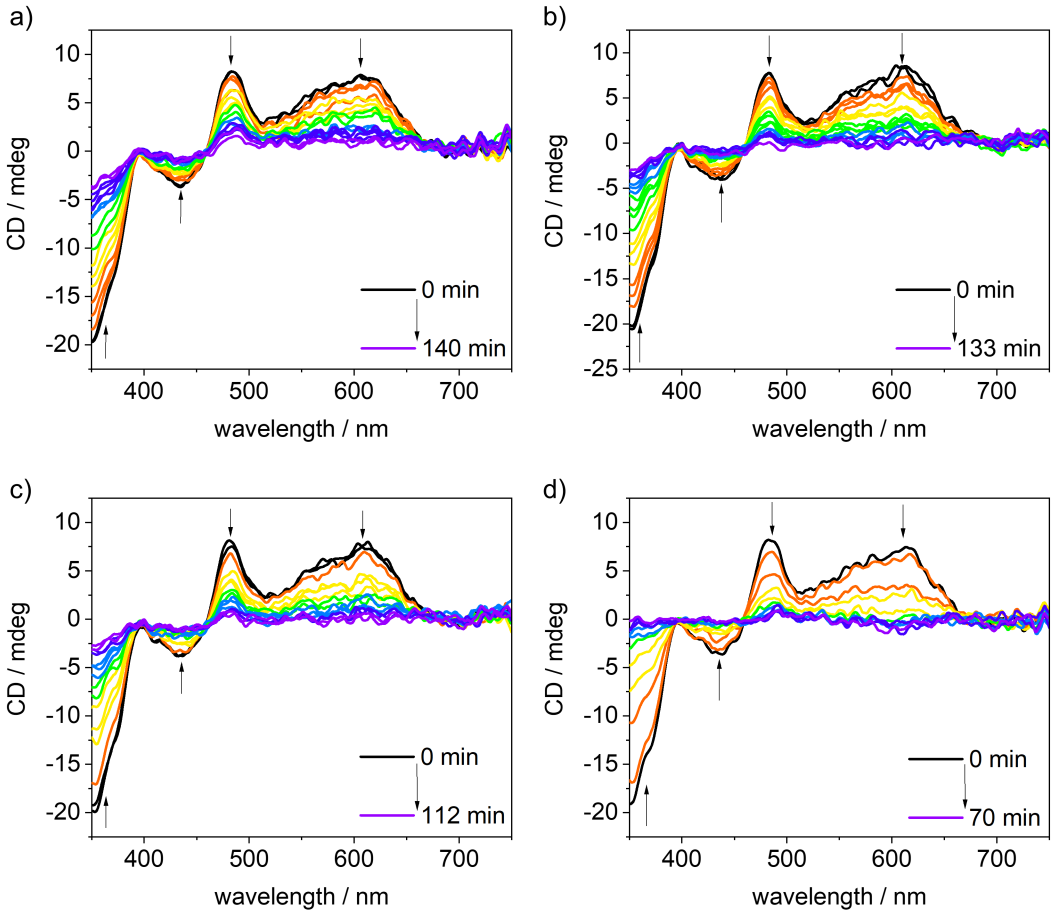

Figure 60 Time-dependent CD spectra of the *P*-atropo-enantiomer of **2a** in 1,1,2,2-tetrachloroethane at a) 383 K, b) 388 K, c) 393 K and d) 398 K.

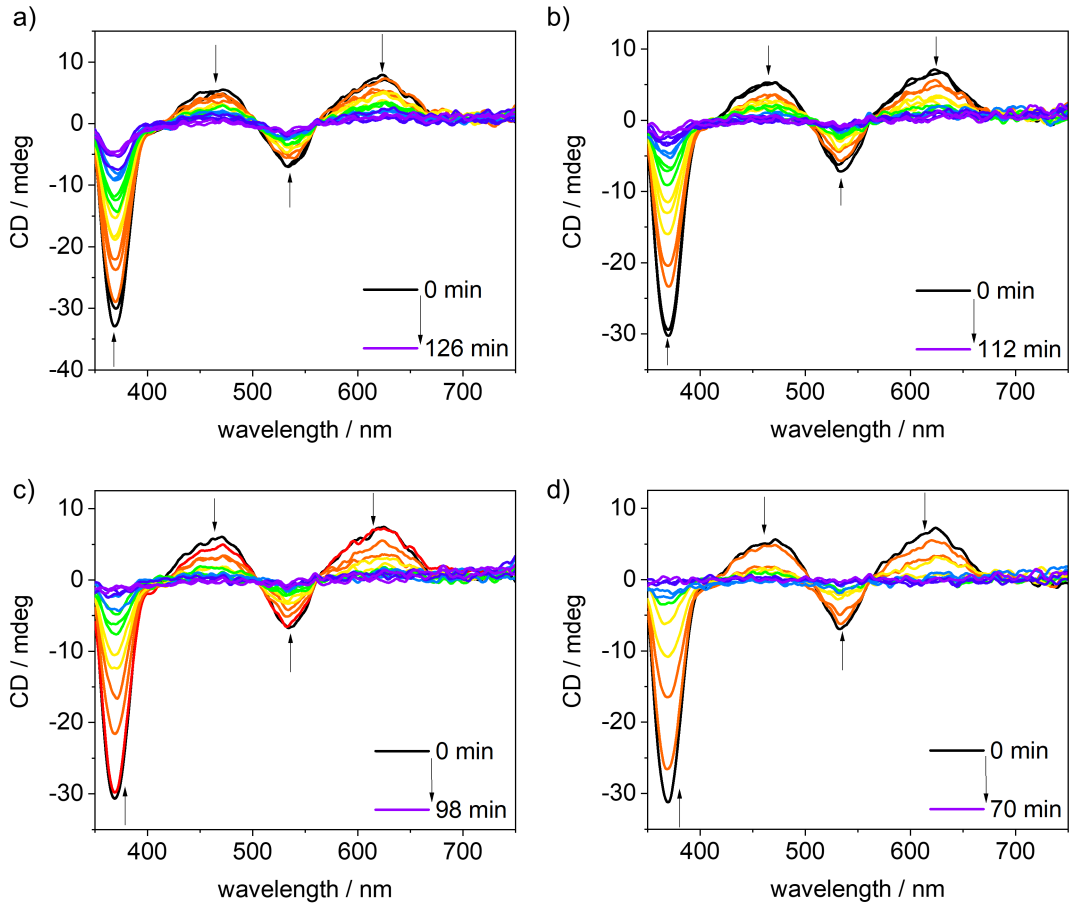

Figure 61 Time-dependent CD spectra of the *P*-atropoenantiomer of **4a** in 1,1,2,2-tetrachloroethane at a) 383 K, b) 388 K, c) 393 K and d) 398 K.

Table 7 Kinetic Data for the racemization process of **2a** and **4a** in 1,1,2,2-tetrachloroethane at four different temperatures obtained by CD spectroscopy.[237]

2a				**4a**			
T **[K]**	***k*** **[10^{-5} s^{-1}]**	$t_{1/2}$ **[min]**	$\Delta G^{\ddagger}$ **[kJ mol^{-1}]**	***T*** **[K]**	***k*** **[10^{-5} s^{-1}]**	$t_{1/2}$ **[min]**	$\Delta G^{\ddagger}$ **[kJ mol^{-1}]**
383	19.7	59	119.6	383	27.1	43	118.6
388	33.1	35	119.8	388	38.5	30	119.3
393	43.1	27	120.2	393	59.1	20	119.2
398	87.2	13	119.5	398	82.8	14	119.6

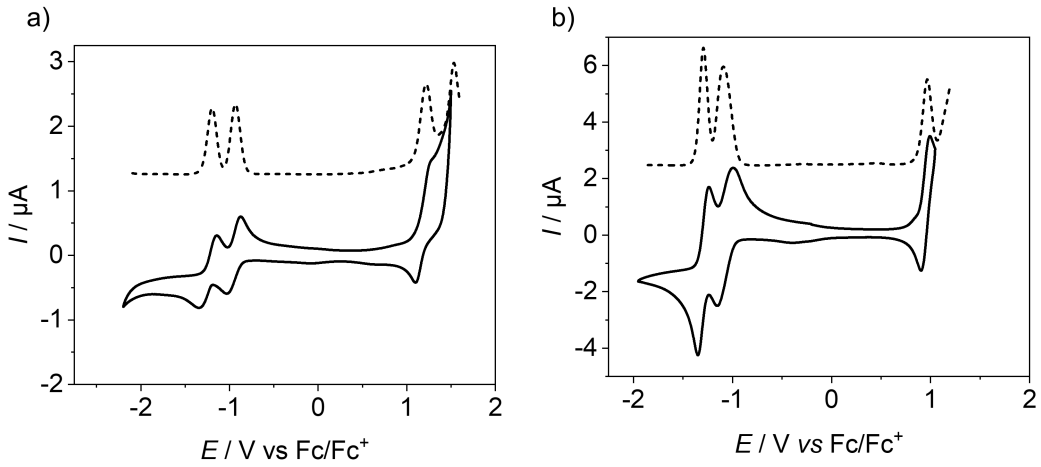

Figure 62 Cyclic voltammograms (solid lines) and square wave voltammograms (dashed lines) of PBIs a) **3a** and b) **4a**. Measurements were performed using DCM solutions ($c_0 \approx 2 \cdot 10^{-4}$ M) at 293 K, using tetrabutylammonium hexafluorophosphate (TBAHFP, 0.1 M) as electrolyte.

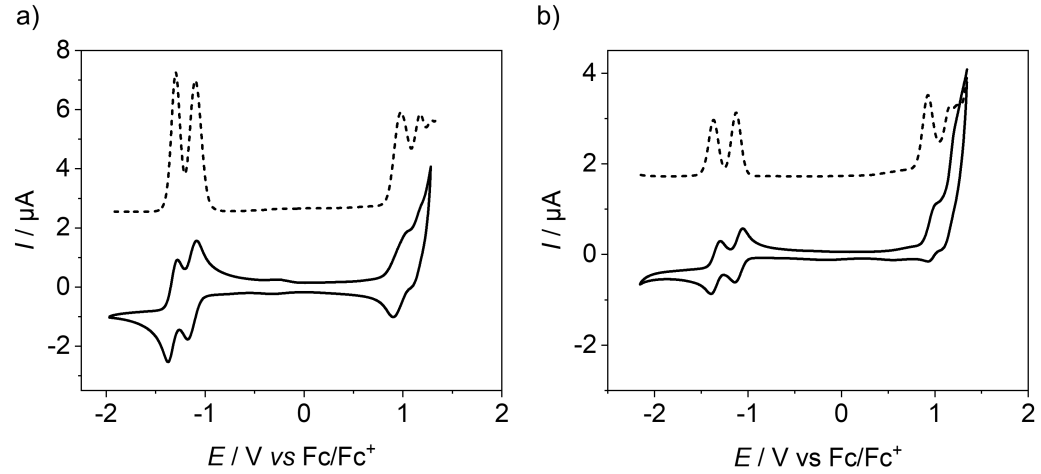

Figure 63 Cyclic voltammograms (solid lines) and square wave voltammograms (dashed lines) of PBI a) **5a** and b) **2b**. Measurements were performed using DCM solutions ($c_0 \approx 2 \cdot 10^{-4}$ M) at 293 K, using TBAHFP (0.1 M) as electrolyte.

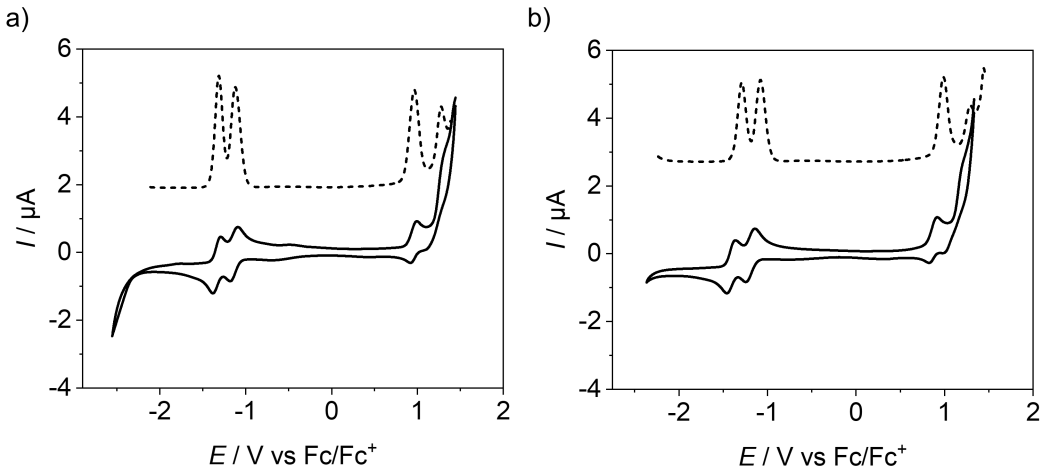

Figure 64 Cyclic voltammograms (solid lines) and square wave voltammograms (dashed lines) of a) **2c** and b) **2d**. Measurements were performed using DCM solutions ($c_0 \approx 2 \cdot 10^{-4}$ M) at 293 K, using TBAHFP (0.1 M) as electrolyte.

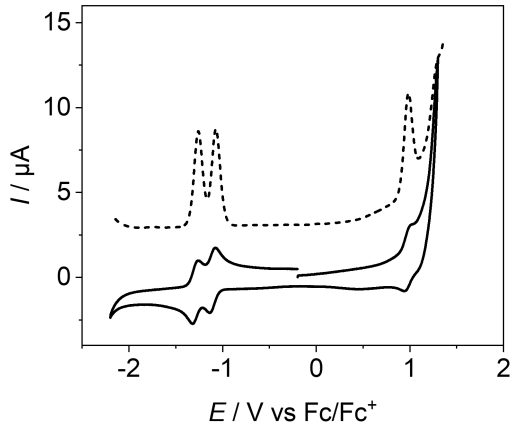

Figure 65 Cyclic voltammogram (solid lines) and square wave voltammogram (dashed lines) of **2e**. Measurements were performed using DCM solutions ($c_0 \approx 2 \cdot 10^{-4}$ M) at 293 K, using TBAHFP (0.1 M) as electrolyte.

Table 8 Summary of the redox properties of **2a**-**2e**. Half-wave potentials were determined by cyclic or square wave voltammetry measured in DCM (0.1 M TBAHFP) vs. Fc/Fc^+ at 293 K.

PBI	E_{red1}[d] [V]	E_{red2}[d] [V]	E_{ox1}[d] [V]	E_{ox2} [d] [V]	E_{HOMO}[a] [eV]	E_{LUMO}[a] [eV]	E_{gap} [eV]
2a	–1.05	–1.21	0.97	-[g]	–6.12	–4.10	2.02
2b	–1.02	–1.25	1.01	1.19	–6.16	–4.13	2.03
2c	–1.12	–1.31	0.96	1.28	–6.11	–4.03	2.08
2d	–1.08	–1.29	0.99	1.29	–6.14	–4.07	2.07
2e	–1.07	–1.26	0.97	-[b]	–6.12	–4.08	2.04
76	–1.00	–1.22	1.30	-[b]	–6.45	–4.15	2.30
77	–1.10	–1.29	0.90	1.21	–6.05	–4.05	2.00
Pyrene	-[b]	-[b]	0.63	-[b]	–5.78	-	-

[a] Calculated according to literature known procedure using the experimentally determined redox potentials (E_{HOMO}= –[E_{ox1} +5.15 eV] and E_{LUMO} = –[E_{red1} +5.15 eV]) and the energy level of Fc/Fc^+ with respect to the vacuum level (–5.15 eV). [b] Not observed.

Table 9 Calculated UV/Vis/NIR transitions for compound **2** using TD-DFT (B3LYP/def2-SVP).

Transition	% Character	Wavelength / nm	Oscillator strength
188 → 189	100	669.44	0.2596
187 → 189	100	485.49	0.0420
186 → 189 188 → 192	97.3 2.7	472.05	0.2050
184 → 189	100	412.04	0.0087

Table 10 Calculated UV/Vis/NIR transitions for compound **3** using TD-DFT (B3LYP/def2-SVP).

Transition	% Character	Wavelength / nm	Oscillator strength
252 → 253	100	792.38	0.1358
251 → 253	100	532.93	0.0272
248 → 253 250 → 253 252 → 256	26.4 68.9 4.7	471.17	0.1506
248 → 253 250 → 253 252 → 256	72.6 25.2 2.2	467.75	0.0622
239 → 253 246 → 253 252 → 254 252 → 255	10.3 42.3 26.4 21.0	407.63	0.0033
239 → 253 246 → 253 252 → 254 252 → 255	36.8 15.3 24.7 23.2	399.83	0.0194
237 → 253 238 → 253 244 → 253 247 → 253	4.0 5.6 8.5 81.9	397.19	0.0154

Table 11 Calculated UV/Vis/NIR transitions for compound **4** using TD-DFT (B3LYP/def2-SVP).

Transition	% Character	Wavelength / nm	Oscillator strength
240 → 241	100	760.46	0.1012
239 → 241	100	624.61	0.0573
238 → 241	100	623.55	0.0431
236 → 241	100	510.93	0.1211
235 → 241	100	466.05	0.2160
234 → 241 240 → 243	97.7 2.3	436.71	0.0248
230 → 241 234 → 241 240 → 243 240 → 247	3.0 2.1 92.6 2.3	400.05	0.0525

Table 12 Calculated UV/Vis/NIR transitions for compound **5** using TD-DFT (B3LYP/def2-SVP).

Transition	% Character	Wavelength / nm	Oscillator strength
236 → 241 240 → 241	3.6 96.4	693.53	0.1344
239 → 241	100	658.56	0.0699
237 → 241	100	599.36	0.0292
236 → 241 240 → 241	96.5 3.5	499.27	0.1542
234 → 241	100	420.41	0.0031
226 → 241 233 → 241 240 → 245	2.3 93.8 3.9	402.74	0.0088
232 → 241 240 → 243	48.2 51.8	396.86	0.0066

Table 13 Calculated UV/Vis/NIR transitions for compound **6** using TD-DFT (B3LYP/def2-SVP).

Transition	% Character	Wavelength / nm	Oscillator strength
316 → 317	100	907.21	0.0101
315 → 317	100	885.97	0.1173
313 → 317	100	743.48	0.0491
312 → 317	100	513.35	0.0619
311 → 317 316 → 318	20.4 79.6	466.17	0.0404
311 → 317 316 → 318	79.4 20.6	453.49	0.2214

4.4.4. NMR spectra

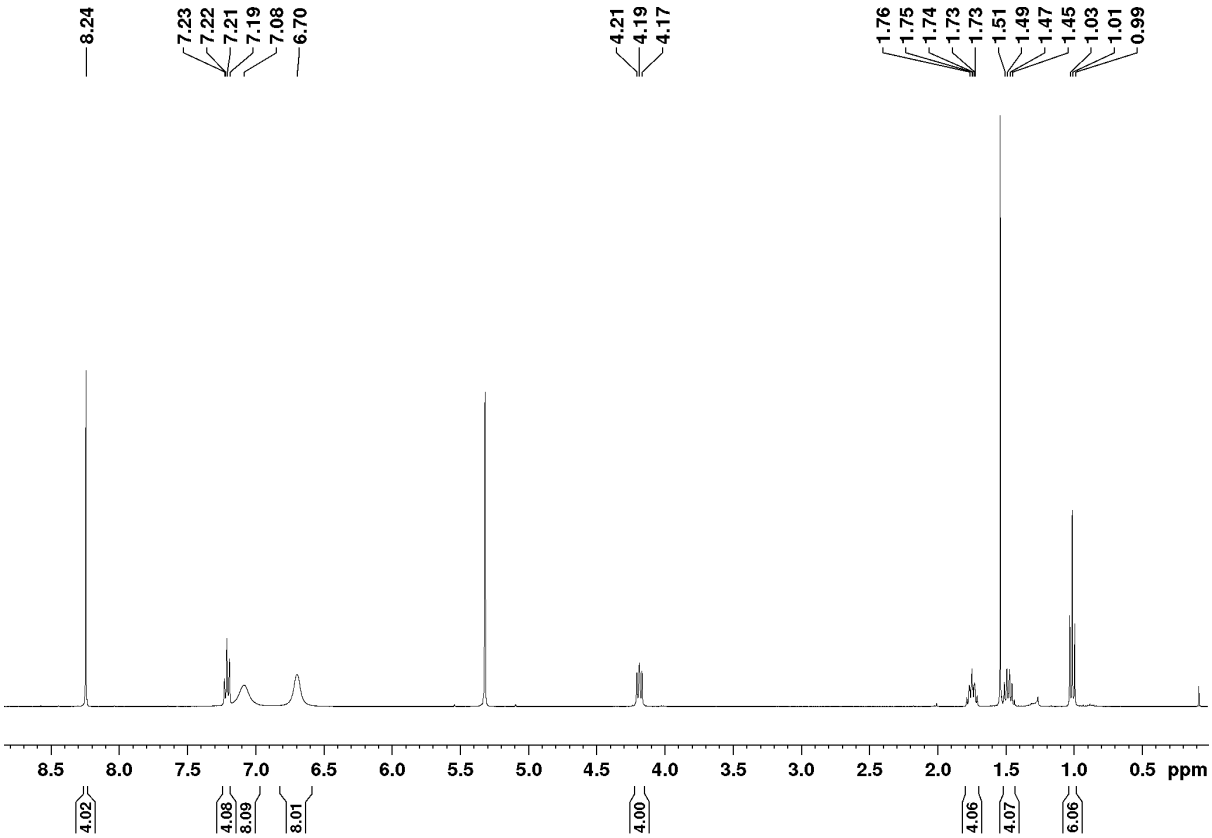

Figure 66 ^{1}H-NMR spectrum of **2a** in CD_2Cl_2 recorded at 295 K.

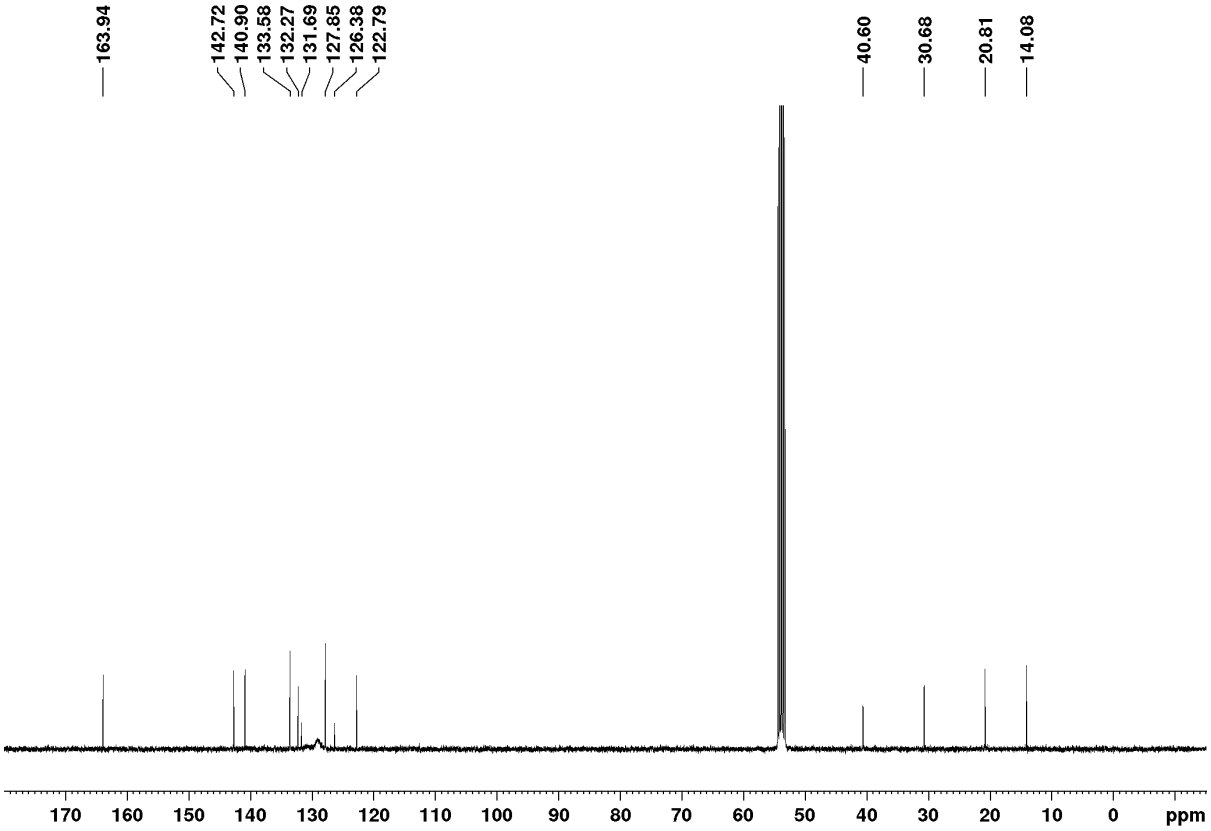

Figure 67 ^{13}C-NMR spectrum of **2a** in CD_2Cl_2 recorded at 295 K.

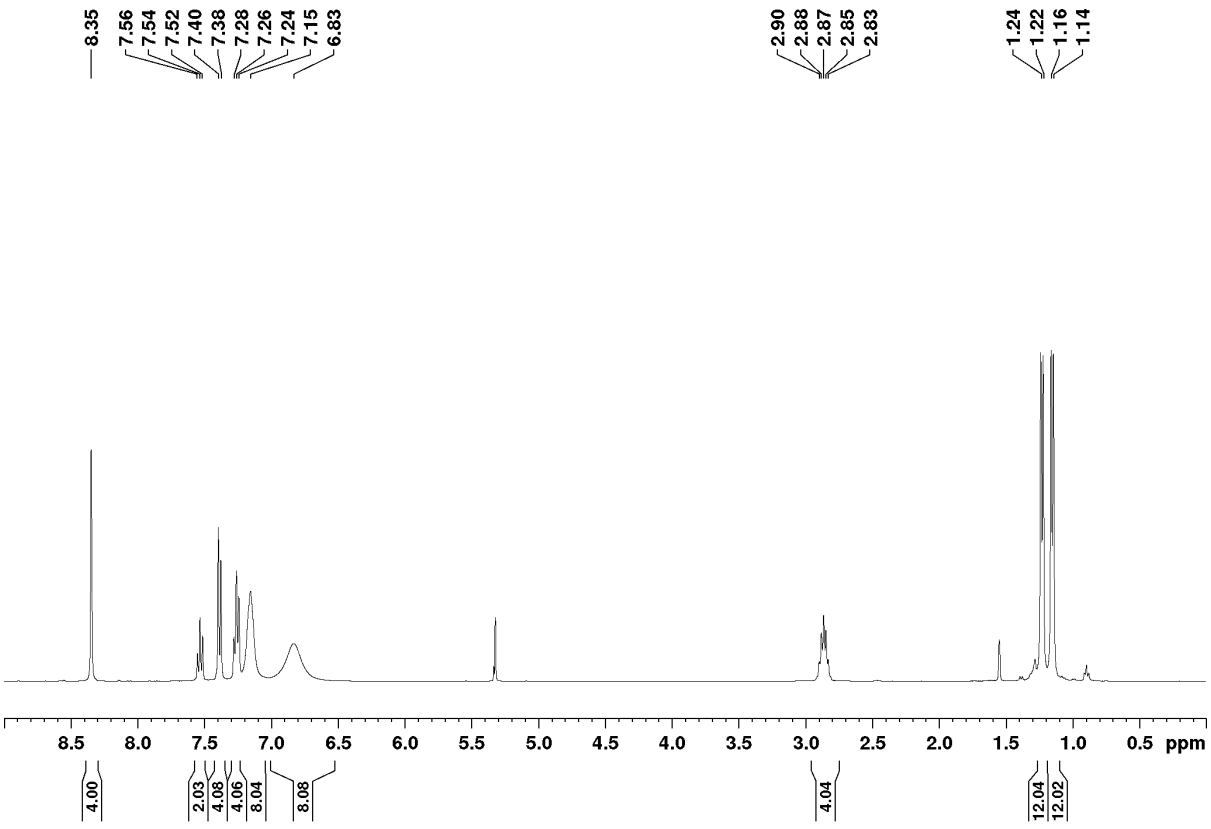

Figure 68 ^{1}H-NMR spectrum of **2b** in CD_2Cl_2 recorded at 295 K.

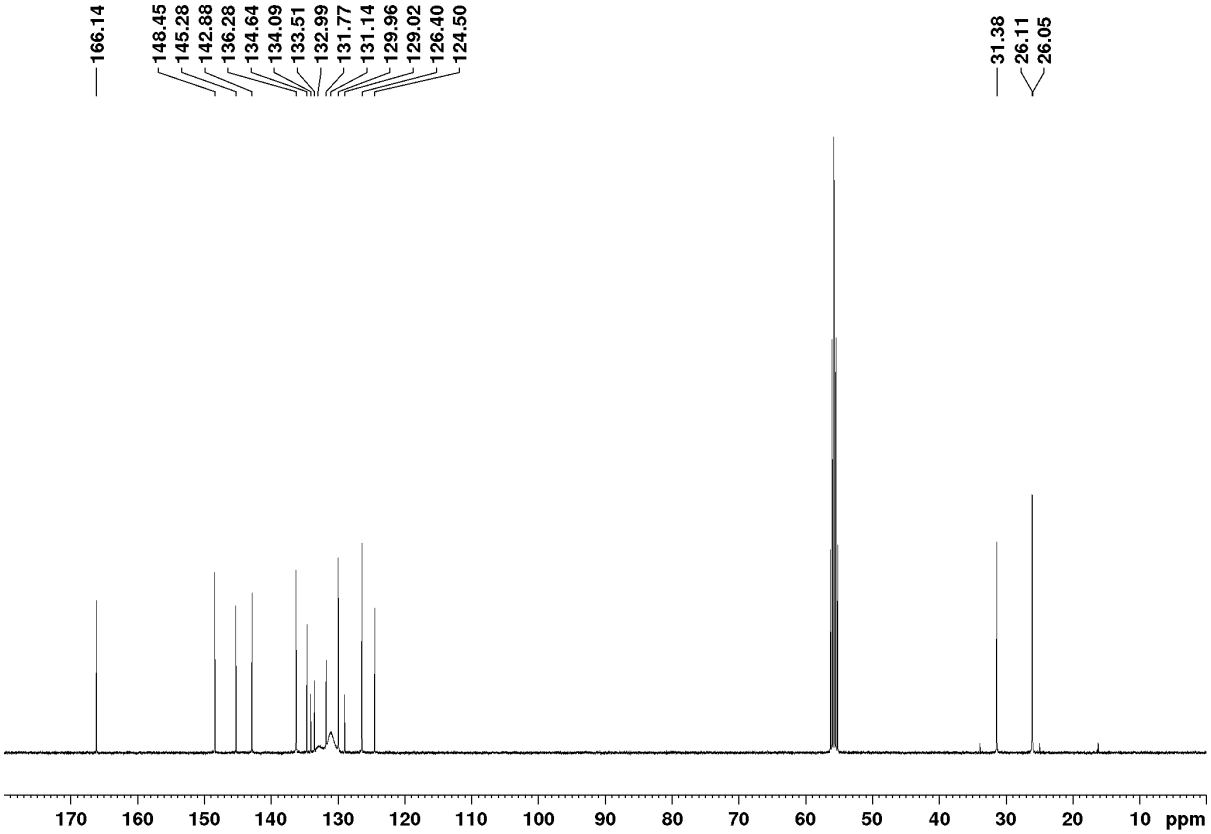

Figure 69 ^{13}C-NMR spectrum of **2b** in CD_2Cl_2 recorded at 295 K.

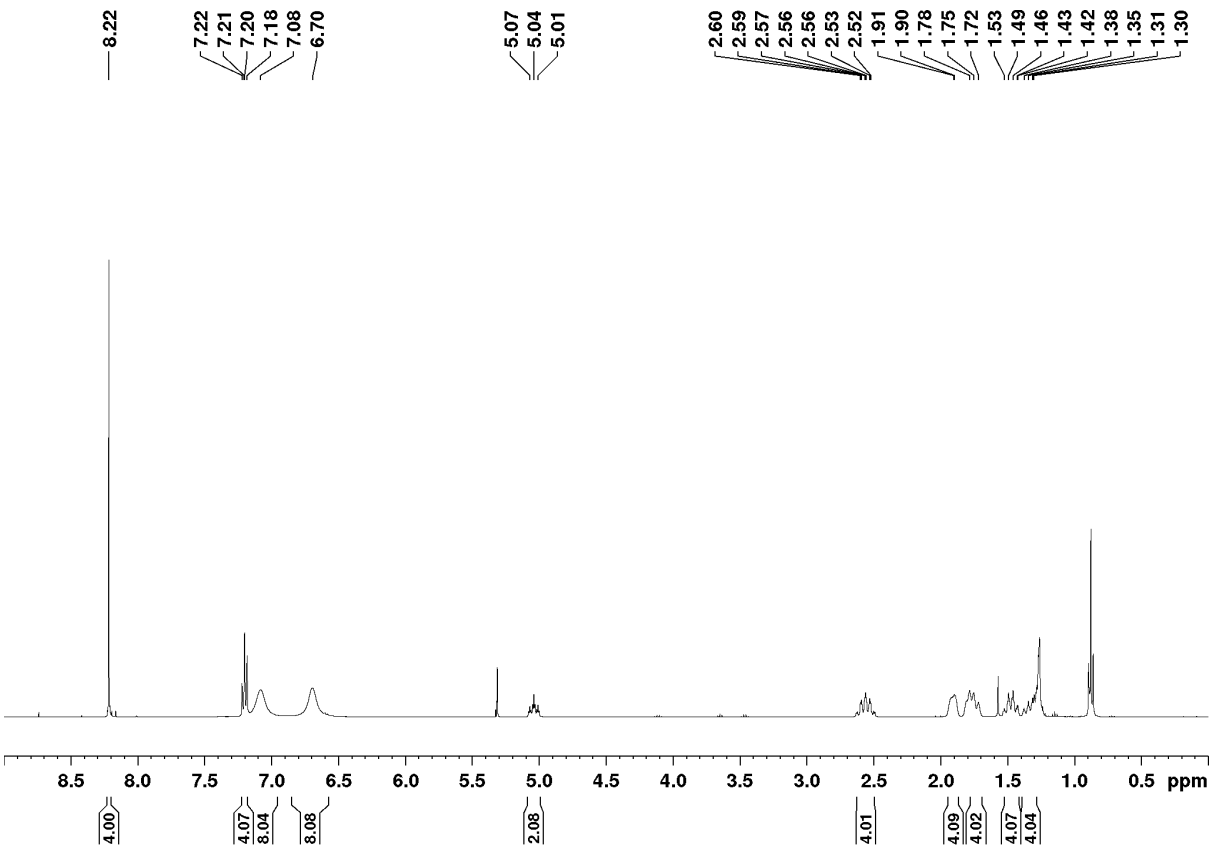

Figure 70 ^{1}H-NMR spectrum of **2c** in CD_2Cl_2 recorded at 295 K.

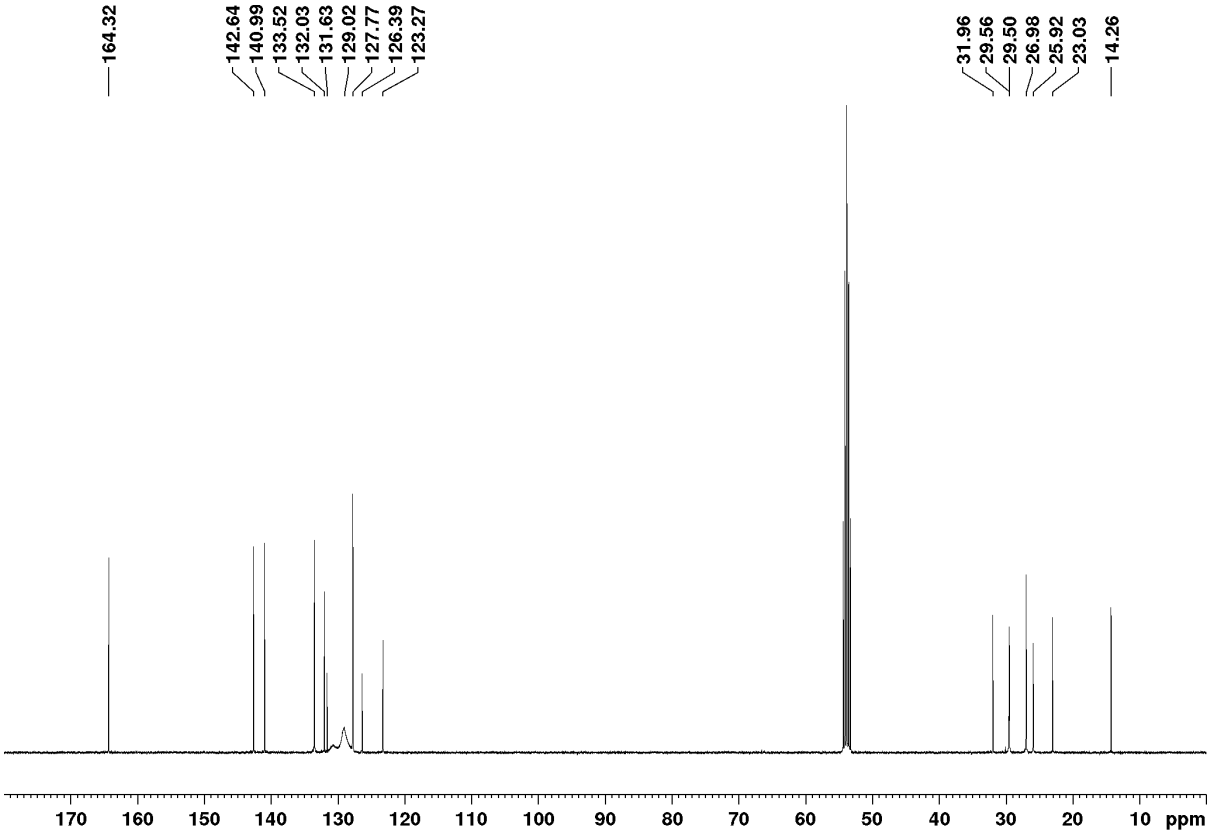

Figure 71 ^{13}C-NMR spectrum of **2c** in CD_2Cl_2 recorded at 295 K.

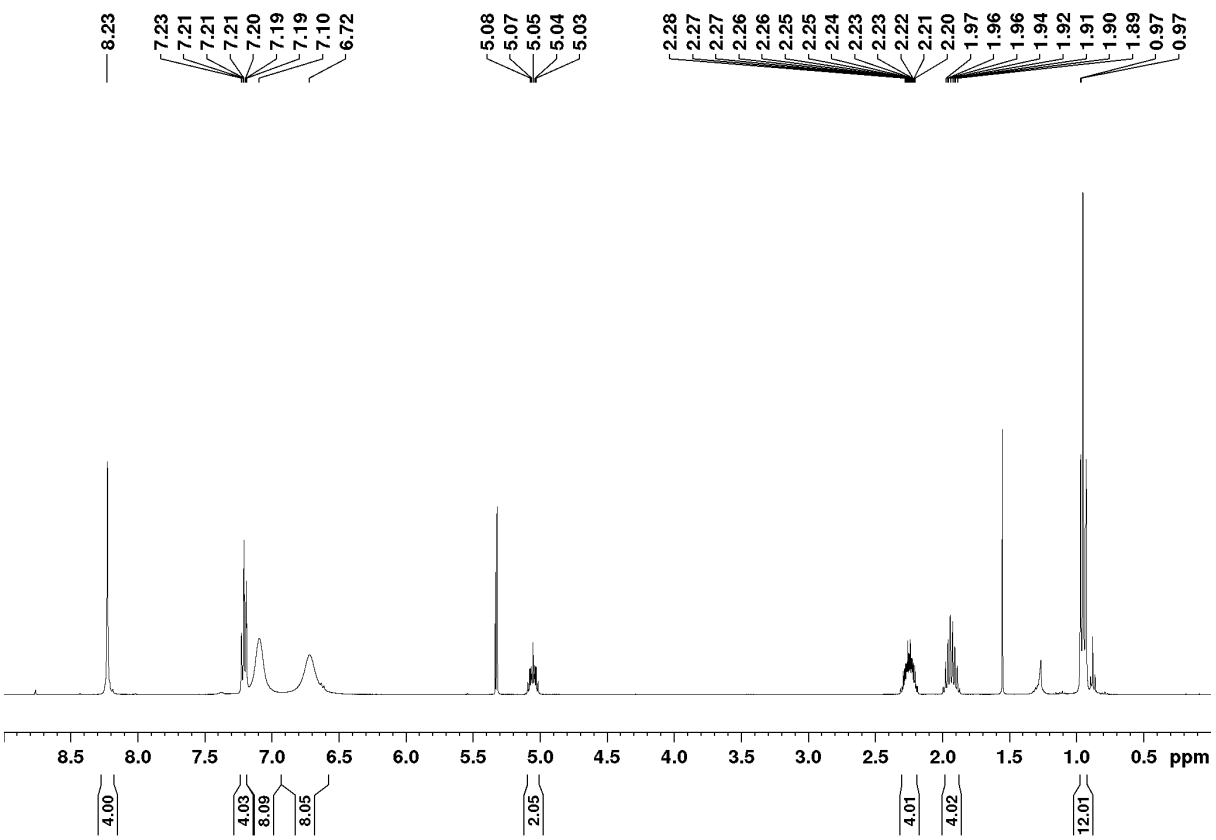

Figure 72 ^{1}H-NMR spectrum of **2d** in CD_2Cl_2 recorded at 295 K.

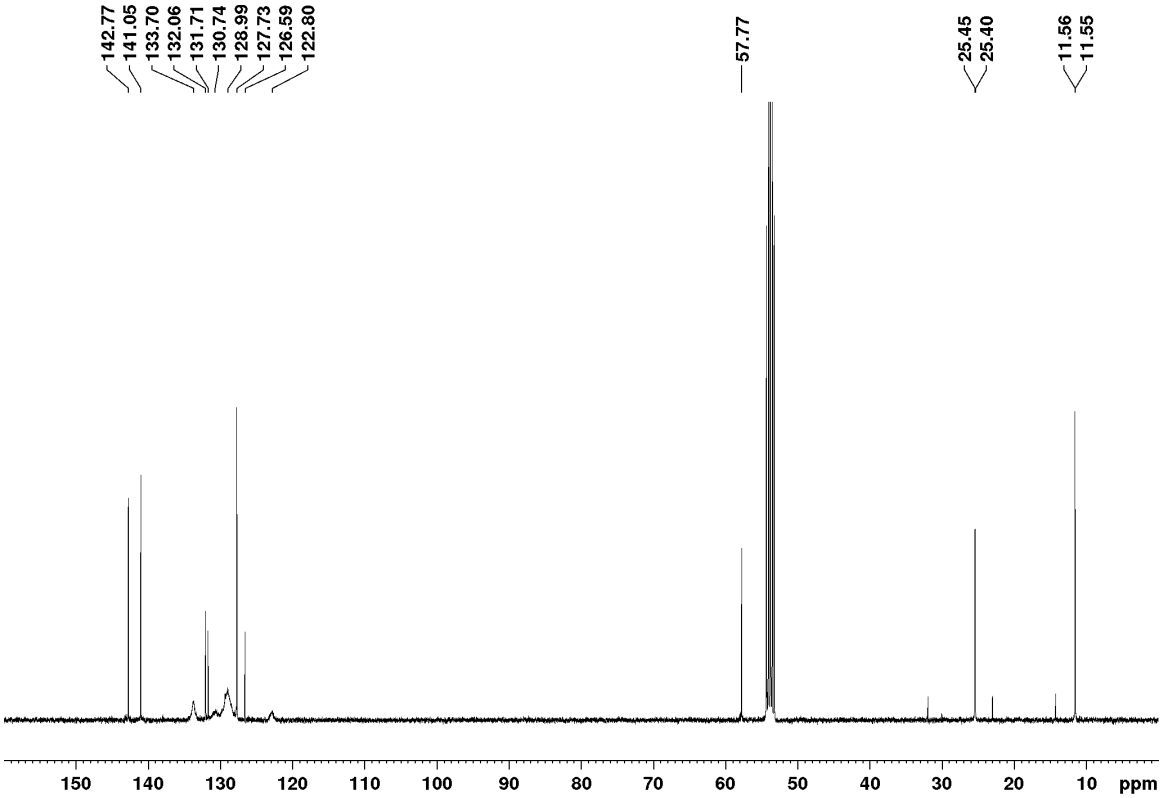

Figure 73 ^{13}C-NMR spectrum of **2d** in CD_2Cl_2 recorded at 295 K.

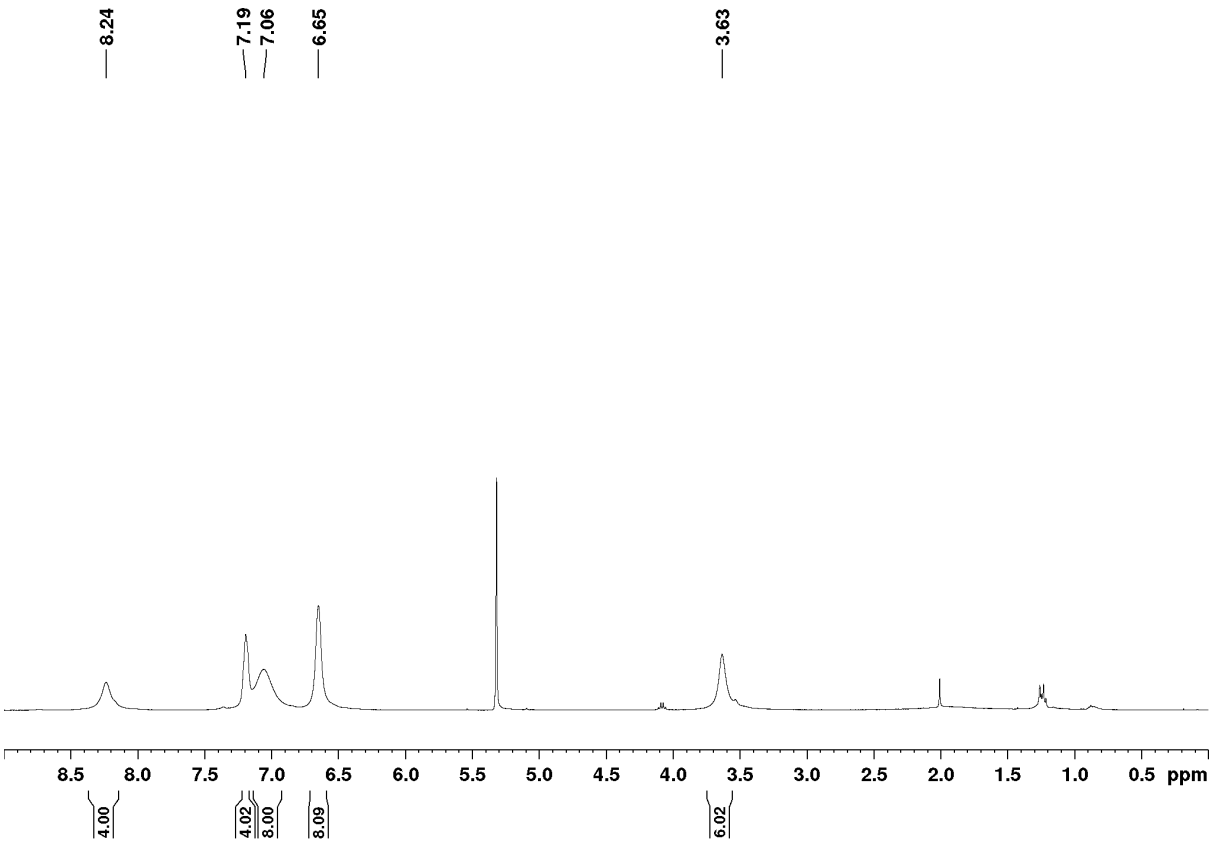

Figure 74 ^{1}H-NMR spectrum of **2e** in CD_2Cl_2 recorded at 295 K.

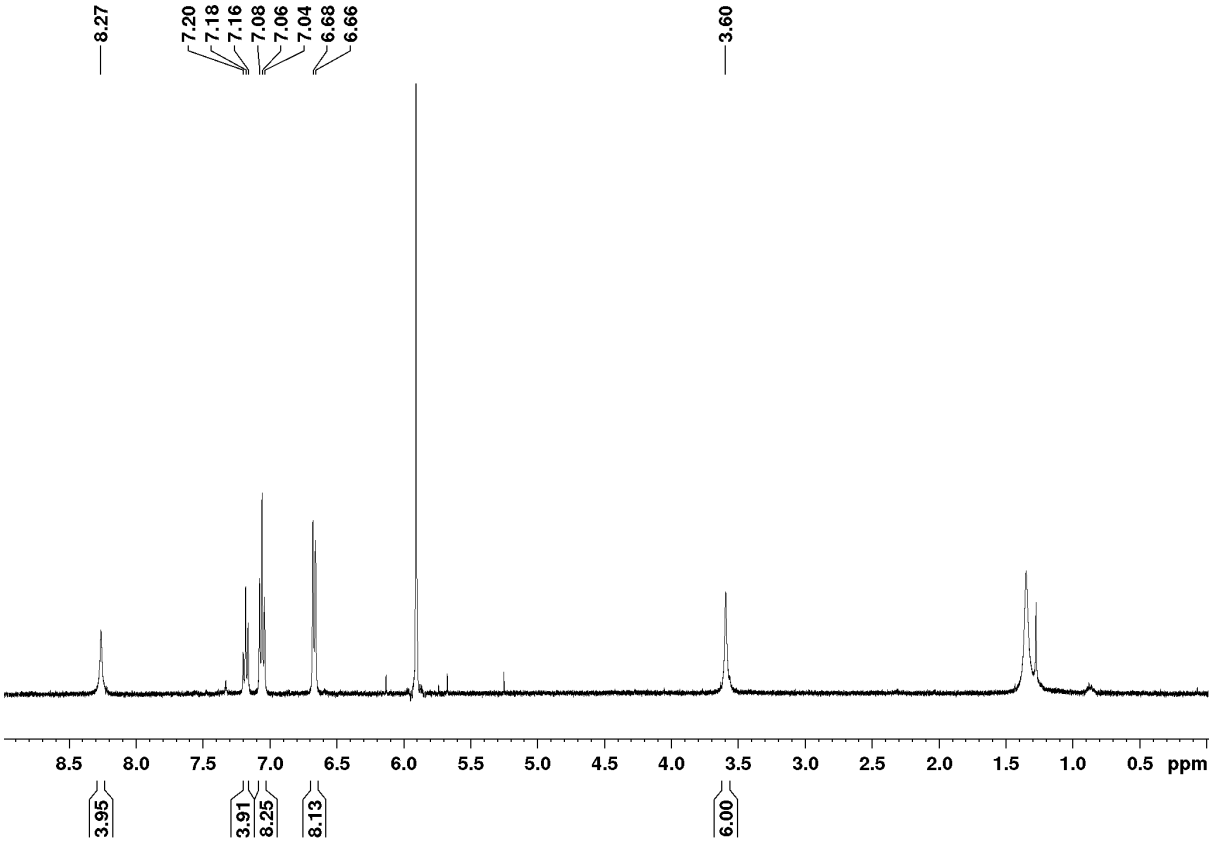

Figure 75 ^{1}H-NMR spectrum of **2e** in $C_2D_2Cl_4$ recorded at 390 K.

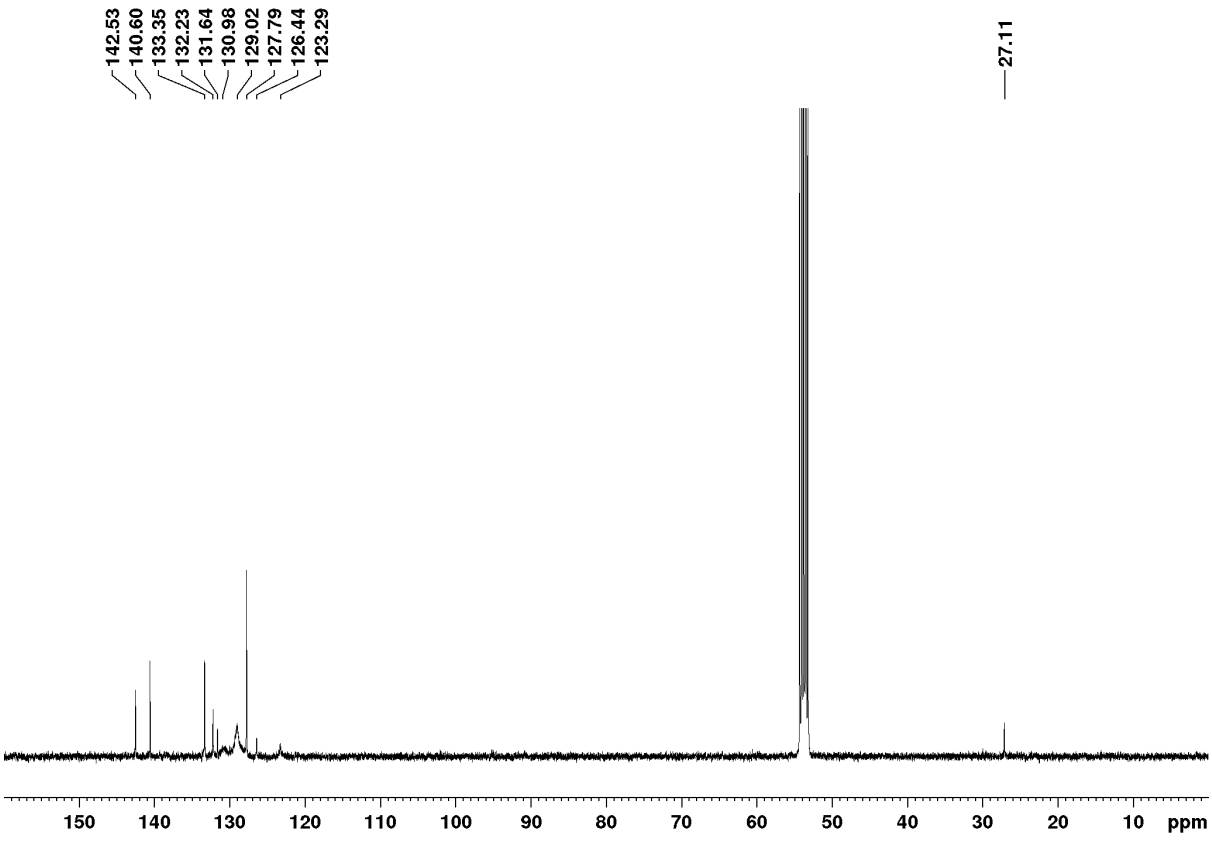

Figure 76 ^{13}C-NMR spectrum of **2e** in CD_2Cl_2 recorded at 295 K.

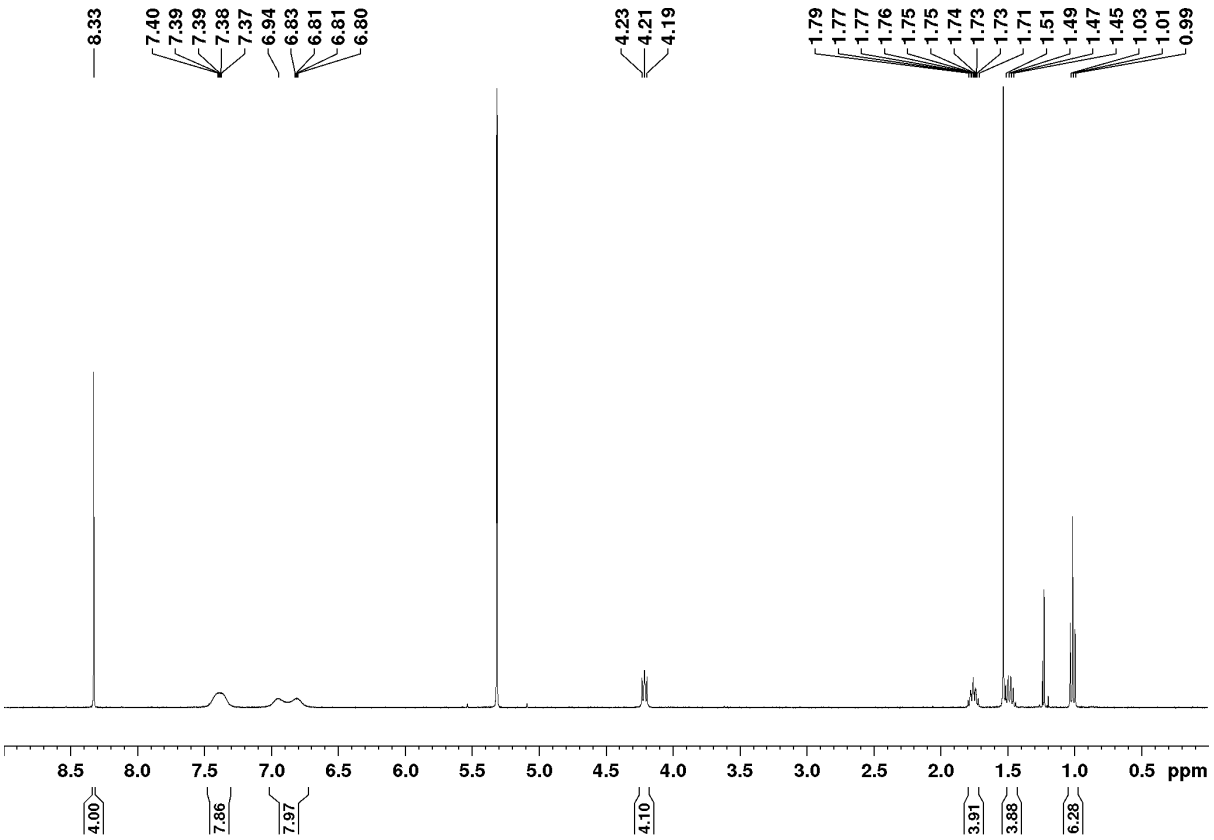

Figure 77 ^{1}H-NMR spectrum of **3a** in CD_2Cl_2 recorded at 295 K.

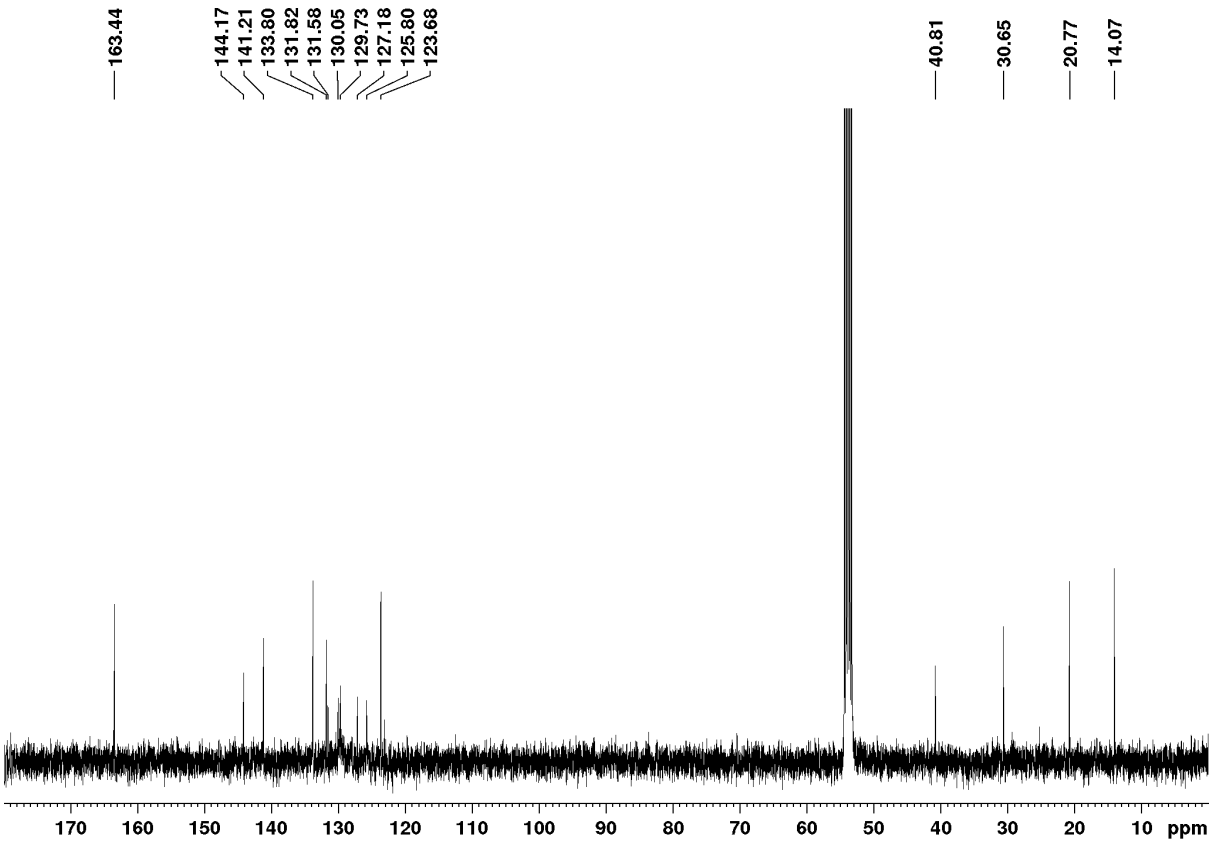

Figure 78 ^{13}C-NMR spectrum of **3a** in CD_2Cl_2 recorded at 295 K.

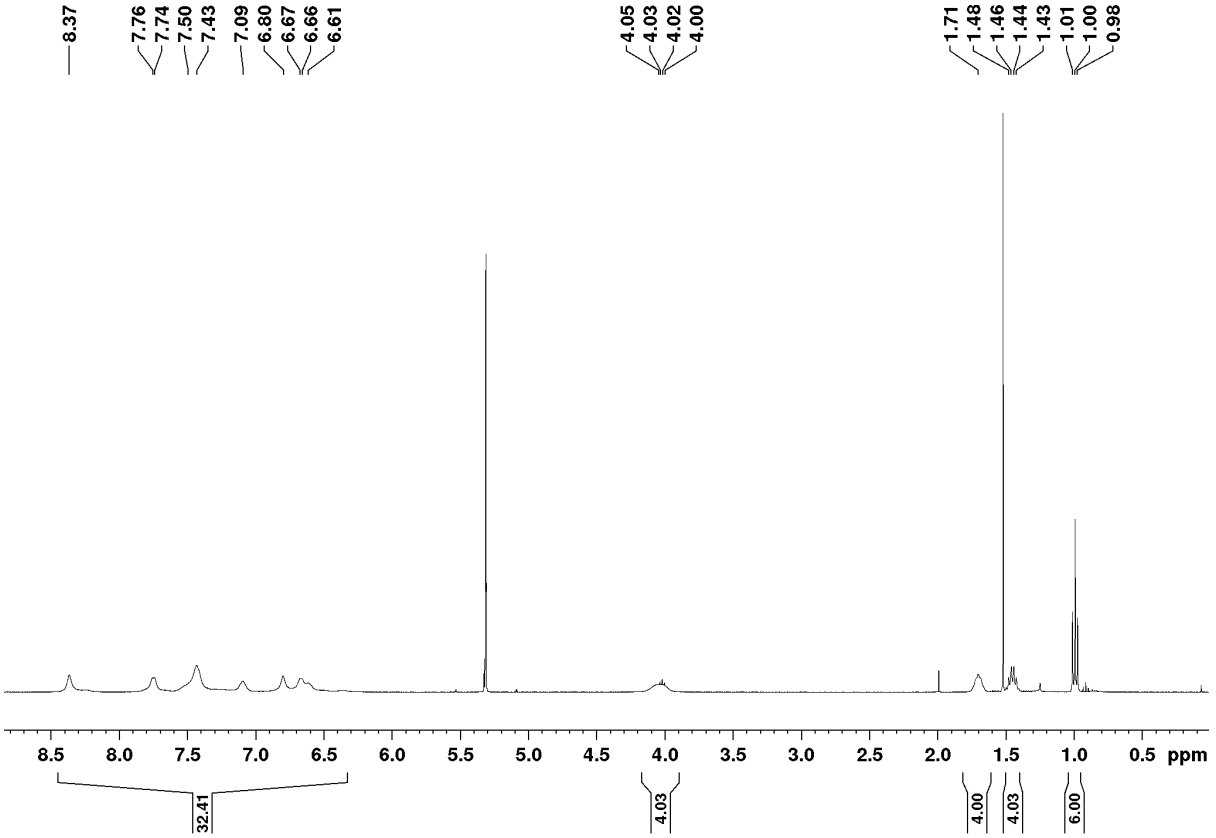

Figure 79 ^{1}H-NMR spectrum of **4a** in CD_2Cl_2 recorded at 295 K.

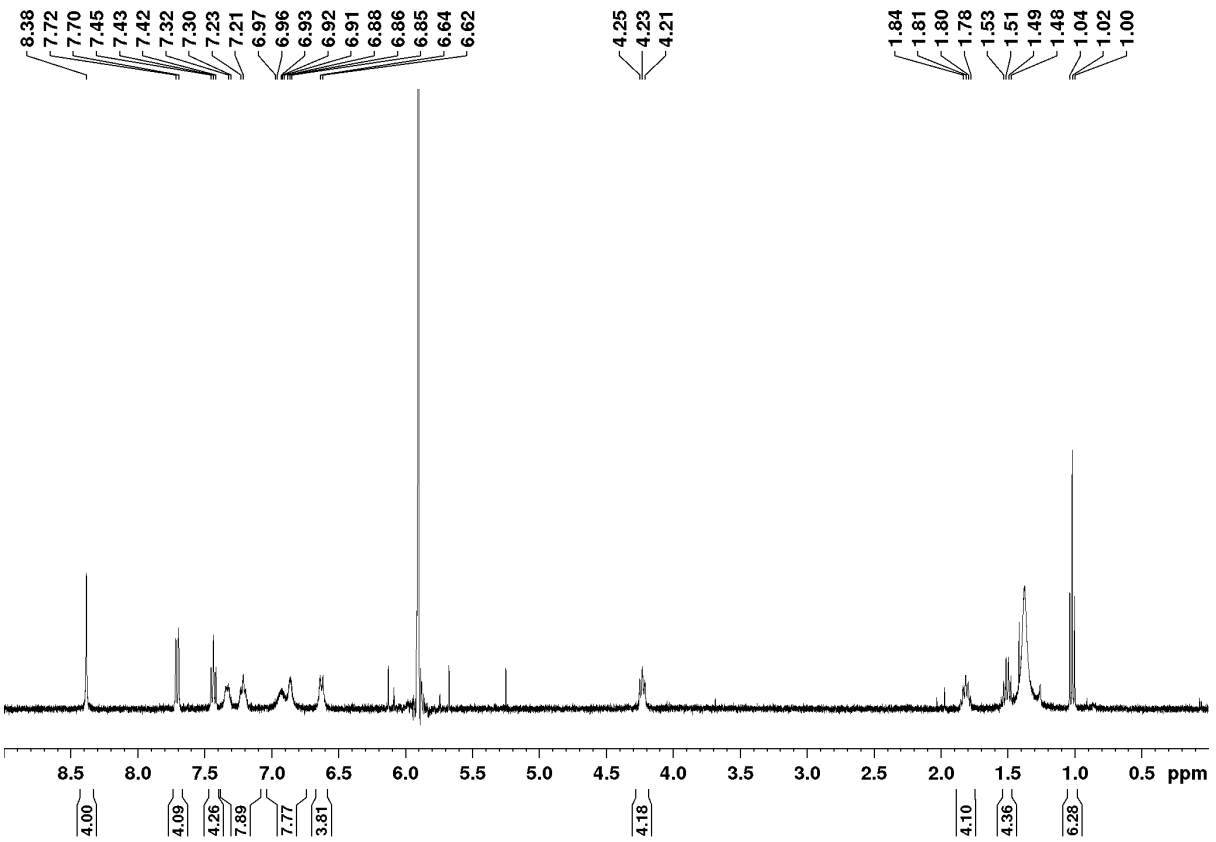

Figure 80 ^{1}H-NMR spectrum of **4a** in $C_2D_2Cl_4$ recorded at 390 K.

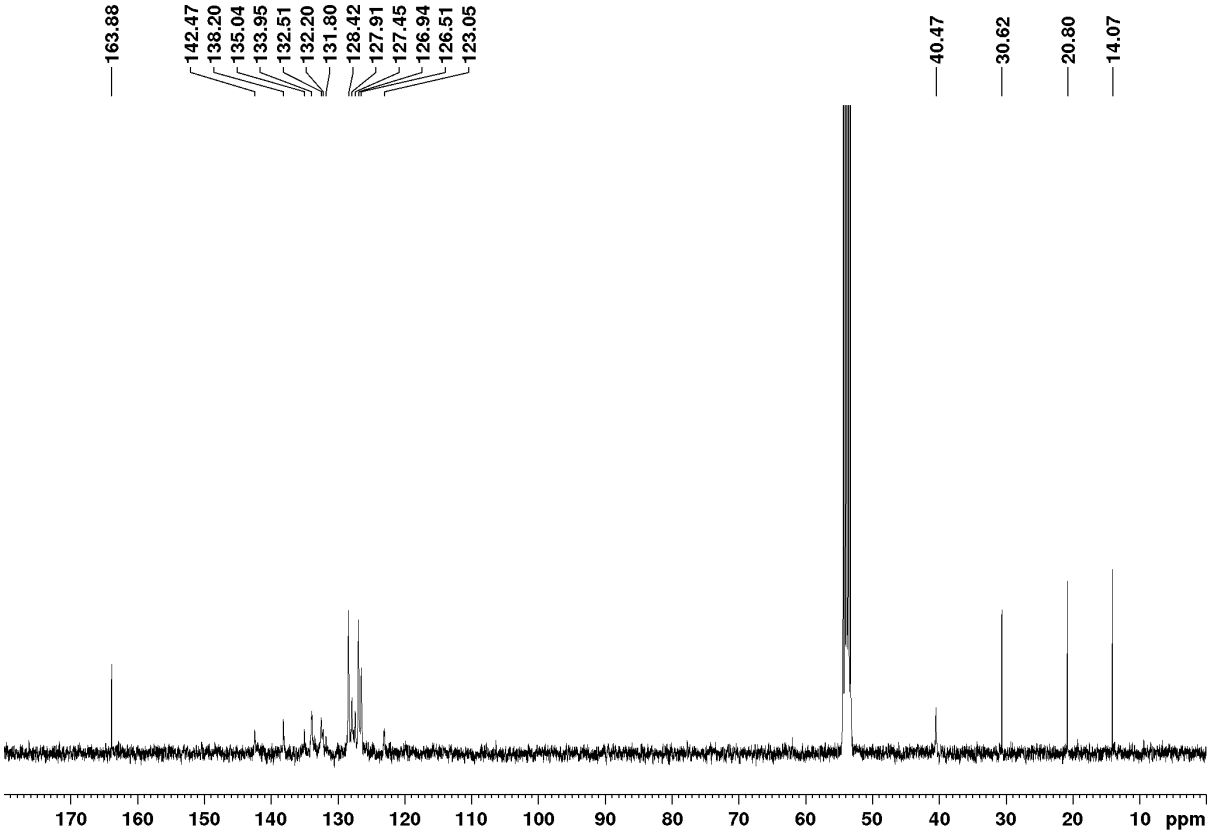

Figure 81 ^{13}C-NMR spectrum of **4a** in CD_2Cl_2 recorded at 295 K.

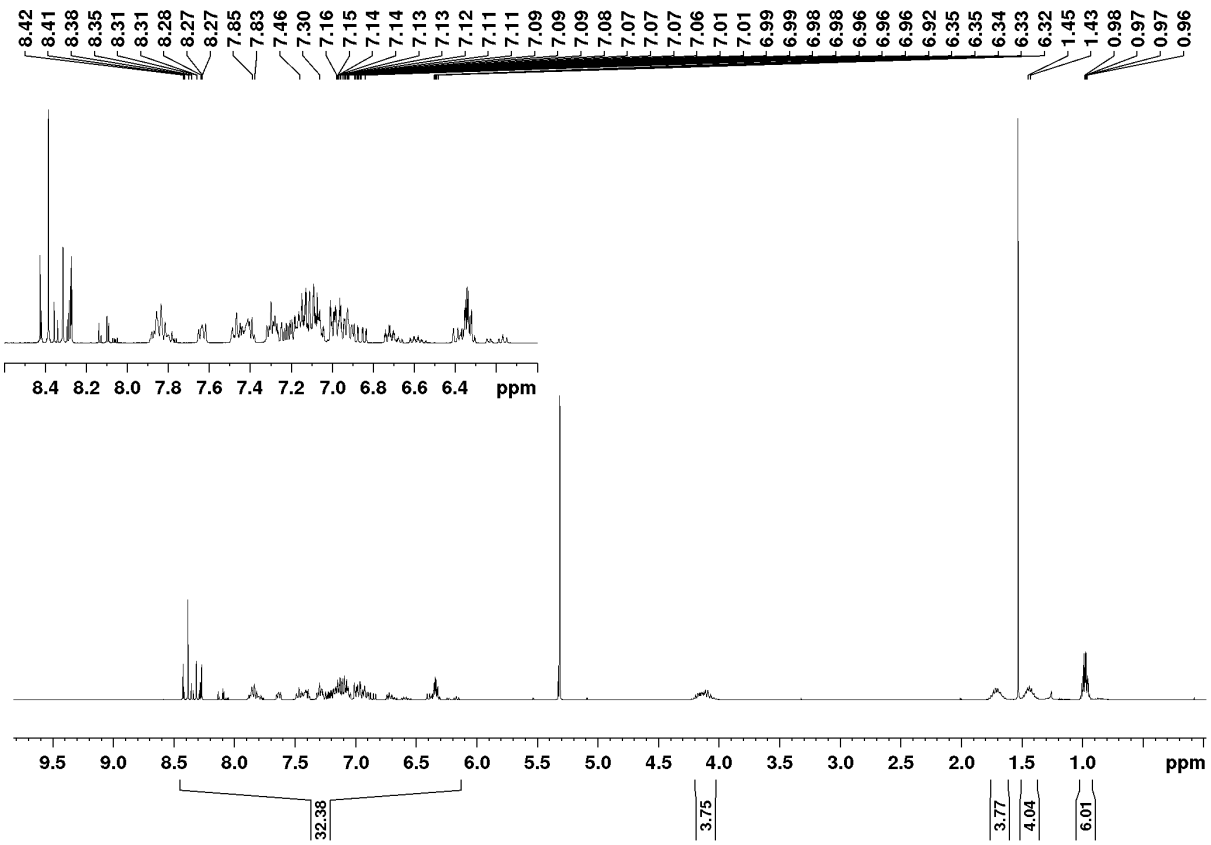

Figure 82 ^{1}H-NMR spectrum of **5a** in CD_2Cl_2 recorded at 295 K.

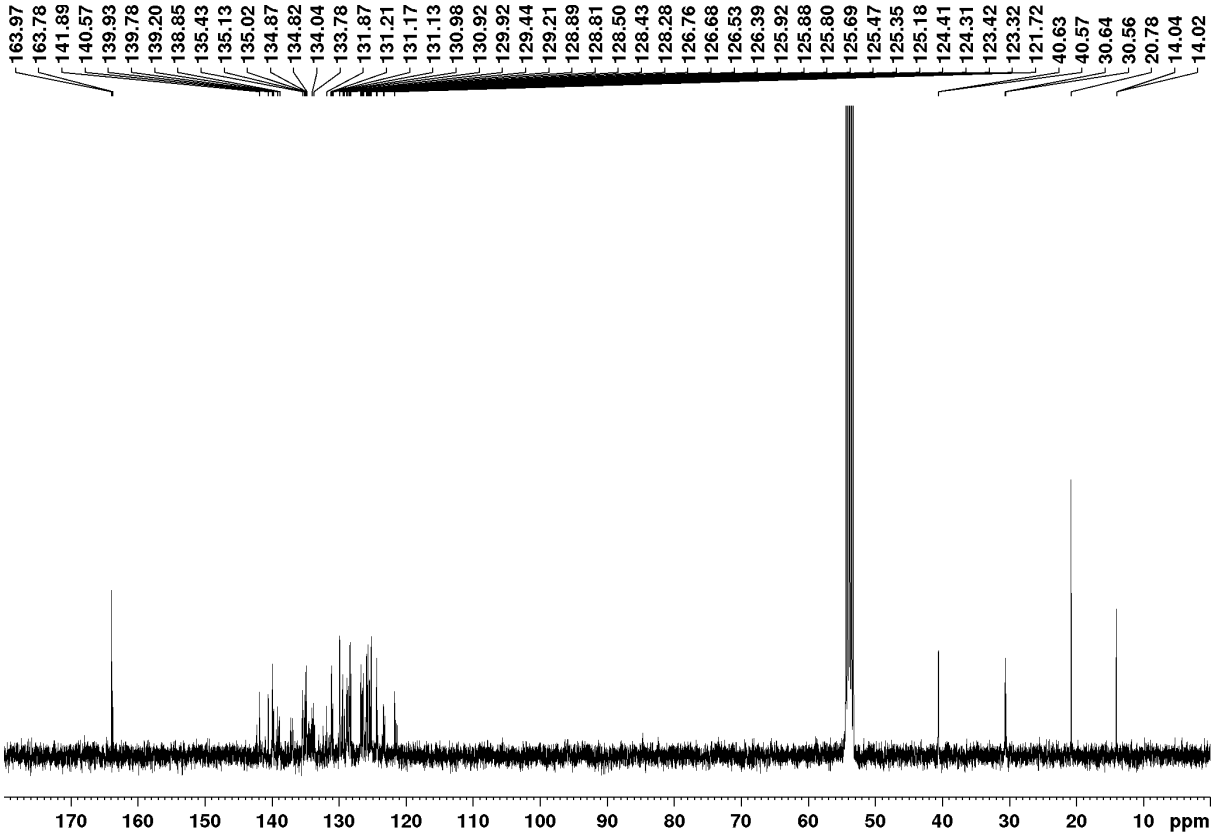

Figure 83 ^{13}C-NMR spectrum of **5a** in CD_2Cl_2 recorded at 295 K.

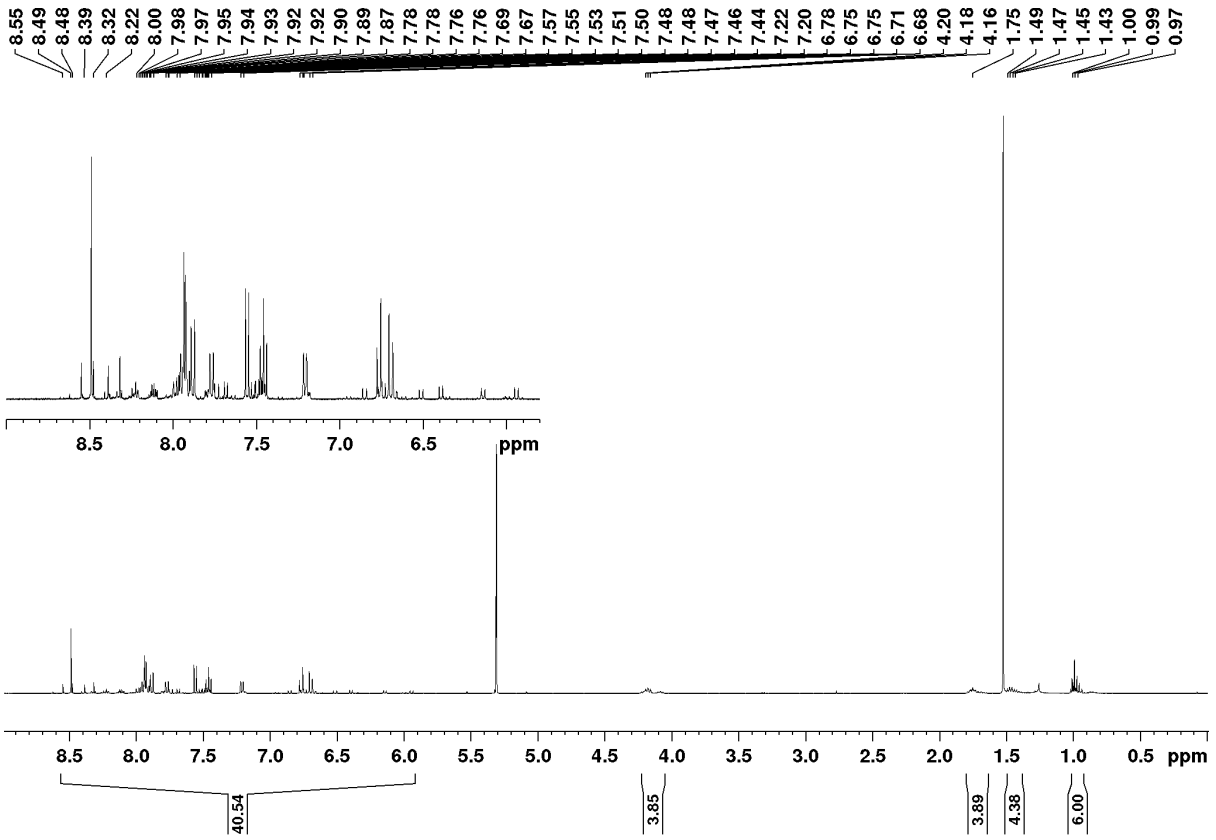

Figure 84 ^{1}H-NMR spectrum of **6a** in CD_2Cl_2 recorded at 295 K.

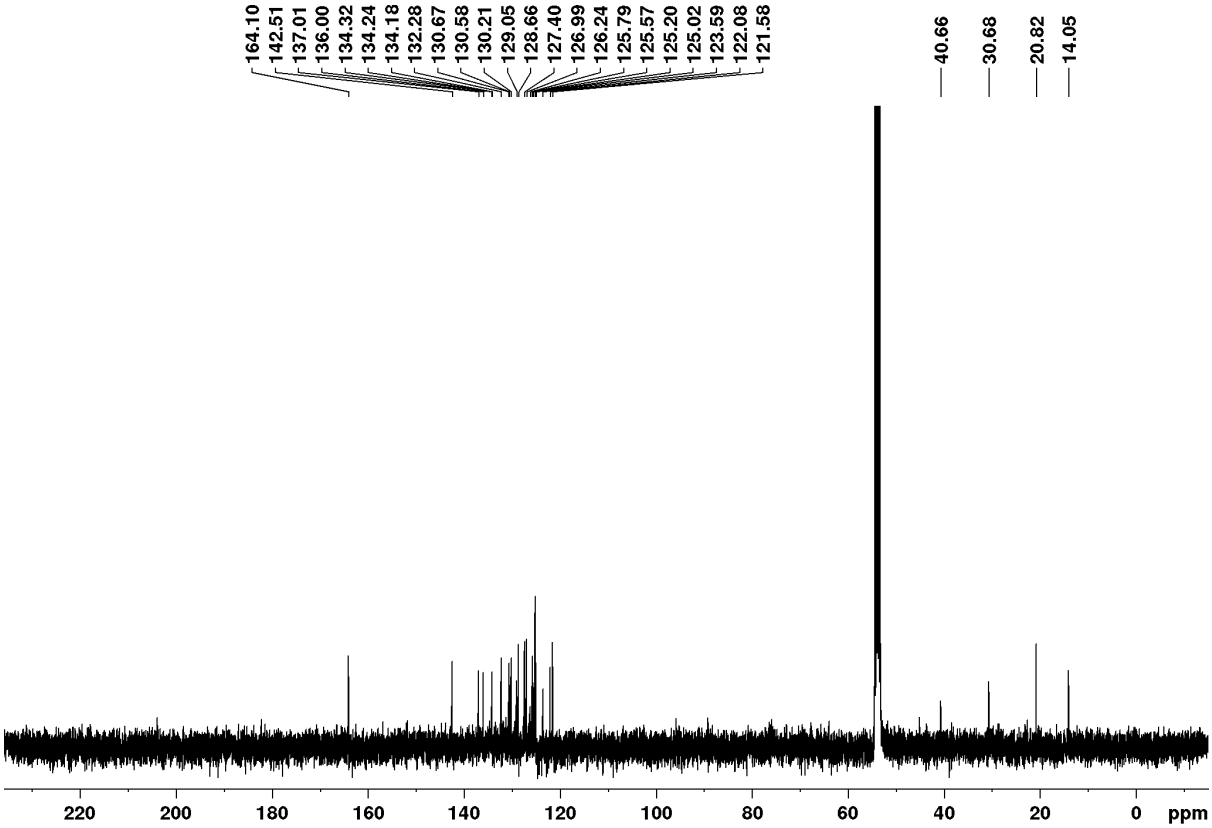

Figure 85 ^{13}C-NMR spectrum of **6a** in CD_2Cl_2 recorded at 295 K.

Chapter 5

Substituent-Dependent Absorption and Fluorescence Properties of Perylene Bisimide Radical Anions and Dianions

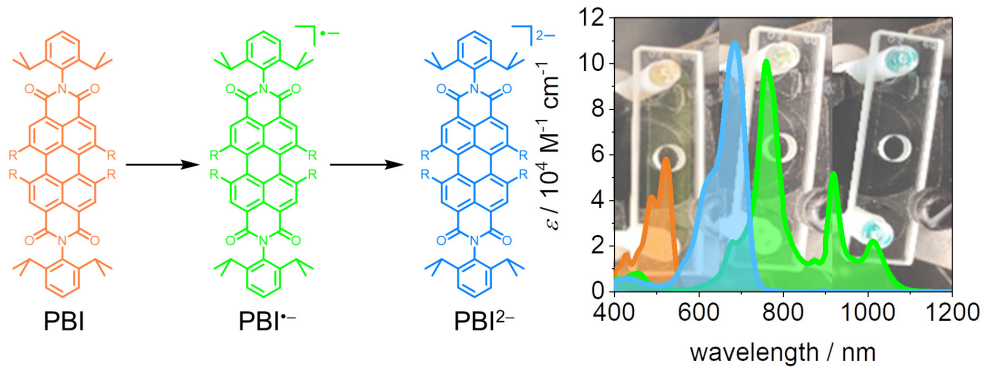

This chapter and the corresponding supporting information has been published:

R. Renner, M. Stolte, J. Heitmüller, T. Brixner, C. Lambert, F. Würthner, *Mater. Horiz.* **2021**, https://doi.org/10.1039/D1MH01019K.

Adapted or reprinted with permission from Ref. [263].

Abstract: Perylene-3,4:9,10-bis(dicarboximides) (PBIs) rank among the most important functional dyes and organic semiconductors but only recently their radical anions and dianions attracted interest for a variety of applications. Here, we systematically elucidate the functional properties (redox, absorption, emission) of five PBI anions and dianions bearing different *bay* substituents attached to the chromophore core. Cyclic voltammetry measurements reveal the influence of the substituents ranging from electron-withdrawing cyano to electron-donating

phenoxy groups on oxidation and reduction potentials that relate to HOMO and LUMO levels ranging from −7.07 eV to −6.05 eV and −5.01 eV to −4.05 eV, respectively. Spectroelectrochemical studies reveal a significant number of intense absorption bands in the NIR-spectral range (750 – 1400 nm) for the radical anions, whereas the dianionic species are characterized by similar spectra as those for the neutral dyes, however being bathochromically shifted and with increased molar extinction coefficients of approximately 100000 M^{-1} cm^{-1}. The increase of the transition dipole moment is up to 56% and accompanied by an almost cyanine-like red-shifted (by 300 nm) absorption spectrum for the most electron-poor tetracyanotetrachloro PBI. Whilst the outstanding fluorescence properties of the neutral PBIs are lost for the radical anions, an appreciable near-infrared (NIR) fluorescence with quantum yield up to 18% is revealed for the dianions by utilization of a custom-built flow-cell spectroelectrochemistry setup. Time-dependent density functional theory calculations help to assign the absorption bands to the respective electronic transitions.

5.1. Introduction

About 100 years ago, perylene-3,4:9,10-bis(dicarboximide) (PBI) dyes firstly attracted attention as vat dyes and later on as industrial pigments.[211,264,265] When used as vat dyes, the water-insoluble PBI pigment is reduced to the soluble leuco form, corresponding to an anionic species, which can be processed easily in textile or paper dying and other applications. Upon exposure of this reduced species to air the dye is re-oxidized, similar as for indigo,[266] giving the colored fabric.[213] Due to the straightforward adjustability of optical (absorption, emission) and electronic (ionization potential, electron affinity) properties of PBIs by substitution, a large variety of PBI derivatives has been developed in particular during the last decade.[13,214] By this means, more sophisticated optoelectronic applications of PBIs emerged in n-channel organic field effect transistors (OFETs),[146,219] ion batteries,[267] electrocatalytic reduction of oxygen to hydrogen peroxide,[268] organic light emitting diodes (OLEDs)[221, 269] and in organic photovoltaics (OPVs).[38,270] These applications, similar to the vat dying process, rely on the electron-deficient character of the PBI core and the formation of comparably stable delocalized radical anions and dianions upon the addition of electrons.[271-273] Likewise, PBIs enjoy great popularity as acceptor components in molecular dyads due to the formation of stable and spectroscopically characteristic anionic species.[274-276] More recently, the use of PBI radical anions and dianions generated by photoexcitation in the presence of triethylamine was further demonstrated as photosensitizer, catalyzing the dehalogenation reaction of a broad variety of aryl halides, further revealing the versatile applicability of the robust reduced PBI species.[277,278] Investigations by transient absorption (TA) spectroscopy proved the efficient photoinduced electron transfer from the excited doublet state of the PBI radical anion to electron acceptors.[279,280] This characteristic of PBIs and related rylene bisimides might be further utilized in the development of new photosensitizers as catalysts for reactions, which would otherwise need highly negative potentials. In this regard Xie and coworkers could just recently demonstrate the stepwise reduction of a PBI dye under irradiation, used for the injection of an electron into TiO_2 nanoparticles coated with platinum as co-catalyst, which could be used for the efficient reduction of water into hydrogen.[281]

Chemical reduction of PBIs remains a field to be further explored, as reports are relatively scarce due to the ambient instability of most reduced PBIs. Accordingly, most anions and dianions reported in literature are generated *in situ* electrochemically or chemically by the reduction with sodium dithionite in deoxygenated water, affording stable solutions for months due to the delocalized aromatic character of these PBI dyes.[271,273,282] Unfortunately, these

species cannot be easily isolated from solution. The first report of an isolated and completely characterized, albeit zwitterionic radical anion which is stable under ambient conditions shows the feasibility of the generation of isolable PBI radical anions in general.[216] This organic zwitterion can be considered as a PBI radical anion, which is stabilized by a σ-bonded imidazolium cation. Furthermore, it can be reduced and oxidized further by titration with tetrabutylammonium fluoride or nitrosyl tetrafluoroborate, respectively. In the same year, an extremely electron-poor PBI, having chlorine atoms attached in *bay* as well as cyano groups in *ortho* positions was isolated and characterized by single crystal X-ray diffraction.[283] Reduction of this molecule with palladium on activated charcoal, hydrogen and sodium hydrogen carbonate gave the PBI dianion disodium salt, which was stable even under ambient conditions for months.[283] In the following years, more examples of ambient stable radical anions and dianions have been reported, using more moderate reducing agents like potassium carbonate in DMF[284,285] or tetraphenylphosphonium iodide.[286]

Usually, characterization of the reduced species remains scarce and only qualitative UV/Vis/NIR absorption spectra of the neutral as well as reduced species are reported, while insights into emission properties are missing. Recently, after Rybtchinski's first observation of fluorescence for the parent core-unsubstituted PBI dianion,[282] we were able to disclose the first example for a fluorescence spectrum for the dianion of a tetraphenoxy-substituted PBI, utilizing a flow-cell setup which enabled the investigation of the emission as well as femtosecond and coherent two-dimensional (2D) electronic spectroscopy measurements.[287] The latter technique indeed points at another major application of PBI dyes as acceptors in donor-acceptor dyads. Here, PBIs are preferred acceptors due to the characteristic signature of the PBI radical anion bands in the NIR spectral range.[288] However, whilst TA signatures can be easily assigned for those PBIs that have been characterized by spectroelectrochemistry, they are not available for the vast majority of core-substituted PBIs that could be of value for such studies due to the tunability of their redox properties. Because until now, a concise series of PBIs with a systematic variation of their redox properties has been missing, we herein investigate PBIs in the neutral as well as in their radical anion and dianion states for a consistent series of five PBI dyes bearing the 2,6-diisopropylphenyl imide substituent and different *bay* substituents by electrochemical and spectroelectrochemical measurements. Further, we also investigate the emission properties for the dianions of this series of PBIs. Within our series, the respective first reduction potential varies by about 1 eV and also comprises planar as well as heavily twisted chromophores. Furthermore, (time-dependent) density functional theory ((TD-)DFT)

calculations have been performed to systematically assess the origin of the observed molecular properties and spectral features of the differently charged species.

5.2. Results and Discussion

5.2.1. Molecular Design and Chemical Reduction

Five PBIs have been chosen for the investigation of their molecular properties in their neutral as well as reduced states. Three of them (**PBI-Cl**, **PBI-H**, **PBI-OPh**) are commonly applied as organic semiconductors[225, 289 - 291] or fluorescent dye derivatives[215] whilst the two others complement the series based on a comparably very high reduction potential (**PBI-ClCN**)[283] and a fixed helical twist (**PBI-Ph**)[40] that seems to be important for the successful application of these PBIs as non-fullerene acceptors in OPV (Figure 86a).[292,293] For all derivatives, the bulky 2,6-diisopropylphenyl (Dipp) has been chosen as imide residue to prevent aggregation and ensure a high solubility.

Generally, either chemical reduction, photoinduced electron transfer or electrochemical reduction can be used to obtain the reduced species of PBIs. Advantageous of the former method would be the straightforward measurement of the desired species by a variety of techniques without the need of elaborate setups due to different measurement geometries and accordingly we first pursued with the reduction with KC_8 in THF.[294] As the stoichiometric addition of the reducing agent did not give the desired dianions, an excess of up to four equivalents of the reducing agent was used. The reaction could be monitored by the naked eye, due to prominent changes of the colored PBI solutions. Upon the addition of 18-crown-6 to the solution, the reaction was significantly accelerated. All obtained products could be dissolved in 1,2-difluorobenzene for the measurement of UV/Vis/NIR absorption spectra. However even under inert conditions, the oxidation of the generated dianions into the radical anions was observed (Figure 96). The increased stability of the radical anions compared to the dianions is quite remarkable and has already been observed for other organic radical anions.[294,295] As the stability of the dianions for hours in solution would be necessary for the full characterization of their optical properties, this reduction method did not provide the needed species with sufficient selectivity. Furthermore, the spectra could only be measured in the rather exotic solvent 1,2-difluorobenzene due to an even more pronounced instability in other solvents. As more common solvents like dichloromethane or chloroform are desirable to be more comparable to literature

reported TA spectra, we focused our attention on the electrochemical reduction to spectroscopically characterize the radical anions and dianions of all PBIs.

5.2.2. Cyclic and Square Wave Voltammetry

The redox properties of the PBI series have been investigated by cyclic voltammetry (CV) and square wave voltammetry (SWV) under identical experimental conditions in dichloromethane (DCM) using tetrabutylammonium hexafluorophosphate (TBAHFP) as electrolyte. The SW voltammograms as well as a schematic diagram of the electrical band gaps are depicted in Figure 86b,c and the half-wave potentials and calculated HOMO and LUMO potentials are listed in Table 14 (Figure 93-95).

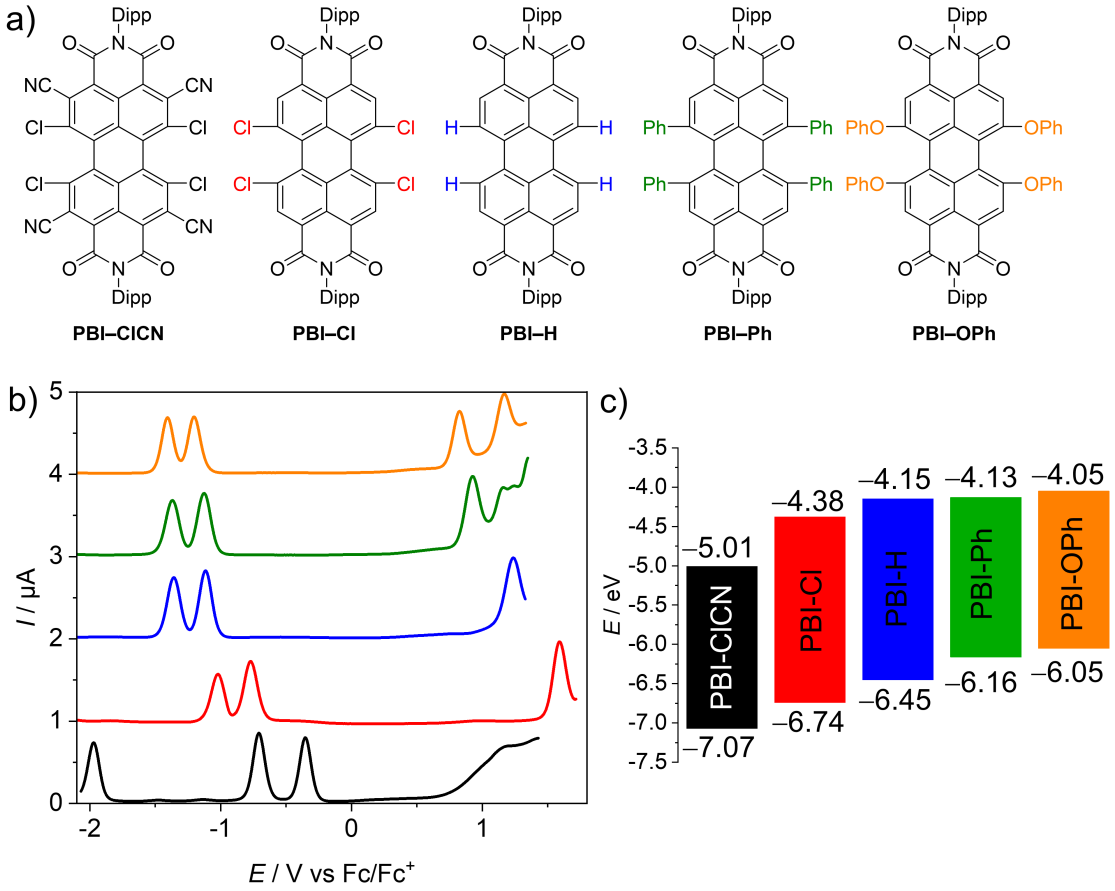

Figure 86 a) Molecular structures of the PBIs investigated by electrochemical reduction. b) Square wave voltammograms of **PBI-ClCN** (black), **PBI-Cl** (red), **PBI-H** (blue), **PBI-Ph** (green) and **PBI-OPh** (orange). Measurements were performed using DCM solutions ($c_0 = 2 \cdot 10^{-4}$ M) at room temperature, using TBAHFP (0.1 M) as electrolyte (scan rate 100 mV s^{-1}, SW amplitude 25 mV, SW frequency 15 Hz). c) Schematic diagram of the electrical band gaps of the investigated PBIs (energy level of Fc/Fc^+ with respect to the vacuum level = –5.15 eV).

At least two reversible reduction waves are observed for all five derivatives. Values range from –0.14 V for the first reduction and –0.48 V for the second reduction of the strongest electron acceptor **PBI-ClCN**, which are in line with reported values for a derivative thereof,[283]

to −1.10 V and −1.29 V for the first and second reduction wave, respectively, for the weakest electron acceptor **PBI-OPh**.[241] The other derivatives follow the expected sequence by exhibiting their first reduction wave at −0.77 V for **PBI-Cl**, −1.00 V for **PBI-H** and −1.02 V for **PBI-Ph**, respectively. The potentials of the second reduction wave follow the same trend with values of −1.02 V, −1.22 V and −1.25 V for the latter three PBIs, respectively. Interestingly, the first and second reduction potentials of the planar **PBI-H** and the heavily twisted **PBI-Ph** are very similar, indicating the comparably small influence of a directly attached aryl unit compared to stronger electron withdrawing groups like halogens or electron donating aryloxy groups on the electronic properties of the molecule. Integration of the first and second reduction peaks in the SW spectra proved that the ratio of the electronic quantity of the reduction processes from PBI to $PBI^{\bullet-}$ and $PBI^{\bullet-}$ to PBI^{2-} is one, substantiating the nature of the proposed reduced species. A third reversible reduction wave at −1.73 V could only be observed for **PBI-ClCN**, accentuating the electron deficiency of this derivative due to the additional cyano groups in *ortho* position.

Table 14 Summary of the redox properties of the investigated PBIs. Half-wave potentials were determined by CV or SWV measurements in DCM (0.1 M TBAHFP) vs. Fc/Fc^+ at room temperature.

	$E_{1/2}^{\text{Red 1}}$ [V]	$E_{1/2}^{\text{Red 2}}$ [V]	$E_{1/2}^{\text{Red 3}}$ [V]	$E_{1/2}^{\text{Ox 1}}$ [V]	$E_{1/2}^{\text{Ox 2}}$ [V]	E_{HOMO} [eV][b]	E_{LUMO} [eV][b]	$\Delta E_{\text{gap}}^{\text{CV}}$ [eV]	$\Delta E_{\text{gap}}^{\text{Opt}}$ [eV]
PBI-ClCN	–0.14	–0.48	–1.73	-[a]	-[a]	–7.07[c]	–5.01	2.06	2.13[d]
PBI-Cl	–0.77	–1.02	-[a]	+1.59	-[a]	–6.74	–4.38	2.36	2.21
PBI-H	–1.00	–1.22	-[a]	+1.30	-[a]	–6.45	–4.15	2.30	2.26
PBI-Ph	–1.02	–1.25	-[a]	+1.01	+1.19	–6.16	–4.13	2.03	1.82
PBI-OPh	–1.10	–1.29	-[a]	+0.90	+1.21	–6.05	–4.05	2.00	1.99

[a] not observed; [b] Calculated according to literature known procedure using the experimentally determined redox potentials ($E_{\text{HOMO}} = -[E_{1/2}^{\text{Ox 1}} + 5.15\ \text{eV}]$ and $E_{\text{LUMO}} = -[E_{1/2}^{\text{Red 1}} + 5.15\ \text{eV}]$) and the energy level of Fc/Fc^+ with respect to the vacuum level (−5.15 eV);[38] [c] Calculated according to $E_{\text{HOMO}} = E_{\text{LUMO}} - E(\lambda_{\text{max}})$. [d] optical band gap higher than electronic band gap probably due to distortion of the band shape due to the overlap of different transitions. Elaborate calculations taking correction factors into account can be found in Table 16 and Table 17.

The effect of the substituents on the redox potentials is even more pronounced for their respective oxidation processes.[241] Due to the highly electron-deficient character of **PBI-ClCN**, no oxidation could be observed within the available potential range of the used electrolyte system, whereas one oxidation process is observed at +1.59 V and +1.30 V for **PBI-Cl** and **PBI-H**, respectively. Due to the shift of the oxidation waves to lower potentials, two oxidations are observable for the other two PBIs at +1.01 V and +1.19 V for **PBI-Ph** and +0.90 V and +1.21 V for **PBI-OPh**. The values are summarized in Table 14. The HOMO and LUMO energy

levels have been calculated from the half-wave potential of the first oxidation and reduction process, which were obtained by the CV measurements with the energy level of the ferrocene/ferrocenium redox couple set to −5.15 eV vs. vacuum.[38] They cover a broad range of almost 1 eV within this series between −7.07 eV and −6.05 eV for the HOMOs and −5.01 eV and −4.05 eV for the LUMOs for **PBI-ClCN** and **PBI-OPh** (Figure 86c), respectively. Notably, **PBI-ClCN** ranks according to this analysis among the most electron-deficient π-cores, comparable to tetracyanoquinodimethane (TCNQ).[217,296]

5.2.3. UV/Vis/NIR Absorption Properties in Neutral and Reduced States

The UV/Vis/NIR absorption spectra of the neutral, radical anionic and dianionic PBIs in DCM could be obtained by electrochemical reduction in situ with a custom built spectroelectrochemical cell and are depicted in Figure 87 and the derived data are collected in Table 15 (for details see Figures 98-107, Table 18). The optical band gap calculated with the help of the absorption spectra of the neutral species and extrapolation by a linear curve (Tauc's plot)[297] is in all cases, except **PBI-ClCN**, lower in energy than the electrical band gap, which is expected since the threshold for the absorption of photons is smaller than the threshold for the creation of an electron-hole pair.[298]

In accordance with earlier results for this and related PBIs,[264] the unsubstituted planar **PBI-H** exhibits an intense absorption band of the S_0-S_1 transition with vibronic progression with an absorption maximum (λ_{max}) at 527 nm and a high molar extinction coefficient (ε_{max}) of 93700 M^{-1} cm^{-1} in DCM. Upon substitution in *bay* position, as it is the case for all other derivatives within this series, the spectra become more broadened, show a decrease in ε_{max} and the vibronic progression of the S_0-S_1 transition is less clearly visible. Furthermore, the S_0-S_2 transition, which is symmetry forbidden for the planar chromophore[199] becomes allowed and can be observed as a second absorption maximum at about 440 nm. This effect is most pronounced for **PBI-Ph**, that constitutes the most twisted chromophore.[40] The attachment of electron withdrawing halogen atoms in *bay* position does not exhibit a large influence on the absolute position of the absorption maximum (**PBI-Cl** 522 nm; **PBI-ClCN** 531 nm) whereas the more electron donating groups like tetraaryl (**PBI-Ph** 609 nm) or tetraaryloxy (**PBI-OPh** 576 nm) afford a significant redshift, reflecting electronic interactions, i.e., electron donation from the *bay* substituents to the PBI core.[203]

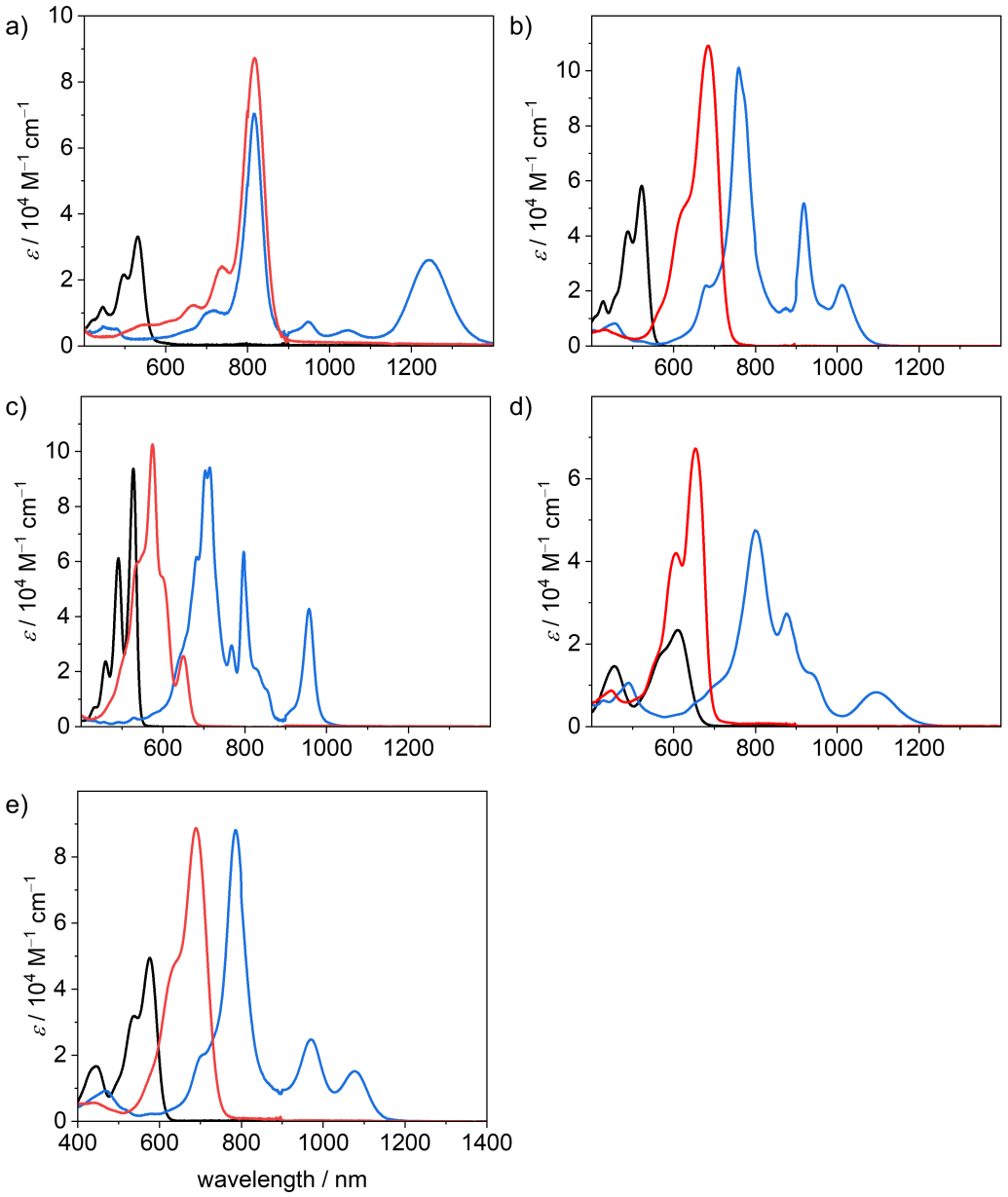

Figure 87 UV/Vis/NIR absorption spectra of the neutral (black), radical anionic (blue) and dianionic (red) PBI species of a) **PBI-ClCN**; b) **PBI-Cl**; c) **PBI-H**; d) **PBI-Ph**; and e) **PBI-OPh** measured in DCM ($c_0 = 4 \cdot 10^{-4}$ M) at room temperature using TBAHFP (0.1 M) as electrolyte.

Under the influence of an electrochemical potential between –0.1 and –1.2 V, significant spectral changes occur for all PBI dyes in DCM. All radical anions exhibit multiple characteristic spectral features in the UV/Vis/NIR region, each with a prominent and broad absorption band at 957 nm or above (**PBI-H**), which is commonly assigned to the D_0-D_1 transition (*vide infra*).[299] In case of **PBI-ClCN** this NIR transition appears at 1243 nm, followed by **PBI-Ph** (1097 nm), **PBI-OPh** (1076 nm) and **PBI-Cl** (1011 nm) (Figure 87). The absorption spectra in the UV/Vis/NIR region of all five radical anions exhibit at least three clearly distinguishable transitions. The most prominent absorption band is also bathochromically shifted with respect to that of the neutral PBIs and is found for all derivatives

between 715 nm for the unsubstituted **PBI-H** and 817 nm for **PBI-ClCN**. Whereas the electron withdrawing groups exert only a minor influence on the wavelength of the lowest energy absorption band in the neutral state, they affect those of all absorption bands in the radical anionic state in a similarly pronounced way as the electron donating substituents. Furthermore, different from **PBI-H** with an almost unchanged ε_{max} value of 94100 M^{-1} cm^{-1} upon reduction to the radical anion, significant increase between 174% (**PBI-Cl**, 101100 M^{-1} cm^{-1}) up to 212% (**PBI-ClCN**, 70300 M^{-1} cm^{-1}) in ε_{max} is found for the main absorption band of all *bay* substituted derivatives. Additionally, at least one further transition can be observed between the absorption maximum for the most intense band and the lowest energy absorption band of the radical anions.

Table 15 Summary of the absorption and emission properties of the investigated PBIs and their electrochemical generated dianions measured in DCM (0.1 M TBAHFP) at room temperature.

	λ_{max} [nm]	ε_{max} [M^{-1} cm^{-1}]	μ_{eg} [D]	λ_{em} [nm][a]	$\Delta\tilde{\nu}_{Stokes}$ [cm^{-1}]	Φ_f [%][b]	τ_F [ns][c]
PBI-ClCN	531	33900	-[d]	575	1510	0.1	0.15, 2.10
PBI-ClCN^{2-}	817	87200	-[d]	-[e]	-[e]	-[e]	-[e]
PBI-Cl	522	58200	8.7	549	940	57	5.06
PBI-Cl^{2-}	684	109100	12.6	722	770	3	2.04
PBI-H	527	93700	8.8	534	210	99	3.72
PBI-H^{2-}	574	102600	3.5	662	300	18	5.92
PBI-Ph	609	23400	6.4	677	1650	46	10.87
PBI-Ph^{2-}	653	67300	10.0	676	520	15	4.36
PBI-OPh	576	49600	8.7	608	915	96	6.01
PBI-OPh^{2-}	689	88700	12.4	738	960	17	3.93

[a] Fluorescence spectra of PBI^{2-} have been measured in front-face geometry (22.5°) and all spectra are corrected against the photomultiplier sensitivity and the lamp intensity; [b] Fluorescence quantum yields of the neutral PBIs were determined using the dilution method (OD < 0.05) and *N*,*N*'-bis(2,6-diisopropylphenyl)-perylene-3,4:9,10-bis(dicarboximide) (Φ_f = 1.00 in $CHCl_3$) or *N*,*N*'-bis(2,6-diisopropylphenyl)-1,6,7,12-tetraphenoxy-perylene-3,4:9,10-bis(dicarboximide) (for **PBI-OPh**, Φ_f = 0.96 in $CHCl_3$)[215] as reference. Fluorescence quantum yields of PBI^{2-} were determined relative to PBI by excitation at 385 nm (**PBI-Cl**), 415 nm (**PBI-H**), 490 nm (**PBI-Ph**) and 398 nm (**PBI-OPh**); [c] Fluorescence lifetimes were determined with EPL picosecond pulsed diode lasers for time-correlated single photon counting (λ_{ex} = 530 nm (**PBI-ClCN**), λ_{ex} = 550 nm (**PBI-Cl**, **PBI-H**, **PBI-OPh**), λ_{ex} = 560 nm (**PBI-Ph**), λ_{ex} = 725 nm (**PBI-Cl^{2-}**), λ_{ex} = 662 nm (**PBI-H^{2-}**), λ_{ex} = 725 nm (**PBI-Cl^{2-}**), λ_{ex} = 677 nm (**PBI-Ph^{2-}**), λ_{ex} = 735 nm (**PBI-OPh^{2-}**)); [d] Significant overestimation due to multiple transitions present in the S_0-S_1 absorption band; [e] Not observed

For the unsubstituted derivative **PBI-H**, even more distinguishable absorption features than for the other PBIs are found, which originate from the more rigid and planar π-scaffold, similar to

the neutral species. These intense and characteristic absorption bands make the here investigated PBI derivatives particularly valuable for the investigation of photoinduced electron transfer processes in molecular dyads as well as solid state materials.[300]

Upon further reduction at a bias between −0.4 and −1.3 V, the absorption spectra of all PBI dianions simplify to one prominent absorption band that is located between 650 and 900 nm. This hypsochromic shift with respect to the NIR bands of the radical anion species is accompanied by an additional increase in band intensity. Thus, the values for ε_{max} increase further for all derivatives to more than 100000 M^{-1} cm^{-1} in case of **PBI-Cl** (684 nm) and **PBI-H** (574 nm) and to more than twice the intensity of the respective neutral species in case of **PBI-Ph** (67300 M^{-1} cm^{-1} at 653 nm) and **PBI-ClCN** (87200 M^{-1} cm^{-1} at 817 nm). Surprisingly, only the dianion of the parent **PBI-H** displays an optical spectrum of rather different shape with a transition at 649 nm of lower intensity (25600 M^{-1} cm^{-1}) followed by a strong absorbing and structured absorption spectrum at about 570 nm. The increase in tinctorial strength for these PBI dianions is indeed remarkable. Integration of the respective isolated longest wavelength S_0-S_1 absorption bands of the neutral and the dianionic species shows again an increase in the transition dipole moments μ_{eg} from 8.7 to 12.6 D (**PBI-Cl**), 6.4 to 10.0 D (**PBI-Ph**) and 8.7 to 12.4 D (**PBI-OPh**) for all derivatives except **PBI-H**, where it decreases from 8.8 to 3.5 D (Table 15). Some of these values might be overestimated due to the presence of multiple transitions in the respective S_0-S_1 absorption band (*vide infra*).

5.2.4. Fluorescence Properties in the Neutral and Dianionic State

The fluorescence spectra, fluorescence quantum yields (Φ_F) as well as fluorescence lifetimes (τ_F) of the five neutral PBIs and four dianionic PBIs could be obtained within a SEC flow-cell setup (Figure 88, Table 15, Figure 97b, 109-111). As expected, all radical anions showed no emission. The Φ_F of the dianions were determined relative to the respective neutral species within one SEC run while the fluorescence decay curves were recorded by time-correlated single-photon counting (TCSPC) in front-face geometry (22.5°). All emission spectra of the neutral and dianionic PBIs show mirror-like shape with respect to their corresponding absorption spectra, with the exception of **PBI-Ph^{2-}** which exhibits an unexpected narrow fluorescence band with a well-defined vibronic progression. All *bay* substituted PBIs show almost equal (**PBI-OPh^{2-}**) or even decreased Stokes shifts ($\Delta\tilde{\nu}_{Stokes}$) in their dianionic state, while the unsubstituted **PBI-H** exhibited a slight increase from 210 cm^{-1} (PBI) to 300 cm^{-1} (PBI^{2-}), which is still smaller than $\Delta\tilde{\nu}_{Stokes}$ of the other derivatives due to the more rigid

framework and lack of substituents. The same holds true for τ_F, which is increased again only for **PBI-H** from 3.72 ns (PBI) to 5.92 ns (PBI^{2-}), while it is decreased in all other derivatives upon reduction.

The Φ_f of all dianions are significantly reduced as expected for the emission due to the decreased band gap[14] but are still appreciably high with 18% at 662 nm (**PBI-H^{2-}**) and 17% at 738 nm (**PBI-OPh^{2-}**) compared to e.g. higher rylene dyes emitting in the region between 650 and 950 nm.[301,302] For **PBI-Cl^{2-}** an emission maximum at 722 nm, with reduced $\Delta\tilde{\nu}_{Stokes}$ of 770 cm^{-1} and the most pronounced decrease of the quantum yield within this series is noted from 57% (PBI) to 3% (PBI^{2-}). **PBI-Ph** exhibits a large $\Delta\tilde{\nu}_{Stokes}$ of 1650 cm^{-1} affording λ_{em} of 677 nm. This indicates the participation of the core-substituents in the lowest excited state upon photoexcitation and following structural relaxation.[275] Interestingly, the Φ_f of the arylated dye does not decrease as significantly upon reduction as the other derivatives, from 46% of the neutral **PBI-Ph** to 15% for **PBI-Ph^{2-}**. Together with the structured fluorescence spectrum such high quantum yield corroborates the rigidification effect impaired by the four phenyl units that are interlocked based on crystallographic evidence from related chromophores.[210] The neutral **PBI-ClCN** exhibits only very weak fluorescence upon excitation at 490 nm, with a λ_{em} at 575 nm and a Φ_f of merely 0.1%. Because this is much lower than the reported quantum yield of 11% of the neutral congener with electron-withdrawing fluoroalkyl chains in imide position we attribute the fluorescence quenching to a photo-induced electron transfer from the Dipp substituent into the highly electron-deficient core.[303] Similar processes have been reported for more electron-rich imide substituents to the parent electron-poor PBI.[275,304]

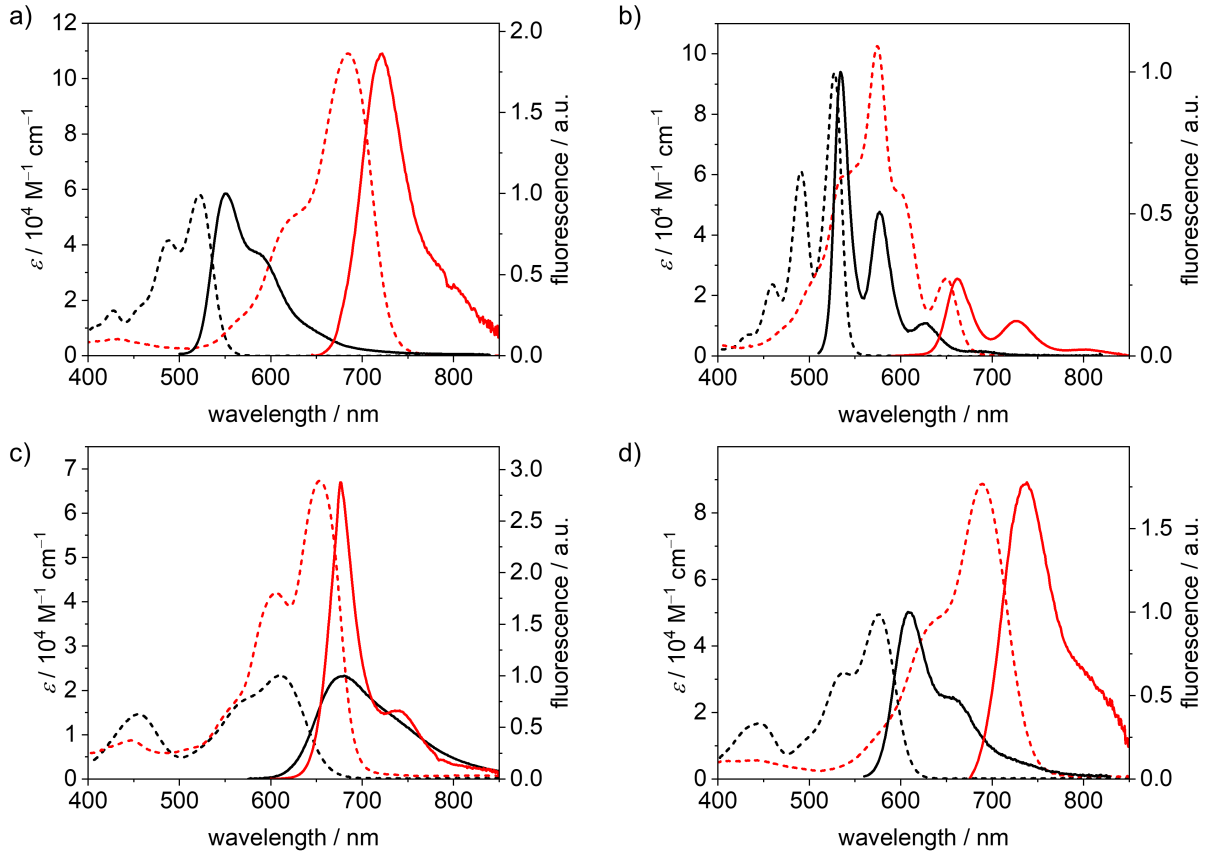

Figure 88 UV/Vis/NIR absorption spectra (dashed line) as well as the fluorescence spectra (solid line) of the neutral (black) and dianionic (red) a) **PBI-Cl**, b) **PBI-H**, c) **PBI-Ph** and d) **PBI-OPh** measured in DCM (c_0 = $4 \cdot 10^{-4}$ M for absorption, c_0 = $1 \cdot 10^{-5}$ M for fluorescence of PBI and c_0 = $1 \cdot 10^{-4}$ M for fluorescence of PBI^{2-}) at room temperature using TBAHFP (0.1 M) as electrolyte.

The decrease of Φ_F upon reduction for all derivatives can be ascribed to an increase of the rate of non-radiative decay processes, as expected due to the smaller band gap for the dianionic state.[305] The trend observed in τ_F corresponds to the trend obtained for the natural lifetimes τ_0 by analysis according to the Strickler-Berg relationship.[306] For **PBI-H**, τ_0 is slightly increased in the dianion (3.64 ns to 3.75 ns), while for the other three derivatives **PBI-Cl** (5.14 ns to 4.50 ns), **PBI-Ph** (17.5 ns to 5.08 ns) and **PBI-OPh** (6.89 ns to 5.22 ns) τ_0 is decreased in the measured reduced state of the molecules due to the increase of the transition dipole moment and oscillator strength. The radiative decay rates k_r obtained by this analysis nevertheless decrease in all derivatives upon reduction, while the non-radiative decay rates k_{nr} are increased, confirming the experimental results of the decreasing quantum yields in the PBI dianions.

5.2.5. Theoretical Investigations

In order to further elucidate the trends observed by optical spectroscopy upon electrochemical reduction, (time-dependent) density functional theory ((TD-)DFT) calculations were

performed. For simplicity, the imide residues were replaced by methyl groups, as their impact on the molecular properties of the chromophore is negligible.[212]

The geometry-optimized structures of all derivatives with the exception of **PBI-H** exhibit a large twist of the two naphthalene subunits between 31.0° (**PBI-OPh**) and 39.5° (**PBI-ClCN**). This results in a distortion of the PBI π-MO system. In all derivatives the LUMO of the neutral PBI, the SOMO of the radical anion ($PBI^{\bullet-}$) and the HOMO of the dianion (PBI^{2-}) are visually indistinguishable and thus in Figure 89 (Figure 113-114) only the MOs of the neutral PBI are shown.

As depicted in Figure 89d for the tetrachlorinated **PBI-Cl** there are significant changes in bond length upon reduction from the neutral to the dianionic state. Whilst the changes in bond length are comparably minor for the inner bonds of the perylene (<3 pm), the conjugated outer perimeter experiences a significant alteration where bonds either get shorter by up to 3.8 pm from 148.5 pm to 144.7 pm or longer by up to 3.4 pm from 138.0 pm to 141.4 pm. This change in bond length relates to a reversal of single versus double bond character that is in accordance with the bonding character between the involved atoms in the LUMO (Figure 89b). As a consequence, the PBI skeleton of **PBI-Cl** (and likewise the other derivatives) is contracted by about 66 pm along the long molecular axis upon twofold reduction and expanded by about 57 pm along the short axis. It is interesting to relate these bond length alterations to the carbon-carbon bond stretching vibration that occurs upon photoexcitation of PBI into the S_1 state, i.e., promotion of an electron from the HOMO into the LUMO, and that causes the characteristic vibronic progression in the absorption and fluorescence bands of PBIs. The most striking change of bond length concerns the bonds connecting the two naphthalene subunits, e.g., in the tetrachlorinated **PBI-Cl** from 146.8 pm for the neutral PBI via 144.8 pm for the radical anion to 143.1 pm in the dianion (Table 19). This decreased bond length in the dianion for the central connections between the naphthalene subunits as well as the bond length alterations for the peripheral C-C carbon chain is in accordance with calculations by Iron, Rybtchinski and co-workers for the unsubstituted PBI[271,282] and our experimental results by single-crystal X-ray analysis for a derivative of **PBI-ClCN**.[283] This corroborates a stiffening of the π-scaffold for the central ring and planarization of the PBI core with a reduction of the twist angle from 35.4° to 31° in **PBI-Cl** due to the additional electron density in the system (Table 19).

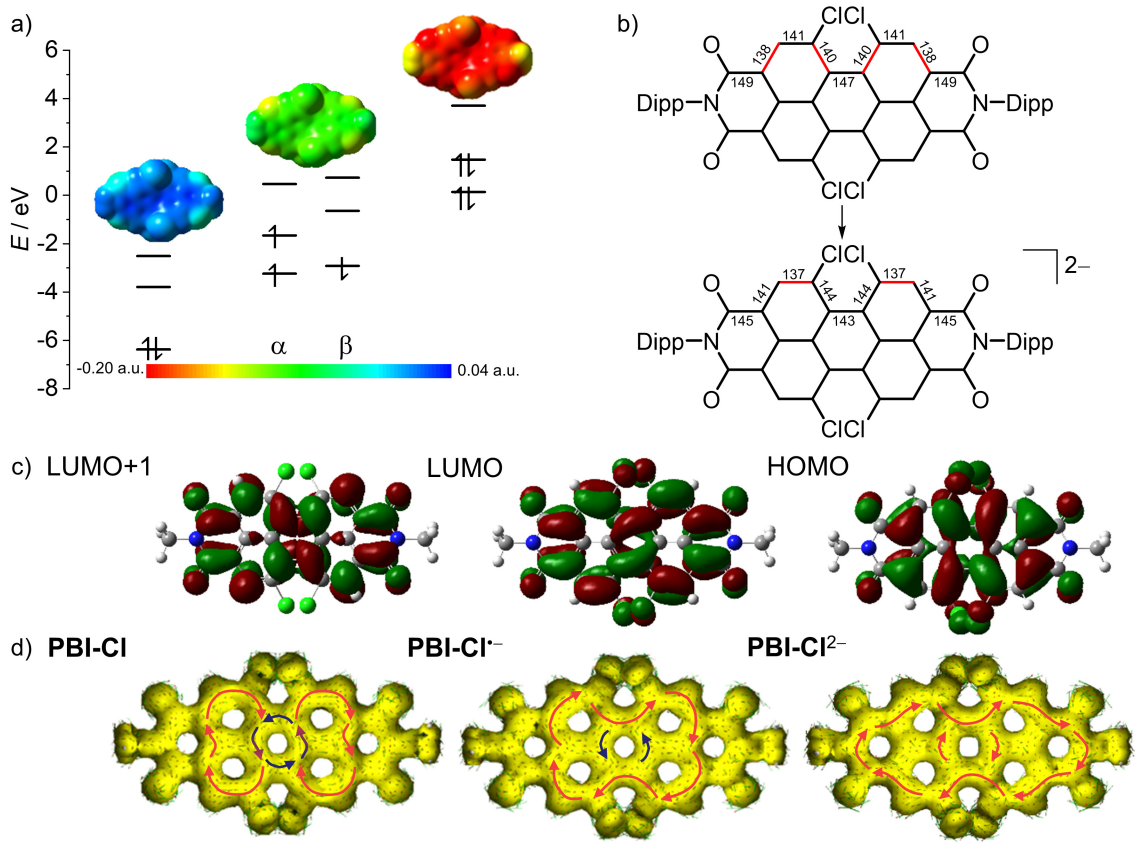

Figure 89 a) HOMO, LUMO and LUMO+1 levels as obtained from DFT calculations of **PBI-Cl** (left), the corresponding α- and β-spin MO levels of **PBI-Cl**$^{\bullet-}$ (middle) and HOMO–1, HOMO and LUMO levels of **PBI-Cl**$^{2-}$ (right), as well as the electrostatic potential maps of the respective derivative (top, isovalue 0.020 a.u.). b) Calculated bond length for perylene carbon-carbon bonds in neutral and dianionic state in pm (for details, see Table 19). Bonds drawn in red indicate a high double-bond character. c) HOMO, LUMO and LUMO+1 (bottom to top) of **PBI-Cl**. The corresponding orbitals of **PBI-Cl**$^{\bullet-}$ and **PBI-Cl**$^{2-}$ are visually indistinguishable. Orbitals and electrostatic potential maps were calculated using DFT (B3LYP/6-31g(d)). d) Calculated AICD isosurface plots of **PBI-Cl**, **PBI-Cl**$^{\bullet-}$ and **PBI-Cl**$^{2-}$. Clockwise ring current is depicted with red arrows and counter-clockwise ring current with blue arrows (isosurface value 0.025).

The transitions to the excited states obtained by TD-DFT calculations are in good accordance with the experimental results concerning the number and the intensities of the observed transitions (Figure 112, Table 20-34) While the calculated transition energies agree reasonably well with the neutral PBIs, e.g., **PBI-H** with 488 and 527 nm for the calculated and experimental spectra, respectively, they deviate in some examples of the radical anions and dianions quite severely. Nevertheless, the bathochromic shift of the radical anion spectra visible in all derivatives, as well as the subsequent hypsochromic shift of the most prominent transitions of the dianions is substantiated by the theoretical results. The calculated energies for the allowed optical transitions could be correlated to the respective experimental values well enough by shifting the whole spectrum, so that the transitions with the highest oscillator strength exhibits the same energy as the absorption maximum in the experimental absorption spectrum, allowing for an assignment of the individual absorption bands (Figure 112) with which some further conclusions could be made (*vide infra*).

According to the calculations, for the neutral state of the most electron-deficient **PBI-ClCN**, two transitions are quite close in energy around 570 nm and thus no clear separation thereof can be observed in the experimental spectra (Table 20). In the other three *bay* substituted derivatives, the bands of the experimental spectra could be assigned to the S_0-S_1 transition as well as the S_0-S_2 transition at slightly higher energies. In the planar unsubstituted **PBI-H**, only the S_0-S_1 transition exhibits a noteworthy oscillator strength, corresponding to former reports and the symmetry forbiddance of the S_0-S_2 transition.[203] Due to the spin-separated energy levels in the radical anionic state, the assignment of the transitions is more complex. In the *bay* chlorinated PBIs **PBI-ClCN** and **PBI-Cl** the SOMO-LUMO transition corresponds to the lowest-energy transition in the NIR region and thus can be assigned as D_0-D_1 transition. The same holds true for **PBI-OPh**. In the unsubstituted **PBI-H**, this transition causes the absorption band at 649 nm in the calculated spectrum, while the most bathochromically shifted absorption band corresponds to a transition of the electron from the highest occupied β-spin orbital to the lowest unoccupied β-spin orbital. In the tetraphenyl derivative **PBI-Ph**, the SOMO-LUMO transition corresponds to the absorption maximum at 679 nm while for the lowest-energy absorption band a similar transition of the electron in the β-MO as in **PBI-H** is found. The predictions for optically allowed transitions of PBI radical anions are probably less accurate than the predictions for the neutral and dianionic species due to the radical nature of the PBIs and the neglect of solvent effects.[271]

In the calculated transitions of the dianions, the HOMO-LUMO transition thereof corresponds to the lowest-energy transition in all derivatives except for **PBI-Cl** and **PBI-OPh**. For these two derivatives, the lowest-energy transition is not well described by simple HOMO-LUMO transition but rather by a HOMO-LUMO+1 transition, which suggests that the excitation energy is actually not equal to the HOMO-LUMO orbital energy difference. Thus, even though the calculations are of good assistance in the interpretation of the experimental spectra, the reality might be more complex. In accordance with the experimental UV/Vis/NIR spectrum of **PBI-H^{2-}**, the calculations predict a significantly smaller oscillator strength of 0.0938 for the S_0-S_1 transition than for the S_0-S_2 transition with 0.8905 (see Figure 87c and Table 28). The intensity of absorption bands relates to the oscillator strength or the transition dipole moment. Unfortunately, the experimental determination of the transition dipole moment (μ_{eg}) of some derivatives, especially in their reduced states, is not straightforward for this series of dyes due to significant overlap of different transitions thus overestimating the values significantly (*vide supra*). However, the values for μ_{eg} of neutral **PBI-Cl**, **PBI-H**, **PBI-Ph** and **PBI-OPh** could be determined by integration of the absorption band corresponding to the S_0-S_1 transition of the

experimental spectra to be 8.7 D, 8.8 D, 6.4 D and 8.7 D, which fits reasonably well with the values obtained from TD-DFT calculations of 7.6 D, 8.8 D, 6.6 D and 8.1 D, respectively (Table 35). Theoretical determination of μ_{eg} from the TD-DFT calculations for all species shows a decrease of the transition dipole moment for the lowest energy transition upon the first reduction of the PBIs with the exception of the directly arylated **PBI-Ph**, where μ_{eg} of the radical anion is increased compared to the neutral PBI. Upon further reduction to the dianion, a further increase of μ_{eg} is noted for all PBI dyes with values reaching above 9.0 D for most derivatives. Similar to the previous results (*vide supra*), the calculations predict μ_{eg} of all five neutral PBIs as well as their dianionic states reasonably well (Table 35).

The differences in oscillator strength of the first two transitions of **PBI-H^{2-}** compared to the *bay* substituted PBIs can be rationalized by investigation of the transition density (Figure 116). It can be seen that the transition density of the S_0-S_1 transition of **PBI-H^{2-}** is polarized along the short molecular axis and resembles the transition densities of the S_0-S_2 transitions of the four substituted PBI dianions. In contrast, the S_0-S_2 transition density of **PBI-H^{2-}**, which is polarized along the long molecular axis (*N*,*N*') exhibits a high oscillator strength in the absorption spectrum which is comparable to the S_0-S_1 transitions of the substituted PBI dianions, thus the two differently polarized transitions are interchanged in the planar PBI dianion compared to the *bay* substituted contorted systems.[307]

To further explore the aromaticity of the different reduced species, anisotropy of the induced current-density (AICD) calculations were performed for **PBI-Cl** and **PBI-H** as well as their respective reduced species.[308,309] In both neutral molecules, clockwise diamagnetic ring currents can be observed that are localized in the two naphthalene subunits, suggesting a Clar-type localization of aromaticity, while the central PBI ring exhibits a counter-clockwise paramagnetic ring current, indicating anti-aromaticity (Figure 89c, Figure 117). Upon reduction, the clockwise ring current expands over the whole PBI core along the outer perimeter and the counter-clockwise current in the centre vanishes. This reorganization of the π-electron delocalization has been elucidated before in a theoretical study by Iron and co-workers to explain the high stability of PBI dianions in water due to their increased aromatic character.[271] These results from AICD calculations match quite well to our earlier observations, i.e., the contraction of the bonds connecting the two naphthalene subunits due to increased conjugation and the increase of the absorption coefficients and bathochromic shifts of the absorption bands observed for PBI dianions.

5.3. Conclusion

In this article, the optical properties for a series of five perylene bisimide dyes bearing 2,6-diisopropylphenyl groups in imide position but different *bay* substituents on the π-core have been investigated upon their reduction into radical anion and dianion states in custom-built spectroelectrochemical cells for UV/Vis/NIR absorption and emission studies. Their first reduction potential ranges almost over 1 V from −0.14 V for the most electron-deficient **PBI-ClCN** to −1.10 V for the most electron-rich **PBI-OPh**. A significant bathochromic shift of all absorption spectra upon the first reduction with the most red-shifted maximum at 1243 nm (**PBI-ClCN**) was observed. Upon further reduction, the absorption maxima shift again back hypsochromically compared to the radical anionic spectra. The molar extinction coefficients ε_{max} increase in all derivatives upon reduction to approximately 100000 M^{-1} cm^{-1}, with absorption maxima between 649 nm (**PBI-H**) and 817 nm (**PBI-ClCN**) for the dianions. While fluorescence data of neutral PBI dyes are abundantly reported, we could study and quantify the fluorescence properties (Φ_f, τ_F, $\Delta\tilde{\nu}_{Stokes}$) of the dianions of the whole series in a custom-built flow-cell setup. While the fluorescence quantum yield was reduced for all PBI dianions, due to an increased influence of non-radiative decay pathways, values of up to 18% (662 nm) and 17% (738 nm) were retained for **PBI-H** and **PBI-OPh**, respectively. DFT and TD-DFT calculations assist in the elucidation of the origin of the experimentally observed absorption bands as well as structural changes of all PBIs and their reduced species. They showed a localization of the MOs on the perylene core rather than on the substituents for the relevant energetic states. Furthermore, the experimental spectra could be brought into line with the calculated absorption spectra. Overall, based on our comprehensive library of five PBIs, electronic and optical properties of their radical anions as well as their dianions could be characterized in a systematic manner. This information should be of great value for the analysis of PBI bearing molecular dyads and PBI-based solid-state materials by transient absorption spectroscopy as well as for the utilization of these dyes as sensitizers for photocatalysis.

5.4. Supporting Information for Chapter 5

5.4.1. General Methods

Unless otherwise stated, all chemicals, reagents and solvents were purchased from commercial suppliers and used after appropriate purification. *N*,*N'*-Bis(2,6-diisopropylphenyl)-1,6,7,12-tetraphenylperylene-3,4:9,10-bis(dicarboximide) was synthesized according to literature.[40] The solvents for the reduction and spectroscopic measurements were of HPLC grade and dried prior to use by an Innovative Technology PureSolv solvent purification system (DCM), by refluxing the solvent over sodium followed by distillation onto sodium (THF) or by refluxing the solvent over molecular sieves (4 Å, 1,2-difluorobenzene). Optical measurements were performed under inert conditions. UV/Vis/NIR absorption spectra were recorded on a Jasco V-770 or V-670 spectrometer. Cyclic and square wave voltammetry measurements were conducted on a standard commercial electrochemical analyzer (EC epsilon, BASi instruments, UK) with a three-electrode single-compartment cell. A Pt disc electrode was used as a working electrode, a platinum wire as a counter electrode and an Ag/AgCl reference electrode using ferrocenium/ferrocene (Fc^+/Fc) as an internal standard for the calibration of the potential. The measurements were carried out under an argon atmosphere in DCM and tetrabutylammonium hexafluorophosphate (TBAHFP) was added as supporting electrolyte, resulting in an available redox window from –2.25 V to +1.75 V (vs. Fc/Fc^+). Spectroelectrochemical absorption measurements were recorded in reflection mode in a three-electrode custom-made cell with a 6 mm diameter Pt-disc working electrode, Pt counter and Ag/AgCl leak free reference electrode implemented in an Agilent Cary 5000 UV/Vis/NIR spectrometer. The optical path was adjusted to 100 µm with a micrometer screw. Potentials were applied with a reference 600 potentiostat (Gamry Instruments). Application of potential steps and recording of absorption spectra was automated by a lab view routine. Fluorescence spectra were measured on a FLS980 fluorescence spectrometer (Edinburgh Instruments Ltd.; Inc) and were corrected against the photomultiplier sensitivity and the lamp intensity. For the fluorescence spectra of the PBI dianions, a custom-built flow cell setup has been built into this spectrometer[287] and the measurements were conducted in front-face geometry (22.5°). The fluorescence lifetimes were determined using picosecond pulsed diode lasers (EPL-series, Edinburgh Instruments Ltd.; Inc) and a PMT-900 fast photomultiplier (Edinburgh Instruments Ltd.; Inc.) for time correlated single photon counting (TCSCP). The fitting of the data was carried out using the Exp. Tail Fit or the Exp. Reconvolution Fit (for **PBI-ClCN**) routine supplied by Edinburgh Instruments Ltd.; Inc. Fluorescence quantum yields of the neutral PBIs were determined using the dilution

method (OD < 0.05) and *N*,*N'*-bis(2,6-diisopropylphenyl)perylene-3,4:9,10-bis(dicarboximide) (Φ_f = 1.00 in $CHCl_3$) or *N*,*N'*-bis(2,6-diisopropylphenyl)- 1,6,7,12-tetraphenoxyperylene-3,4:9,10-bis(dicarboximide) (for **PBI-OPh**, Φ_f = 0.96 in $CHCl_3$)[215] as reference. Fluorescence quantum yields of PBI^{2-} were determined relative to the neutral PBI by excitation at 385 nm (**PBI-Cl**), 415 nm (**PBI-H**), 490 nm (**PBI-Ph**) and 398 nm (**PBI-OPh**). Theoretical calculations were performed by the Gaussian software[261] using B3LYP/6-31G(d) level theory for structure optimization and B3LYP/def2-SVP (for **PBI-ClCN**, **PBI-Cl** and **PBI-H**) or ωB97XD/def2-SVP (for **PBI-Ph** and **PBI-OPh**) level theory for TD-DFT simulation of electron transitions, as these basis sets gave the best results in accordance with the experimental data respectively. Transition densities were calculated using the multiwfn program by T. Lu *et al.*[307]

5.4.2. Synthesis

PBA-ClBr and **PBI-ClBr** have been synthesized according to previously reported procedures.[310] For the synthesis of **PBI-ClCN**, a literature known procedure has been modified.[283]

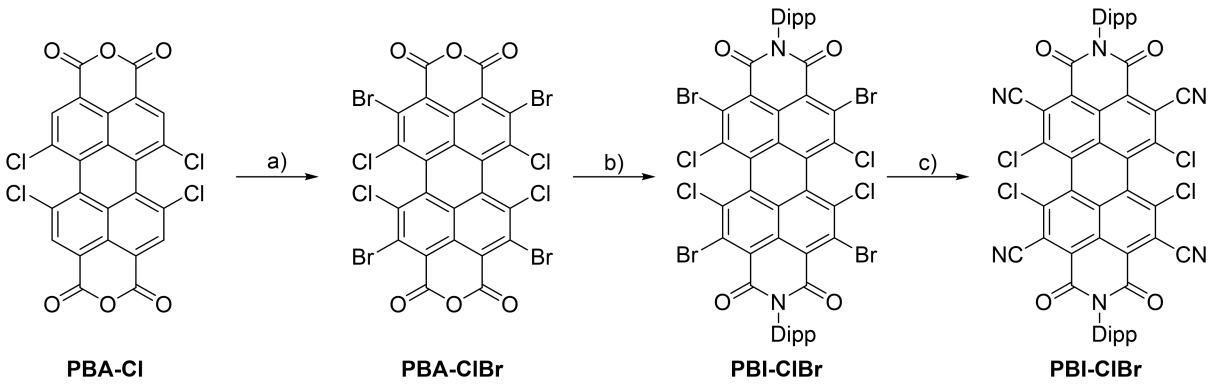

Scheme 6 Synthesis of **PBI-ClCN** a) DBI, 50% oleum, 100 °C, 18 h, 80%; b) 2,6-diisopropylaniline, propionic acid, reflux, 16 h, 79%; c) CuCN, DMF, 140 °C, 3 h, 9%. DBI = dibromoisocyanuric acid.

A solution of 300 mg (258 µmol) **PBI-ClBr** and 138 mg (1.55 mmol) copper cyanide in 30 mL of dry DMF was heated to 140 °C for 3 h under argon. After cooling to room temperature, the mixture was poured on water and extracted with dichloromethane. The solvent was removed under reduced pressure and the crude product was purified by column chromatography (dichloromethane) and HPLC (dichloromethane) to give a light red solid.

Yield: 22.2 mg (23.4 µmol, 9%). ^{1}H NMR (400 MHz, CD_2Cl_2): δ = 7.61 (t, 2H), 7.43 (d, 4H), 2.67 (sept, 4H), 1.21 (d, 12H), 1.20 (d, 12H); ^{13}C NMR (100 MHz, CD_2Cl_2): δ = 159.3, 146.0, 140.4, 132.5, 131.0, 129.2, 129.1, 127.4, 125.0, 123.4, 118.7, 113.2, 29.9, 24.21, 24.16; HRMS

(ESI, negative mode, acetonitrile/chloroform 1:1): *m/z* calculated for $C_{52}H_{34}Cl_4N_6O_4^-$ 946.1401 $[M]^-$; found: 946.1430; m.p.>350 °C.

Typical procedure for the chemical reduction

Under an argon atmosphere in a Schlenk flask, the respective PBI (5 µmol), potassium graphite (2.70 mg, 20 µmol, 4 eq) and 18-crown-6 (5.29 mg, 20 µmol, 4 eq) were dissolved in THF and stirred at room temperature for one hour. Afterwards, the solvent was removed *in vacuo* and the residue washed with hexane and toluene. Then the obtained solid was dissolved in 1,2-difluorobenzene and immediately put into a UV/Vis/NIR spectrometer to characterize the obtained species.

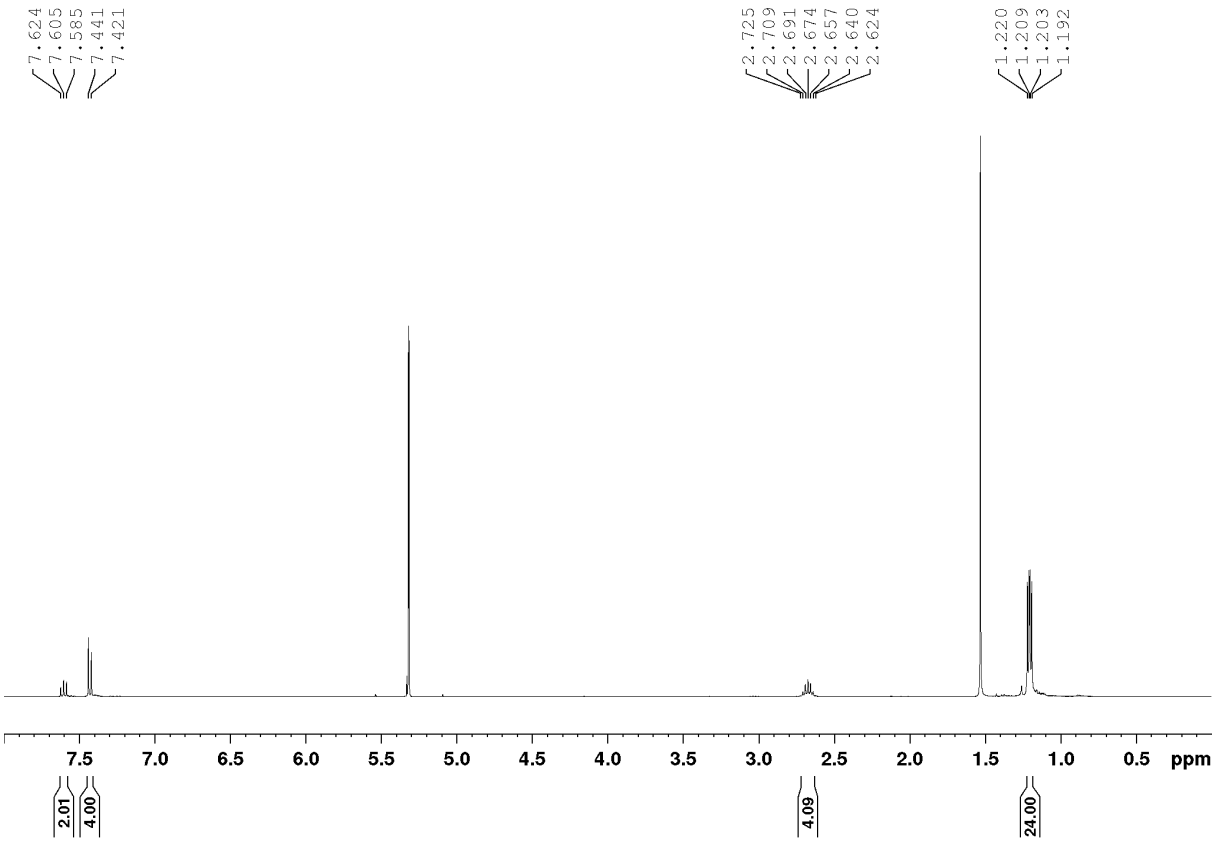

Figure 90 ^{1}H-NMR (400 MHz) spectrum of **PBI-ClCN** in CD_2Cl_2 at room temperature.

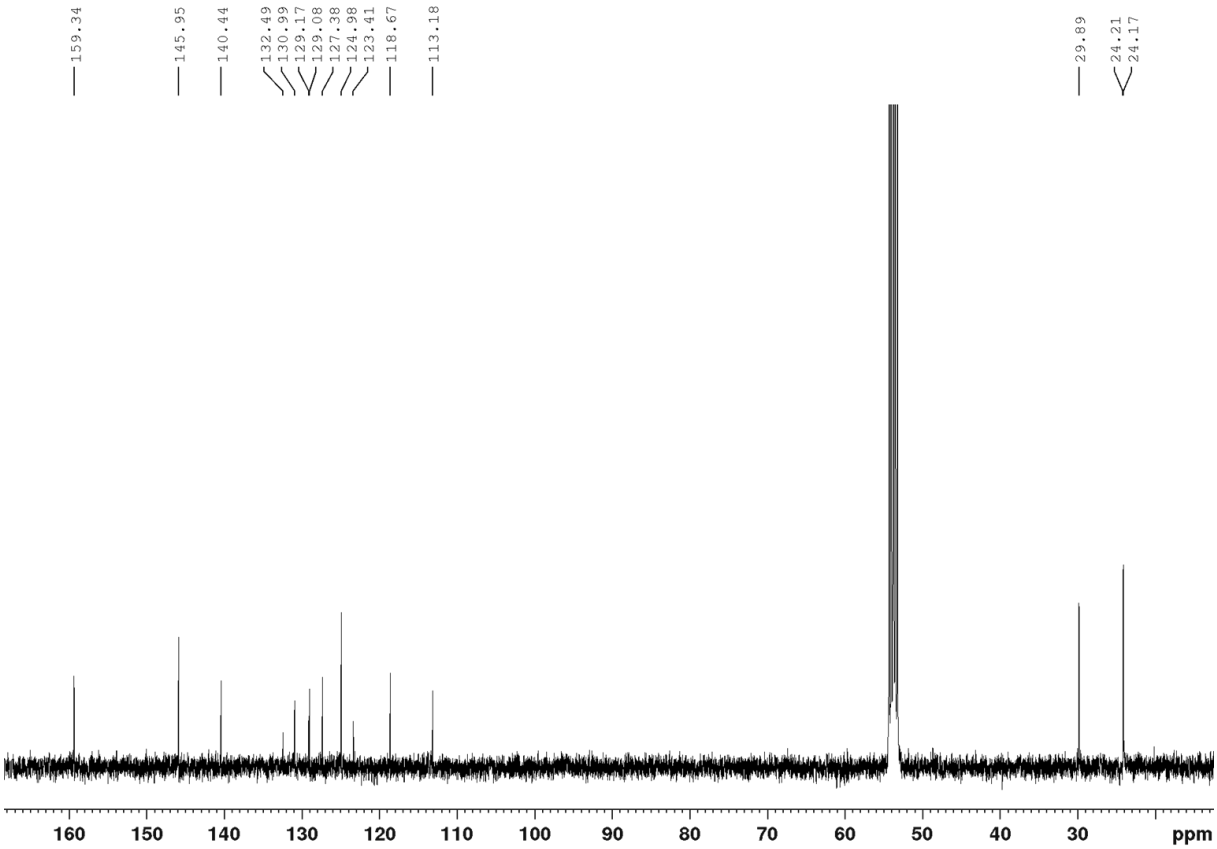

Figure 91 ^{13}C-NMR (100 MHz) spectrum of **PBI-ClCN** in CD_2Cl_2 at room temperature.

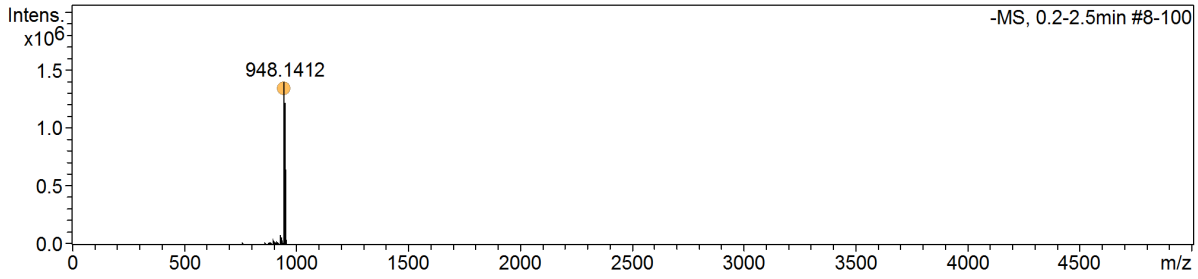

Figure 92 ESI-MS spectrum of **PBI-ClCN.**

5.4.3. Electrochemical Measurements

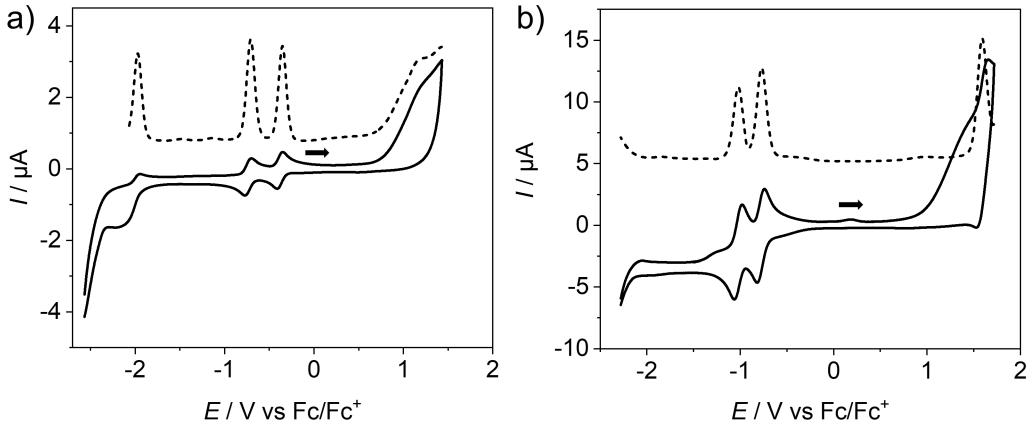

Figure 93 Cyclic voltammograms (solid lines) and square wave voltammograms (dashed lines) of a) **PBI-ClCN** and b) **PBI-Cl**. Measurements were performed using DCM ($c_0 = 2 \cdot 10^{-4}$ M) at room temperature, using TBAHFP (0.1 M) as electrolyte (scan rate 100 mV s^{-1}, the scan direction is indicated by the small arrow, SW amplitude 25 mV, SW frequency 15 Hz).

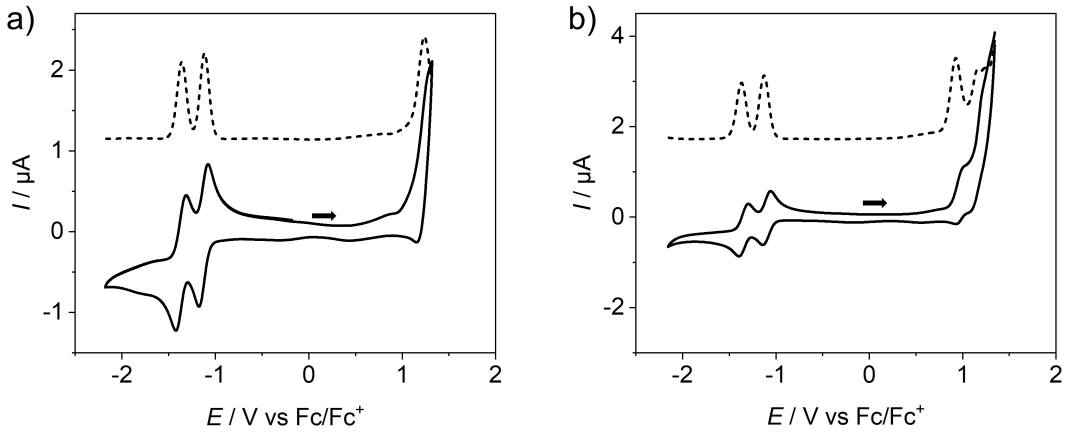

Figure 94 Cyclic voltammograms (solid lines) and square wave voltammograms (dashed lines) of a) **PBI-H** and b) **PBI-Ph**. Measurements were performed using DCM ($c_0 = 2 \cdot 10^{-4}$ M) at room temperature, using TBAHFP (0.1 M) as electrolyte (scan rate 100 mV s^{-1}, the scan direction is indicated by the small arrow, SW amplitude 25 mV, SW frequency 15 Hz).

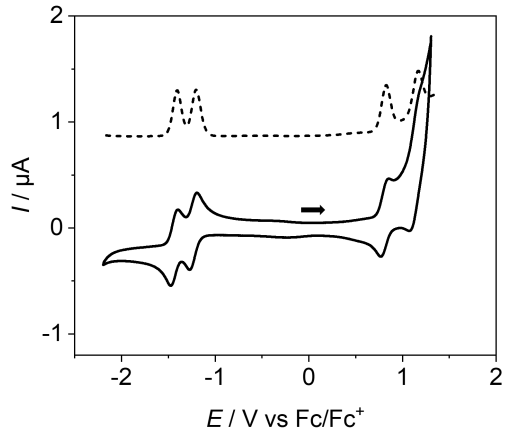

Figure 95 Cyclic voltammogram (solid line) and square wave voltammogram (dashed line) of **PBI-OPh**. Measurements were performed using DCM (c_0 = $2 \cdot 10^{-4}$ M) at room temperature, using TBAHFP (0.1 M) as electrolyte (scan rate 100 mV s^{-1}, the scan direction is indicated by the small arrow, SW amplitude 25 mV, SW frequency 15 Hz).

Table 16 Electron affinities of the different investigated PBIs as isolated molecule (A_g), as molecular solid (A_c) and in solution (A_{sol}) calculated according to Ref. [311].

	PBI-ClCN	**PBI-Cl**	**PBI-H**	**PBI-Ph**	**PBI-OPh**
A_g	2.96 eV	2.31 eV	2.07 eV	2.05 eV	1.96 eV
A_c	4.30 eV	3.63 eV	3.38 eV	3.36 eV	3.27 eV
A_{sol}	5.01 eV	4.38 eV	4.15 eV	4.13 eV	4.05 eV

Table 17 Ionization energies of the different investigated PBIs as isolated molecule (I_g), as molecular solid (I_c) and in solution (I_{sol}) calculated according to Ref. [311].

	PBI-ClCN	**PBI-Cl**	**PBI-H**	**PBI-Ph**	**PBI-OPh**
I_g	-	7.45 eV	6.94 eV	6.43 eV	6.23 eV
I_c	-	6.60 eV	6.17 eV	5.74 eV	5.58 eV
I_{sol}	-	6.74 eV	6.45 eV	6.16 eV	6.05 eV

5.4.4. Optical Measurements

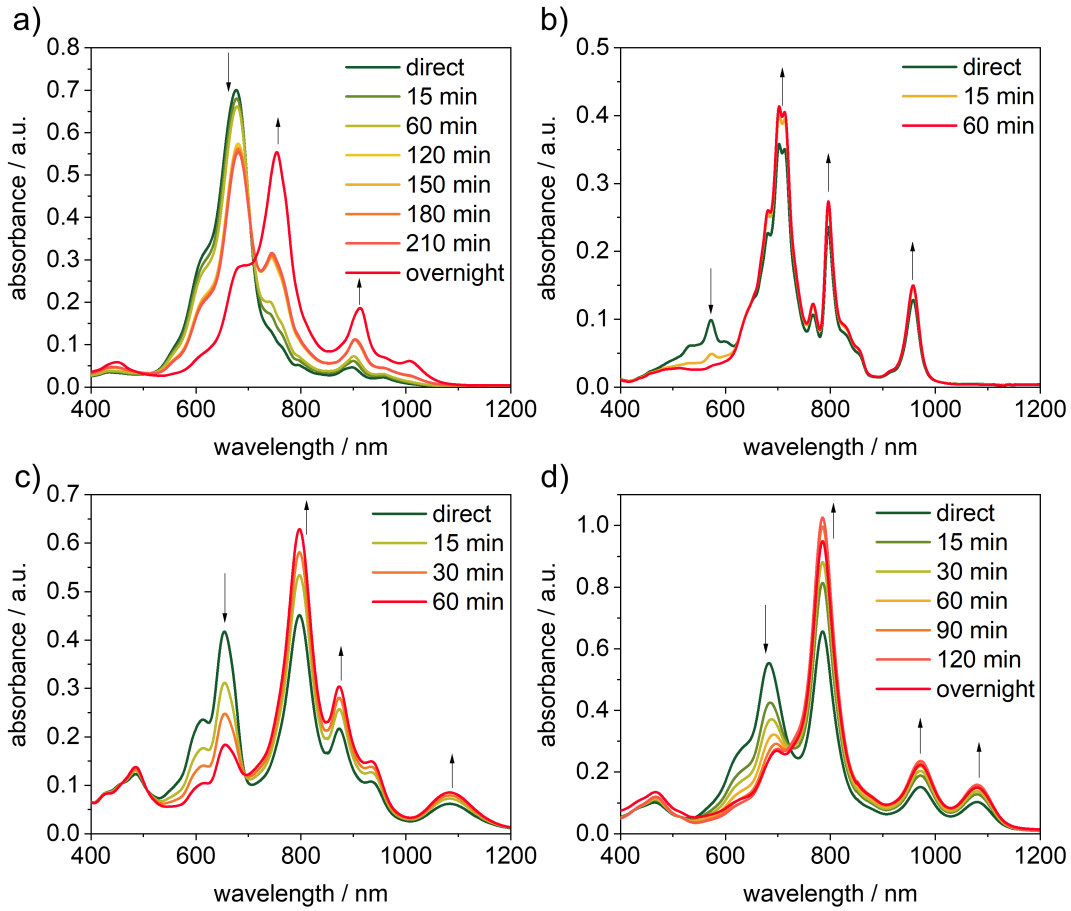

Figure 96 UV/Vis/NIR absorption spectra of mixed solutions of PBI^{2-} and $PBI^{\bullet-}$ generated by chemical reduction of a) **PBI-Cl**, b) **PBI-H**, c) **PBI-Ph** and d) **PBI-OPh** with KC_8 measured in 1,2-difluorobenzene at room temperature stored under inert conditions during the measurements.

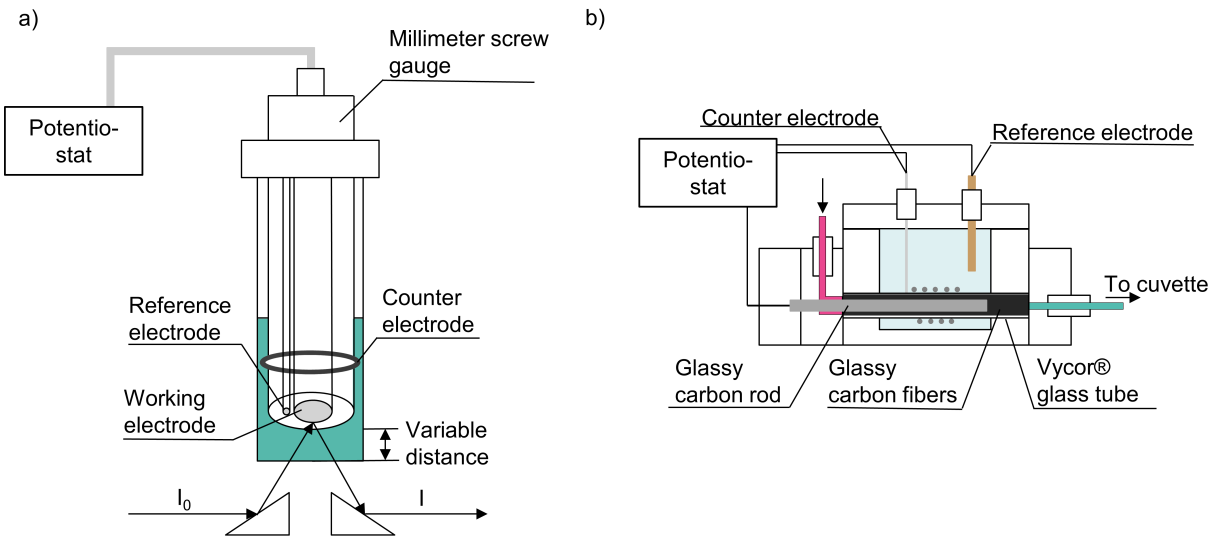

Figure 97 Schematic illustration of the custom built spectroelectrochemical cells for a) absorption measurements adapted from Borg *et al.*[312] and b) fluorescence measurements as described by Heitmüller *et al.* Adapted with permission from Ref. [287] with permission from Elsevier.

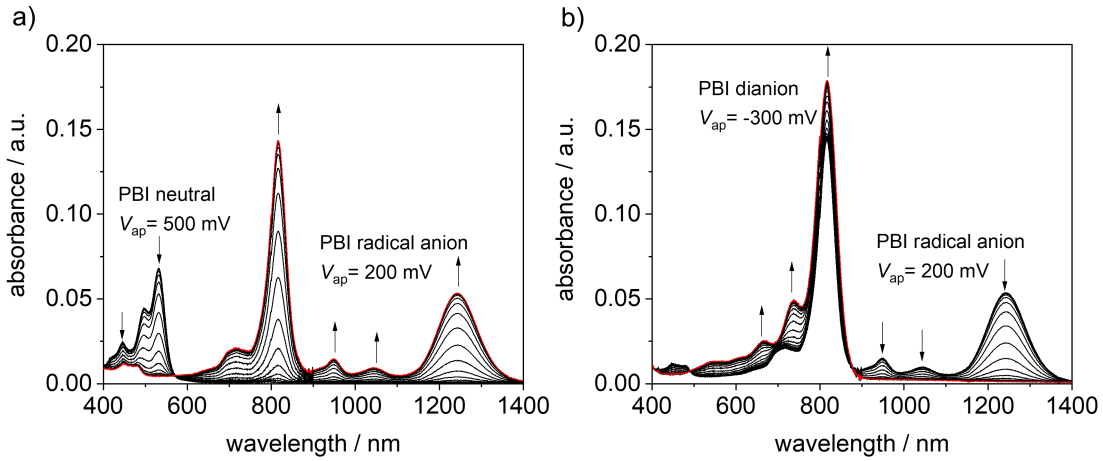

Figure 98 UV/Vis/NIR absorption changes upon electrochemical reduction of a) **PBI-ClCN** to **PBI-ClCN**$^{\bullet-}$ (in steps of 20 mV) at potentials from +500 to +200 mV. b) **PBI-ClCN**$^{\bullet-}$ to **PBI-ClCN**$^{2-}$ (in steps of 20 mV) at potentials from +200 to –300 mV ($c_0 = 2 \cdot 10^{-4}$ M, 0.1 M TBAHFP, DCM).

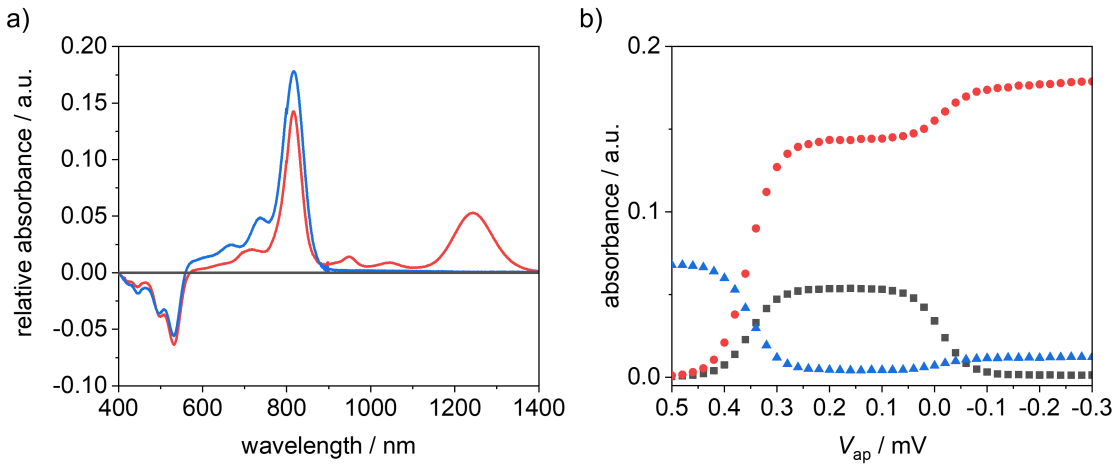

Figure 99 a) Plots of the relative changes upon reduction of **PBI-ClCN** compared to the neutral state; b) Plots of the absorbance in dependance of the applied voltage V_{ap} at 1243 nm (grey squares), 817 nm (red circle) and 531 nm (blue triangle).

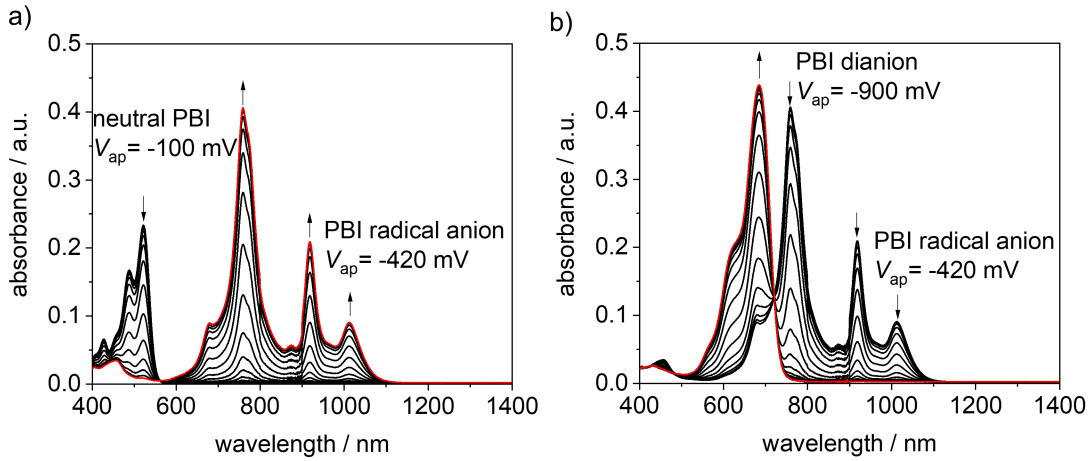

Figure 100 UV/Vis/NIR absorption changes upon electrochemical reduction of a) **PBI-Cl** to **PBI-Cl**$^{\bullet-}$ (in steps of 20 mV) at potentials from –100 to –420 mV; b) **PBI-Cl**$^{\bullet-}$ to **PBI-Cl**$^{2-}$ (in steps of 20 mV) at potentials from –420 to –900 mV ($c_0 = 4 \cdot 10^{-4}$ M, 0.1 M TBAHFP, DCM).

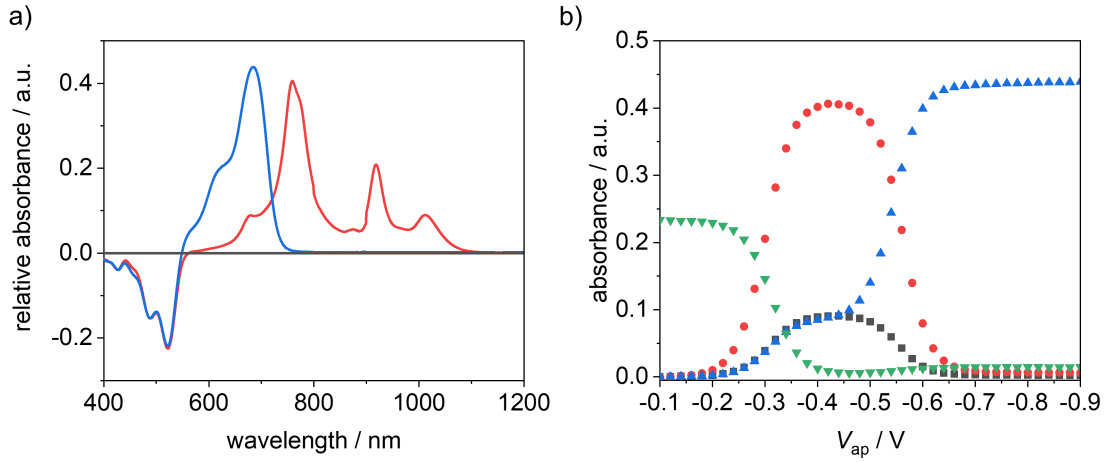

Figure 101 a) Plots of the relative changes upon reduction of **PBI-Cl** compared to the neutral state; b) Plots of the absorbance in dependance of the applied voltage V_{ap} at 1011 nm (grey squares), 759 nm (red circle), 684 nm (blue triangle) and 522 nm (green inverse triangle).

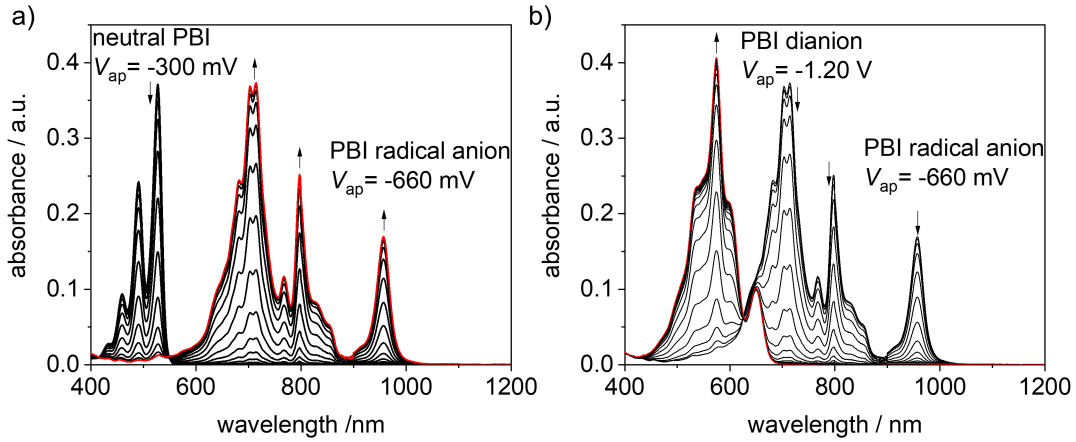

Figure 102 UV/Vis/NIR absorption changes upon electrochemical reduction of a) **PBI-H** to **PBI-H**$^{\bullet-}$ (in steps of 20 mV) at potentials from –300 to –660 mV; b) **PBI-H**$^{\bullet-}$ to **PBI-H**$^{2-}$ (in steps of 20 mV) at potentials from –660 mV to –1.20 V ($c_0 = 4 \cdot 10^{-4}$ M, 0.1 M TBAHFP, DCM).

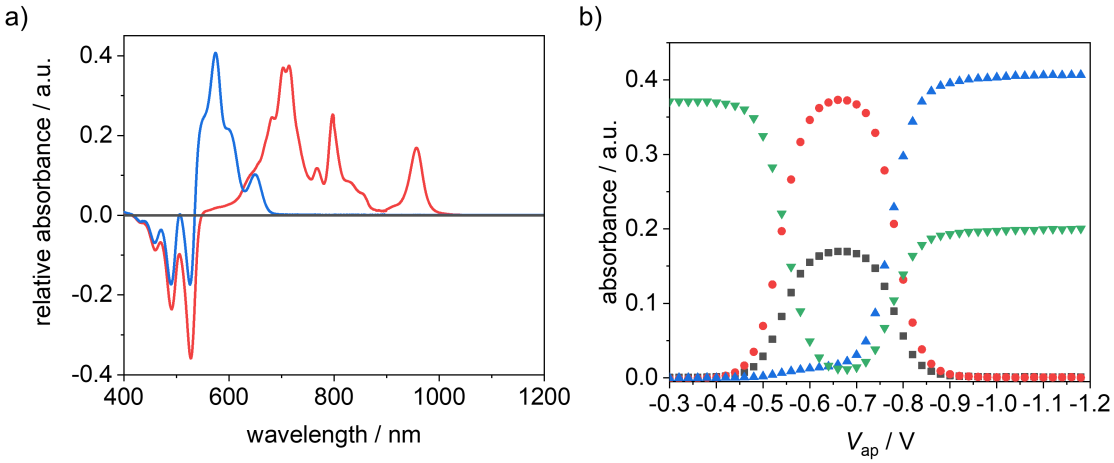

Figure 103 a) Plots of the relative changes upon reduction of **PBI-H** compared to the neutral state; b) Plots of the absorbance in dependance of the applied voltage V_{ap} at 957 nm (grey squares), 715 nm (red circle), 574 nm (blue triangle) and 527 nm (green inverse triangle).

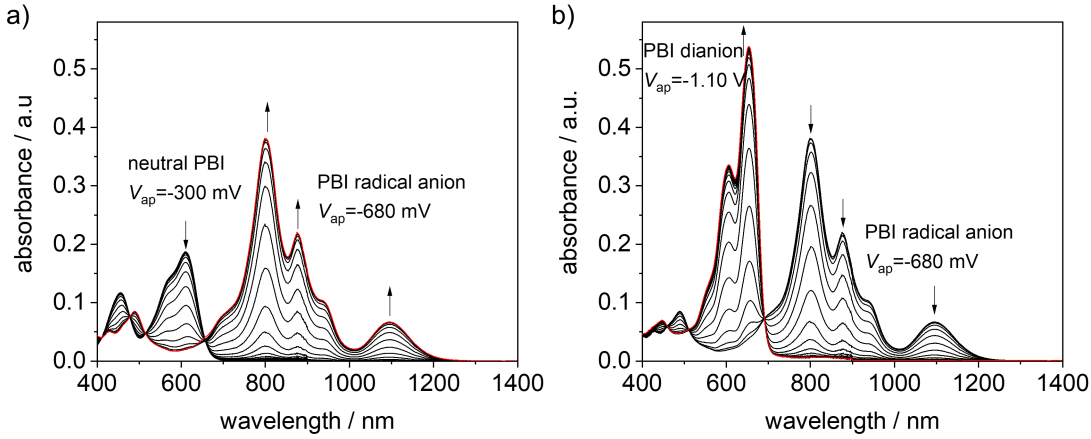

Figure 104 UV/Vis/NIR absorption changes upon electrochemical reduction of a) **PBI-Ph** to **PBI-Ph**$^{\bullet-}$ (in steps of 20 mV) at potentials from –300 to –680 mV. b) **PBI-Ph**$^{\bullet-}$ to **PBI-Ph**$^{2-}$ (in steps of 20 mV) at potentials from –680 to –1.10 V ($c_0 = 8 \cdot 10^{-4}$ M, 0.1 M TBAHFP, DCM).

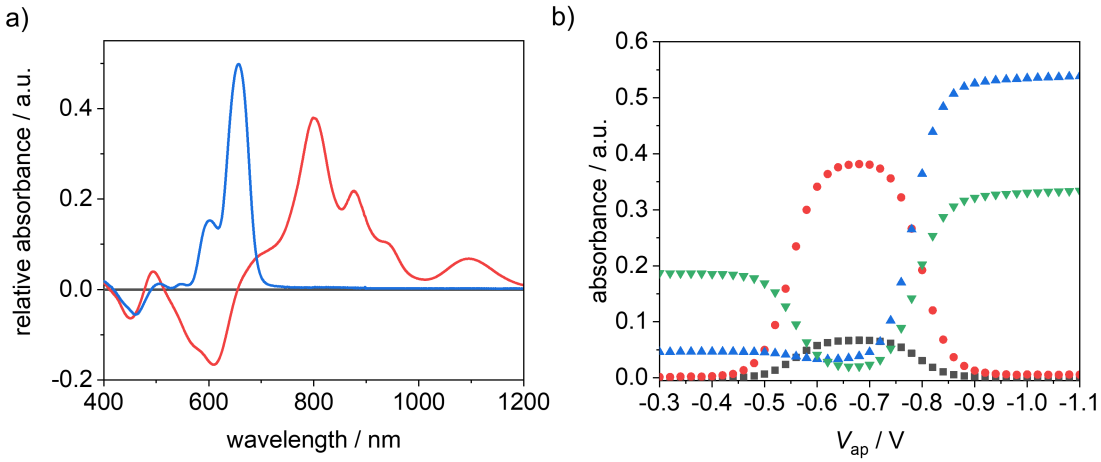

Figure 105 a) Plots of the relative changes upon reduction of **PBI-Ph** compared to the neutral state; b) Plots of the absorbance in dependance of the applied voltage V_{ap} at 1097 nm (grey squares), 799 nm (red circle), 653 nm (blue triangle) and 609 nm (green inverse triangle).

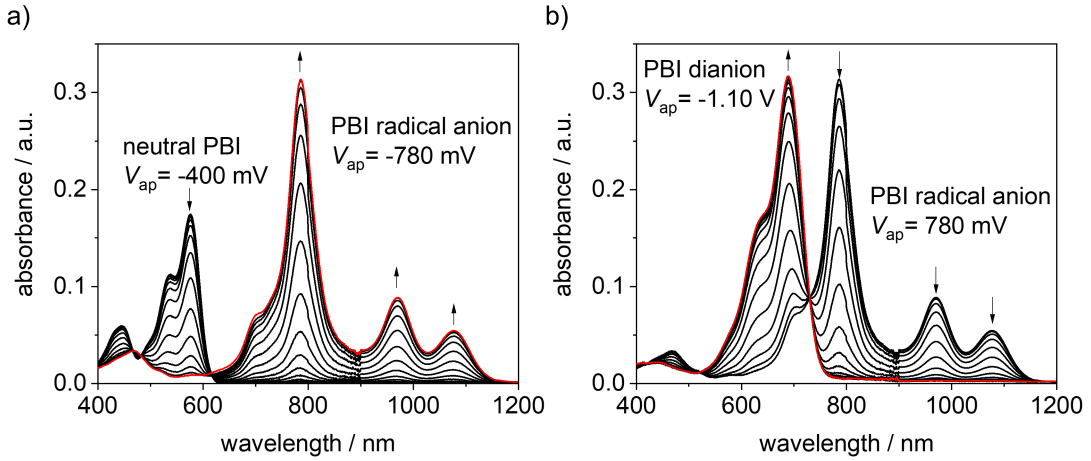

Figure 106 UV/Vis/NIR absorption changes upon electrochemical reduction of c) **PBI-OPh** to **PBI-OPh**$^{\bullet-}$ (in steps of 20 mV) at potentials from –400 to –780 mV; d) **PBI-OPh**$^{\bullet-}$ to **PBI-OPh**$^{2-}$ (in steps of 20 mV) at potentials from –780 mV to –1.10 V ($c_0 = 3.6 \cdot 10^{-4}$ M, 0.1 M TBAHFP, DCM).

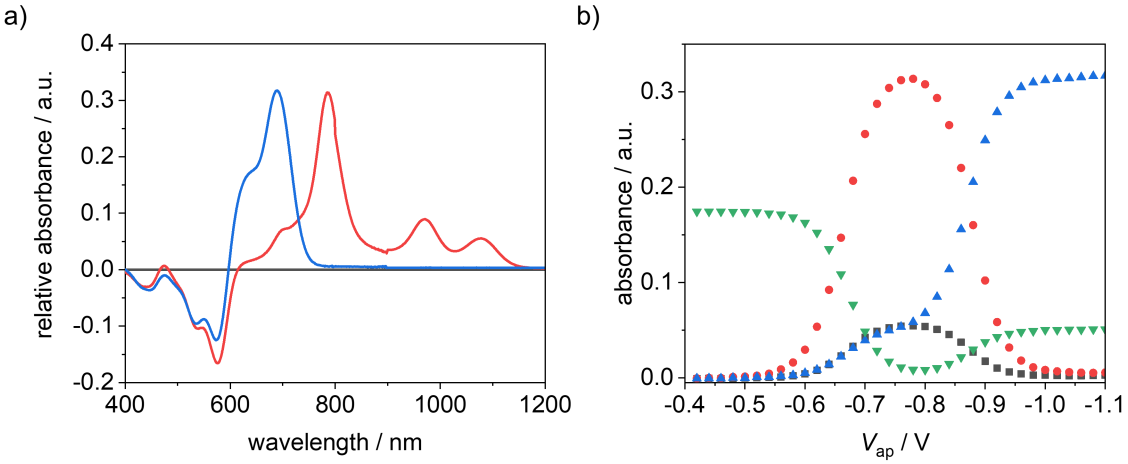

Figure 107 a) Plots of the relative changes upon reduction of **PBI-OPh** compared to the neutral state; b) Plots of the absorbance in dependance of the applied voltage V_{ap} at 1076 nm (grey squares), 785 nm (red circle), 689 nm (blue triangle) and 576 nm (green inverse triangle).

Table 18 Summary of the absorption properties of the investigated PBIs and their electrochemical reduced species measured in DCM (0.1 M TBAHFP) at room temperature.

	λ_{abs} [nm]			ε_{max} [M^{-1} cm^{-1}]		
	PBI	$PBI^{\bullet-}$	PBI^{2-}	PBI	$PBI^{\bullet-}$	PBI^{2-}
PBI-ClCN	531*	1243	817*	33900*	26100	87200*
	496	1043	737	22100	4800	24200
	446	947	669	12200	7400	12300
		817*			70300*	
		714			10700	
PBI-Cl	522*	1011	684*	58200*	22100	109100*
	489	918		41600	51800	
	428	759*		16300	101100*	
		679			22000	
PBI-H	527*	957	649	93700*	42800	25600
	491	797	574*	61300	63500	102600*
	459	768		23600	29500	
		715*			94100*	
		703			93000	
		682			61700	
PBI-Ph	609*	1097	653*	23400*	8300	67300*
	454	877	606	14600	27300	4200
		799*	447		47600*	8800
		489			10600	
PBI-OPh	576*	1076	689*	49600*	15100	88700*
	539	971		31900	24800	
	443	785*		16700	88700*	

*main absorption peak.

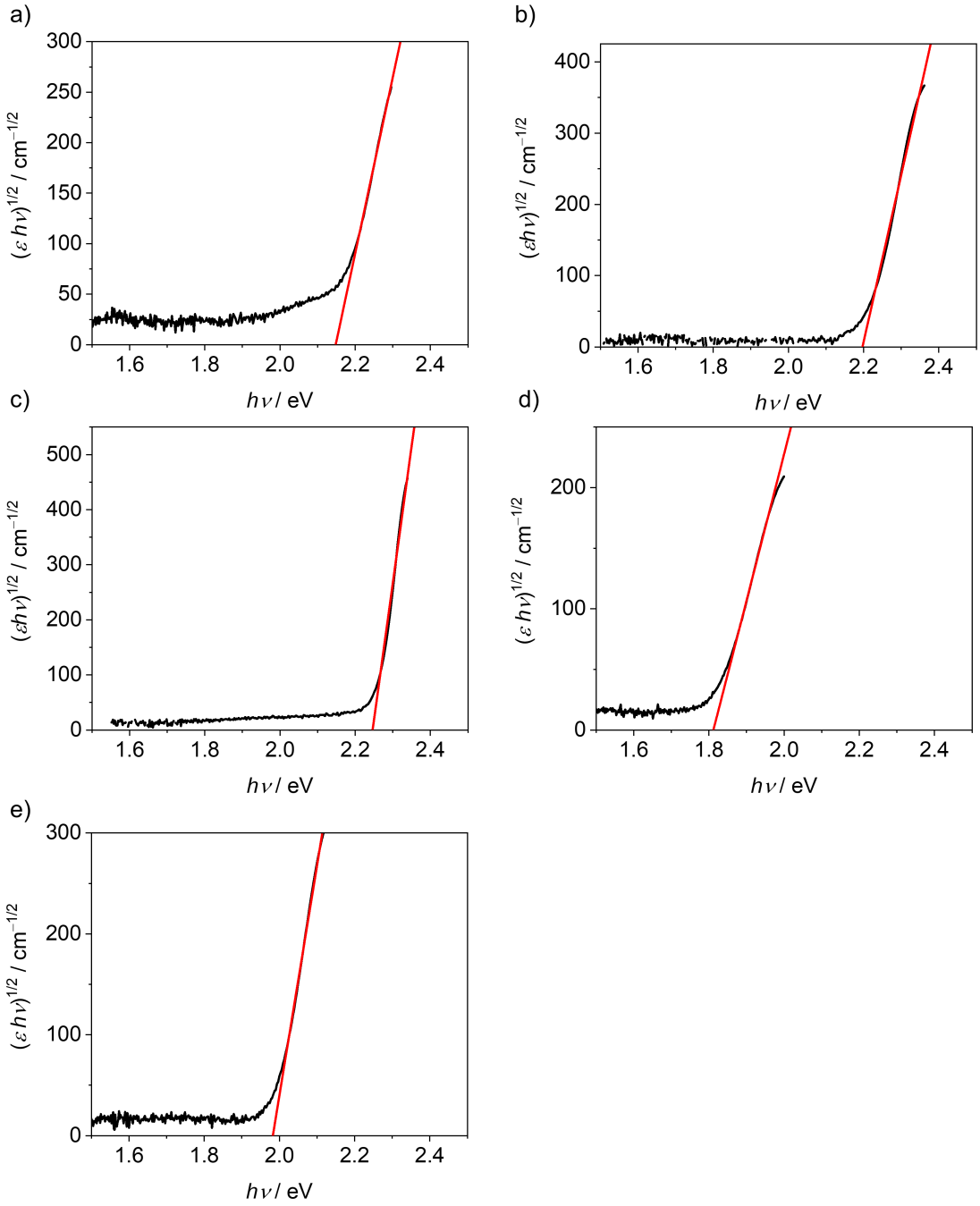

Figure 108 Tauc plots (black) including the linear fit (red) of a) **PBI-ClCN**, b) **PBI-Cl**, c) **PBI-H**, d) **PBI-Ph** and e) **PBI-OPh**. The absorption band used to obtain the Tauc plots always corresponds to the S_0-S_1 transition of the neutral PBI.

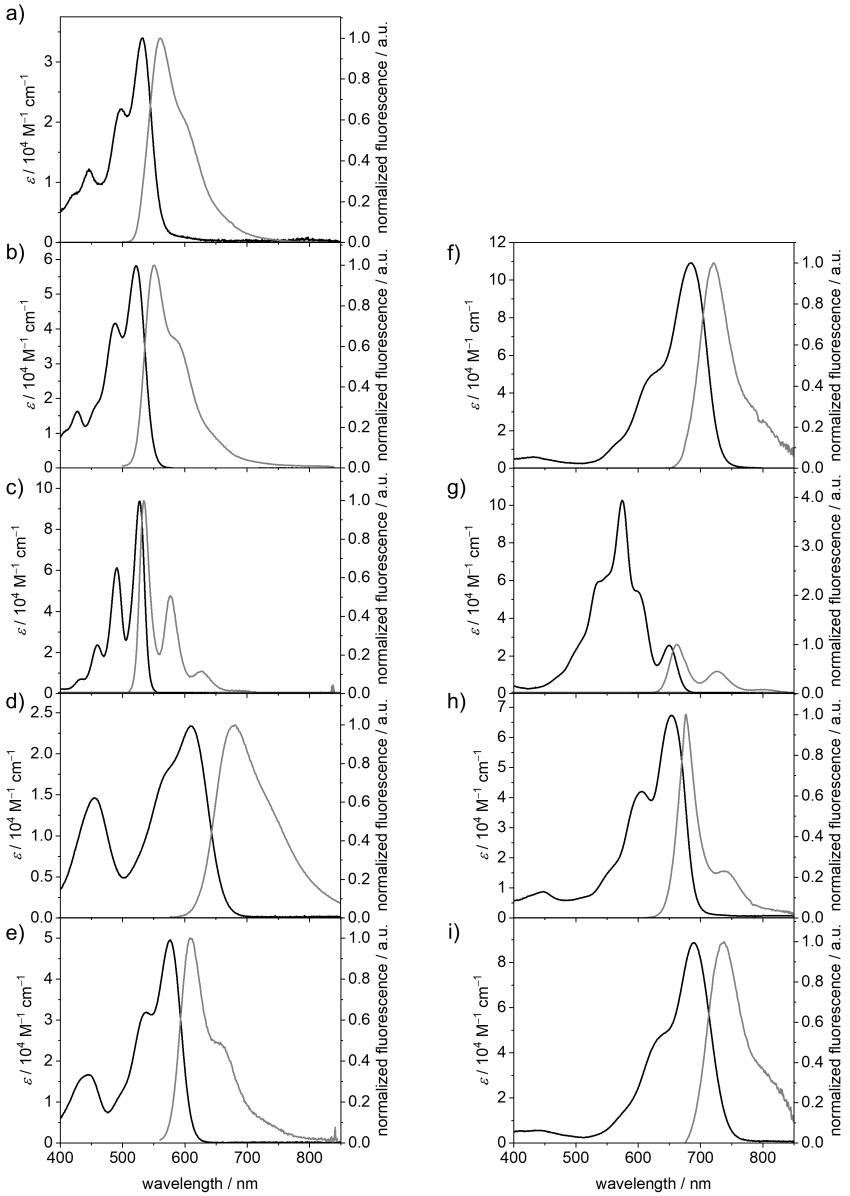

Figure 109 UV/Vis/NIR absorption and fluorescence emission spectra of the neutral (a-e) and dianionic (f-i) PBI species of a) **PBI-ClCN**; b), f) **PBI-Cl**; c), g) **PBI-H**; d), h) **PBI-Ph**; and e), i) **PBI-OPh** measured in DCM (c_0 = $4 \cdot 10^{-4}$ M for absorption, $c_0 = 1 \cdot 10^{-5}$ M for fluorescence of PBI and $c_0 = 1 \cdot 10^{-4}$ M for fluorescence of PBI^{2-}) at room temperature using TBAHFP (0.1 M) as electrolyte.

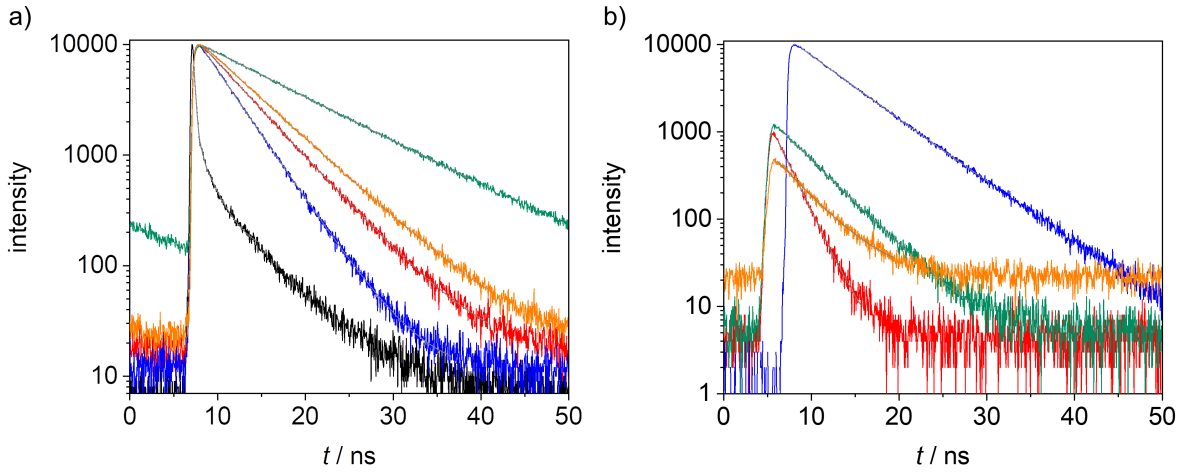

Figure 110 Fluorescence decay in dichloromethane at 293 K for **PBI-ClCN** (black), **PBI-Cl** (red), **PBI-H** (blue), **PBI-Ph** (green) and **PBI-OPh** (orange) in their a) neutral as well as b) dianionic state ($c_0 = 1 \cdot 10^{-5}$ M for lifetime of PBI and $c_0 = 1 \cdot 10^{-4}$ M for lifetime of PBI^{2-}).

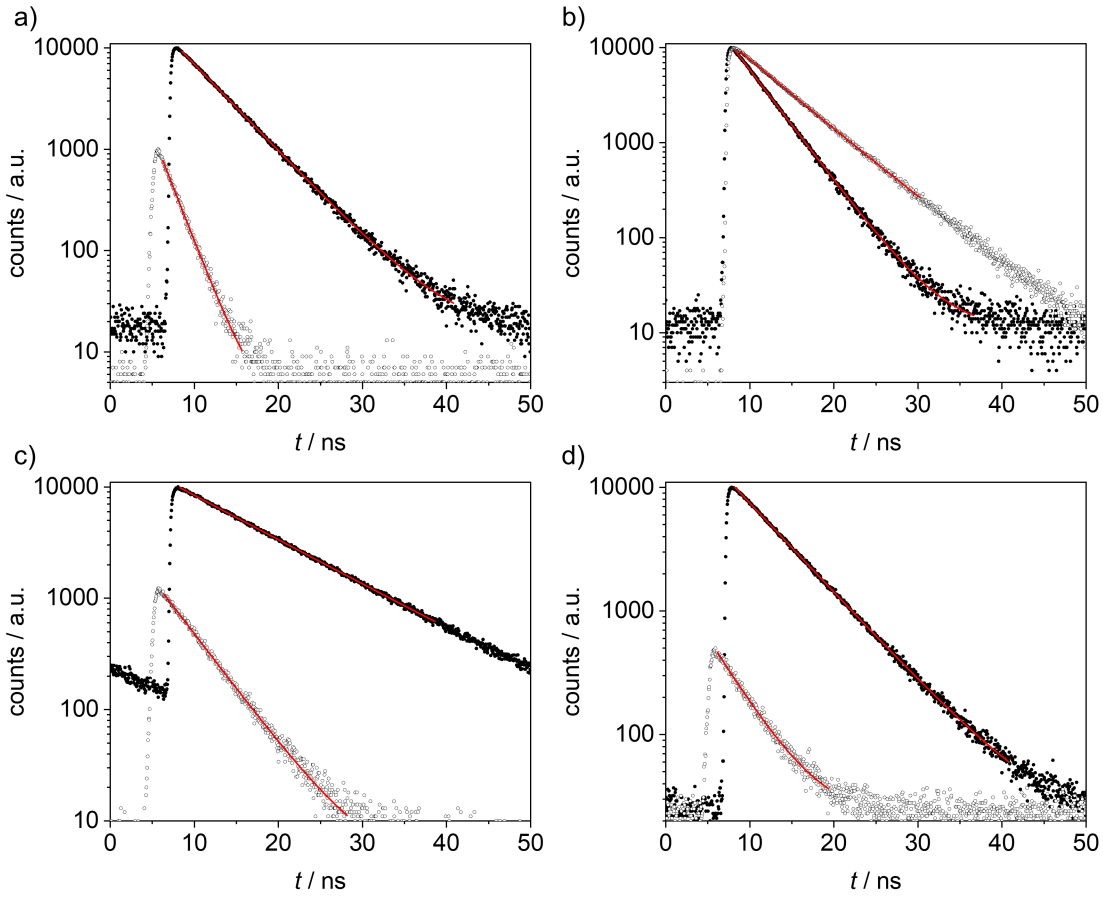

Figure 111 Fluorescence decay of the neutral (solid circles) and dianionic (open circels) a) **PBI-Cl**, b) **PBI-H**, c) **PBI-Ph** and d) **PBI-OPh** in dichloromethane at 293 K ($c_0 = 1 \cdot 10^{-5}$ M for lifetime of PBI and $c_0 = 1 \cdot 10^{-4}$ M for lifetime of PBI^{2-}).

5.4.5. Theoretical Investigation

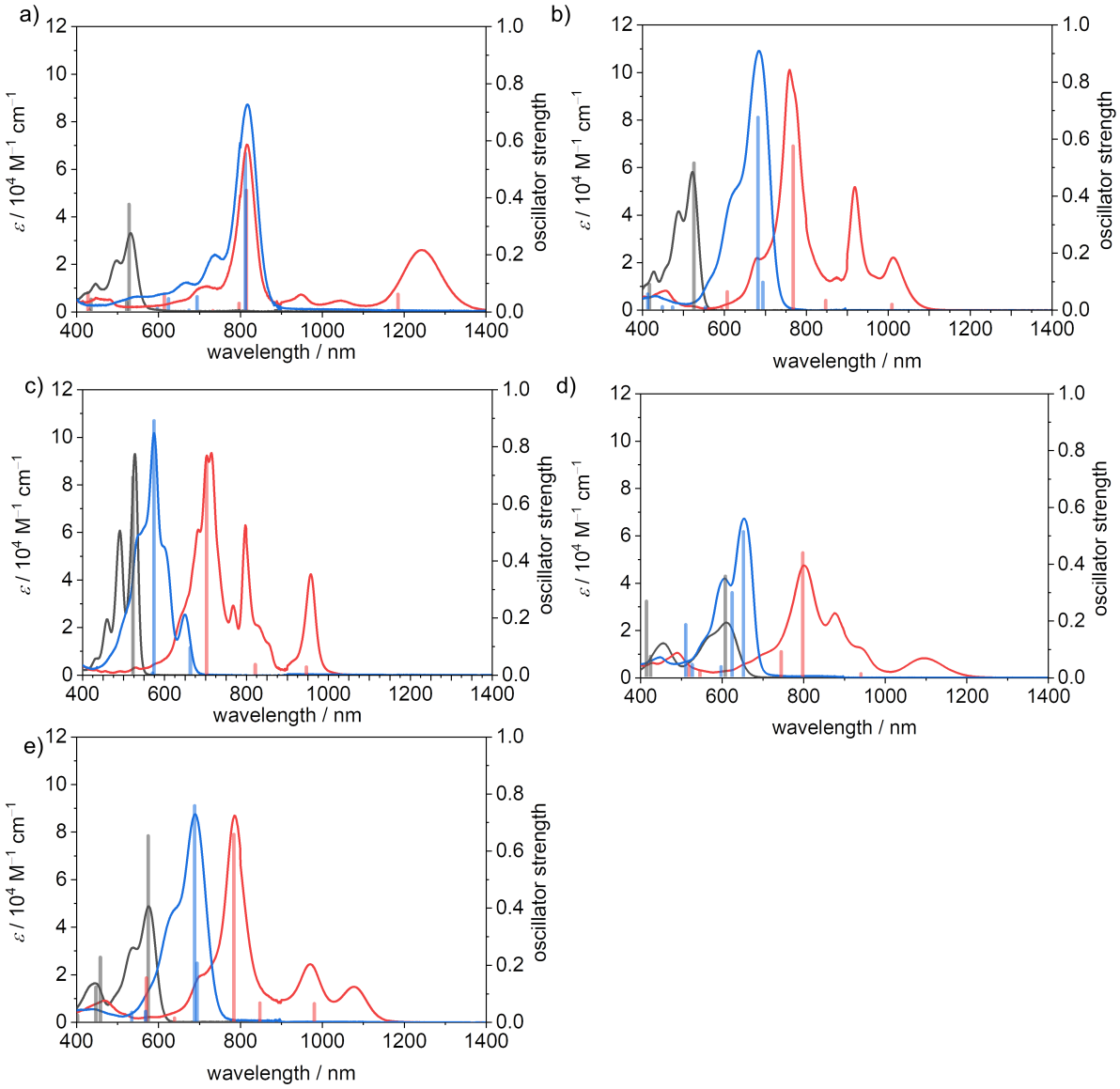

Figure 112 UV/Vis/NIR absorption spectra of PBI (dark grey) and the electrochemically generated $PBI^{\bullet-}$ (red) and PBI^{2-} (blue) of a) **PBI-ClCN**, b) **PBI-Cl**, c) **PBI-H**, d) **PBI-Ph** and e) **PBI-OPh** measured in DCM (c_0 = $4 \cdot 10^{-4}$ M) at room temperature using TBAHFP (0.1 M) as electrolyte, as well as the calculated transitions thereof (lighter color) using TD-DFT (a) – c) B3LYP/def-SVP and d)-e) ωB97XD/def2-SVP).

The calculated transitions in Figure 112 have been shifted, so that the transition with the highest oscillator strength corresponds in energy to the wavelength of the absorption maximum.

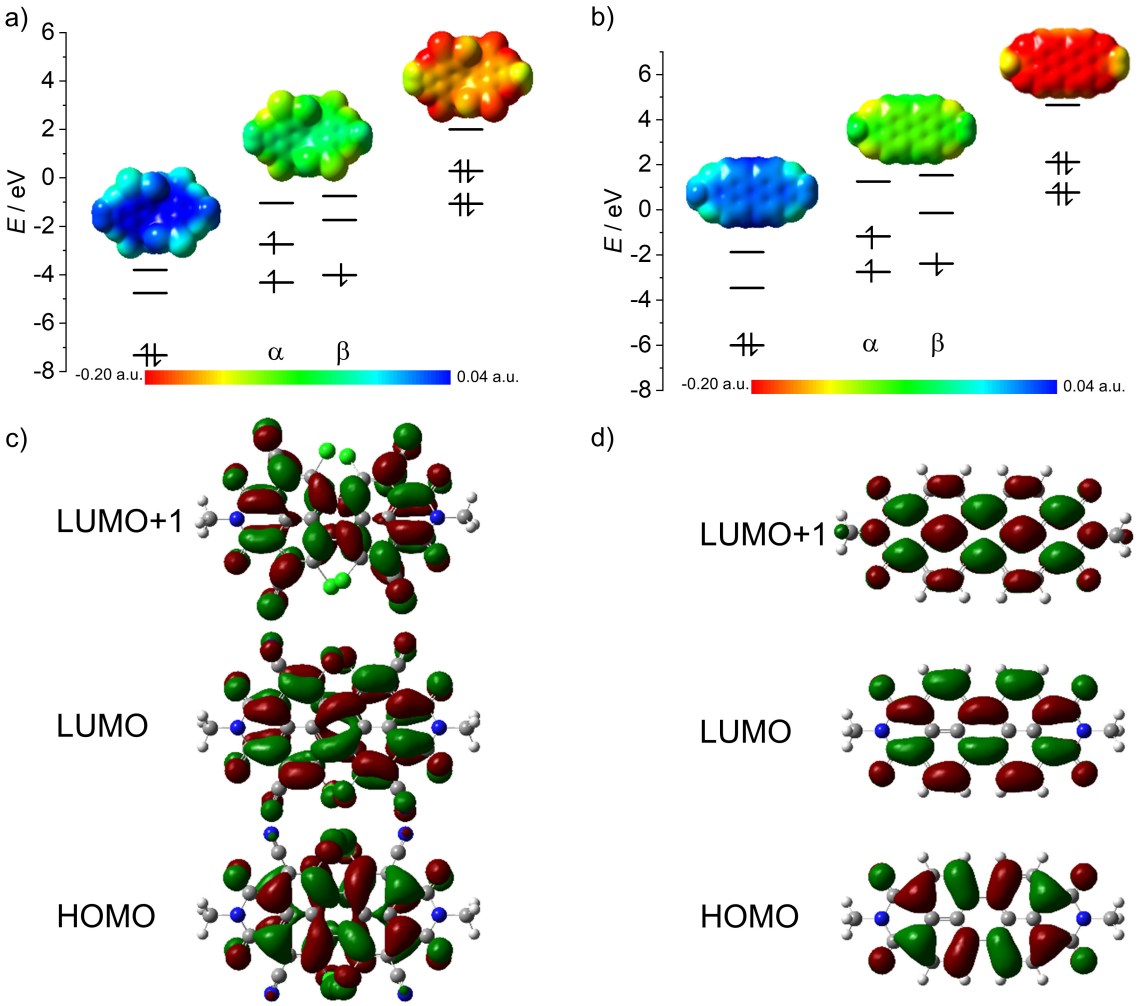

Figure 113 HOMO, LUMO and LUMO+1 levels as obtained from DFT calculations of a) **PBI-ClCN** (left), the corresponding α- and β-spin MO levels of **PBI-ClCN**$^{\bullet-}$ (middle) and HOMO–1, HOMO and LUMO levels of **PBI-ClCN**$^{2-}$ (right), as well as the electrostatic potential maps of the respective derivative (top, isovalue 0.020 a.u.) and b) **PBI-H** as well as the respective reduced states. HOMO, LUMO and LUMO+1 (bottom to top) of c) **PBI-ClCN** and d) **PBI-H**. The corresponding orbitals of **PBI-ClCN**$^{\bullet-}$ and **PBI-ClCN**$^{2-}$ and **PBI-H**$^{\bullet-}$ and **PBI-H**$^{2-}$ respectively are visually indistinguishable. Orbitals and electrostatic potential maps were calculated using DFT (B3LYP/6-31g(d)).

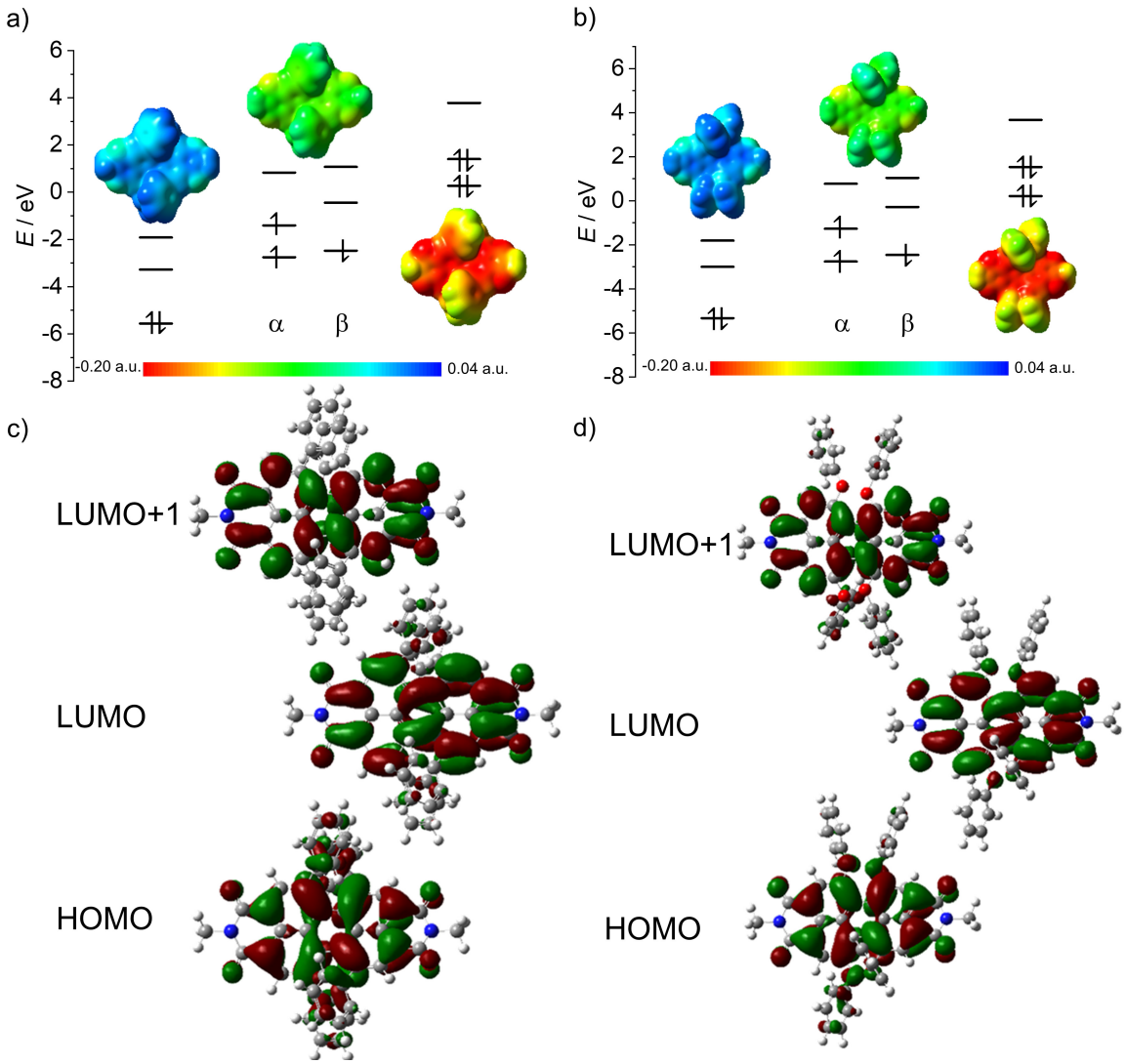

Figure 114 HOMO, LUMO and LUMO+1 levels as obtained from DFT calculations of a) **PBI-Ph** (left), the corresponding α- and β-spin MO levels of **PBI-Ph**$^{\bullet-}$ (middle) and HOMO–1, HOMO and LUMO levels of **PBI-Ph**$^{2-}$ (right), as well as the electrostatic potential maps of the respective derivative (top, isovalue 0.020 a.u.) and b) **PBI-OPh** as well as the respective reduced states. HOMO, LUMO and LUMO+1 (bottom to top) of c) **PBI-Ph** and d) **PBI-OPh**. The corresponding orbitals of **PBI-Ph**$^{\bullet-}$ and **PBI-Ph**$^{2-}$ and **PBI-OPh**$^{\bullet-}$ and **PBI-OPh**$^{2-}$ respectively are visually indistinguishable. Orbitals and electrostatic potential maps were calculated using DFT (B3LYP/6-31g(d)).

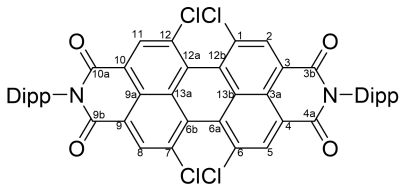

Figure 115 Chemical structures and atom numbering of **PBI-Cl**.

Table 19 Comparison of the calculated bond distances and torsion angles of **PBI-Cl**, **PBI-Cl$^{\bullet-}$** and **PBI-Cl^{2-}**. The numbering of carbon atoms is according to Figure 115.

	PBI-Cl	**PBI-Cl$^{\bullet-}$**	**PBI-Cl^{2-}**
C-C (C6a-C6b, C12a-C12b)	146.8 pm	144.8 pm	143.1 – 143.2 pm
C-C (C1-C2, C5-C6, C7-C8, C11-C12)	140.6 pm	138.6 pm	136.9 – 137.0 pm
C-C (C2-C3, C4-C5, C8-C9, C10-C11)	138.0 pm	139.6 - 139.7 pm	141.3 – 141.4 pm
C-C (C3-C3a, C4-C3a, C9-C9a, C10-C9a)	141.3 pm	141.4 - 141.5 pm	141.6 – 141.7 pm
C-C (C3a-C13b, C9a-C13a)	142.0 pm	142.9 pm	143.9 pm
C-C (C13b-C12b, C13b-C6a, C13a-C6b, C13a-C12a)	143.5 pm	143.6 pm	143.8 pm
C-C (C1-C12b, C6-C6a, C7-C6b, C12-C12a)	140.4 pm	142.2 pm	143.8 – 143.9 pm
C-C (C3-C3b, C4-C4a, C9-C9b, C10-C10a)	148.5 pm - 148.6 pm	146.5 - 146.6 pm	144.7 pm
Torsion angle	35.4°	33.4°/33.5°	31.2°/31.4°

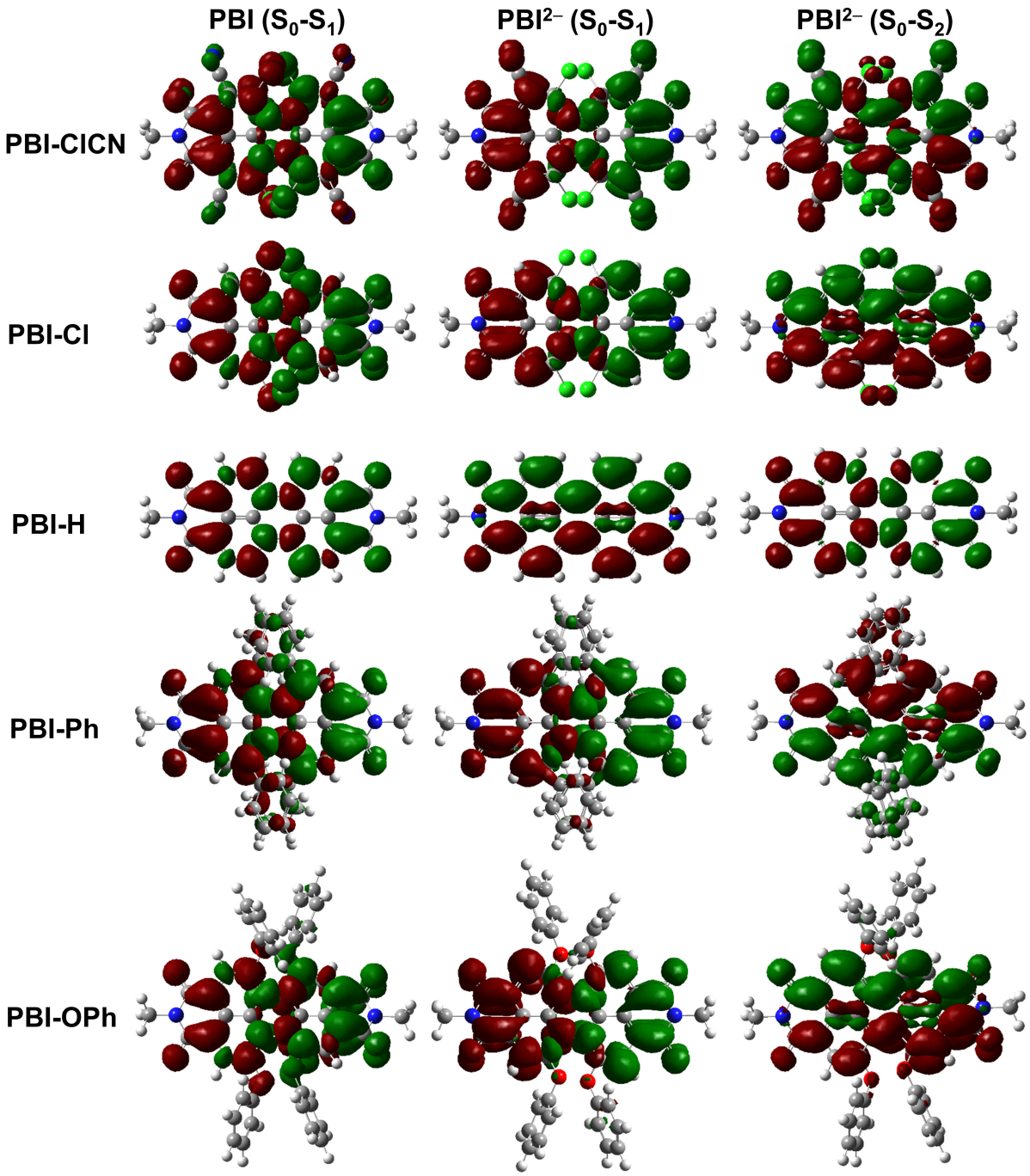

Figure 116 Transition densities (isovalue = 0.0004 a.u.) of the neutral S_0-S_1 (left) and dianionic S_0-S_1 (middle) as well as dianionic S_0-S_2 (right) transitions of **PBI-ClCN**, **PBI-Cl**, **PBI-H**, **PBI-Ph** and **PBI-OPh**.

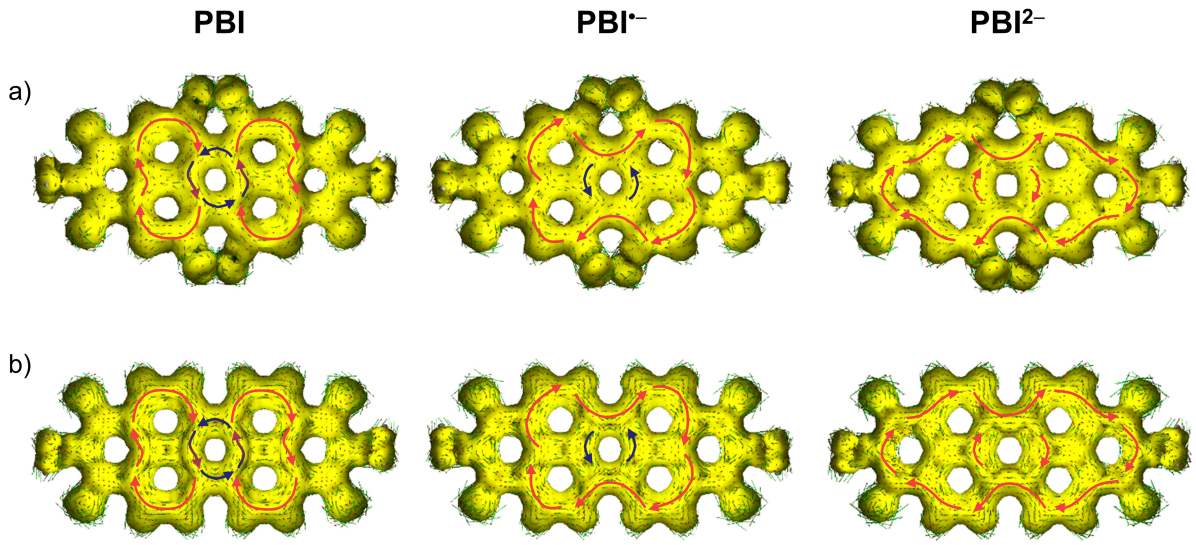

Figure 117 Calculated AICD isosurface plots of PBI, $PBI^{\bullet-}$ and PBI^{2-} of a) **PBI-Cl** and b) **PBI-H**. Clockwise ring current is depicted with red arrows and counter clockwise ring current with blue arrows (isosurface value 0.025).

Table 20 Calculated UV/Vis/NIR transitions for **PBI-ClCN**.

Transitions	% character	λ_{cal} [nm]	Oscillator strength *f*
162 → 165 164 → 165	6.53 93.5	571.03	0.3743
162 → 165 163 → 166 164 → 165	88.5 4.49 7.02	564.01	0.0302
157 → 165 159 → 165 161 → 165	9.01 28.7 62.3	464.71	0.410
156 → 165 158 → 165 160 → 165	34.3 20.3 45.4	460.32	0.0028
155 → 165 156 → 165 157 → 165 159 → 165 161 → 165	2.52 2.40 32.6 27.0 35.5	455.02	0.0641
156 → 165 158 → 165 160 → 165 164 → 169	8.81 39.9 49.0 2.26	438.60	0.0187
154 → 165 156 → 165 158 → 165 160 → 165	3.32 53.5 37.0 6.18	425.93	0.0082
155 → 165 157 → 165 159 → 165 164 → 166	15.0 11.5 9.96 52.4	419.07	0.0158
155 → 165 157 → 165 159 → 165 164 → 166	15.2 30.5 35.4 18.9	416.80	0.0492

Table 21 Calculated UV/Vis/NIR transitions for **PBI-ClCN$^{\bullet-}$**.

Transitions	% character	λ_{cal} [nm]	Oscillator strength *f*
165A → 166A 164B → 165B	75.9 24.1	1036.86	0.0585
165A → 166A 164B → 165B 165A ← 166A	24.3 74.5 1.2	665.96	0.4235
165A → 167A 161B → 165B	98.4 1.58	647.56	0.0267
165A → 168A	100	584.36	0.0011
160A → 166A 164A → 168A 159B → 165B 160B → 166B 161B → 165B	2.91 1.60 1.13 1.62 92.7	465.21	0.0597
161A → 166A 158B → 165B 160B → 165B 161B → 166B	4.14 2.39 90.5 3.01	448.09	0.0090

Table 22 Calculated UV/Vis/NIR transitions for **PBI-ClCN^{2-}**.

Transitions	% character	λ_{cal} [nm]	Oscillator strength *f*
165 → 166 165 ← 166	95.1 4.92	719.15	0.5538
165 → 167 165 → 169	83.6 16.4	601.17	0.0499
165 → 168	100	581.34	0.0029
165 → 167 165 → 169	15.5 84.5	531.39	0.0429
164 → 167 164 → 169 165 → 171	2.21 4.32 93.5	342.52	0.0047

Table 23 Calculated UV/Vis/NIR transitions for **PBI-Cl**.

Transitions	% character	λ_{cal} [nm]	Oscillator strength *f*
140 → 141	100	526.58	0.5139
139 → 141 140 → 145	97.5 2.48	418.46	0.0874
136 → 141	100	393.88	0.0058
131 → 142 132 → 141 133 → 141 135 → 141	2.15 35.6 12.7 49.5	372.17	0.0268
130 → 141 131 → 141 134 → 141	3.66 32.0 64.4	370.97	0.0073
132 → 141 133 → 141 135 → 141 140 → 142	5.34 27.9 4.45 62.3	631.66	0.0038
130 → 141 131 → 141 134 → 141 140 → 143	18.3 58.9 20.1 2.69	358.91	0.0040
132 → 141 133 → 141 135 → 141	47.8 4.46 47.8	355.69	0.0536

Table 24 Calculated UV/Vis/NIR transitions for **PBI-Cl$^{\bullet-}$**.

Transitions	% character	λ_{cal} [nm]	Oscillator strength *f*
141A → 142A 140B → 141B	61.4 38.6	830.49	0.0172
141A → 143A 139B → 141B	98.6 1.38	667.64	0.0311
141A → 142A 140B → 141B	38.9 61.1	587.89	0.5735
141A → 144A 139B → 141B	2.17 97.8	427.16	0.0617
136B → 142B 137B → 141B 138B → 142B 139B → 141B	2.68 93.1 3.09 1.15	414.57	0.0015

Table 25 Calculated UV/Vis/NIR transitions for **PBI-Cl^{2-}**.

Transitions	% character	λ_{cal} [nm]	Oscillator strength *f*
141 → 143	100	583.22	0.0947
141 → 142 141 ← 142	96.98 3.02	571.34	0.6747
141 → 144	100	441.88	0.0074
140 → 143 141 → 145 141 → 146	3.40 4.81 91.8	362.02	0.0082
140 → 143 141 → 146	97.4 2.64	337.46	0.0090
141 → 149 141 → 150	41.3 58.7	300.87	0.0534

Table 26 Calculated UV/Vis/NIR transitions for **PBI-H**.

Transitions	% character	λ_{cal} [nm]	Oscillator strength *f*
108 → 109 108 ← 109	97.4 2.59	524.36	0.6922
102 → 109 104 → 109	23.8 76.2	380.11	0.0049
102 → 109 104 → 109	74.9 25.1	365.08	0.0015

Table 27 Calculated UV/Vis/NIR transitions for **PBI-H$^{\bullet-}$**.

Transitions	% character	λ_{cal} [nm]	Oscillator strength *f*
109A → 111A 108B → 109B	27.1 72.9	773.90	0.0253
109A → 110A	100	648.62	0.0342
103A → 110A 109A → 111A 108B → 109B	1.17 72.8 26.1	530.10	0.7603

Table 28 Calculated UV/Vis/NIR transitions for **PBI-H^{2-}**.

Transitions	% character	λ_{cal} [nm]	Oscillator strength *f*
109 → 110	100	570.61	0.0938
109 → 111 109 ← 111	97.9 2.07	482.09	0.8905
109 → 112	100	487.44	0.0044

Table 29 Calculated UV/Vis/NIR transitions for **PBI-Ph**.

Transitions	% character	λ_{cal} [nm]	Oscillator strength *f*
188 → 189	100	570.60	0.3555
186 → 190 187 → 189 188 → 193	2.37 94.8 2.82	386.66	0.0718
177 → 189 186 → 189 187 → 190 188 → 192	5.17 84.4 3.47 6.99	377.15	0.2671
178 → 189 179 → 189 181 → 189 188 → 191	4.57 69.0 6.37 20.0	344.60	0.0086
176 → 189 179 → 189 187 → 189 188 → 191 188 → 193	2.93 14.6 3.51 73.8 5.22	311.14	0.0062
175 → 189 176 → 190 177 → 189 180 → 189 183 → 189 185 → 189 186 → 191 188 → 190	17.0 8.68 9.72 7.49 29.4 20.0 2.51 5.20	306.00	0.0030
172 → 191 175 → 190 176 → 189 176 → 195 177 → 190 188 → 191	2.34 16.6 68.7 5.10 3.96 3.26	307.70	0.0023
175 → 189 176 → 190 177 → 189 180 → 189 183 → 189 185 → 189 188 → 190	28.9 11.9 16.6 4.13 28.4 6.71 3.30	303.94	0.0079

Table 30 Calculated UV/Vis/NIR transitions for **PBI-Ph**$^{\bullet-}$.

Transitions	% character	λ_{cal} [nm]	Oscillator strength *f*
189A → 190A	26.8	821.94	0.0108
185B → 190B	1.52		
188B → 189B	71.7		
185A → 191A	1.66	679.33	0.4376
189A → 190A	72.5		
189A → 193A	1.31		
185B → 190B	1.55		
188B → 189B	23.0		
188A → 200A	1.28	626.34	0.0888
189A → 191A	97.6		
186B → 189B	1.12		
188A → 191A	7.39	503.73	0.0035
188A → 194A	2.47		
189A → 192A	70.1		
189A → 202A	8.49		
184B → 189B	2.05		
187B → 189B	3.79		
188B → 191B	5.68		
188A → 192A	6.02	456.13	0.0041
188A → 202A	1.17		
189A → 194A	78.0		
189A → 199A	6.10		
189A → 201A	7.53		
188B → 192B	1.18		
188A → 191A	13.8	426.04	0.0184
189A → 192A	17.7		
189A → 200A	6.95		
170B → 189B	1.62		
184B → 189B	10.4		
187B → 189B	26.0		
188B → 191B	23.6		
183A → 193A	1.29	399.00	0.0318
186A → 192A	5.49		
187A → 191A	1.23		
188A → 195A	4.49		
189A → 193A	83.6		
189A → 204A	1.59		
186B → 192B	2.31		
188A → 191A	1.62	382.54	0.0111
180B → 191B	1.17		
184B → 189B	35.9		
186B → 190B	6.89		
187B → 189B	49.7		
188B → 191B	4.74		

Table 31 Calculated UV/Vis/NIR transitions for **PBI-Ph^{2-}**.

Transitions	% character	λ_{cal} [nm]	Oscillator strength f
189 → 190 189 → 193	92.9 7.11	575.80	0.5119
189 → 191 189 → 199	96.6 3.45	548.14	0.2973
189 → 192 189 → 200 189 → 202	93.3 3.18 3.52	520.90	0.0359
188 → 192 189 → 194 189 → 199 189 → 201	2.52 50.9 31.5 15.0	450.41	0.0440
189 → 190 189 → 193	7.55 92.4	433.96	0.1845
189 → 192 189 → 95 189 → 200	2.11 95.4 2.48	387.68	0.0106
189 → 194 189 → 199	48.1 51.9	374.13	0.0375

Table 32 Calculated UV/Vis/NIR transitions for **PBI-OPh**.

Transitions	% character	λ_{cal} [nm]	Oscillator strength *f*
204 → 205	100	477.05	0.6518
194 → 205 197 → 205 202 → 205 203 → 205	2.48 3.52 10.4 83.6	359.77	0.2252
197 → 205 201 → 205 202 → 205 203 → 205	6.19 12.0 72.6 9.12	348.76	0.1206
197 → 205 201 → 205 202 → 205 203 → 207 204 → 207	5.08 62.7 22.6 4.36 5.25	303.96	0.0225
189 → 205 204 → 206	5.99 94.0	298.51	0.0031
187 → 205 188 → 205 190 → 205 197 → 205 198 → 205 199 → 205 200 → 205 203 → 205 204 → 207 204 → 208	3.95 4.29 11.8 23.1 2.68 7.84 10.2 9.09 22.9 4.16	292.17	0.0130
188 → 205 190 → 205 194 → 205 197 → 205 199 → 205 200 → 205 201 → 205 204 → 207	5.82 5.06 9.93 4.03 7.11 25.6 11.0 31.5	290.90	0.0156

Table 33 Calculated UV/Vis/NIR transitions for **PBI-OPh**$^{\bullet-}$.

Transitions	% character	λ_{cal} [nm]	Oscillator strength *f*
205A → 206A	73.3	767.46	0.0624
204B → 205B	26.7		
204A → 217A	1.17	634.20	0.0644
205A → 207A	98.8		
198A → 207A	1.47	570.46	0.6470
205A → 206A	25.6		
198B → 206B	1.99		
204B → 205B	70.9		
204A → 218A	2.11	424.98	0.0117
205A → 208A	22.4		
205A → 210A	2.70		
205A → 211A	3.70		
205A → 212A	22.5		
205A → 213A	8.06		
205A → 214A	32.7		
205A → 215A	4.50		
205A → 218A	1.33		
204A → 207A	1.24	356.10	0.1527
196B → 205B	3.21		
197B → 205B	5.12		
202B → 205B	3.42		
202B → 206B	2.46		
203B → 205B	79.4		
203B → 206B	5.11		
204A → 207A	2.82	349.43	0.0285
195B → 205B	1.44		
196B → 205B	6.79		
201B → 205B	6.44		
202B → 205B	72.6		
202B → 206B	5.76		
203B → 205B	1.73		
203B → 206B	2.39		
204A → 207A	6.83	328.69	0.0108
205A → 210A	5.16		
205A → 212A	4.90		
205A → 214A	1.64		
205A → 217A	11.1		
205A → 218A	17.5		
196B → 205B	20.4		
204B → 207B	32.4		

Table 34 Calculated UV/Vis/NIR transitions for **PBI-OPh^{2-}**.

Transitions	% character	λ_{cal} [nm]	Oscillator strength *f*
205 → 206	4.54	555.80	0.2046
205 → 207	70.3		
205 → 208	2.66		
205 → 209	18.0		
205 → 211	4.50		
205 → 206	97.2	550.25	0.7577
205 → 207	2.82		
205 → 207	6.39	430.38	0.0355
205 → 208	26.6		
205 → 209	22.4		
205 → 210	2.30		
205 → 211	3.78		
205 → 212	5.88		
205 → 216	30.3		
205 → 221	2.32		
205 → 208	45.1	429.54	0.0054
205 → 209	10.4		
205 → 210	17.0		
205 → 211	3.23		
205 → 212	2.60		
205 → 213	8.10		
205 → 217	4.71		
205 → 220	4.83		
205 → 222	3.98		
205 → 207	4.40	412.89	0.0018
205 → 208	12.5		
205 → 209	40.8		
205 → 210	31.9		
205 → 211	5.27		
205 → 213	5.03		
205 → 207	14.0	396.20	0.0321
205 → 208	9.85		
205 → 209	11.5		
205 → 210	15.8		
205 → 212	20.5		
205 → 216	28.4		
205 → 207	3.88	392.47	0.0241
205 → 210	17.9		
205 → 211	73.9		
205 → 212	4.27		
205 → 208	9.04	380.94	0.0126
205 → 210	17.0		
205 → 211	5.89		
205 → 212	13.9		
205 → 213	21.5		
205 → 216	20.4		
205 → 217	3.10		
205 → 219	3.32		
205 → 220	5.89		
205 → 211	4.97	363.43	0.0446
205 → 212	56.2		
205 → 213	30.7		
205 → 216	8.15		
205 → 213	3.38	350.44	0.0162
205 → 214	93.9		
205 → 216	2.67		

Table 35 Experimental and calculated transition dipole moments (μ_{eg}) of the PBIs in Debye

	μ_{eg} (Experimental) [D][a]			μ_{eg} (Calculated) [D][b]		
	PBI	**PBI$^{\bullet-}$**	**PBI^{2-}**	**PBI**	**PBI$^{\bullet-}$**	**PBI^{2-}**
PBI-ClCN	–[c]	–[c]	–[c]	6.7	3.6	9.2
PBI-Cl	8.7	3.8	12.6	7.6	1.7	9.1
PBI-H	8.8	3.4	3.5	8.8	2.2	3.4
PBI-Ph	6.4	3.1	10.0	6.6	8.0	8.0
PBI-OPh	8.7	3.5	12.4	8.1	3.2	9.4

[a] Obtained by integration of the respective S_0-S_1 or D_0-D_1 transition (see Table 36). [b] Taken from the TD-DFT calculations of the absorption spectra performed by the Multiwfn program.[307] [c] Not determined due to possible significant overestimation as multiple transitions are present in the respective absorption bands.

The transition dipole moment (μ_{eg}) has been calculated from the integral of the lowest energy absorption band according to equation (Eq. 3)

$$\left|\mu_{eg}\right|^2 = \frac{3hc\varepsilon_0 \ln 10}{2\pi^2 N_A} \cdot \int_{\tilde{\nu}_1}^{\tilde{\nu}_2} \frac{\varepsilon(\tilde{\nu})}{\tilde{\nu}} d\tilde{\nu} \qquad \text{(Eq. 3)}$$

with the molar extinction coefficient $\varepsilon(\tilde{\nu})$, speed of light c = 2.9979·10^{10} cm s^{-1}, Planck's constant h = 6.6262·10^{-34} J s, permittivity ε_0 = 8.8542·10^{-12} F m^{-1} and Avogadro's number N_A = 6.0221·10^{23} mol^{-1}.

Table 36 Integration areas for the determination of the transition dipole moments (μ_{eg}) according to equation Eq. 3 of the PBIs from the experimental absorption spectra (Table 35).

	PBI	**PBI$^{\bullet-}$**	**PBI^{2-}**
PBI-Cl	440-580 nm	980-1125 nm	530-760 nm
PBI-H	400-600 nm	900-1025 nm	630-700 nm
PBI-Ph	510-715 nm	1010-1285 nm	525-735 nm
PBI-OPh	480-625 nm	1030-1165 nm	515-790 nm

Chapter 6

Summary and Conclusion

The increased research interest in polycyclic aromatic hydrocarbons (PAHs) due to their favorable properties for the application in organic electronics like organic solar cells (OSCs), organic thin film transistors (OTFTs) and organic light emitting diodes (OLEDs), has led to a rapid development in the bottom-up synthesis of tailor-made novel materials with high carbon content (*Chapter 2.1*). In recent years, the higher solubility and resulting easier processability of nonplanar PAHs have been one of the driving forces in the development of methods to introduce distortion into π-systems. Examples on how to achieve this have been discussed in *Chapter 2.2*, including the variation of the ring size to achieve Gaussian positive curvature with rings containing less than six carbon atoms, e.g., in corannulene and sumanene or Gaussian negative curvature by including larger, especially seven membered rings. Furthermore, the introduction of groups in steric vicinity to achieve distortion through steric repulsion as well as the connection of planar scaffolds via 3D linkers have been elucidated. Examples including two or more of these motifs furthermore showed the vast possibilities in the design of novel nonplanar PAHs. The group of nonplanar organic dicarboximides, e.g., rylene imides have received considerable attention due to their good electron accepting properties as well as intriguing structural variability and high conformational stability upon proper substitution (*Chapter 2.3*). Especially perylene bis(dicarboximides) (PBIs) have been shown to be highly functional due to their strong and distinct light absorption, which can be tuned readily by proper substitution and fluorescence quantum yields up to unity. Thus, the main focus of this thesis was to synthesize novel nonplanar PAHs based on corannulene and PBI π-scaffold and elucidate their properties and self-assembly in solution as well as in the solid state.

Based on the previously investigated corannulene bis(dicarboximide) **1b**,[165] the highly soluble corannulene bis(dicarboximide) **1a** with long trialkylphenyl chains in imide position could be obtained by Suzuki-coupling and direct arylation of corannulene diboronic acid ester and the corresponding naphthalene imide precursors (*Chapter 3*, Figure 118). The bowl-to-bowl inversion was studied by temperature-dependent ^{1}H-NMR studies, revealing a rate constant *k*

of 65.2 s^{-1} and a free energy of activation of 78.4 kJ mol^{-1} indicating a slow bowl-to-bowl inversion at room temperature, which should not disturb the envisioned aggregation. Despite the similar properties of the monomeric **1a** and **1b** in dichloromethane (DCM) solution, aggregation could only be observed for **1a** upon dissolution in less polar solvents like methyl cyclohexane, toluene or CCl_4. Investigation by UV/Vis/NIR as well as ^{1}H- and DOSY-NMR spectroscopy resulted in the assignment of the aggregated species to thermodynamically stable dimers.

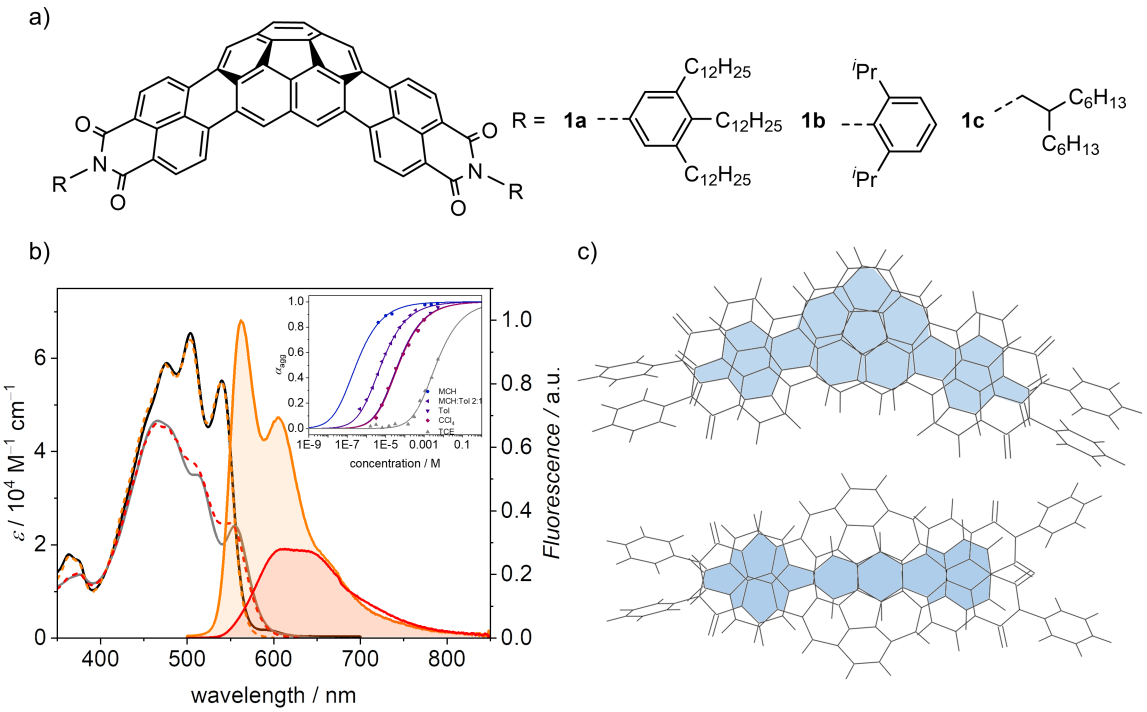

Figure 118 a) Chemical structure of electron-poor corannulene dicarboximides **1a-1c**. b) The UV/Vis/NIR absorption spectra (monomer: black, dimer: grey), fluorescence (solid line) and excitation spectra (dashed line) of monomer (orange) as well as dimer (red) of **1a** in toluene at room temperature (monomer: $c_0 = 1 \cdot 10^{-7}$ M, dimer: $c_0 = 2 \cdot 10^{-3}$ M). Inset: Molar fraction of aggregated molecules α_{agg} as a function of the concentration in different solvents fitted with the dimer model. c) Comparison of the minimal π-overlap of the two proposed structures for the dimer of **1a**.

The extraordinary stability was again highlighted by comparison of the dimerization constants of **1a** in different solvents to a PBI congener bearing the same imide residue, which self-assembles in an isodesmic fashion. In every solvent, the dimerization constant of **1a** is approximately two orders of magnitude higher than the isodesmic aggregation constant of the PBI. The color of emitted light of **1a** has been found to change from yellow for the monomer to red for the dimer, which is reflected by a bathochromic shift and broadening of the emission spectrum upon dimerization. Two structures were proposed for the arrangement of the two molecules of **1a** in a dimer of which the one with parallel aligned chromophores is governed by larger π-π-interactions and the structure with antiparallel aligned molecules by dipolar interactions (Figure 118c). An additional derivative of **1a**, with more flexible alkyl chains in

imide position **1c** has been synthesized as well within this thesis. Further organic photovoltaic (OPV) studies in OSCs in combination with the donor polymer **PCE-10** yielded a highest to date reported maximum power conversion efficiency PCE_{max} of up to 2.1% for a corannulene derivative.[313]

Changing the central π-system from corannulene to perylene, nonplanar PBIs **2a-6a** were obtained by fourfold substitution of a tetrachlorinated PBI precursor with various aromatic groups in *bay* position by Suzuki-coupling (*Chapter 4*). The large aryl groups impose a high sterical crowding in the *bay* area which results in the distortion of the chromophore core. The structure of three of these molecules could for the first time be unambiguously determined by single crystal X-ray analysis, confirming the highly twisted arrangement of the two naphthalene planes in the PBI core with twist angles up to 36.6° for **4a** as well as the presence of two atropo-enantiomers due to the axial chirality of the core (Figure 119b). While the solid-state arrangement of the phenyl-derivative (**2c**) and 2-naphthyl-derivative (**4a**) has been shown to be predominantly determined by interactions between the chromophore cores, the packing in **6a**, however, is governed by the largest pyrene substituents, since they exhibit the same packing, also found in pristine pyrene single crystals. Conformational analysis in solution by ^{1}H-NMR spectroscopy showed the ability of the smaller aryl residues to rotate freely around the C-C bond connecting them to the chromophore, while larger substituents tend to form a total of up to fourteen stable conformational isomers, which could be successfully distinguished by extensive analysis of the ^{1}H-NMR spectra. The stability of the isomers as well as the ability of the substituents to rotate has furthermore been shown to be dependent on the position of the attachment in the aryl-substituent. In the 2-naphthyl (**4a**) derivative, rotation of the naphthyl residues could be observed by ^{1}H-NMR spectroscopy while in the 1-naphthyl (**5a**) derivative, only a mixture of all fourteen possible conformational isomers could be found, indicating the high stability of each conformation. UV/Vis/NIR and fluorescence spectroscopy showed reduced molar absorption coefficients as well as a significant bathochromic shift compared to the planar unsubstituted PBI. The atropo-enantiomers of **2a-2e**, **3a** and **4a** could be separated by chiral HPLC and analyzed by circular dichroism (CD) and circularly polarized luminescence (CPL) spectroscopy, showing a mirror image relation with broad monosignate bands for the S_0-S_1 transition and a bisignate Cotton effect for the S_0-S_2 transition. Temperature-dependent CD studies were conducted to evaluate the stability of the atropo-enantiomers towards racemization. The free enthalpies of activation were determined to be 119.6 kJ mol^{-1} and 118.6 kJ mol^{-1} for **2a** and **4a**, respectively. This demonstrates the high conformational stability at room temperature, which enables the separation of both atropo-enantiomers.

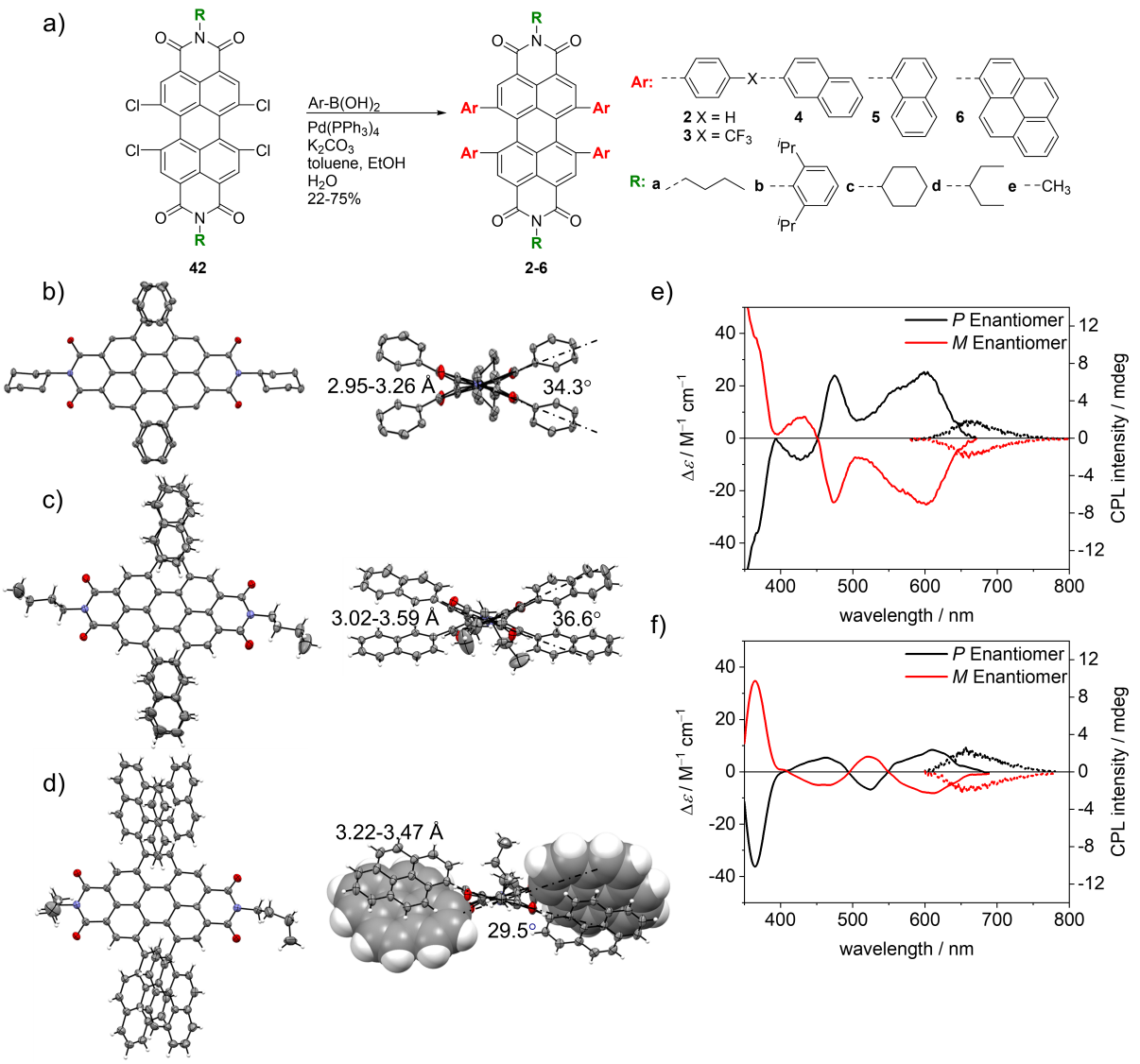

Figure 119 a) Chemical structures of synthesized tetraarylated PBIs **2a-6a**. Single crystal X-ray structures of the *M*-atropo-enantiomer of b) **2c**, c) **4a** and d) **6a** obtained from a racemic mixture of the respective PBI. CD and CPL spectra of e) **2a** and f) **4a** in DCM ($c_0 = 2 \cdot 10^{-6}$ M) at room temperature.

The CPL spectra are among the most bathochromic shifted spectra of small organic molecules with g_{lum} values of 10^{-3} which is in the typical order of magnitude for small organic molecules.

In order to gain concise insights into the absorption and emission properties of a series of five PBIs upon reduction to the radical anion and dianion, experimental and theoretical methods were combined (*Chapter 5*). The four *bay* substituted PBIs **PBI-ClCN**, **PBI-Cl**, **PBI-Ph** and **PBI-OPh** and the unsubstituted **PBI-H** were investigated by electrochemical as well as spectroscopic methods (Figure 120). Cyclovoltammetry (CV) and square wave voltammetry (SWV) measurements illustrate the large range of the first reduction potentials of nearly 1 V between the most electron rich and poor PBI.

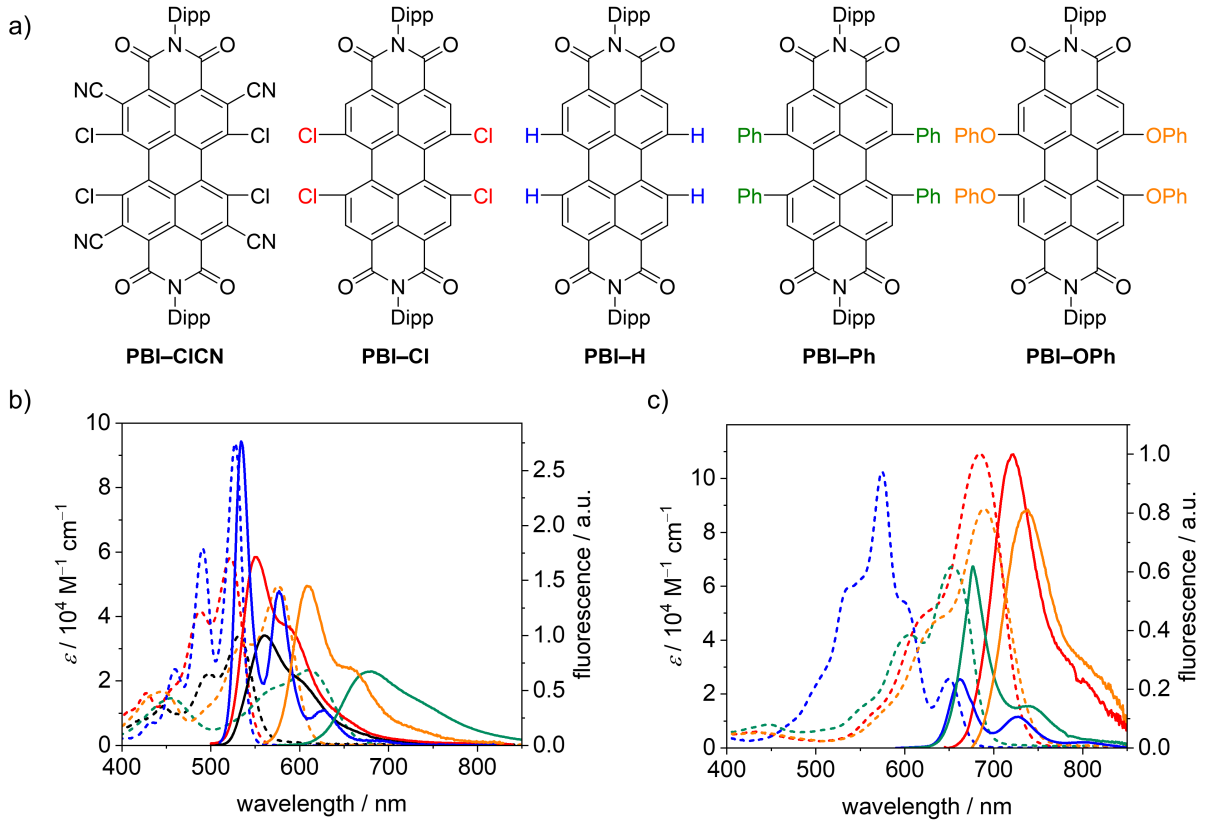

Figure 120 a) Chemical structure of the PBIs investigated in their neutral and reduced states and the respective absorption (dashed) and emission (solid) spectra of the b) neutral and c) dianionic PBIs in DCM (**PBI-ClCN** (black), **PBI-Cl** (red), **PBI-H** (blue), **PBI-Ph** (green) and **PBI-OPh** (orange), $c_0 = 4 \cdot 10^{-4}$ M for absorption, $c_0 = 1 \cdot 10^{-5}$ M for fluorescence of PBI and $c_0 = 1 \cdot 10^{-4}$ M for fluorescence of PBI^{2-} at room temperature using TBAHFP (0.1 M) as electrolyte.

While the chemical reduction of these PBIs was successful in obtaining the desired reduced species, it failed in long-term stability of the PBI anions, which was needed for the optical measurements as the reoxidation could be monitored by absorption spectroscopy. Thus, the radical anions and dianions were generated in situ electrochemically for the optical characterization. Spectroelectrochemical UV/Vis/NIR measurements revealed bathochromic shifts of up to 286 nm of the absorption maxima compared to the spectra of the neutral PBIs upon the first reduction, with the most red-shifted band being relatively far in the NIR region up to 1243 nm for **PBI-ClCN**. Upon further reduction to the dianions, a hypsochromic shift of different extent was observed for all derivatives and the molar extinction coefficient increased to approximately 100000 M^{-1} cm^{-1}. The emission properties of the reduced PBIs were furthermore studied in a custom-built cell, revealing the non-emissive character of the radical anions and a decrease of the fluorescence quantum yields for the dianions compared to their neutral states. This has been ascribed to an increased number of nonradiative decay pathways in the dianions but still afforded NIR fluorescence of up to 18% for **PBI-H^{2-}**. DFT and TD-DFT calculations were conducted to help in the interpretation of the electronic and structural

changes as well as to rationalize the experimental absorption spectra. Especially the low oscillator strength for the S_0-S_1 transition of the dianion of **PBI-H** compared to the other dianions of *bay* substituted derivatives was found to stem from the difference in transition density. These investigations enabled the establishment of a systematic library of opto-electronic properties of PBIs in their different reduced states, which will enable researchers in the field of transient absorption to compare their obtained data with the herein presented.

In conclusion, different nonplanar PAHs with corannulene or perylene as the central π-system were successfully synthesized and investigated in this thesis. The investigations covered the self-assembly behavior of novel corannulene derivatives in solution and the systematic variation of the imide and *bay* residues in tetraarylated PBIs, resulting in structural and chemical changes, which proof to be useful in the deeper understanding of the intermolecular interactions, especially in the solid state. The concise elucidation of the properties of a series of PBIs in their neutral and reduced states should be of value for the analysis of PBI based molecules and materials by transient absorption spectroscopy. Some of the herein described dinaphthylcorannulene[313] and twisted perylene derivatives[314] have already been applied successfully as NFA material in OSCs.

Chapter 7

Zusammenfassung und Fazit

Aufgrund der vorteilhaften Eigenschaften für die Anwendung in der organischen Elektronik wie beispielsweise organischen Solarzellen (OSC), organischen Dünnschichttransistoren (OTFT) und organischen Leuchtdioden (OLED) hat sich das Forschungsinteresse an polyzyklischen aromatischen Kohlenwasserstoffen (PAK) erhöht. Dies führte zu einer rasanten Entwicklung bei deren Synthese, ausgehend von kleineren Molekülen als Vorstufen von maßgeschneiderten neuartigen Materialien mit hohem Kohlenstoffgehalt (*Kapitel 2.1*). In den letzten Jahren war eine der treibenden Kräfte bei der Entwicklung von PAKs die Einführung von Störungen der Planarität, womit eine höhere Löslichkeit und sich eine daraus resultierende leichtere Verarbeitungsfähigkeit ergibt. Beispiele dafür, wie dies erreicht werden kann, wurden in *Kapitel 2.2* erörtert, einschließlich der Variation der Ringgröße zur Realisierung einer positiven Gauß'schen Krümmung mit Ringen, die weniger als sechs Kohlenstoffatome enthalten, z.B. in Corannulen und Sumanen, oder einer negativen Gauß'schen Krümmung durch Integration größerer, insbesondere siebengliedriger Ringe. Darüber hinaus wurden die Einführung von Gruppen, welche in räumlicher Nähe zueinander stehen zur Realisierung von Verzerrungen aufgrund sterischer Abstoßung sowie die Verbindung von planaren Gerüsten mittels 3D-Verbindungseinheiten aufgeklärt. Beispiele, die zwei oder mehr dieser Motive enthalten, zeigten darüber hinaus die weitreichenden Möglichkeiten für das Design neuartiger nicht-planarer PAK. Die Familie der nicht-planaren organischen Dicarboximide, z.B. Rylenimide, erhielt aufgrund ihrer guten Elektronenakzeptoreigenschaften sowie ihrer faszinierenden strukturellen Variabilität und hohen Konformationsstabilität bei geeigneter Substitution große Aufmerksamkeit (*Kapitel 2.3*). Insbesondere Perylen-bis(dicarboximide) (PBIs) haben sich aufgrund ihrer starken und charakteristischen Lichtabsorptionsfähigkeit, die durch geeignete Substitution leicht eingestellt werden kann und Fluoreszenzquantenausbeuten bis zu 100% als hochfunktionell erwiesen. Das Hauptaugenmerk dieser Arbeit lag daher auf der Synthese neuartiger nicht-planarer PAK auf der Basis von Corannulen und PBI π-Gerüsten sowie der Untersuchung ihrer Eigenschaften und ihres Selbstorganisationsvermögens in Lösung und im Festkörper.

Ausgehend von dem zuvor untersuchten Corannulen-bis(dicarboximid) **1b**,[165] konnte das gut lösliche Corannulen-bis(dicarboximid) **1a** mit langen Trialkylphenylketten in Imidposition durch Suzuki-Kupplung und direkte Arylierung von Corannulendiborsäureester mit den entsprechenden Naphthalimid-Vorstufen erhalten werden (*Kapitel 3*, Abbildung 1). Die Schaleninversion wurde mittels temperaturabhängiger ^{1}H-NMR Studien untersucht, welche eine Geschwindigkeitskonstante k von 65.2 s^{-1} und eine freie Aktivierungsenergie von 78.4 kJ mol^{-1} zeigten, was auf eine langsame Schaleninversion bei Raumtemperatur hindeutet, die die angestrebte Aggregation nicht beeinträchtigen sollte. Trotz der ähnlichen Eigenschaften der monomeren Moleküle **1a** und **1b** in Dichlormethan (DCM), konnte die Aggregation lediglich für **1a** in weniger polaren Lösungsmitteln wie Methylcyclohexan, Toluol oder CCl_4 beobachtet werden. Untersuchungen mittels UV/Vis/NIR sowie ^{1}H- und DOSY-NMR Spektroskopie ergaben eine Einordnung der aggregierten Spezies als thermodynamisch stabile Dimere.

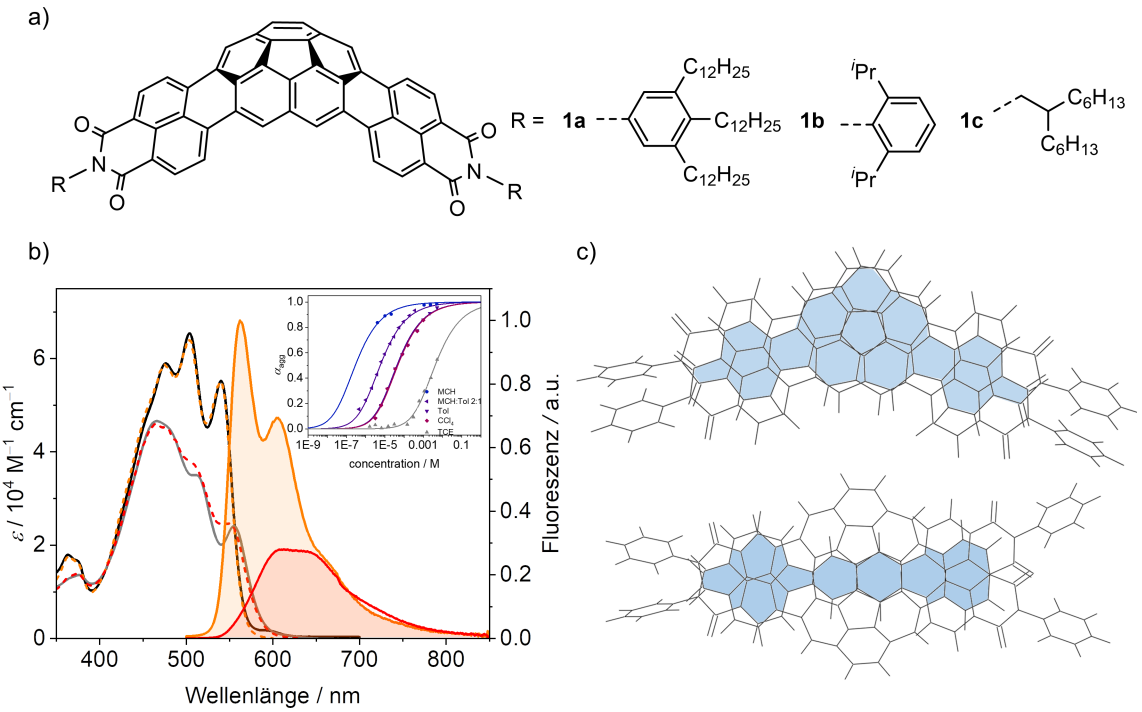

Die außergewöhnliche Stabilität der Dimere wurde durch den Vergleich der Dimerisierungskonstanten von **1a** in verschiedenen Lösungsmitteln mit einem verwandten PBI, welches denselben Imidrest aufweist und nach dem isodesmischen Modell aggregiert,

hervorgehoben. Die Dimerisierungskonstante von **1a** ist in jedem untersuchten Lösungsmittel etwa zwei Größenordnungen größer als die isodesmische Aggregationskonstante des PBIs. Die Farbe des von **1a** emittierten Lichts verändert sich von gelb für das Monomer zu rot für das Dimer, was sich ebenfalls in einer bathochromen Verschiebung und einer Verbreiterung des Emissionsspektrums widerspiegelt. Für die Anordnung der beiden Moleküle von **1a** in einem Dimer wurden zwei mögliche Strukturen vorgeschlagen, von denen diejenige mit parallel ausgerichteten Chromophoren durch größere π-π-Wechselwirkungen und die Struktur mit antiparallel ausgerichteten Molekülen durch dipolare Wechselwirkungen favorisiert wird (Abbildung 1c). Ein weiteres Derivat von **1a** mit flexiblen Alkylketten in der Imidposition **1c** wurde im Rahmen dieser Arbeit ebenfalls synthetisiert. Weitere Studien zur Anwendung dieses Derivates **1c** in organischer Photovoltaik (OPV) in OSCs in Kombination mit dem Donorpolymer **PCE-10** ergaben die bisher höchste berichtete maximale Energieumwandlungseffizienz PCE_{max} für ein Corannulenderivat von bis zu 2.1%.[313]

Durch die Änderung des zentralen π-Systems von Dinaphthylcorannulen zu Perylen konnten die nicht-planaren PBIs **2a-6a** durch vierfache Substitution einer vierfachchlorierten PBI-Vorstufe mit verschiedenen aromatischen Gruppen in Buchtposition durch Suzuki-Kupplung erhalten werden (*Kapitel 4*). Die großen Arylgruppen weisen einen hohen sterischen Anspruch auf, was zu einer Verdrehung des Chromophorkerns führt. Die Struktur von drei dieser Moleküle konnte erstmals durch röngenkristallographische Analyse bestimmt werden, wobei die stark verdrehte Anordnung der beiden Naphthalinebenen im PBI-Kern mit Verdrehungswinkeln von bis zu 36.6° für **4a**, sowie die Anwesenheit von zwei Atropo-Enantiomeren aufgrund der axialen Chiralität des Kerns, bestätigt wurden (Abbildung 2b). Während die Packung des Phenyl-Derivats (**2c**) und des 2-Naphthyl-Derivats (**4a**) im Festkörper in erster Linie durch Wechselwirkungen zwischen den Chromophorkernen bestimmt wird, wird die Packung von **6a** im Festkörper von den sterisch anspruchsvollen Pyrensubstituenten kontrolliert, da diese die gleiche Anordnung aufweisen, die auch in reinen Pyren Einkristallen zu finden ist. Die Analyse der Konformation in Lösung mittels ^{1}H-NMR Spektroskopie zeigte, dass die kleineren Arylreste in der Lage sind, frei um die C-C-Bindung zum Chromophor zu rotieren, während größere Substituenten bis zu insgesamt vierzehn Stereoisomere liefern, die durch eine umfassende Analyse der ^{1}H-NMR Spektren erfolgreich unterschieden werden konnten. Die Stabilität der Isomere, sowie die Fähigkeit der Rotation der Arylsubstituenten ist des Weiteren von der Position der Bindung im Aryl-Substituenten abhängig. Im 2-Naphthylderivat (**4a**) konnte die Rotation der Naphthylreste mittels ^{1}H-NMR Spektroskopie beobachtet werden, während im 1-Naphthylderivat (**5a**) lediglich eine Mischung

aller vierzehn möglichen Stereoisomere gefunden werden konnte, was auf die hohe Stabilität jedes einzelnen Isomers hindeutet.

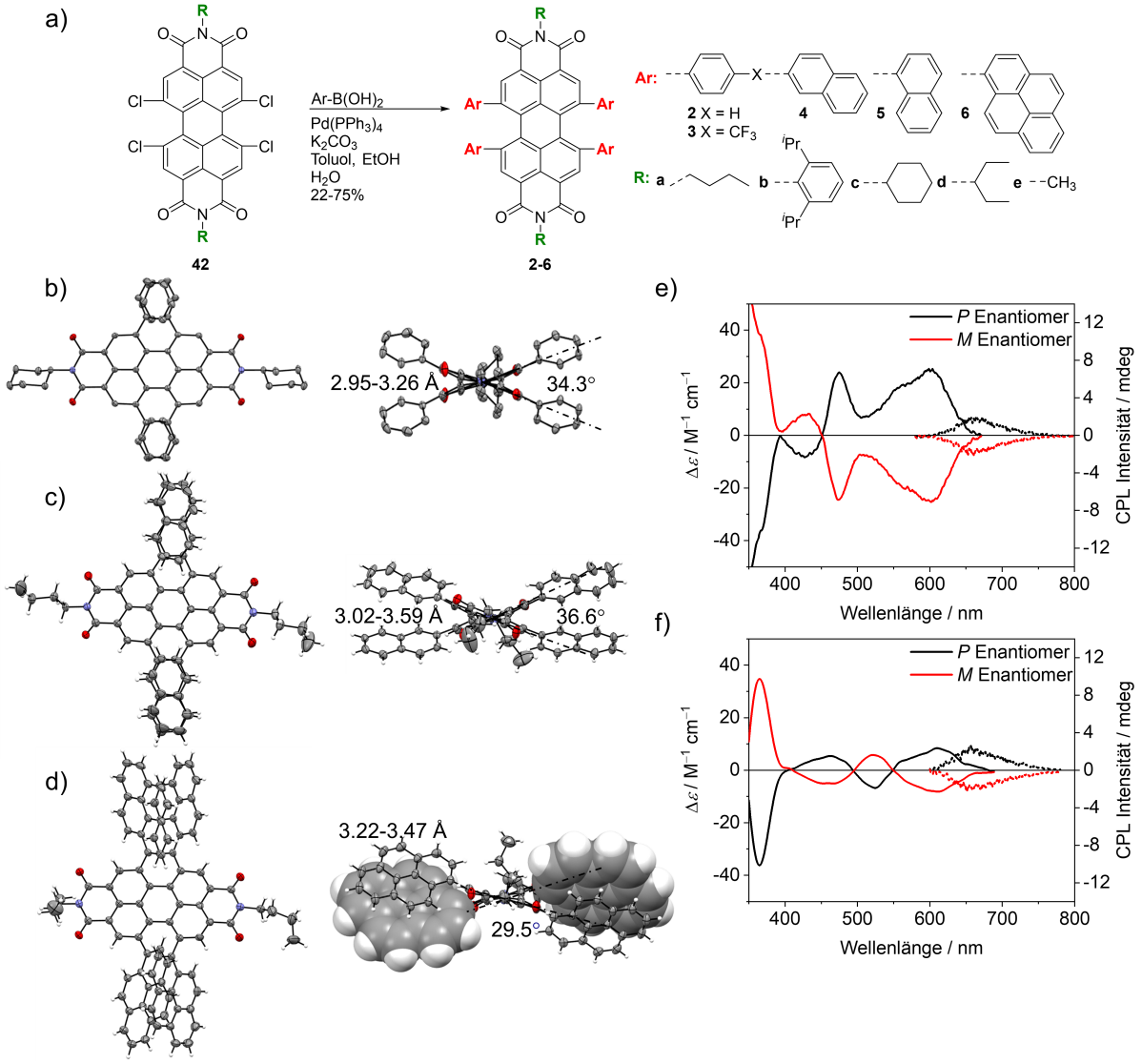

Abbildung 2 a) Chemische Struktur der synthetisierten tetraarylierten PBIs **2a-6a**. Mittels Röntgenstrukturanalyse erhaltene Einkristallstrukturen der *M*-Atropo-Enantiomere von b) **2c**, c) **4a** und d) **6a**. CD und CPL Spektren von e) **2a** und f) **4a** in DCM ($c_0 = 2 \cdot 10^{-6}$ M) bei Raumtemperatur.

Die UV/Vis/NIR- und Fluoreszenzspektren zeigten reduzierte molare dekadische Absorptionskoeffizienten sowie eine signifikante bathochrome Verschiebung im Vergleich zu einem planaren, unsubstituierten PBI. Die Atropo-Enantiomere von **2a-2e**, **3a** und **4a** konnten mit Hilfe von HPLC an einer chiralen stationären Phase getrennt werden und mittels Zirkulardichroismus (CD) und zirkular polarisierter Lumineszenzspektroskopie (CPL) charakterisiert werden. Dabei zeigte sich eine spiegelbildliche Beziehung mit breiten Banden für den S_0-S_1 Übergang und einem bisignaten Cotton-Effekt für den S_0-S_2 Übergang. Temperaturabhängige CD-Studien wurden durchgeführt, um die Stabilität der Atropo-Enantiomere gegenüber Razemisierung einzuschätzen. Die freien Aktivierungsenthalpien

konnten hierbei mit 119.6 kJ mol^{-1} und 118.6 kJ mol^{-1} für **2a** und **4a** bestimmt werden. Dies zeigt die hohe Konformationsstabilität bei Raumtemperatur, die die Trennung der beiden Atropo-Enantiomere ermöglichte. Die CPL-Spektren gehören zu den am stärksten bathochrom verschobenen Spektren kleiner organischer Moleküle mit g_{lum} Werten von 10^{-3}, was in der typischen Größenordnung für kleine Moleküle liegt.

Um präzise Einblicke in die Absorptions- und Emissionseigenschaften einer Reihe von fünf PBIs und deren Radikalanionen und Dianionen durch Reduktion zu erhalten, wurden experimentelle und theoretische Methoden kombiniert (*Kapitel 5*). Die vier buchtsubstituierten PBIs **PBI-ClCN**, **PBI-Cl**, **PBI-Ph** and **PBI-OPh** sowie das unsubstituierte **PBI-H** wurden sowohl mittels elektrochemischer als auch mit spektroskopischen Methoden untersucht (Abbildung 3). Cyclovoltammetrie- (CV) und Rechteckwellenvoltammetrie (SWV) Messungen verdeutlichen den großen Bereich von fast 1 V, der zwischen dem elektronenreichsten und elektronenärmsten PBI abgedeckt wird. Zwar war es möglich, die gewünschten reduzierten Spezies durch chemische Reduktion erfolgreich zu erhalten, jedoch scheiterten die optischen Messungen dieser Spezies an deren rascher Reoxidation, welche mittels Absorptionsspektroskopie verfolgt werden konnte. Aufgrund dessen wurden die Radikalanionen und die Dianionen der PBIs für deren optische Charakterisierung in-situ elektrochemisch erzeugt. Spektroelektrochemische UV/Vis/NIR-Messungen zeigten eine bathochrome Verschiebung der Absorptionsmaxima der Radikalanionen um bis zu 286 nm im Vergleich zu den Spektren der neutralen PBIs, wobei die am stärksten rotverschobenen Banden vergleichbar weit im NIR-Bereich liegen, mit einer Verschiebung bis zu 1243 nm für **PBI-ClCN**. Bei der Reduktion zu den Dianionen durch das Anlegen eines negativeren Potenzials konnte bei allen Derivaten eine hypsochrome Verschiebung der Absorptionsspektren unterschiedlichen Ausmaßes festgestellt werden. Der molare Extinktionskoeffizient stieg für beinahe alle PBIs auf 100000 M^{-1} cm^{-1}.

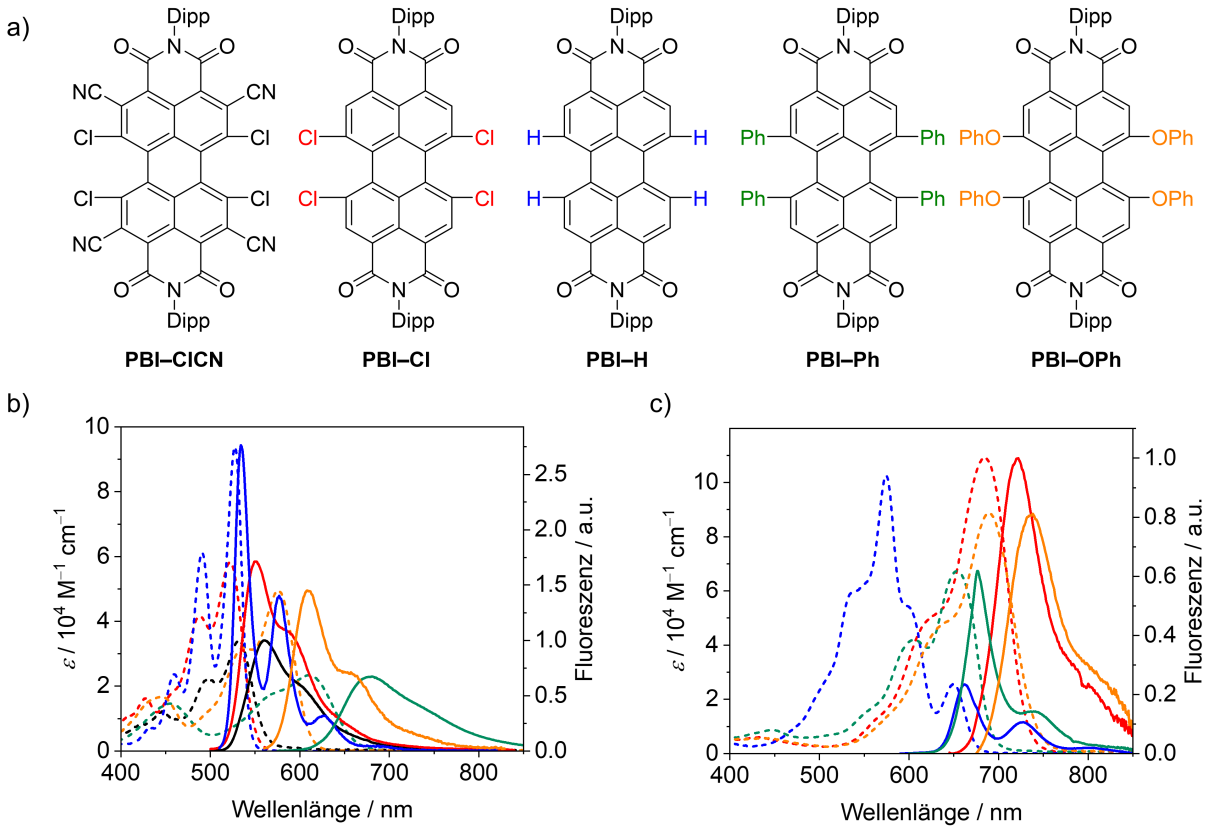

Abbildung 3 a) Chemische Struktur der untersuchten PBIs, welche in ihrem neutralen und reduziertem Zustand untersucht wurden und die jeweiligen Absorptions- (gestrichelte Linie) und Emissionsspektren (durchgezogene Linie) der b) neutralen und c) dianionischen PBIs in DCM. (**PBI-ClCN** (schwarz), **PBI-Cl** (rot), **PBI-H** (blau), **PBI-Ph** (grün) und **PBI-OPh** (orange), $c_0 = 4 \cdot 10^{-4}$ M für die Absorption, $c_0 = 1 \cdot 10^{-5}$ M für die Fluoreszenz des PBI und $c_0 = 1 \cdot 10^{-4}$ M für die Fluoreszenz von PBI^{2-} bei Raumtemperatur unter Verwendung von TBAHFP (0.1 M) als Leitsalz.

Die Emissionseigenschaften der reduzierten PBIs wurde darüber hinaus in einer für diesen Zweck angepassten Zelle untersucht. Dabei zeigte sich, dass die Radikalanionen nicht emittierend sind und die Fluoreszenzquantenausbeute der Dianionen im Vergleich zu ihren neutralen Zuständen abnimmt. Dies wurde auf eine erhöhte Menge nichtstrahlender Desaktivierungswege in den Dianionen zurückgeführt, welche jedoch immer noch eine NIR-Fluoreszenz von bis zu 18% für **PBI-H^{2-}** erreichten. Desweiteren wurden DFT und TD-DFT-Rechnungen durchgeführt, um die elektronischen und strukturellen Veränderungen besser interpretieren zu können und die experimentell erhaltenen Absorptionsspektren zu erklären. Insbesondere die niedrige Oszillatorstärke für den S_0-S_1 Übergang des Dianions von **PBI-H** im Vergleich zu den Dianionen der anderen buchtsubstituierten PBIs konnte durch diese Berechnungen auf einen Unterschied in der Übergangsdichte zurückgeführt werden. Diese Untersuchungen ermöglichten die Erstellung einer systematischen Bibliothek der optoelektronischen Eigenschaften von fünf verschiedener PBIs und deren verschiedener reduzierter Zustände, welches Forschern insbesondere auf dem Gebiet der transienten

Absorptionsspektroskopie den Nachweis für die Population dieser transienten Spezies ermöglicht.

Zusammenfassend kann festgehalten werden, dass in dieser Arbeit verschiedene nicht-planare Imid-substituierte PAK mit Dinaphthylcorannulen und Perylen als zentralem π-System erfolgreich synthetisiert und untersucht werden konnten. Die Studien umfassten das Selbstorganisationsverhalten neuartiger Corannulenderivate in Lösung und die systematische Variation der Imid- und Buchtreste in vierfach arylierten PBIs. Diese führten zu strukturellen und chemischen Veränderungen, welche sich als nützlich für das tiefere Verständnis der intermolekularen Wechselwirkungen, insbesondere im Festkörper, erwiesen. Die präzise Aufklärung der Eigenschaften einer Reihe von PBIs in ihren neutralen und reduzierten Zuständen dürfte sich des Weiteren in Zukunft für die Analyse von Molekülen und Materialien, welche auf PBIs basieren mittels transienter Absorptionsspektroskopie als nützlich erweisen. Einige der hier beschriebenen Bisimide der Dinaphthylcorannulene[313] sowie kernverdrillten Perylene[314] konnten bereits erfolgreich als Akzeptormaterialien in organischen Solarzellen eingesetzt werden.

Chapter 8

Individual Contribution

The coauthors of the manuscripts included in this cumulative thesis are informed and agree with the reprint and the respective individual contributions as stated below.

Self-Assembly of Bowl-Shaped Naphthalimide-Annulated Corannulene

R. Renner, M. Stolte, F. Würthner, *ChemistryOpen* **2020**, *9*, e1900291.

author	**R. R.**	**M. S.**	**F. W.**
Design der Studie	30%	10%	60%
Synthese	100%	-	-
Charakterisierung	100%	-	-
Optische Untersuchungen	80%	20%	-
NMR Untersuchungen	95%	5%	-
Verfassen der Veröffentlichung	55%	35%	10%
Korrektur der Veröffentlichung	10%	35%	55%
Koordination der Veröffentlichung	20%	20%	60%

Chiral Perylene Bisimide Dyes by Interlocked Arene Substituents in the Bay Area

R. Renner, B. Mahlmeister, O. Anhalt, M. Stolte, F. Würthner, *Chem. Eur. J.* **2021**, *27*, https://doi.org/10.1002/chem.202101877.

author	**R. R.**	**B. M.**	**O. A.**	**M. S.**	**F. W.**
Design der Studie	30%	-	-	-	70%
Synthese	100%	-	-	-	-
Aufreinigung	100%	-	-	-	-
Charakterisierung der Moleküle	100%	-	-	-	-
Optische Untersuchungen	80%	20%	-	-	-
Elektrochemische Untersuchungen	100%	-	-	-	-
Kristallstrukturanalyse	-	-	100%	-	-
Theoretische Berechnungen	100%	-	-	-	-
Verfassen der Veröffentlichung	65%	10%	-	15%	10%
Korrektur der Veröffentlichung	15%	10%	-	25%	50%
Koordination der Veröffentlichung	20%	-	-	20%	60%

Substituent-Dependent Absorption and Fluorescence Properties of Perylene Bisimide Radical Anions and Dianions

R. Renner, M. Stolte, J. Heitmüller, T. Brixner, C. Lambert, F. Würthner, *Mater. Horiz.* **2021**, https://doi.org/10.1039/D1MH01019K.

author	**R. R.**	**M. S.**	**J. H.**	**T. B.**	**C. L.**	**F. W.**
Design der Studie	30%	-	-	-	-	70%
Synthese	100%	-	-	-	-	-
Cyclovoltammetrie	100%	-	-	-	-	-
Spektroelektrochemie	100%	-	-	-	-	-
Fluoreszenzuntersuchung	50%	25%	25%	-	-	-
DFT Rechnungen	100%	-	-	-	-	-
Verfassen der Veröffentlichung	60%	15%	5%	5%	5%	10%
Korrektur der Veröffentlichung	15%	20%	5%	5%	5%	50%
Koordination der Veröffentlichung	20%	10%	10%	5%	5%	50%

Chapter 9

Acknowledgement/Danksagung

Mein besonderer Dank gilt meinem Doktorvater Prof. Dr. Frank Würthner, für das Überlassen des interessanten und sehr spannenden Forschungsthemas, seiner stetigen Unterstützung und zahlreichen hilfreichen Ratschläge. Ebenso bedanke ich mich für seine wissenschaftliche Betreuung sowie gleichzeitigen gewährten Freiheit während der Promotionszeit. Darüber hinaus möchte ich mich für die Bereitstellung der hervorragenden Arbeitsbedingungen bedanken.

Weiterhin möchte ich mich bei Dr. Matthias Stolte, Dr. Kazutaka Shoyama, Dr. David Bialas und Dr. Chantu Saha-Möller für die Hilfe bei fachlichen Fragestellungen sowie die Betreuung im Rahmen der Subgroups bedanken. Im Speziellen bedanke ich mich sehr bei Dr. Matthias Stolte für die Hilfe beim Verfassen und Überarbeiten von Manuskripten.

Ebenfalls möchte ich mich bei Dr. Kazutaka Shoyama, Dr. David Bialas und Dr. Joachim Lindner für die Hilfe und Durchführung von theoretischen Rechnungen bedanken. Dr. Vladimir Stepanenko bin ich für die AFM-Aufnahmen zum Dank verpflichtet. Bei Michael Moos möchte ich mich für die Einführung und Hilfe bei der Messung der Spektroelektrochemie bedanken. Für die Durchführung und Auswertung der Kristallstrukturanalysen möchte ich Olga Anhalt ganz besonders danken. Dr. Matthias Grüne und Patrizia Altenberger danke ich für die Aufnahme diverser NMR-Spektren und Hilfe bei Fragen bezüglich verschiedener NMR Experimente. Ebenfalls bedanke ich mich bei Dr. Michael Büchner und Juliane Adelmann für die massenspektrometrischen Untersuchungen.

Des Weiteren gilt mein Dank Petra Seufert-Baumbach, Anja Rausch und Julius Albert für die Bestellung von Materialien und Chemikalien und die Organisation eines reibungslosen Laboralltags. Bei Christiana Toussaint, Eleonore Klaus, Sarah Bullnheimer und Lisa Weidner bedanke ich mich für die Hilfe bei bürokratischen und organisatorischen Belangen.

Für das Korrekturlesen der Doktorarbeit bedanke ich mich bei Alexander Schulz, Tobias Tröster und Dr. Matthias Stolte.

Für die synthetische Unterstützung bedanke ich mich bei Julius Albert und Anja Rausch, sowie meiner Auszubildenden Sarah Eitel. Auch bedanke ich mich hierfür bei meiner Bachelorandin Elisabeth Mayerhöfer sowie meinen Praktikanten Tobias Tröster, Samuel Trimble, Tobias Flegler, Florian Seebauer und Lukas Stumpf.

Ein weiterer großer Dank geht an alle ehemaligen und aktuellen Mitglieder der Arbeitskreise Würthner, Beuerle und Nowak-Krol für ihre Hilfsbereitschaft und das wunderbare Arbeitsklima, sowie die schöne gemeinsame Zeit während der letzten Jahre.

Zuletzt möchte ich mich noch bei meiner Familie, Freunden und Tobias bedanken, für die andauernde Unterstützung während meines Studiums und der Doktorarbeit, die mir immer bedingungslos zur Seite standen und ohne die das alles nicht möglich gewesen wäre.

Chapter 10

List of Publications

Unprecedented Efficient Structure Controlled Phosphorescence of Silver(I) Clusters Stabilized by Carba-closo-dodecaboranylethynyl Ligands

M. Hailmann, N. Wolf, R. Renner, T. C. Schäfer, B. Hupp, A. Steffen, M. Finze, *Angew. Chem. Int. Ed.* **2016**, *55*, 10507-10511; *Angew. Chem.* **2016**, *128*, 10663-10667.

Silver(I) Clusters with Carba-closo-dodecaboranylethynyl Ligands: Synthesis, Structure and Phosphorescene

M. Hailmann, N. Wolf, R. Renner, B. Hupp, A. Steffen, M. Finze, *Chem. Eur. J.* **2017**, *23*, 11684-11693.

Self-Assembly of Bowl-Shaped Naphthalimide-Annulated Corannulene

R. Renner, M. Stolte, F. Würthner, *ChemistryOpen* **2020**, *9*, e1900291.

Bowl-Shaped Naphthalimide-Annulated Corannulene as Nonfullerene Acceptor in Organic Solar Cells

K. Menekse, R. Renner, B. Mahlmeister, M. Stolte, F. Würthner, *Org. Mater.* **2020**, *2*, 229-234.

Coherent two-dimensional electronic spectroelectrochemistry

J. Heitmüller, K. Eckstein, R. Renner, M. Stolte, T. Hertel, F. Würthner, T. Brixner, *Spectrochim. Acta A* **2021**, *253*, 119567.

Chiral Perylene Bisimide Dyes by Interlocked Arene Substituents in the Bay Area

R. Renner, B. Mahlmeister, O. Anhalt, M. Stolte, F. Würthner, *Chem. Eur. J.* **2021**, *27*, https://doi.org/10.1002/chem.202101877.

Substituent-Dependent Absorption and Fluorescence Properties of Perylene Bisimide Radical Anions and Dianions

R. Renner, M. Stolte, J. Heitmüller, T. Brixner, C. Lambert, F. Würthner, *Mater. Horiz.* **2021**, accepted manuscript, https://doi.org/10.1039/D1MH01019K.

Site-Specific Chemical Doping Reveals Electron Atmospheres at the Surfaces of Organic Semiconductor Crystals

T. He, M. Stolte, Y. Wang, R. Renner, P. Ruden, F. Würthner, C. D. Frisbie, *Nat. Mater.* **2021**, accepted manuscript, https://doi.org/10.21203/rs.3.rs-140330/v1.

Chapter 11

Bibliography

[1] J. Lasota, S. Łyszczarz, P. Kempf, M. Kempf, E. Błońska, *Water Air Soil Pollut.* **2021**, *232*, 74.

[2] C. A. Menzie, B. B. Potocki, J. Santodonato, *Environ. Sci. Technol.* **1992**, *26*, 1278-1284.

[3] K. Ravindra, R. Sokhi, R. Van Grieken, *Atmos. Environ.* **2008**, *42*, 2895-2921.

[4] C. Wang, S. Zhou, S. Wu, J. Song, Y. Shi, B. Li, H. Chen, *Water Sci. Technol.* **2017**, *76*, 2150-2157.

[5] J. de Boer, M. Wagelmans, *Clean – Soil, Air, Water* **2016**, *44*, 648-653.

[6] J.-G. Lee, S.-Y. Kim, J.-S. Moon, S.-H. Kim, D.-H. Kang, H.-J. Yoon, *Food Chem.* **2016**, *199*, 632-638.

[7] A. L. C. Lima, J. W. Farrington, C. M. Reddy, *Environ. Forensics* **2005**, *6*, 109-131.

[8] Y. V. Pashin, L. M. Bakhitova, *Environ. Health Perspect.* **1979**, *30*, 185-189.

[9] V. Girardin, M. Grung, S. Meland, *Sci. Rep.* **2020**, *10*, 10958.

[10] O. O. Alegbeleye, B. O. Opeolu, V. A. Jackson, *Environ. Manage.* **2017**, *60*, 758-783.

[11] L. Salem, *J. Am. Chem. Soc.* **1968**, *90*, 543-552.

[12] S. E. Stein, R. L. Brown, *J. Am. Chem. Soc.* **1987**, *109*, 3721-3729.

[13] F. Würthner, C. R. Saha-Möller, B. Fimmel, S. Ogi, P. Leowanawat, D. Schmidt, *Chem. Rev.* **2016**, *116*, 962-1052.

[14] L. Chen, C. Li, K. Müllen, *J. Mater. Chem. C* **2014**, *2*, 1938-1956.

[15] L. J. Allamandola, A. G. G. M. Tielens, J. R. Barker, *Astrophys. J. Suppl. Ser.* **1989**, *71*, 733-775.

[16] A. G. G. M. Tielens, *Annu. Rev. Astron. Astrophys.* **2008**, *46*, 289-337.

[17] X. Gu, X. Zhang, H. Ma, S. Jia, P. Zhang, Y. Zhao, Q. Liu, J. Wang, X. Zheng, J. W. Y. Lam, D.Ding, B. Z. Tang, *Adv. Mater.* **2018**, *30*, 1801065.

[18] C. Ji, W. Cheng, Q. Yuan, K. Müllen, M. Yin, *Acc. Chem. Res.* **2019**, *52*, 2266-2277.

[19] M. Gingras, *Chem. Soc. Rev.* **2013**, *42*, 968-1006.

[20] M. Gingras, G. Félix, R. Peresutti, *Chem. Soc. Rev.* **2013**, *42*, 1007-1050.

[21] M. Gingras, *Chem. Soc. Rev.* **2013**, *42*, 1051-1095.

[22] K. S. Novoselov, A. K. Geim, S. V. Morozov, D. Jiang, Y. Zhang, S: V. Dubonos, I. V. Grigorieva, A. A. Firsov, *Science* **2004**, *306*, 666-669.

[23] A. K. Geim, *Angew. Chem. Int. Ed.* **2011**, *50*, 6966-6985.

[24] K. S. Novoselov, *Angew. Chem. Int. Ed.* **2011**, *50*, 6986-7002.

[25] T. Cao, F. Zhao, S. G. Louie, *Phys. Rev. Lett.* **2017**, *97*, 216803.

[26] S. Fujii, M. Ziatdinov, M. Ohtsuka, K. Kusakabe, M. Kiguchi, T. Enoki, *Faraday Discuss*, **2014**, *173*, 173-199.

[27] X.-Y. Wang, X. Yao, K. Müllen, *Sci. China Chem.* **2019**, *62*, 1099-1144.

[28] D. Zhang, L. Duan, *J. Phys. Chem. Lett.* **2019**, *10*, 2528-2537.

[29] P. Sonar, M. S. Soh, Y. S. Cheng, J. T. Henssler, A. Sellinger, *Org. Lett.* **2010**, *12*, 3292-3295.

[30] K. Bgattacharyya, T. K. Mukhopadhyay, A. Datta, *Phys. Chem. Chem. Phys.* **2016**, *18*, 14886-14839.

[31] X. Cui, C. Xiao, L. Zhang, Y. Li, Z. Wang, *Chem. Commun.* **2016**, *52*, 13209-13212.

[32] C. Aumaitre, J.-F. Morin, *Chem. Rev.* **2019**, *19*, 1142-1154.

[33] L. Zhang, Y. Cao, N. S. Colella, Y. Liang, J.-L. Brédas, K. N. Houk, A. L. Briseno, *Acc. Chem. Res.* **2015**, *48*, 500-509.

[34] H. W. Kroto, J. R. Heath, S. C. O'Brien, R. F. Curl, R. E. Smalley, *Nature* **1985**, *318*, 162-163.

[35] The Nobel Prize in Chemistry **1996**, nobelprize.org/prizes/chemistry/1996/summary, Retrieved 29.06.2021.

[36] 2008 Kavli Prize Laureates in Nanoscience, https://kavliprize.org/prizes-and-laureates/prizes/2008-kavli-prize-laureates-nanoscience, Retrieved 29.06.2021.

[37] R.-Q. Lu, Y.-Q. Zheng, Y.-N. Zhou, X.-Y. Yan, T. Lei, K. Shi, Y. Zhou, J. Pei, L. Zoppi, K. K. Baldridge, J. S. Siegel, X.-Y. Cao, *J. Mater. Chem. A* **2014**, *2*, 20515-20519.

[38] A. Nowak-Król, K. Shoyama, M. Stolte, F. Würthner, *Chem. Commun.* **2018**, *54*, 13763-13772.

[39] W. Jiang, Y. Li, Z. Wang, *Acc. Chem. Res.* **2014**, *47*, 3135-3147.

[40] B. Pagoaga, L. Giraudet, N. Hoffmann, *Eur. J. Org. Chem.* **2014**, 5178-5195.

[41] Y. Xu, J. Zheng, J. O. Lindner, X. Wen, N. Jiang, Z. Hu, L. Liu, F. Huang, F. Würthner, Z. Xie, *Angew. Chem. Int. Ed.* **2020**, *59*, 10363-10367.

[42] D. Inan, R. K. Dubey, W. F. Jager, F. C. Grozema, *J. Phys. Chem. C.* **2019**, *123*, 36-47.

[43] R. Rieger, K. Müllen, *J. Phys. Org. Chem.* **2010**, *23*, 315-325.

[44] A. Narita, X.-Y. Wang, X. Feng, K. Müllen, *Chem. Soc. Rev.* **2015**, *44*, 6616-6643.

[45] X. Feng, W. Pisula, K. Müllen, *Pure Appl. Chem.* **2009**, *81*, 2157-2251.

[46] A. T. Balaban, F. Harary, *Tetrahedron* **1968**, *24*, 2505-2516.

[47] M. D. Guillén, P. Sopelana, *Polycyclic aromatic hydrocarbons in diverse foods* in Food safety: Contaminants and toxins, ed. J. P. F. D'Mello, 175-197, CAB International, Wallingford, Oxon, UK, **2003**.

[48] K. M. Magiera, V. Aryal, W. A. Chalifoux, *Org. Biomol. Chem.* **2020**, *18*, 2372-2386.

[49] S. R. Bheemireddy, P. C. Ubaldo, A. D. Finke, L. Wang, K. N. Plunkett, *J. Mater. Chem. C.* **2016**, *4*, 3963-3969.

[50] M. Ball, Y. Zhong, Y. Wu, C. Schenck, F. Ng, M. Steigerwald, S. Xiao, C. Nuckolls, *Acc. Chem. Res.* **2015**, *48*, 267-276.

[51] R. Kumar, H. Aggarwal, A. Srivastava, *Chem. Eur. J.* **2020**, 10653-10675.

[52] M. A. Majewski, M. Stępień, *Angew. Chem. Int. Ed.* **2019**, *58*, 86-116.

[53] J. H. Dopper, H. Wynberg, *Tetrahedron Lett.* **1972**, *9*, 763-766.

[54] B. Kumar, R. Bhola, T. Bally, A. Valente, M. K. Cyrański, Ł. Dobrzycki, S. M. Spain, P. Rempała, M. R. Chin, B. T. King, *Angew. Chem. Int. Ed.* **2010**, *49*, 399-402.

[55] B. Kumar, B. T. King, *J. Org. Chem.* **2012**, *23*, 10617-10622.

[56] W. E. Barth, R. G. Lawton, *J. Am. Chem. Soc.* **1966**, *88*, 380-381.

[57] A. Sygula, P. W. Rabideau, *J. Am. Chem. Soc.* **2000**, *122*, 6323-6324.

[58] A. M. Butterfield, B. Gilomen, J. S. Siegel, *Org. Process Res. Dev.* **2012**, *16*, 664-676.

[59] G. Mehta, S. R. Shah, K. Ravikumar, *J. Chem. Soc., Chem. Commun.* **1993**, 1006-1008

[60] H. Sakurai, T. Daiko, T. Hirao, *Science* **2003**, *301*, 5641, 1878.

[61] N. Ikuma, Y. Yoshida, Y. Yakiyama, N. Ngamsomprasert, H. Sakurai, *Chem. Lett.* **2018**, *47*, 736-739.

[62] S. Alvi, R. Ali, *Beilstein J. Org. Chem.* **2020**, *16*, 2212-2259.

[63] M. Saito, H. Shinokubo, H. Sakurai, *Mater. Chem. Front.* **2018**, *2*, 635-661.

[64] S. Higashibayashi, S. Onogi, H. K. Srivastava, G. N. Sastry, Y.-T. Wu, H. Sakurai, *Angew. Chem. Int. Ed.* **2013**, *52*, 7314-7316.

[65] L. T. Scott, M. M. Hashemi, M. S. Bratcher, *J. Am. Chem. Soc.* **1992**, *114*, 1920-1921.

[66] G. N. Sastry, H. S. P. Rao, R. Bednarek, U. D. Priyakumar, *Chem. Commun.* **2000**, 843-844.

[67] A. H. Abdourazak, A. Sygula, P. W. Rabideau, *J. Am. Chem. Soc.* **1993**, *115*, 3010-3011.

[68] B. D. Steinberg, E. A. Jackson, A. S. Filatov, A. Wakamiya, M. A. Petrukhina, L. T. Scott, *J. Am. Chem. Soc.* **2009**, *131*, 10537-10545.

[69] R. B. M. Ansems, L. T. Scott, *J. Am. Chem. Soc.* **2000**, *122*, 2719-2724.

[70] A. H. Abdourazak, Z. Marcinow, A. Sygula, R. Sygula, P. W. Rabideau, *J. Am. Chem. Soc.* **1995**, *117*, 6410-6411.

[71] S. Hagen, M. S. Bratcher, M. S. Erickson, G. Zimmermann, L. T. Scott, *Angew. Chem. Int. Ed. Engl.* **1997**, *36*, 406-408.

[72] S. Mizyed, P. E. Georghiou, M. Bancu, B. Cuadra, A. K. Rai, P. Cheng, L. T. Scott, *J. Am. Chem. Soc.* **2001**, *123*, 12770-12774.

[73] Y.-Y. Xu, H.-R. Tian, S.-H. Li, Z.-C. Chen, Y.-R. Yao, S.-S. Wang, X. Zhang, Z.-Z. Zhu, S.-L. Deng, Q. Zhang, S. Yang, S.-Y. Xie, R.-B. Huang, L.-S. Zheng, *Nat. Commun.* **2019**, *10*, 485.

[74] J. S. Siegel, T. J. Seiders, *Chem. Br.* **1995**, *31*, 313-316.

[75] X. Xiong, C.-L. Deng, B. F. Minaev, G. V. Baryshnikov, X.-S. Peng, H. N. C. Wong, *Chem. Asian J.* **2015**, *10*, 969-975.

[76] K. Yamamoto, T. Harada, M. Nakazaki, *J. Am. Chem. Soc.* **1983**, *105*, 7171-7172.

[77] K. Yamamoto, T. Harada, Y. Okamoto, H. Chikamatsu, M. Nakazaki, Y. Kai, T. Nakao, M. Tanaka, S. Harada, N. Kasai, *J. Am. Chem. Soc.* **1988**, *110*, 3578-3584.

[78] K. Kawai, K. Kato, L. Peng, Y. Segawa, L. T. Scott, K. Itami, *Org. Lett.* **2018**, *20*, 1932-1935.

[79] A. Pradhan, P. Dechambenoit, H. Bock, F. Durola, *J. Org. Chem.* **2013**, *78*, 2266-2274.

[80] Z. Qiu, S. Asako, Y. Hu, C.-W. Ju, T. Liu, L. Rondin, D. Schollmeyer, J.-S. Lauret, K. Müllen, A. Narita, *J. Am. Chem. Soc.* **2020**, *142*, 14814-14819.

[81] J. M. Farrell, V. Grande, D. Schmidt, F. Würthner, *Angew. Chem. Int. Ed.* **2019**, *58*, 16504-16507.

[82] C. Zhu, K. Shoyama, F. Würthner, *Angew. Chem. Int. Ed.* **2020**, *59*, 21505-21509.

[83] J. Luo, X. Xu, R. Mao, Q. Miao, *J. Am. Chem. Soc.* **2012**, *134*, 13796-13803.

[84] S. Hayakawa, A. Kawasaki, Y. Hong, D. Uraguchi, T. Ooi, D. Kim, T. Akutagawa, N. Fukui, H. Shinokubo, *J. Am. Chem. Soc.* **2019**, *141*, 19807-19816.

[85] S. H. Pun, Y. Wang, M. Chu, C. K. Chan, Y. Li, Z. Liu, Q. Miao, *J. Am. Chem. Soc.* **2019**, *141*, 9680-9686.

[86] H. Erdtman, H.-E. Högberg, *Tetrahedron Lett*. **1970**, *11*, 3389-3392.

[87] K. Y. Chernichenko, V. V. Sumerin, R. V. Shpanchenko, E: S. Balenkova, V. G. Nednajdenko, *Angew. Chem. Int. Ed.* **2006**, *45*, 7367-7370.

[88] C.-N. Feng, M.-Y. Kuo, Y.-T. Wu, *Angew. Chem. Int. Ed.* **2013**, *52*, 7791-7794.

[89] A. Sygula, F. R. Fronczek, R. Sygula, P. W. Rabideau, M. M. Olmstead, *J. Am. Chem. Soc.* **2007**, *129*, 3842-3843.

[90] K. Kawasumi, Q. Zhang, Y. Segawa, L. T. Scott, K. Itami, *Nat. Chem.* **2013**, *5*, 739-744.

[91] M. Rickhaus, M. Mayor, M. Juríček, *Chem. Soc. Rev.* **2016**, *45*, 1542-1556.

[92] Y. Shen, C. F. Chen, *Chem. Rev.* **2012**, *112*, 1463-1535.

[93] J. M. Schulman, R. L. Disch, *J. Phys. Chem. A* **1999**, *103*, 6669-6672.

[94] B. M. Deb, G. Kavu, *Can. J. Chem.* **1980**, *58*, 258-262.

[95] T. J. Katz, L. B. Liu, N. D. Willmore, J. M .Fox, A. L. Rheingold, S. H. Shi, C. Nuckolls, B. H. Rickman, *J. Am. Chem. Soc.* **1997**, *119*, 10054-10063.

[96] R. Weitzenböck, H. Lieb, *Monatsh. Chem.* **1912**, *33*, 549-565.

[97] R. Weitzenböck, A. Klingler, *Monatsh. Chem.* **1918**, *39*, 315-323.

[98] R. Weitzenböck, A. Klingler, *J. Chem. Soc.* **1918**, *114*, 494

[99] M. Scholz, M. Mühlstaed, F. Dietz, *Tetrahedron Lett.* **1967**, *8*, 665-668.

[100] J. Elm, J. Lykkebo, T. J. Sørensen, B. W. Laursen, K. V. Mikkelsen, *J. Phys. Chem. A* **2011**, *115*, 12025-12033.

[101] C. Goedicke, H. Stegemeyer, *Tetrahedron Lett.* **1970**, *11*, 937-940.

[102] T. Hartung, R. Machleid, M. Simon, C. Golz, M. Alcarazo, *Angew. Chem. Int. Ed.* **2020**, *59*, 5660-5664.

[103] K. Mori, T. Murase, M. Fujita, *Angew. Chem. Int. Ed.* **2015**, *54*, 6847-6851.

[104] P. Ravat, R. Hinkelmann, D. Steinebrunner, A. Prescimone, I. Bodoky, M. Juríček. *Org. Lett.* **2017**, *19*, 3707-3710.

[105] S. K. Collins, M. P. Vachon, *Org. Biomol. Chem.* **2006**, *4*, 2518-2524.

[106] H. J. Lindner, *Tetrahedron* **1975**, *31*, 281-284.

[107] J. Barroso, J. L. Caballos, S. Pan, F. Murillo, X. Zarate, M. A. Fernandez-Herrera, G. Merino, *Chem. Commun.* **2018**, *54*, 188-191.

[108] A. Pradhan, P. Dechambenoit, H. Bock, F. Durola, *Angew. Chem. Int. Ed.* **2011**, *50*, 12582-12585.

[109] N. P. Hacker, F. W. McOmie, J. Meunier-Piret, M. Van Meerssche, *J. Chem. Soc., Perkin Trans. 1* **1982**, 19-23.

[110] L. Barnett, D. M. Ho, K. K. Baldridge, R. A. Pascal, *J. Am. Chem. Soc.* **1999**, *121*, 727-733.

[111] E. Clar, J. F. Stephen, *Tetrahedron* **1965**, *21*, 467-470.

[112] S. Xiao, M. Myers, Q. Miao, S. Sanaur, K. Pang, M. L. Steigerwald, C. Nuckolls, *Angew. Chem. Int. Ed.* **2005**, *44*, 7390-7394.

[113] V. Berezhnaia, M. Roy, N. Vanthuyne, M. Villa, J.-V. Naubron, J. Rodriguez, Y. Coquerel, M. Gingras, *J. Am. Chem. Soc.* **2017**, *139*, 18508-18511.

[114] T. Hosokawa, Y. Takahashi, T. Matsushima, S. Watanabe, S. Kikkawa, I. Azumaya, A. Tsurusaki, K. Kamikawa, *J. Am. Chem. Soc.* **2017**, *139*, 18512-18521.

[115] S. Xiao, S. J. Kang, Y. Wu, S. Ahn, J. B. Kim, Y.-L. Loo, T. Siegrist, M. L. Steigerwald, H. Li, C. Nuckolls, *Chem. Sci.* **2013**, *4*, 2018-2023.

[116] S. Ma, J. Gu, C. Lin, Z. Luo, Y. Zhu, J. Wang, *J. Am. Chem. Soc.* **2020**, *142*, 16887-16893.

[117] W. Yang, J. H. S. K. Monteiro, A. de Bettencourt-Dias, V. J. Catalano, W. A. Chalifoux, *Angew. Chem. Int. Ed.* **2016**, *55*, 10427-10430.

[118] W. Yang, R. R. Kazemi, N. Karunathilake, V. J. Catalano, M. A. Alpuche-Aviles, W. A. Chalifoux, *Org. Chem. Front.* **2018**, *5*, 2288-2295.

[119] W. Yang, G. Longhi, S. Abbate, A. Lucotti, M. Tommasini, C. Villani, V. J. Catalano, A. O. Lykhin, S. A. Varganov, W. A. Chalifoux, *J. Am. Chem. Soc.* **2017**, *139*, 13102-13109.

[120] B. A. R. Günther, S. Höfener, U. Zschieschang, H. Wadepohl, H. Klauk, L. H. Gade, *Chem. Eur. J.* **2019**, *25*, 14669-14678.

[121[B. Kohl, F. Rominger, M. Mastalerz, *Org. Lett.* **2014**, *16*, 704-707.

[122] B. Kohl, F. Rominger, M. Mastalerz, *Chem. Eur. J.* **2015**, *21*, 17308-17313.

[123] B.-L. Hu, C. An, M. Wagner, G. Ivanova, A. Ivanova, M. Baumgarten, *J. Am. Chem. Soc.* **2019**, *141*, 5130-5134.

[124] S. R. Peurifoy, J. C. Russell, T. J. Sisto, Y. Yang, X. Roy, C. Nuckolls, *J. Am. Chem. Soc.* **2018**, *140*, 10960-10964.

[125] F. E. Golling, M. Quernheim, M. Wagner, T. Nishiuchi, K. Müllen, *Angew. Chem. Int. Ed.* **2014**, *53*, 1525-1528.

[126] M. Quernheim, F. E. Golling, W. Zhang, M. Wagner, H.-J. Räder, T. Nishiuchi, K. Müllen, *Angew. Chem. Int. Ed.* **2015**, *54*, 10341-10346.

[127] S. Kammermeier, P. G. Jones, R. Herges, *Angew. Chem. Int. Ed. Engl.* **1996**, *35*, 2669-2671.

[128] T. Kawase, H. R. Darabi, M. Oda, *Angew. Chem. Int. Ed. Engl.* **1996**, *35*, 2664-2666.

[129] R. Umeda, T. Morinaka, M. Sonoda, Y. Tobe, *J. Org. Chem.* **2005**, *70*, 6133-6136.

[130] D. Lu, H. Wu, Y. Dai, H. Shi, X. Shao, S. Yang, J. Yang, P. Du, *Chem. Commun.* **2016**, *52*, 7164-7167.

[131] M. Ohkita, K. Ando, T. Tsuji, *Chem. Commun.* **2001**, 2570-2571.

[132] S. Lee, E. Chénard, D. L. Gray, J. S. Moore, *J. Am. Chem. Soc.* **2016**, *138*, 13814-13817.

[133] S. Hitosugi, W. Nakanishi, T. Yamasaki, H. Isobe, *Nat. Commun.* **2011**, *2*, 492.

[134] T. Matsuno, S. Kamata, S. Hitosugi, H. Isobe, *Chem. Sci.* **2013**, *4*, 3179-3183.

[135] T. Iwamoto, E. Kayahara, N. Yasuda, T. Suzuki, S. Yamago, *Angew. Chem. Int. Ed.* **2014**, *53*, 6430-6434.

[136] K. S. Unikela, T. L. Roemmele, V. Houska, K. E. McGrath, D. M. Tobin, L. N. Dawe, R. T. Boeré, G. J. Bodwell, *Angew. Chem. Int. Ed.* **2018**, *57*, 1707-1711.

[137] Q. Huang, G. Zhuang, H. Jia, M. Qian, S. Cui, S. Yang, P. Du, *Angew. Chem. Int. Ed.* **2019**, *58*, 6244-6249.

[138] Y. Nakagawa, R. Sekiguchi, J. Kawakami, S. Ito, *Org. Biomol. Chem.* **2019**, *17*, 6843-6853.

[139] D. Lu, G. Zhuang, H. Wu, S. Wang, S. Yang, P. Du, *Angew. Chem. Int. Ed.* **2017**, *56*, 158-162.

[140] H. Jia, G. Zhuang, Q. Huang, J. Wang, Y. Wu, S. Cui, S. Yang, P. Du, *Chem. Eur. J.* **2020**, *26*, 2159-2163.

[141] G. Povie, Y. Segawa, T. Nishihara, Y. Miyauchi, K. Itami, *Science* **2017**, *356*, 172-175.

[142] T. Matsushima, S. Kikkawa, I. Azumaya, S. Watanabe, *ChemistryOpen* **2018**, *7*, 278-281.

[143] T. Fujikawa, D. V. Preda, Y. Segawa, K. Itami, L. T. Scott, *Org. Lett.* **2016**, *18*, 3992-3995.

[144] K. Kato, Y. Segawa, L. T. Scott, K. Itami, *Angew. Chem. Int. Ed.* **2018**, *57*, 1337-1341.

[145] F. Würthner, P. Osswald, R. Schmidt, T. E. Kaiser, H. Mansikkamäki, M. Könemann, *Org. Lett.* **2006**, *8*, 3765-3768.

[146] R. Schmidt. J. H. Oh, Y.-S. Sun, M. Deppisch, A.-M. Krause, K. Radacki, H. Braunschweig, M. Könemann, P. Erk, Z. Bao, F. Würthner, *J. Am. Chem. Soc.* **2009**, *131*, 6215-6228.

[147] M. Oki, *Recent Advances in Atropisomerism* in Topics in Stereochemistry Vol 14; ed. Allinger, N. L., Eliel, E. E., Wilen S. H.; 1-81, Wiley-Interscience, New York, **1983**.

[148] P. Osswald, M. Reichert, G. Bringmann, F. Würthner, *J. Org. Chem.* **2007**, *72*, 3403-3411.

[149] W. Qiu, S. Chen, X. Sun, Y. Liu, D. Zhu, *Org. Lett.* **2006**, *8*, 867-870.

[150] M. Weh, J. Rühe, B. Herbert, A.-M. Krause, F. Würthner, *Angew. Chem. Int. Ed.* **2021**, *60*, 15323-15327.

[151] H. Qian, Z. Wang, W. Yue, D. Zhu, *J. Am. Chem. Soc.* **2007**, *129*, 10664-10665.

[152] Y. Zhen, C. Wang, Z. Wang, *Chem. Commun.* **2010**, *46*, 1926-1928.

[153] Y. Shi, H. Qian, Y. Li, W. Yue, Z. Wang, *Org. Lett.* **2008**, *10*, 2337-2340.

[154] H. Qian, F. Negri, C. Wang, Z. Wang, *J. Am. Chem. Soc.* **2008**, *130*, 17970-17976.

[155] H. Qian, W. Yue, Y. Zhen, S. Di Motta, E. Di Donato, F. Negri, J. Qu, W. Xu, D. Zhu, Z. Wang, *J. Org. Chem.* **2009**, *74*, 6275-6282.

[156] Y. Zhen, W. Yue, Y. Li, W. Jiang, S. Di Motta, E. Di Donato, F. Negri, S. Ye, Z. Wang, *Chem. Commun.* **2010**, *46*, 6078-6080.

[157] G. Liu, C. Xiao, F. Negri, Y. Li, Z. Wang, *Angew. Chem. Int. Ed.* **2020**, *59*, 2008-2012.

[158] Y. Zhong, B. Kumar, S. Oh, M. T. Trinh, Y. Wu, K. Elbert, P. Li, X. Zhu, S. Xiao, F. Ng, M. L. Steigerwald, C. Nuckolls, *J. Am. Chem. Soc.* **2014**, *136*, 8122-8130.

[159] W. Yue, A. Lv, J. Gao, W. Jiang, L. Hao, C. Li, Y. Li, L. E. Polander, S. Barlow, W. Hu, S. Di Motta, F. Negri, S. R. Marder, Z. Wang, *J. Am. Chem. Soc.* **2012**, *134*, 5770-5773.

[160] G. Liu, C. Xiao, F. Negri, Y. Li, Z. Wang, *Angew. Chem. Int. Ed.* **2020**, *59*, 2008-2012.

[161] D. Meng, G. Liu, C. Xiao, Y. Shi, L. Zhang, L. Jiang, K. K. Baldridge, Y. Li, J. S. Siegel, Z. Wang, *J. Am. Chem. Soc.* **2019**, *141*, 5402-5408.

[162] S. Chen, D. Meng, J. Huang, N. Liang, Y. Li, F. Liu, H. Yan, Z. Wang, *CCS Chem.* **2021**, *3*, 78-84.

[163] G. Battagliarin, S. R. Puniredd, S. Stappert, W. Zajaczkowski, S. Wang, C. Li, W. Pisula, K. Müllen, *Adv. Funct. Mater.* **2014**, *24*, 7530-7537.

[164] Y. Geerts, H. Quante, H. Platz, R. Mahrt, M. Hopmeier, A. Böhm, K. Müllen, *J. Mater. Chem.* **1998**, *8*, 2357-2369.

[165] K. Shoyama, D. Schmidt, M. Mahl, F. Würthner, *Org. Lett.* **2017**, *19*, 5328-5331.

[166] K. Shoyama, F. Würthner, *J. Am. Chem. Soc.* **2019**, *141*, 13008-13012.

[167] K. Shi, T. Lei, X.-Y. Wang, J.-Y. Wang, J. Pei, *Chem. Sci.* **2014**, *5*, 1041-1045.

[168] R. Chen, R.-Q. Lu, K. Shi, F. Wu, H.-X. Fang, Z.-X. Niu, X.-Y. Yan, M. Luo, X.-C. Wang, C.-Y. Yang, X.-Y. Wang, B. Xu, H. Xia, J. Pei, X.-Y. Cao, *Chem. Commun.* **2015**, *51*, 13768-13771.

[169] G. Zhang, J. Tan, L. Zhou, C. Liu, J. Liu, Y. Zou, A. Narita, Y. Hu, *Org. Lett.* **2021**, https://doi.org/10.1021/acs.orglett.1c00678.

[170] F. Saal, F. Zhang, M. Holzapfel, M. Stolte, E. Michail, M. Moos, A. Schmiedel, A.-M. Krause, C. Lambert, F. Würthner, P. Ravat, *J. Am. Chem. Soc.* **2020**, *142*, 21298-21303.

[171] R. Renner, M. Stolte, F. Würthner, *ChemistryOpen* **2020**, *9*, 32-39.

[172] F. J. Lovas, R. J. McMahon, J. U. Grabow, M. Schnell, J. Mack, L. T. Scott, R. L. Kuczkowski, *J. Am. Chem. Soc.* **2005**, *127*, 4345-4349.

[173] E. M. Muzammil, D. Halilovic, M. C. Stuparu, *Commun. Chem.* **2019**, *2*, 58.

[174] J. Guilleme, E. Cavero, T. Sierra, J. Ortega, C. L. Folcia, J. Etxebarria, T. Torres, D. Gonzalez-Rodriguez, *Adv. Mater.* **2015**, *27*, 4280-4284

[175] C. G. Claessens, D. Gonzalez-Rodriguez, B. del Rey, T. Torres, G. Mark, H. P. Schuchmann, C. von Sonntag, J. G. MacDonald, R. S. Nohr, *Eur. J. Org. Chem.* **2003**, *14*, 2547-2551.

[176] J. M. Lehn, *PNAS* **2002**, *99*, 4763-4768.

[177] J. M. Lehn, *Science* **2002**, *295*, 2400-2403.

[178] S. Sreejith, N. V. Menon, Y. Wang, H. Joshi, S. Liu, K. C. Chong, Y. Kang, H. Sun, M. C. Stuparu, *Mater. Chem. Front.* **2017**, *1*, 831-837.

[179] J. M. Fernandez-Garcia, P. J. Evans, S. Medina Rivero, I. Fernandez, D. Garcia-Fresnadillo, J. Perles, J. Casado, N. Martin, *J. Am. Chem. Soc.* **2018**, *140*, 17188-17196.

[180] L. N. Dawe, T. A. AlHujran, H. A. Tran, J. I. Mercer, E. A. Jackson, L. T. Scott, P. E. Georghiou, *Chem. Commun.* **2012**, *48*, 5563-5565.

[181] W. Sun, Y. Wang, L. Ma, L. Zheng, W. Fang, X. Chen, H. Jiang, *J. Org. Chem.* **2018**, *83*, 14667-14675.

[182] K. Yoshida, A. Osuka, *Chem. Eur. J.* **2015**, *21*, 11727-11734.

[183] J. Guilleme, J. Arago, E. Orti, E. Cavero, T. Sierra, J. Ortega, C. L. Folcia, J. Etxebarria, D. Gonzalez-Rodriguez, T. Torres, *J. Mater. Chem. C* **2015**, *3*, 985-989.

[184] M. A. Petrukhina, *Dalton Trans.* **2019**, *48*, 5125-5130.

[185] S. N. Spisak, A. V. Zabula, A. S. Filatov, A. Y. Rogachev, M. A. Petrukhina, *Angew. Chem. Int. Ed.* **2011**, *50*, 8090-8094.

[186] A. Haupt, D. Lentz, *Chem. Eur. J.* **2018**, *25*, 3440-3454.

[187] A. Haupt, R. Walter, B. Loll, D. Lentz, *Eur. J. Org. Chem.* **2018**, 6338-6342.

[188] K. Shoyama, M. Mahl, S. Seifert, F. Würthner, *J. Org. Chem.* **2018**, *83*, 5339-5346.

[189] Z. J. Chen, B. Fimmel, F. Würthner, *Org. Biomol. Chem.* **2012**, *10*, 5845-5855.

[190] Z. J. Chen, A. Lohr, C. R. Saha-Möller, F. Würthner, *Chem. Soc. Rev.* **2009**, *38*, 564-584.

[191] F. Würthner, Z. J. Chen, V. Dehm, V. Stepanenko, *Chem. Commun.* **2006**, 1188-1190.

[192] F. Fennel, J. Gershberg, M. Stolte, F. Würthner, *Phys. Chem. Chem. Phys.* **2018**, *20*, 7612-7620.

[193] J. Gershberg, F. Fennel, T. H. Rehm, S. Lochbrunner, F. Würthner, *Chem. Sci.* **2016**, *7*, 1729-1737.

[194] A. R. Monahan, A. F. Deluca, J. A. Brado, *J. Phys. Chem.* **1972**, *76*, 446-449.

[195] F. Würthner, C. Thalacker, S. Diele, C. Tschierske, *Chem. Eur. J.* **2001**, *7*, 2245-2253.

[196] F. Würthner, S. Yao, T. Debaerdemaeker, R. Wortmann, *J. Am. Chem. Soc.* **2002**, *124*, 9431-9447.

[197] Z. Chen, V. Stepanenko, V. Dehm, P. Prins, L. D. A. Siebbeles, J. Seibt, P. Marquetand, V. Engel, F. Würthner, *Chem. Eur. J.* **2007**, *13*, 436-449.

[198] J. M. Lim, P. Kim, M-C. Yoon, J. Sung. V. Dehm, Z. Chen, F. Würthner, D. Kim, *Chem. Sci.* **2013**, *4*, 388-397.

[199] K. Nagarajan, A.R. Mallia, K. Muraleedharan, M. Hariharan, *Chem. Sci.* **2017**, *8*, 1776-1782.

[200] F. C. Spano, A*cc. Chem. Res.* **2010**, *43*, 429-439.

[201] T. Brixner, R. Hildner, J. Köhler, C. Lambert, F. Würthner, *Adv. Energy Mater.* **2017**, *7*, 1700236.

[202] A. Sygula, S. Saebø, *Int. J. Quantum Chem.* **2009**, *109*, 65-72.

[203] Z. Chen, U. Baumeister, C. Tschierske, F. Würthner, *Chem. Eur. J.* **2007**, *13*, 450-465.

[204] Y. Zhong, T. J. Sisto, B. Zhang, K. Miyata, X.-Y. Zhu, M. L. Steigerwald, F. Ng, C. Nuckolls, *J. Am. Chem. Soc.* **2017**, *139*, 5644-5647.

[205] J. J. P. Stewart, *J. Mol. Model.* **2007**, *13*, 1173-1213.

[206] J. Řezáč, P. Hobza, *J. Chem. Theory Comput.* **2012**, *8*, 141–151.

[207] MOPAC2016, Version: 16.230L, James J. P. Stewart, *Stewart Computational Chemistry*, Colorado Springs, CO, USA, web: HTTP://OpenMOPAC.net (**2016**).

[208] H. Friebolin, *Basic One- and Two-Dimensional NMR Spectroscopy*, 319-323, Wiley-VCH, Weinheim, **2005**.

[209] R. Neufeld, D. Stalke, *Chem. Sci.* **2015**, *6*, 3354-3364.

[210] R. Renner, B. Mahlmeister, O. Anhalt, M. Stolte, F. Würthner, *Chem. Eur. J.* **2021**, accepted manuscript, https://doi.org/10.1002/chem.202101877.

[211] K. Hunger, W. Herbst, *Pigments, Organic* in Ullmann's Encyclopedia of Industrial Chemistry, Wiley-VCH, Weinheim, **2000**.

[212] F. Würthner, *Chem. Commun.* **2004**, 1564-1579.

[213] M. Greene, *High Performance Pigments*, Chapter 16, Wiley-VCH, Weinheim, **2009**.

[214] A. Nowak-Król, F. Würthner, *Org. Chem. Front.* **2019**, *6*, 1272-1318.

[215] G. Seybold, G. Wagenblast, *Dyes Pigm.* **1989**, *11*, 303-317.

[216] D. Schmidt, D. Bialas, F. Würthner, *Angew. Chem. Int. Ed.* **2015**, *54*, 3611-3614.

[217] S. Kumar, J. Shukla, Y. Kumar, P. Mukhopadhyay, *Org. Chem. Front.* **2018**, *5*, 2254-2276.

[218] M. Gsänger, J. H. Oh, M. Könemann, H. W. Höffken, A.-M. Krause, Z. Bao, F. Würthner, *Angew. Chem. Int. Ed.* **2010**, *49*, 740-743.

[219] B. A. Jones, A. Facchetti, M. R. Wasielewski, T. J. Marks, *J. Am. Chem. Soc.* **2007**, *129*, 15259-15278.

[220] J. Qu, J. Zhang, A. C. Grimsdale, K. Müllen, F. Jaiser, X. Yang, D. Neher, *Macromolecules* **2004**, *37*, 8297-8306.

[221] S. V. Dayneko, M. Rahmati, M. Pahlevani, G. C. Welch, *J. Mater. Chem. C* **2020**, *8*, 2314-2319.

[222] R. Hecht, J. Kade, D. Schmidt, A. Nowak-Król, *Chem. Eur. J.* **2017**, *23*, 11620-11628.

[223] L. Li, Y.-J. Hong, D.-Y. Chen, M.-J. Lin, *Chem. Eur. J.* **2017**, *23*, 16612-16620.

[224] L. Li, H.-X. Gong, D.-Y. Chen, M.-J. Lin, *Chem. Eur. J.* **2018**, *24*, 13188-13196.

[225] B. E. Hardin, E. T. Hoke, P. B. Armstrong, J.-H. Yum, P. Comte, T. Torres, J. M. J. Fréchet, M. K. Nazeeruddin, M. Grätzel, M. D. McGehee, *Nat. Photonics* **2009**, *37*, 406-411.

[226] N. Zink-Lorre, E. Font-Sanchis, Á. Sastre-Santos. F. Fernández-Lázaro, *Chem. Commun.* **2020**, *56*, 3824-3838.

[227] Q. Li, X. Hao, J. Guo, X.-K. Ren, S. Xia, W. Zhang, Y. Feng, *Macromol. Rapid Commun.* **2019**, *40*, 1800916.

[228] C. Kohl, T. Weil, J. Qu, K. Müllen, *Chem. Eur. J.* **2004**, *10*, 5297-5310.

[229] F. C. De Schryver, T. Vosch, M. Cotlet, M. Van der Auweraer, K. Müllen, J. Hofkens, *Acc. Chem. Res.* **2005**, *38*, 514-522.

[230] T. Teraoka, S. Hiroto, H. Shinokubo, *Org. Lett.* **2011**, *13*, 2532-2535.

[231] G. Battagliarin, C. Li, V. Enkelmann, K. Müllen, *Org. Lett.* **2011**, *13*, 3012-3015.

[232] F. Würthner, V. Stepanenko, Z. Chen, C. R. Saha-Möller, N. Kocher, D. Stalke, *J. Org. Chem.* **2004**, *69*, 7933-7939.

[233] C. Li, H. Wonneberger, *Adv. Mater.* **2012**, *24*, 613-636.

[234] M. Queste, C. Cadiou, B. Pagoaga, L. Giraudet, N. Hoffmann, *New J. Chem.* **2010**, *34*, 2537-2545.

[235] Q. Yan, D. Zhao, *Org. Lett.* **2009**, *11*, 3426-3429.

[236] R. Mishra, R. Regar, V. Singh, P. Panini, R. Singhal, M. L. Keshtov, G. D. Sharma, J. Sankar, *J. Mater. Chem. A* **2018**, *6*, 574-582.

[237] P. Osswald, F. Würthner, *J. Am. Chem. Soc.* **2007**, *129*, 14319-14326.

[238] M. M. Safont-Sempere, P. Osswald, M. Stolte, M. Grüne, M. Renz, M. Kaupp, K. Radacki, H. Braunschweig, F. Würthner, *J. Am. Chem. Soc.* **2011**, *133*, 9580-9591.

[239] F. Würthner, *Pure Appl. Chem.* **2006**, *78*, 2341-2349.

[240] M. Stolte, R. Hecht, Z. Xie, L. Liu, C. Kaufmann, A. Kudzus, D. Schmidt, F. Würthner, *Adv. Optical Mater.* **2020**, *8*, 2000926.

[241] P. Leowanawat, A. Nowak-Król, F. Würthner, *Org. Chem. Front.* **2016**, *3*, 537-544.

[242] G. R. Desiraju, A. Gavezzotti, *Acta Cryst.* **1989**, *B45*, 473-482.

[243] F. P. Gasparro, N. H. Kolodny, *J. Chem. Educ.* **1977**, *54*, 258-261.

[244] H. Langhals, S. Demming, H. Huber, *Spectrochim. Acta* **1988**, *44*, 1189-1193.

[245] P. Ravat, *Chem. Eur. J.* **2021**, *27*, 3957-3967.

[246] A. Nowak-Król, M. I. S. Röhr, D. Schmidt, F. Würthner, *Angew. Chem. Int. Ed.* **2017**, *56*, 11774–11778.

[247] R. Sens, K. H. Drexhage, *J. Lumin.* **1981**, *24*, 709-712.

[248] W. H. Laarhoven, W. J. C. Prinsen, *Top. Curr. Chem.* **1984**, *125*, 63-130.

[249] A. I. Meyers, R. J. Himmelsbach, *J. Am. Chem. Soc.* **1985**, *107*, 682-685.

[250] P. Reine, A. M. Ortuño, I. F. A. Mariz, M. Ribagorda, J. M. Cuerva, A. G. Campaña, E. Maçôas, D. Miguel, *Front. Chem.* **2020**, *8*, 306.

[251] B. Liu, M. Böckmann, W. Jiang, N. L. Doltsinis, Z. Wang, *J. Am. Chem. Soc.* **2020**, *142*, 7092-7099.

[252] J. Wade, J. R. Brandt, D. Reger, F. Zinna, K. Y. Amsharov, N. Jux, D. L. Andrews, M. J. Fuchter, *Angew. Chem. Int. Ed.* **2021**, *60*, 222-227.

[253] L. Zhang, I. Song, J. Ahn, M. Han, M. Linares, M. Surin, H.-J. Zhang, J. H. Oh, J. Lin, *Nat. Commun.* **2021**, *12*, 142.

[254] K. Dhbaibi, L. Favereau, M. Srebro-Hooper, M. Jean, N. Vanthuyne, F. Zinna, B. Jamoussi, L. Di Bari, J. Autschbach, J. Crassous, *Chem. Sci.* **2018**, *9*, 735-742.

[255] K. Deuchert, S. Hünig, *Angew. Chem. Int. Ed. Engl.* **1979**, *17*, 875-886.

[256] W. Geuder, S. Hünig, A. Suchy, *Tetrahedron* **1986**, *42*, 1665-1677.

[257] F. Würthner, A. Sautter, J. Schilling, *J. Org. Chem.* **2002**, *67*, 3037-3044.

[258] S. Mathew, M. R. Johnston, *Chem. Eur. J.* **2009**, *15*, 248-253.

[259] K. Mahata, P. D. Frischmann, F. Würthner, *J. Am. Chem. Soc.* **2013**, *135*, 15656-15661.

[260] G. M. Sheldrick, *Acta Crystallogr. A* **2008**, 64, 112-122.

[261] Gaussian 16, Revision C.01, M. J. Frisch, G. W. Trucks, H. B. Schlegel, G. E. Scuseria, M. A. Robb, J. R. Cheeseman, G. Scalmani, V. Barone, G. A. Petersson, H. Nakatsuji, X. Li, M. Caricato, A. V. Marenich, J. Bloino, B. G. Janesko, R. Gomperts, B. Mennucci, H. P. Hratchian, J. V. Ortiz, A. F. Izmaylov, J. L. Sonnenberg, D. Williams-Young, F. Ding, F. Lipparini, F. Egidi, J. Goings, B. Peng, A. Petrone, T. Henderson, D. Ranasinghe, V. G. Zakrzewski, J. Gao, N. Rega, G. Zheng, W. Liang, M. Hada, M. Ehara, K. Toyota, R. Fukuda, J. Hasegawa, M. Ishida, T. Nakajima, Y. Honda, O. Kitao, H. Nakai, T. Vreven, K. Throssell, J. A. Montgomery, Jr., J. E. Peralta, F. Ogliaro, M. J. Bearpark, J. J. Heyd, E. N. Brothers, K. N. Kudin, V. N. Staroverov, T. A. Keith, R. Kobayashi, J. Normand, K. Raghavachari, A. P. Rendell, J. C. Burant, S. S. Iyengar, J. Tomasi, M. Cossi, J. M. Millam, M. Klene, C. Adamo, R. Cammi, J. W. Ochterski, R. L. Martin, K. Morokuma, O. Farkas, J. B. Foresman, and D. J. Fox, Gaussian, Inc., Wallingford CT, **2016**.

[262] J. Merz, J. Fink, A. Friedrich, I. Krummenacher, H. H. Al Mamari, S. Lorenzen, M. Hähnel, A. Eichhorn, M. Moos, M. Holzapfel, H. Braunschweig, C. Lambert, A. Steffen, L. Ji, T. B. Marder, *Chem. Eur. J.* **2017**, *23*, 13164-13180.

[263] R. Renner, M. Stolte, J. Heitmüller, T. Brixner, C. Lambert, F. Würthner, *Mater. Horiz.* **2021**, https://doi.org/10.1039/D1MH01019K.

[264] C. Huang, S. Barlow, S. R. Marder, *J. Org. Chem.* **2011**, *76*, 2386-2407.

[265] W. Herbst, K. Hunger, *Industrial Organic Pigments: Production, Properties, Applications*, 3rd ed., Wiley-VCH, Weinheim, **2004**.

[266] E. Steingruber, *Indigo and Indigo Colorants* in Ullmann's Encyclopedia of Industrial Chemistry, Wiley-VCH, Weinheim, **2004**.

[267] H.-G. Wang, S. Yuan, D.-I. Ma, X.-I. Huang, F.-I. Meng, X.-B. Zhang, *Adv. Energy Mater.* **2014**, *4*, 1301651.

[268] M. Warczak, M. Gryszel, M. Jakesova, V. Đerek, E. D. Głowacki, *Chem. Commun.* **2018**, *54*, 1960-1963.

[269] G. Li, Y. Zhao, J. Li, J. Cao, J. Zhu, X. W. Sun, Q. Zhang, *J. Org. Chem.* **2015**, *80*, 196-203.

[270] X. Zhan, Z.-A. Tan, B. Domercq, Z. An, X. Zhang, S. Barlow, Y. Li, D. Zhu, B. Kippelen, S. R. Marder, *J. Am. Chem. Soc.* **2007**, *129*, 7246-7247.

[271] M. A. Iron, R. Cohen, B. Rybtchinski, *J. Phys. Chem.* **2011**, *115*, 2047-2056.

[272] V. V. Roznyatovskiy, D. M. Gradner, S. W. Eaton, M. R. Wasielewski, *Org. Lett.* **2014**, *16*, 696-699.

[273] R. O. Marcon, S. Brochsztain, *Langmuir* **2007**, *23*, 11972-11976.

[274] B. Rybtchinski, L. E. Sinks, M. R. Wasielewski, *J. Am. Chem. Soc.* **2004**, *126*, 12268-12269.

[275] W. Kim, T. Kim, S. Kang, Y. Hong, F. Würthner, D. Kim, *Angew. Chem. Int. Ed.* **2020**, *132*, 8571-8578.

[276] M. S. Rodríguez-Morgande, T. Torres, C. Atienza-Castellanos, D. M. Guldi, *J. Am. Chem. Soc.* **2006**, *128*, 15145-15154.

[277] I. Ghosh, T. Ghosh, J. I. Bardagi, B. König, *Science* **2014**, *346*, 725-728.

[278] H.-X. Gong, Z. Cao, M.-H. Li, S.-H. Liao, M.-J. Lin, *Org. Chem. Front.* **2018**, *5*, 2296-2302.

[279] C. J. Zeman, S. Kim, F. Zhang, K. S. Schanze, *J. Am. Chem. Soc.* **2020**, *142*, 2204-2207.

[280] C. Rosso, G. Filippini, M. Prato, *Eur. J. Org. Chem.* **2021**, 1193-1200.

[281] Y. Xu, J. Zheng, J. O. Lindner, X. Wen, N. Jiang, Z. Hu, L. Liu, F. Huang, F. Würthner, Z. Xie, *Angew. Chem. Int. Ed.* **2020**, *59*, 10363-10367.

[282] E. Shirman, A. Ustinov, N. Ben-Shitrit, H. Weissman, M. A. Iron, R. Cohen, B. Rybtchinski, *J. Phys. Chem. B* **2008**, *112*, 8855-8858.

[283] S. Seifert, D. Schmidt, F. Würthner, *Chem. Sci*. **2015**, *6*, 1663-1667.

[284] Q. Li, H. Guo, X. Yang, S. Zhang, H. Zhang, *Tetrahedron*, **2017**, *73*, 6632-6636.

[285] E. He, J. Wang, H. Liu, Z. He, H. Zhao, W. Bao, R. Zhang, H. Zhang, *J. Mater. Sci.* **2016**, *51*, 9229-9238.

[286] Y. Kumar, S. Kumar, D. Bansal, P. Mukhopadhyay, *Org. Lett.* **2019**, *21*, 2185-2188.

[287] J. Heitmüller, K. Eckstein, R. Renner, M. Stolte, T. Hertel, F. Würthner, T. Brixner, *Spectrochim. Acta, Part A* **2021**, *253*, 119567.

[288] P. E. Hartnett, C. M. Mauck, M. A. Harris, R. M. Young, Y.-L. Wu, T. J. Marks, M. R. Wasielewski, *J. Am. Chem. Soc.* **2017**, *139*, 749-756.

[289] L. H. Slooff, E. E. Bende, A. R. Burgers, T. Budel, M. Pravettoni, R. P. Kenny, E. D: Dunlop, A. Büchtemann, *phys. stat. sol. (RRL)* **2008**, *2*, 257-259

[290] Z. Chen, M. G. Debije, T. Debaerdemaeker, P. Osswald, F. Würthner, *ChemPhysChem* **2004**, *5*, 137-140.

[291] R. Kinderman, L. H. Slooff, A. R. Burgers, N. J. Bakker, A. Büchtemann, R. Danz, J. A. M. van Rosmalen, *J. Sol. Energy Eng.* **2007**, *129*, 277-282.

[292] Y. H. Cai, L. J. Huo, X. B. Sun, D. H. Wei, M. S. Tang, Y. M. Sun, *Adv. Energy Mater.* **2015**, *5*, 1500032.

[293] Y. H. Cai, X. Y. Guo, X. B. Sun, D. H. Wei, M. M. Yu, L. J. Huo, Y. M. Sun, *Sci. China Mater.* **2016**, *59*, 427-434.

[294] B. A. R. Günther, S. Höfener, R. Eichelmann, U. Zschieschang, H. Wadepohl, H. Klauk, L. H. Gade, *Org. Lett.* **2020**, *22*, 2298-2302.

[295] L. Ji, M. Haehnel, I. Krummenacher, P. Biegger, F. L. Geyer, O. Tverskoy, M. Schaffroth, J. Han, A. Dreuw, T. B. Marder, U. H. F. Bunz, *Angew. Chem. Int. Ed.* **2016**, *55*, 10498-10501.

[296] M. Kozaki, K. Sugimura, H. Ohnishi, K. Okada, *Org. Lett.* **2006**, *8*, 5235-5238.

[297] A. A. Haidry, J. Puskelova, T. Plecenik, P. Durina, J. Gregus, M. Truchly, T. Roch, M. Zahoran, M. Vargova, P. Kus, A. Plecenik, G. Plesch, *Appl. Surf. Sci.* **2012**, *259*, 270-275.

[298] H. Fritzsche, *J. Non-Cryst. Solids* **1971**, *6*, 49-71.

[299] D. Gosztola, M. P. Niemczyk, W. Svec, A. S. Lukas, M. R. Wasielewski, *J. Phys. Chem. A* **2000**, *104*, 6545-6551.

[300] M. Bixon, J. Jortner, J. Cortes, H. Heitele, M. E. Michel-Beyerle, *J. Phys. Chem.* **1994**, *98*, 7289-7299.

[301] F. Nolde, J. Qu, C. Kohl, N. G. Pschirer, E. Reuther, K. Müllen, *Chem. Eur. J.* **2005**, *11*, 3959-3967.

[302] F. O. Holtrup, G. R. J. Müller, H. Quante, S. De Feyter, F. C. De Schryver, K. Müllen, *Chem. Eur. J.* **1997**, *3*, 219-225.

[303] S. Seifert, Doctoral dissertation, Julius-Maximilians-Universität Würzburg, **2017**.

[304] E. H. A. Beckers, S. C. J. Meskers, A. P. H. J. Schenning, Z. Chen, F. Würthner, R. A. J. Janssen, *J. Phys. Chem. A* **2004**, *108*, 6933-6937.

[305] R. Englman, J. Jortner, *Mol. Phys.* **1970**, *18*, 145-164.

[306] S. J. Strickler, R. A. Berg, *J. Chem. Phys.* **1962**, *37*, 814-822.

[307] T. Lu, F. Chen, *J. Comput. Chem.* **2012**, *33*, 580-592.

[308] R. Herges, D. Geuenich, *J. Phys. Chem. A* **2001**, *105*, 3214-3220.

[309] D. Geuenich, K. Hess, F. Köhler, R. Herges, *Chem. Rev.* **2005**, *105*, 3758-3772.

[310] W. Yue, W. Jiang, M. Bockmann, N. L. Doltsinis, Z. H. Wang, *Chem. Eur. J.* **2014**, *20*, 5209-5213.

[311] J. Sworakowski, J. Lipiński, K. Janus, *Org. Electron.* **2016**, *33*, 300-310.

[312] S. J. Borg, S. P. Best, *J. Electroanal. Chem.* **2002**, *535*, 57-64.

[313] K. Menekse, R. Renner, B. Mahlmeister, M. Stolte, F. Würthner, *Org. Mater.* **2020**, *2*, 229-234.

[314] B. Mahlmeister, R. Renner, O. Anhalt, M. Stolte, F. Würthner, manuscript in preparation.